Development of the Zinc-Chlorine Battery for Utility Applications

EM-1051, Parts 4–Appendixes
Research Project 226-3

Interim Report, April 1979
Work Period January 1, 1977– March 31, 1978

Prepared by

ENERGY DEVELOPMENT ASSOCIATES
A Gulf + Western Company
1100 W. Whitcomb Avenue
Madison Heights, Michigan 48071

Prepared for

Electric Power Research Institute
3412 Hillview Avenue
Palo Alto, California 94304

EPRI Project Manager
J. Birk
Fossil Fuel and Advanced Systems Division

ORDERING INFORMATION

Requests for copies of this report should be directed to Research Reports Center (RRC), Box 10090, Palo Alto, CA 94303, (415) 961-9043. There is no charge for reports requested by EPRI member utilities and affiliates, contributing nonmembers, U.S. utility associations, U.S. government agencies (federal, state, and local), media, and foreign organizations with which EPRI has an information exchange agreement. On request, RRC will send a catalog of EPRI reports.

NOTICE

Prepared by
Energy Development Associates
Madison Heights, Michigan

ABSTRACT

The zinc-chlorine battery system is presently under development as a peak-shaving energy-storage device for the electric-utility industry. The technical feasibility of this battery system for the peak-shaving application was confirmed in an earlier program, RP226-1. A subsequent program, RP226-2, resulted in: (a) a successful demonstration of an 18-kWh breadboard system; and (b) preparation of two conceptual designs of a 100-MWh (20MW) zine-chlorine battery plant. Cost analyses for the two conceptual designs indicated that these battery plants, located at utility substations, would be highly competitive with combustion turbines from an electricity-cost standpoint. The two principal thrusts of this follow-on program, Phase I of RP226-3, were: (1) preparation and analysis of a new 100-MWh plant design; and (2) design, fabrication, and initial testing of a 45-Wh battery module--the basic unit of the new 100-MWh plant design. Development programs on electrode research, electrolyte optimization, cell design, battery-performance verification, and low-cost materials and processes were conducted in support of these objectives.

A new conceptual design of a 100-MWh battery plant located at a utility substation was prepared. This design, designated Mark 4, is based on the concept of fully-integrated zinc-chlorine hydrate battery modules, i.e. each module contains not only the battery stack but also chlorine-hydrate formation, storage, and decomposition equipment. The battery plant comprises thirty-six independent strings--each string consisting of 44 series-connected 66-kWh battery modules. A conceptual manufacturing plan for a production rate of 100 battery modules per day was prepared. The installed cost of the 100-MWh battery plant was estimated to be $26/kWh plus $91/kW (1977 $). The safety, environmental, and legal aspects of siting 100-MWh zinc-chlorine battery plants at substations in residential areas were also analyzed. The Mark 4 design is judged to be optimal in the areas of performance, safety, and manufacturability, while comparing favorably in cost and reliability to earlier designs.

The Mark 4 module prototype was designed, fabricated, assembled, and tested during Phase I. The 45-kWh module, which performed well as a system, delivered in excess of the design level for dc energy output. However, the efficiency, at 50%, was lower than the design target of 63%. The two major contributors to the reduced efficiency

have been identified. Both of these design-related problems will be addressed during the refurbishing of the battery module which is planned for Phase II of RP226-3.

The significant accomplishments in the development program during Phase I are as follows: (1) qualification of porous graphites--the chlorine-electrode material--and plastics which meet the cost criteria for commercialization; (2) development of an in-situ technique for chlorine-electrode activation which shortens the time required from ten or more days to a matter of hours; (3) invention of a dendrite-inhibiting additive which will result in higher-efficiency lower-cost battery stacks; (4) understanding the major cause of significant levels of hydrogen evolution in battery systems, e.g., the 18-kWh battery of RP226-2; and (5) demonstration of 500 charge-discharge cycles--20-25% of the commercialization target--on a 1.7-kWh system without performance deterioration.

EPRI PERSPECTIVE

PROJECT DESCRIPTION

EPRI, DOE and EDA are engaged in a closely coordinated major program to develop a zinc-chlorine battery for utility energy storage. The EPRI portion of this program is to provide the necessary technology base; the goal of the DOE-sponsored portion of the program is to design and construct a 5-MWh battery for BEST facility testing. The EPRI-sponsored work is covered in a 39-month, $7.6 million contract initiated in January, 1977; the costs are equally shared by EDA and EPRI. The DOE portion is covered in a separate 33-month, $11.5 million contract with EDA initiated in January, 1979. This report reviews progress of the EPRI-EDA contract for the period from January, 1977 through March, 1978.

PROJECT OBJECTIVE

The ultimate objective of this effort is the commercialization of battery energy storage systems for utility application. A major objective was to build and test a 45-kWh module. This module is the basic building block of a battery energy storage system. Further objectives were to develop the components and subsystems for this module. In addition, work to demonstrate cycle-life potential, to identify failure mechanisms, and to ascertain the economic viability of the technology has continued.

PROJECT RESULTS

The scale-up hardware from a 20-kWh breadboard system (late-1976) to a 45-kWh fully-integrated battery module (early-1978) was accomplished. However, the performance of the first 45-kWh module was low; energy efficiency was only about 50% compared to a design goal of 63%. This problem is receiving major attention in the present phase of the project. Recent results of cell tests suggest that the problem can be resolved. Four more 45-kWh modules will be tested in 1979. Performance of these will give us insight into the status of the technology and the likelihood of technical success.

Before a 5-kWh battery prototype can be fabricated and tested in the BEST facility, several questions need to be answered and some major problems remain to be solved.

These include the demonstration of (1) adequate performance and life using low-cost chlorine electrodes, (2) zinc electrodes having improved-capacity and greater reliability, and (3) reliable and durable 50-kWh battery modules. In addition, adequate safety of commercial battery systems must be assured, as these batteries may be sited at substations in residential areas. These needs are now being addressed as part of the DOE and EPRI programs at EDA.

The zinc-chlorine system continues to be a strong contender for use as an energy-storage system for electric utilities. However, problems continue to make this a difficult effort and commercial hardware is likely to be 5-10 years away.

James R. Birk, Project Manager
Fossil Fuel and Advanced Systems Division

ACKNOWLEDGMENTS

Energy Development Associates

P. Symons
C. Warde
P. Carr

F. Baker
H. Catherino
C. Chi
M. Hammond
G. Henriksen

H. Bjorkman
W. Coughlin
A. Laethem
A. Stein
C. Whittlesey

D. Aller
C. Blevins
A. Chu
C. Flenniken
P. Racenis
G. Sussman
P. Tylutki

Wayne State University

J. Jorné
J. Kim
D. Kralik

Purdue University

W. Leidenfrost
J. Loveley
B. Korenic

CONTENTS

PART IV

CELL AND BATTERY TESTING

Section 22

INTRODUCTION TO PART IV

Part IV presents the test results for cells and batteries other than the 45kWh battery module, which is described in Part III. In Table 22-1, these systems are listed along with their installation dates, their significance to the overall program, and the test activities performed on them during Phase I.

Table 22-1

BATTERY TESTING PROGRAM

System	Installation Date	Significance	Activities During Phase I
20kWh battery system	1976	Flat-plate chlorine electrode technology. Demonstrated advanced battery-design technology.	Mechanical and electrochemical evaluation and testing.
8.3kWh Submodule	1977	Basic unit of 45kWh battery module.	Electrochemical and design evaluations.
1.7kWh battery with graphite chlorine electrodes	1976	Use of graphite chlorine electrodes. First system automated with microprocessor.	Cycling for efficiency and life data. Limited statistical testing program.
1kWh battery with ruthenized-titanium chlorine	1975	Demonstrated 100 cycles at 75% electrochemical energy efficiency in 1975. Delivered energy increased to 1.4kWh in 1976.	On cycle test for efficiency and life data.
2 single cells	1975	Graphite chlorine electrodes.	Cells terminated.
Chlorine-chlorine cells	--	Accelerated life testing on graphite chlorine electrodes.	Cell designed and test plan devised. Experimental program will be initiated during Phase II.

The 20kWh system was designed, built, and cycled in 1976 and early 1977 as part of RP226-2 (22-1). Upon completion of RP226-2, this system became part of the battery-testing program. As described in Section 23, a thorough evaluation of its design was made which resulted in some minor changes to the battery stack. Based on measurements of parasitic currents (inter-cell leakage) and corrosion currents (chlorine diffusion to the zinc electrode), further improvements in battery performance were realized. More importantly, the information obtained from the detailed evaluation of this system was applied to the design of the 45kWh modules.

The 8.3kWh submodules, six of which form the battery stack in the 45kWh module, were used to evaluate both the engineering aspects and electrochemical operation of the 45kWh battery system. The evaluation techniques used on these submodules were similar to those used on the 20kWh battery. The testing of these submodules is discussed in Section 24.

The 1.7kWh battery with porous-graphite chlorine electrodes was built in 1976 (22-2). Testing of this system was fully automated in early 1977 when installation of a microprocessor-based control system was successfully completed. This control system has greatly increased the cycling rate on the system and the enhanced cycling reliability has encouraged the use of statistical techniques to evaluate battery performance in a limited testing program. To attest to the success of the microprocessor, a total of 446 cycles were accumulated during Phase I of the current EPRI program, for a total of 500 cycles. The average energy efficiency was 63.9% ± 1.0%. The performance of this system during Phase I is discussed in Section 25.

A 1kWh battery system with ruthenia-catalyzed porous-titanium chlorine electrodes was built and successfully tested in 1975 (22-3). In 1976, the delivered energy was increased to 1.4kWh (22-4). As described in Section 26, this battery system accumulated 188 cycles in 1977 for a total of 323 cycles with an average energy efficiency of 67.3%. The hardwired-logic controller on this system has failed and testing has been voluntarily terminated.

To supplement the data from batteries on life test, two single cells are also on life test (22-5). These single cells started operation in 1975 and were the first cells to be placed on life test. The significance of these cells was initially due to their accumulation of cycles, but this significance has been greatly diminished with the automation of the 1.7kWh battery which also uses porous graphite as the chlorine-electrode material. Data for these cells is presented in Section 27.

An accelerated testing program is scheduled to begin in mid-1978. At present, the graphite chlorine electrode is thought to be the life-limiting factor in the zinc-chlorine battery. Using chlorine-chlorine cells, this program is designed to provide detailed information on the causes of chlorine-electrode degradation. Details of this project are discussed in Section 28.

REFERENCES

22-1 Development of High-Efficiency Cost-Effective Zinc-Chlorine Batteries for Utility Peak-Shaving -- 1976. Palo Alto, Calif.: Electric Power Research Institute, 1978, EM-711, Part III, Section 5.

22-2 Reference 22-1, Part III, Section 3.

22-3 Evaluation of a 1kWh Zinc-Chlorine Battery System. Palo Alto, Calif.: Electric Power Research Institute, 1976, EM-249.

22-4 Reference 22-1, Part III, Section 2.

22-5 Reference 22-1, Part II, Section 4.

Section 23

TESTING OF THE 20kWh BATTERY SYSTEM

INTRODUCTION

The 20kWh battery was constructed under RP226-2. The engineering and design specifications, assembly, and initial battery testing are reported in the 1976 Final Report (23-1). The following is a brief review of the initial battery operations.

- During December 1976, operation of the stack with cylinder chlorine for discharge resulted in a delivered energy which exceeded 19kWh. The average energy efficiency was 64%.
- Coupling of the stack and store during December and January was considered unwise due to the hydrogen generation found during discharge.
- The hydrogen generation was thought to be related to the potassium chloride employed in the preparation of the electrolyte.
- After resolution of the hydrogen problem, the stack and store were coupled and the battery was run as a system.
- At this point, dendrites appeared. A full charge could not be put on the battery, as dendrites appeared between the second and fourth hour of the desired five-hour charge.
- The dendrites were found not to be associated with the bulk of the zinc plate, but rather with the plate edges. This suggested that the problem was related to electrode alignment or electrode masking.
- During the month of May, the ten consecutive cycles required by contract were obtained. The delivered energy averaged 15kWh at an electrochemical energy efficiency of 60%.

In June, 1977, the 20kWh battery was handed over to the stack-development group. The primary purpose of this assignment was to increase an understanding of the important factors in battery-stack design. These factors include cell imbalance, parasitic currents, electrode masking and alignment, electrolyte-flow distribution, corrosion couples, and dendrites.

The most significant stack-design aspect of the 20kWh battery is the use of flat-plate chlorine electrodes in the unit cells. The 20kWh battery remains the only large-scale battery utilizing this concept. Due to the economics and waste associated with machined-electrode technology, flat-plate electrodes will probably be the basis of future cell designs. Consequently, the experience gained with the 20kWh battery system will be invaluable in providing for this transition.

The secondary purpose of this assignment was to upgrade the electrochemical performance of the battery stack. The goal was to provide a delivered energy in excess of 19kWh at an energy efficiency greater than 65%.

20kWh STACK DEVELOPMENT

The primary obstacles which prevented the achievement of the electrochemical goals of the 20kWh battery were considered to be dendrites and cell imbalance. The early appearance of dendrites precluded the battery from being charged to full capacity, and reduced coulombic efficiency. Cell imbalance refers to the variation in the voltage time profiles of the individual unit cells during discharge. This also reduced coulombic efficiency.

In order to resolve these difficulties, and to increase an understanding of the important factors in stack design, the following approach was taken. First, the causes of the dendrites and cell imbalance were determined by parasitic current measurements, and by visual observation of the zinc morphology. Then various experimental modifications were performed on four cells (10R, 9R, 8R, and 7R). The results of these modifications and of the parasitic current measurements provided the basis for modifications to the entire battery stack.

Cell Modification Experiments

The zinc morphologies were examined on four unit cells (10R, 9R, 8R, and 7R). Figure 23-1 illustrates the placement of these cells in the stack. These cells were disassembled from the stack after the battery was charged well beyond the appearance of dendrites. The dendrites were found to be heaviest at the bottom of the plates near the Cl_2 bus (chlorine electrode bus) side. They also ran across the bottom of the plates, and vertically along the Cl_2 bus side. It further was found that the top and bottom corners of the plates near the Zn bus (zinc electrode bus) side were bared of zinc. The zinc plates then were peeled off and weighed. The results can be seen in Table 23-1. The pattern of decreasing zinc deposition was

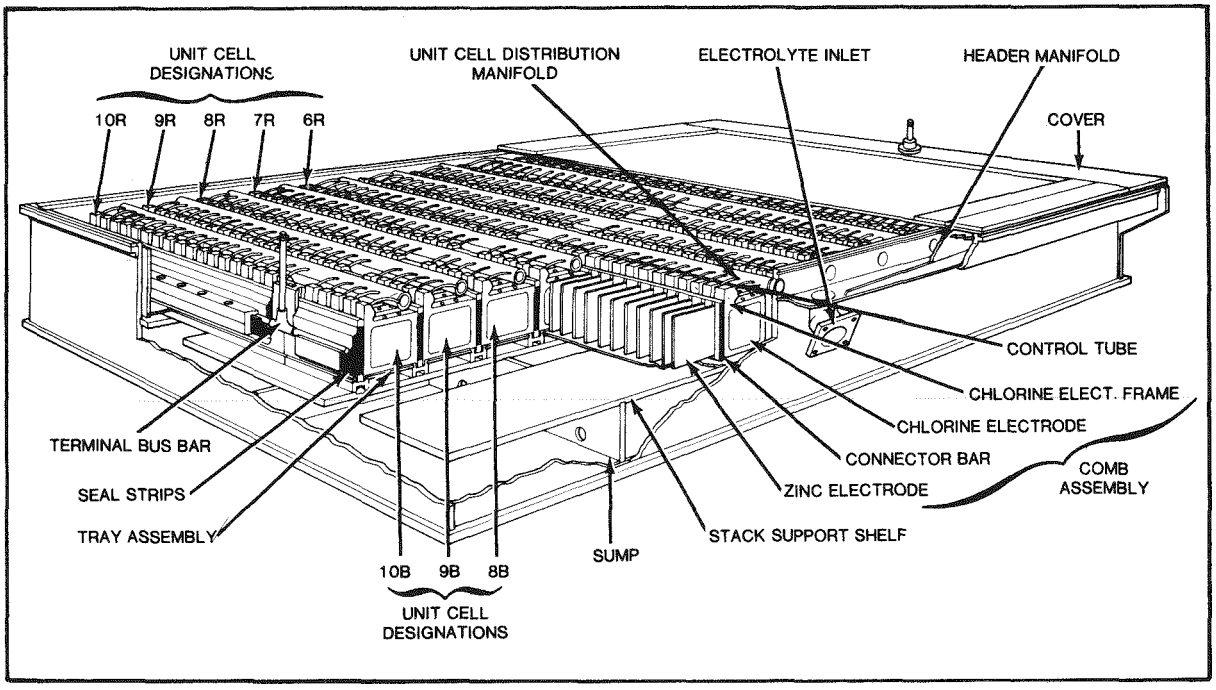

Figure 23-1. Cutaway Drawing of 20kWh Battery Stack

Table 23-1

PATTERN OF ZINC DEPOSITION IN UNIT CELLS

Unit Cell	Average Weight/Plate
10R	15.295g
9R	15.130g
8R	14.418g
7R	13.975g

felt to be due to parasitic current losses. The percentage weight difference between 10R and 7R is 7.8%.

The thickness variation on the zinc plates also was examined. Four plates from cell number 10R and two plates from cell number 9R were selected. The differences were measured with a micrometer. The overall thickness of the plates was found to vary

between 0.012 and 0.0165 in. Measurements between the top and bottom of the plates showed no differences on some of the plates, while on others the bottoms were 0.001- to 0.002-in. thicker than the tops. However, from side to side, the Cl_2 bus side was consistently thicker than the Zn bus side. This difference was approximately 18%.

The chlorine electrodes also were examined. Although a few chlorine electrodes in cell 8R had cracked, inspection of the other cells revealed no cracked electrodes. Samples of a tar-like material found in the end electrode packs of the unit cells were saved for later analysis.

From these observations, several test modifications were made to the four disassembled cells in an effort to increase the capacity and energy efficiency of the cells. The battery was then cycled twice, and charged beyond the appearance of dendrites. The four modified unit cells were again disassembled, and compared with the zinc morphology observed before. These results, and the results from the parasitic current measurements described below, formed the basis for modifications to the entire stack.

Parasitic Current Measurements

From the previous observations, a definite pattern of decreasing zinc deposition from the end cells to the center cells was shown. This was thought to be attributable to the effects of parasitic currents, leakage currents, or electrolyte flow distribution. Parasitic currents in this context are those currents which flow in the electrolyte through the battery by way of the manifolds that feed electrolyte to the cells, and tubes in which electrolyte flows from the cells. Leakage currents are those currents that flow around the unit cell bus bars due to imperfect sealing. The electrolyte flow distribution referred to is determined by the electrolyte inlet and header manifold construction (see Figure 23-1). It has been observed that the flow of electrolyte to the center cells is greater than to the end cells.

Measurements of parasitic current, as well as leakage current and corrosion current (rate of chlorine reaction at the zinc substrate electrode) were also made on the 20kWh battery. Figure 23-2 illustrates the results of the measurements.

The intercell leakage current was obtained by filling the cell compartments with electrolyte, turning off the electrolyte pump, and measuring the current. When the curve is extrapolated to the normal charging potential of 23 volts, the resulting current drawn is significant. Although other mechanisms, such as the deposition of

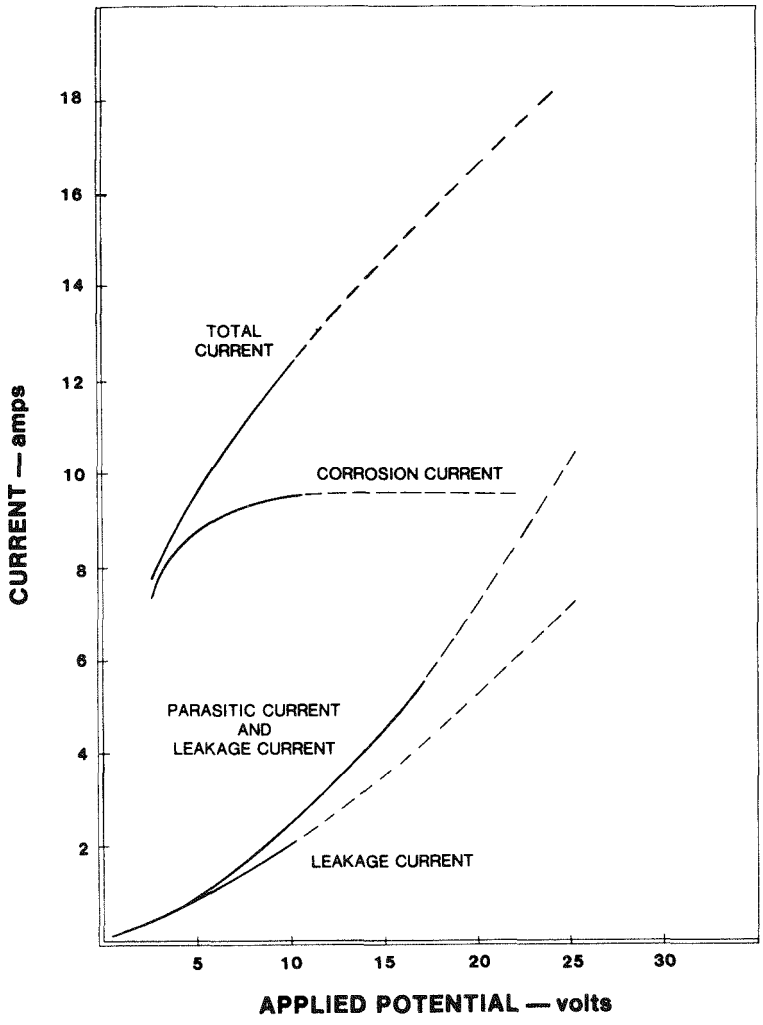

Figure 23-2. Measurements of parasitic current, leakage current, and corrosion current of 20kWh battery.

impurities and the electrolysis of water, undoubtedly accounted for much of this current, it was decided that the design for the electrode bus-to-tray seals should be improved. The parasitic current was obtained by measuring the current with the pump operating at normal speed. Together with the leakage current, at an applied voltage of 23V, the total current would be approximately 3.5% of the normal charging current, 260 amps. The corrosion current was found by adding one g/ℓ dissolved chlorine to the electrolyte, and subtracting out the parasitic and leakage current contributions. This value is approximately 9.5 amps, or 1.65mA/cm^2 per gram/liter of dissolved chlorine. This rate of chlorine attack on zinc during

a 5-hour charge and 5-hour discharge accounts for 7.3% coulombic loss over the cycle. However, this rate is less during discharge because the chlorine activity is decreased due to electrochemical consumption at the chlorine electrodes.

Stack Modifications

The results of the parasitic current measurements and the previous cell modifications were used to formulate a stack rebuild program. The bus-to-tray seals were redesigned in an effort to improve the intercell leakage and reduce the leakage parasitic current contribution. The electrolyte drain paths from the unit cells were redesigned to form cups and tubes to reduce the outlet parasitic current contribution. Re-evaluation of the parasitic currents after the modifications were completed showed significant improvement in both the leakage and parasitic currents. A comparison of the data obtained before and after the modifications is shown in Figure 23-3.

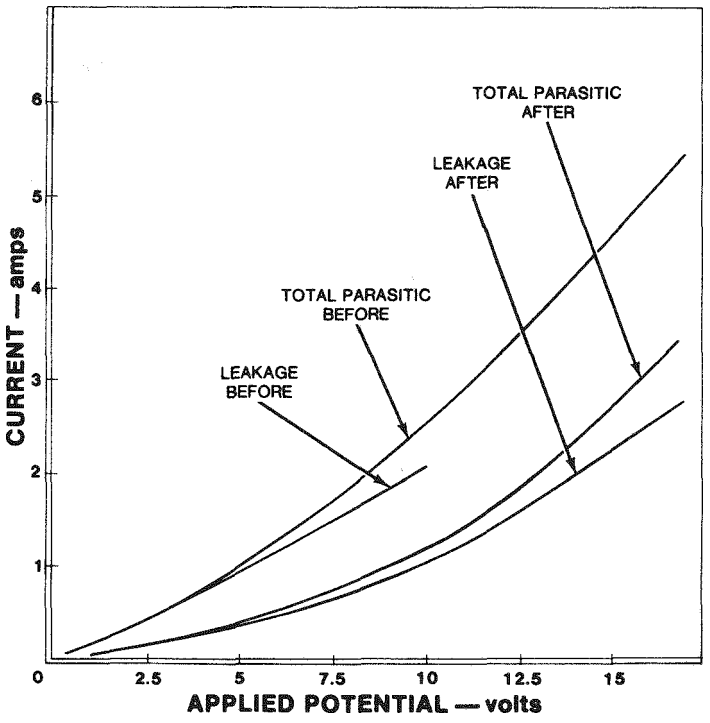

Figure 23-3. Comparison of currents prior to and after cell modifications.

Subsequent cycling of the battery showed no significant increase in electrochemical energy efficiency. However, dendrite formation on charge was substantially decreased, and the appearance of dendrites was delayed. Dendrites were now being detected at 1150 Ah, whereas, before the stack rebuild, dendrites were detected between 900 and 1000 Ah. This allowed for delivered energies of 18kWh to be achieved.

As a result of the minimal improvements in the battery's performance, unit cell 8R was re-examined in terms of its vastly improved performance during the earlier cell modifications. The major changes in this cell were the replacement of some of the chlorine electrodes, and a new bus bar which provided an interference fit connection of the chlorine electrodes to the bus. In order to evaluate these changes separately, all of the chlorine electrodes in cell 1R were replaced with new ones, and the original chlorine electrodes in cell 2R were re-connected to use an interference fit.

Several subsequent battery cycles showed significant coulombic improvement in cell 1R, as well as voltaic improvement. However, no noticeable improvement was found in cell 2R. The improvement seen in cells 1R and 8R imply degradation of the chlorine electrodes in the 20kWh battery. The electrochemical performance of the battery during the initial testing in December, 1976, was quite good, but this could not be repeated in any of the later months. Consequently, the damage, if any, to the chlorine electrodes must have occurred in December.

During the month of December, 1976, high rates of hydrogen evolution were experienced. This caused the pH of the electrolyte to rise over 1 on discharge, and as high as 1.76. Later experiments have shown that at a temperature of 50°C and a pH greater than 1, damage to the chlorine electrodes will occur. Evidence of this was seen in the amounts of particulate graphite in the electrolyte. The reason for the unexpected rate of hydrogen evolution was thought at the time to be caused by the grade of potassium chloride used to support the electrolyte. However, recent experimentation has indicated that the hydrogen evolution also may be related to the activation process.

20kWh SYSTEM DEVELOPMENT

Hardware Modifications

The goal in this phase of the refurbishment program was to simplify the operation of the system. With the emphasis on stack design, all subsystems not essential to

the operation of the stack were eliminated. Figure 23-4 compares the original schematic of the 20kWh battery with a schematic of the battery in its present state. The major hardware deletions were:

- hydrate store
- Cl_2 gas injection pump
- H_2/Cl_2 reactor
- glass wool filter
- in-line spectrophotometer
- sonic flow meter

The electrolyte plumbing external to the stack was also simplified. The battery stack was turned 180° in the hood, thus allowing easier servicing of the electrolyte pump and piping. Chlorine gas was provided during discharge from gas cylinders directly connected to the high pressure side of the electrolyte pump. Finally, the cover to the stack case was replaced due to a fracture in the steel frame.

Recommendations

Three new pieces of hardware have been purchased for the 20kWh battery, and should be installed during Phase II. The first is a set of titanium-clad copper bus bars, which will allow for external electrical connections of the two banks. This will allow measurement of current distribution between the banks. Furthermore, the bus bars are designed to extend through the sides of the battery case instead of the top. This will reduce the difficulties associated with removing the top in order to observe the cells.

The second new piece of hardware is a titanium-coil heat exchanger. It will act both as a heat exchanger and as a medium to enhance chlorine gas absorption during discharge. This heat exchanger will be situated in the main electrolyte plumbing from the pump, as it will be replacing the titanium mesh absorber.

Finally, a ceramic filter also will be placed in the main electrolyte plumbing. This filter will not introduce contaminants to the system, and the cartridge could easily be removed when filtering is not needed.

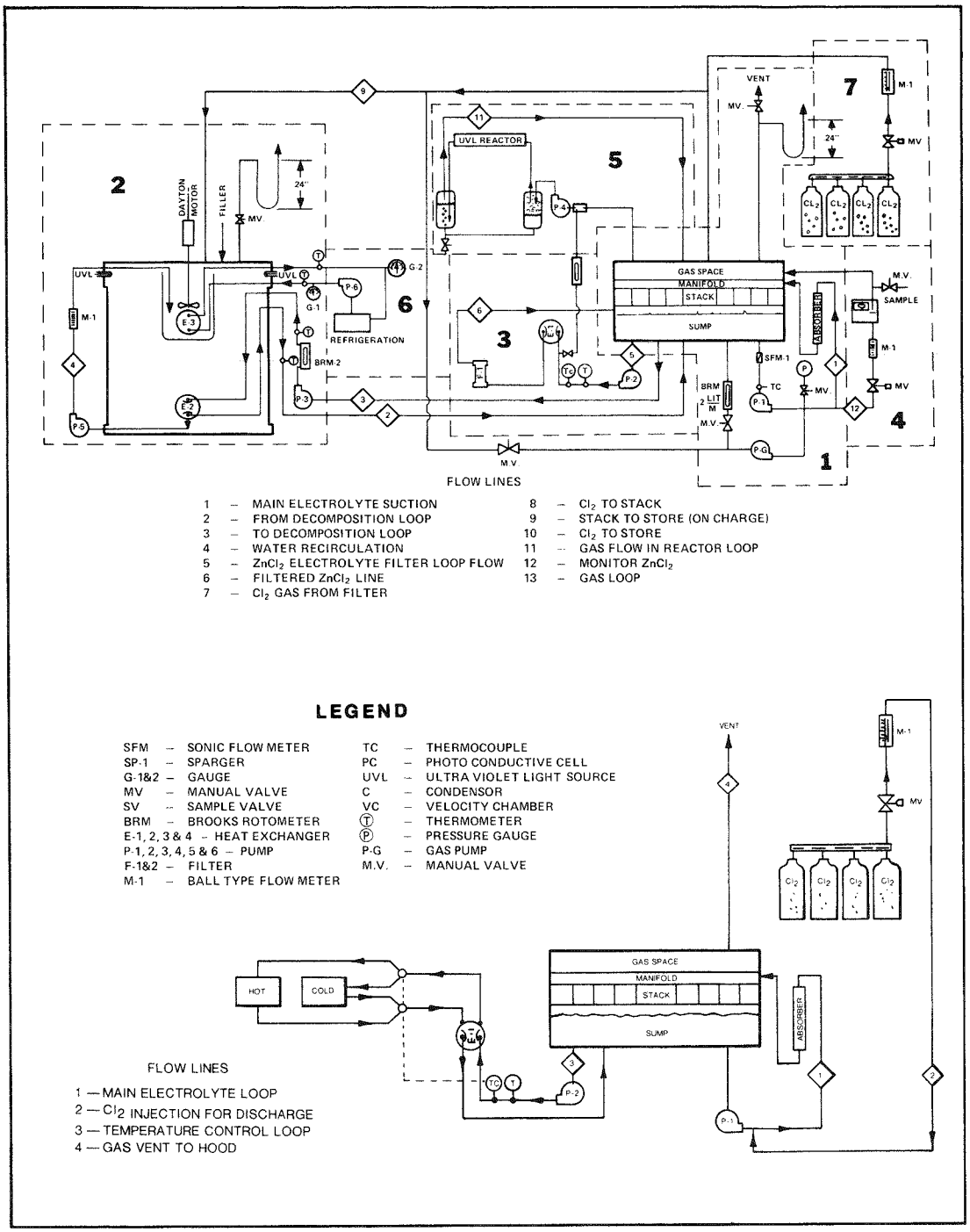

Figure 23-4. Schematics of 20kWh battery systems comparing original layout above with the present modified scheme below.

CONCLUSIONS

In December, 1976, several cycles consistently achieved electrochemical energy efficiencies of 64% at a delivered energy of 19kWh. These results have not been reproduced in any of the subsequent cycles during Phase I. The major difficulties found were dendrites and cell imbalance. The stack rebuild program eliminated many of the causes of the dendrites, and has made inroads for the determination of the cell imbalance. Although parasitic currents and electrolyte flow distribution to the cells would seem the logical cause of cell imbalance, it now seems that the performance of the chlorine electrodes must also be considered.

REFERENCE

23-1 Development of High-Efficiency, Cost-Effective, Zinc-Chlorine Batteries for Utility Peak-Shaving -- 1976. Palo Alto, Calif.: Electric Power Research Institute, 1978, EM-711, Part III, Section 5.

Section 24

TESTING OF THE 8.3kWh SUBMODULE

INTRODUCTION

The 8.3kWh submodule is a complete battery stack and forms a basic building block of the present full-size 45/50kWh integrated battery module being developed for load-leveling use at EDA. A thorough understanding of the operating characteristics of this submodule is needed to upgrade the design and performance of the larger system. This test program was undertaken to develop such understanding. It also was planned to run concurrently with initial testing of the 45kWh integrated battery. In this way it provided a means of screening the submodules used to assemble the large unit and served to supplement the data obtained during full system tests. An operating 8.3kWh system also provides an important link between the full battery and single cells.

The electrochemical efficiency of $ZnCl_2$ batteries depends considerably on the conditions of temperature, pressure, and current density under which it is operated. Also, of course, the electrolyte composition including salts, additives, pH, and dissolved chlorine concentrations are important. Of these parameters, the concentration of dissolved chlorine in the electrolyte theoretically exerts a primary influence on coulombic efficiency. Voltaic efficiency, on the other hand, depends primarily on the activity of the chlorine electrode and on the resistivity of the electrolyte. The morphology of the zinc plated-out during charge is markedly influenced by electrolyte composition as well as current and time parameters. Optimization of the electrochemical energy efficiency of a battery requires selection of operating conditions and electrolyte composition which combine high coulombic and high voltaic efficiencies while allowing dendrite-free full-charge capacity.

OBJECTIVES

The specific objectives of the 8.3kWh testing program can be stated as follows:

- Evaluate performance and make comparisons

  --between submodules and the full 45kWh battery module.

  --between different submodule assemblies.

  --between submodules and single cells.

- Optimize conditions to reach 200mAh/cm^2 capacity at 65% minimum round-trip electrochemical energy efficiency.

- Develop meaningful methods of stack evaluation.

These objectives were pursued by selecting various combinations of operating conditions and electrolyte compositions, and testing each under carefully controlled conditions that matched or could be achieved in the full size 45kWh module. Another criterion for selection was that of maintaining acceptably low levels of hydrogen evolution.

SYSTEM DESIGN AND OPERATION

Submodule Design

The 8.3kWh submodule consists of ten bipolar unit cells in series. Each unit cell contains 22 pairs of electrodes. The profiled (machined cavity) type PG-60 porous-graphite chlorine electrodes are assembled with the respective ATJ graphite zinc electrodes into a bipolar comb-type structure. This stack assembly is contained in a vacuum-formed plastic submodule tray. The assembly is illustrated in Figure 24-1.

The submodule stack and the required electrolyte sump are arranged in a battery case on two levels as shown in Figure 24-2. A photographic view of the assembly with cover removed is shown in Figure 24-3.

The main body of the case is permanently assembled. The top and bottom removable covers are sealed by use of Viton O-Rings and six clamp screws. In practice, the bottom cover normally remains in place. The top cover is removed routinely for inspection or repair of the submodule. The O-ring sealing design provides a satisfactory seal for vacuum operation.

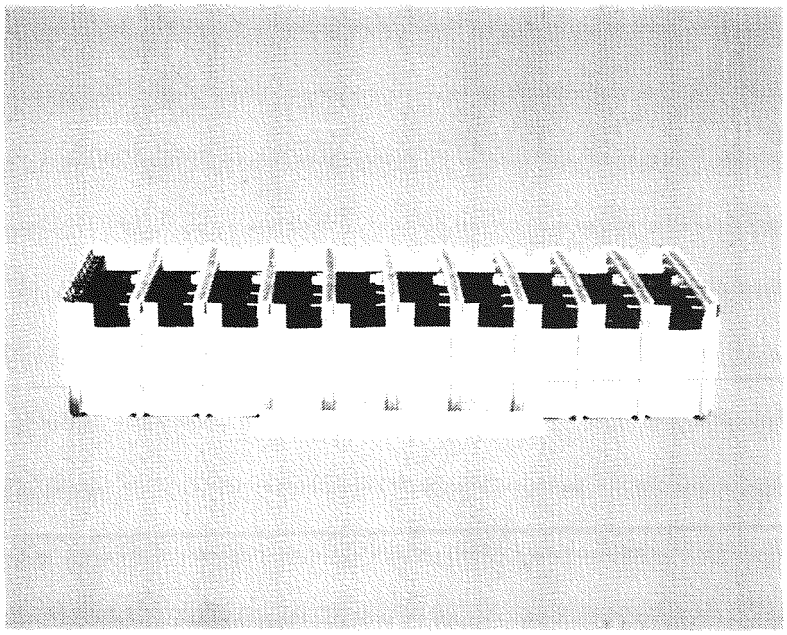

Figure 24-1. Photograph of a Typical 8.3kWh Submodule

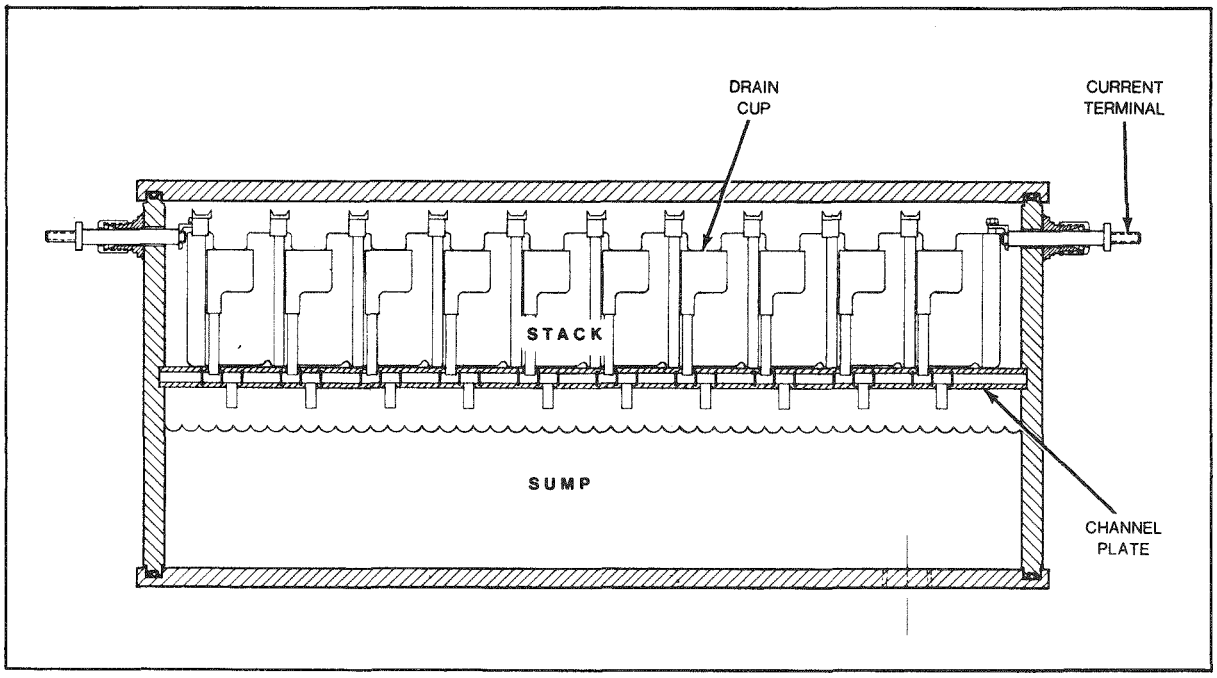

Figure 24-2. Cross-Section of 8.3kWh Submodule in the Test Fixture

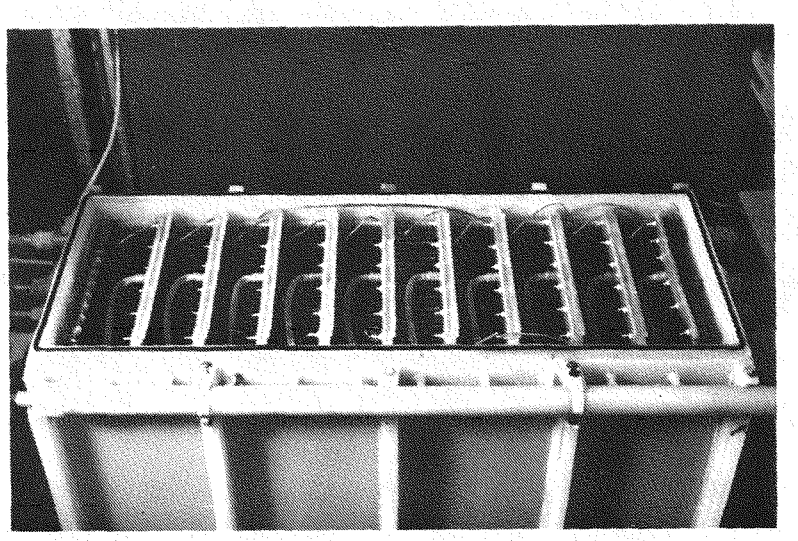

Figure 24-3. Photograph of 8.3kWh submodule in the test stand. Note the ten unit cells each with an electrolyte feed tube centrally supplying the cell distribution manifold.

The channel plate which supports the submodule stack over the sump incorporates a 20-inch long zig-zag channel of 0.5" x 0.5" cross-section for exit flow of electrolyte from each unit cell. Circulating electrolyte first enters a main manifold which distributes flow to the ten unit cells through individual cell distribution manifolds. The outlet flow from each unit cell is collected in a drain cup which conducts the electrolyte back to the sump. This is illustrated in Figure 24-4. The purpose of these lengthy electrolyte passages is to provide sufficient resistance to minimize the flow of parasitic currents between individual cells and to the common sump or pump stream.

Test Stand Design

One of the advantages of working at the sumbodule level rather than in the larger fully-integrated battery module sealed inside its case is the ability to observe, control, and monitor all phases of system. To facilitate this, a special test stand was designed and constructed. The case enclosing the submodule stack is properly

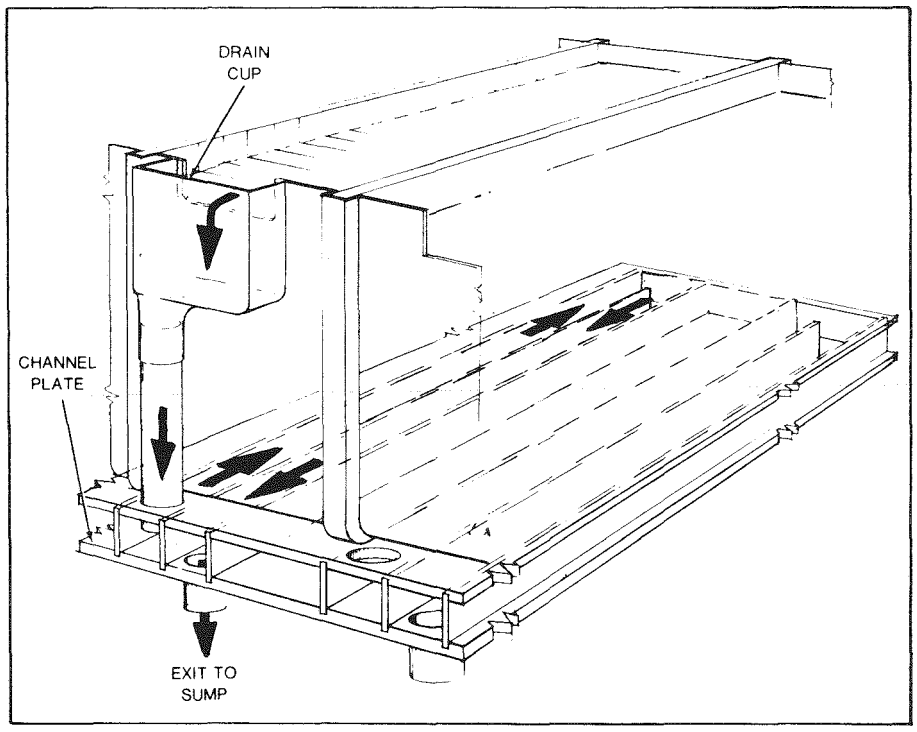

Figure 24-4. Illustration of electrolyte return flow path. Unit cell overflows into drain cup which leads to an extended channel that empties into the sump.

an integral part of this test stand. Figure 24-5 is a diagram of the system and Figure 24-6 is a photograph of the complete stand installed in a vent hood. In addition to the sump and stack which are contained inside the rectangular case, the test stand incorporates a G-10 main electrolyte pump for circulating electrolyte, an in-line heat exchanger for controlling electrolyte temperature, an in-line filter which also serves to separate undissolved gas from the electrolyte fluid, and a G-10 gas pump for controlling stack pressure. During charge, evolved chlorine is vented to the hood. During discharge, cylinder chlorine is injected into the electrolyte stream on the high pressure side of the pump.

Test Stand Capabilities

The design of the test stand provides certain operational features and some special diagnostic capabilities. The stack can be operated under closely controlled reduced pressure down to -11 psig (0.25atm absolute). The reduced stack pressure is established using the G-10 gas pump and monitored by a mercury manometer. Under standard test conditions, the stack pressure during charge is maintained at -5 psig (0.66atm) to simulate the design conditions for the 45kWh peak-shaving battery.

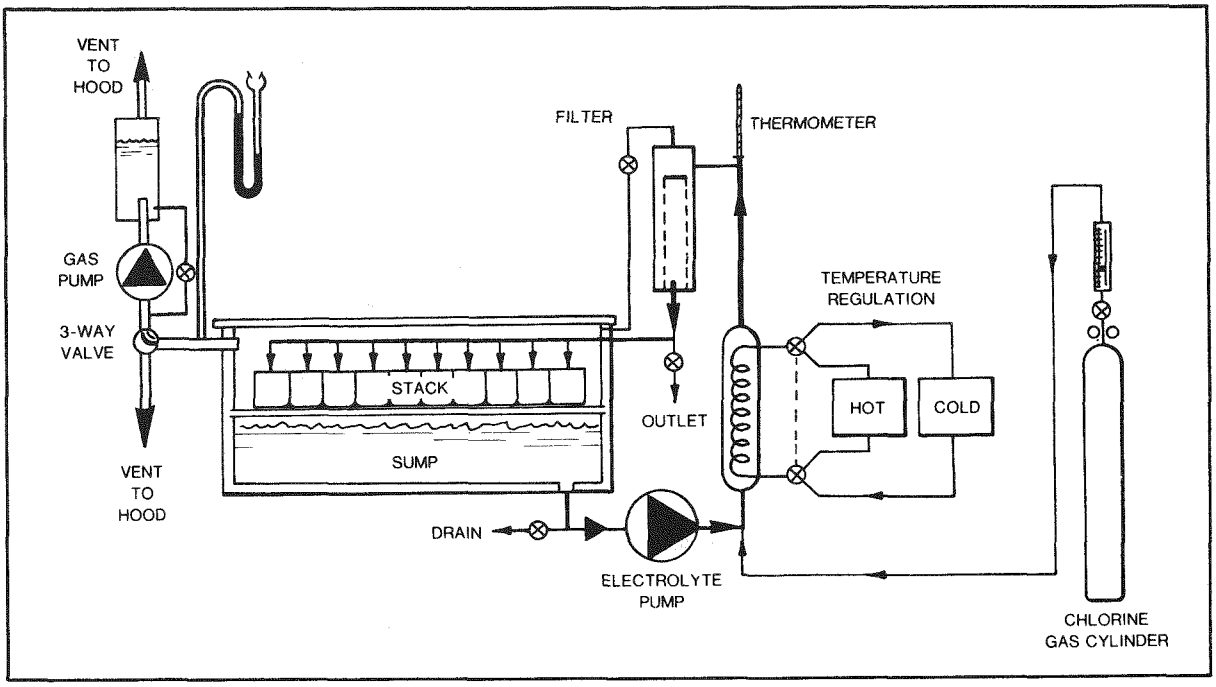

Figure 24-5. Schematic Arrangement of the Special 8.3kWh Test Stand

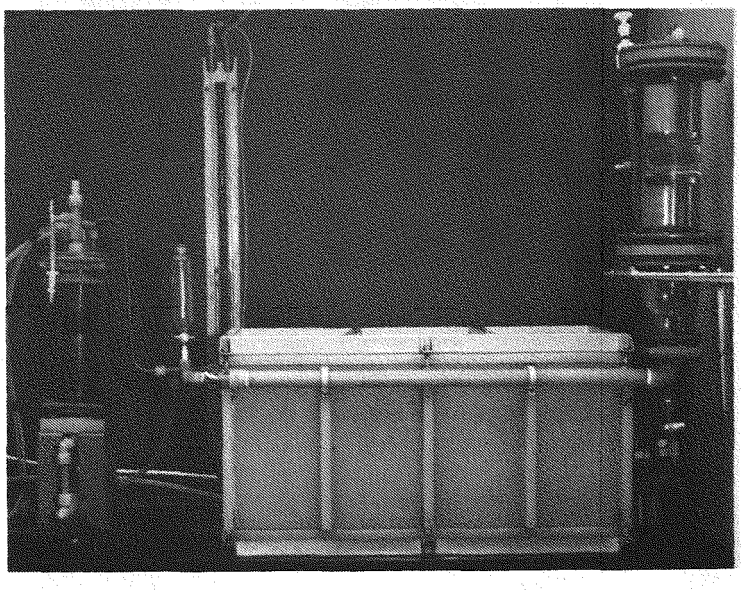

Figure 24-6. Photograph of the 8.3kWh test stand assembled in the laboratory hood.

Electrolyte temperatures ranging from 10 to 65°C can be controlled to within ±3°C by means of constant temperature glycol baths which accept or reject heat from the electrolyte through an in-line heat exchanger. The heat exchanger, consisting of a 20' length of 1/2" I.D. coiled titanium tubing, is installed in the main electrolyte circulating loop.

In addition to the basic components required for operation, the test stand incorporates the following features for diagnostic purposes.

- Individual cell voltage probes for monitoring the ten unit-cell voltages on charge and discharge. The probes are titanium strips, formed into flat springs, which make electrical contact to the individual bipolar buses when inserted between the chlorine-electrode end mask and the zinc bus. Kynar-insulated titanium lead-wires, spot-welded to the spring contactors and sealed via compression-type feed-throughs, allow external monitoring of the cell voltages on strip chart recorders or a DVM.

- Coulombic efficiency monitoring via a digital coulometer. The controlled constant current supplied to the submodule on charge and discharge via an EDA Mark IV controller is monitored through a 100 ampere, 50mV shunt. The corresponding mV drop across the shunt is accumulated with time on charge and discharge to monitor full-power and usable coulombic efficiencies for the submodule. The full-power coulombic efficiency is defined as the amp-minutes (capacity) delivered on discharge at constant current to 1.6 volts/cell ÷ the total charge capacity. The remainder of the usable capacity is removed at a constant voltage of 1.6 volts/cell until the current density drops to 5mA/cm^2. The capacity delivered at this point of discharge ÷ the total charge capacity is defined as the usable coulombic efficiency.

- Energy efficiency monitoring via a digital watt-hour meter. The submodule end-bus probe voltages and corresponding amp-minutes on charge and discharge are accumulated by the watt-hour meter to provide a measure of the full-power and usable energy efficiency of the submodule.

Additional data; viz., stack pressure, chlorine concentration in the electrolyte, electrolyte specific gravity, electrolyte pH, etc.; are also recorded for diagnostic purposes.

System Operation

Preparation for charging the submodule consists of adjusting the temperature of the electrolyte to the desired level and pre-chlorinating the electrolyte using cylinder chlorine. All meters are zeroed and the proper electrolyte flow rate is set. The constant current charge is initiated once these conditions are stabilized and the

chlorine injection is terminated. When charging under vacuum, the gas pump is operated and controlled to establish the desired reduced pressure in the stack compartment prior to initiating the charge.

During charge the desired conditions of current density, stack pressure, electrolyte temperature, flow rate, etc., are maintained and the dependent parameters of Sp. Gr., pH, chlorine concentration, amp-mins, watt-hrs, etc., are routinely recorded. At the end of charge, the meters are reset and the discharge conditions established.

The discharge is performed in a similar manner while a controlled rate of cylinder chlorine is injected into the electrolyte on the high-pressure side of the electrolyte pump. Full-power and usable coulombic and energy outputs are recorded and the efficiencies calculated. After the usable outputs are obtained, the remaining zinc is stripped from the stack to obtain bare substrates throughout before initiating the next cycle.

During most of the cycles performed in Phase I, the electrolyte volume was 36-40 liters and the initial electrolyte pH was set at $\sim$0.1 to simulate the conditions in the 45kWh battery module. Similarly the initial Zn^{++} concentration was set between 2.9 and 3.0 molar. The test stand has an electrolyte volume capacity of $\sim$50 liters to permit evaluation of lower initial Zn^{++} concentrations and reduced concentration swings.

RESULTS

For this program, submodules were selected from the inventory of assemblies to be employed in the two 45/50kWh integrated battery modules being readied for test at EDA. The selected submodules were installed, one at a time, in the test stand case and run through several cycles each. For convenience the submodules have been assigned the numbers #1, #2, #3, and #3M (modified) indicating the sequence in which they were used. Also for convenient reference, all test runs were identified by consecutive cycle numbers throughout the program.

The data obtained during 26 different test cycles with four different submodules are summarized in Table 24-1. The "full-power" information relates to the accumulated coulombs discharged at constant current until the cut-off voltage of 1.6 volts/cell is reached. The "usable" data corresponds to the accumulated coulombs obtained by continued discharge at a constant 1.6 volts/cell down to a cut-off current density of 5mA/cm^2.

Table 24-1

DATA FROM CYCLE TESTS OF 8.3kWh SUBMODULES

	Cycle No.	Electrolyte Composition	Temp. (°C) C/D	Press. (atm) C/D	Current Density (mA/cm^2) C/D	Charge Capacity mAh/cm^2	Coulombic Efficiency (%) Full Power	Coulombic Efficiency (%) Usable	Energy Efficiency (%) Full Power	Energy Efficiency (%) Usable
Submodule #1	1	A	25/35		27.3/31.2	100.4				
	2	B	35/35		27.3/31.2	197.2				
	3	B	35/35		29.1/32.8	135.1	57.7			
	4	B	30/35		29.1/32.8	127.7	66.5	70.5	57.0	60.6
Submodule #2	5	B	30/35	.66/.66	29/32.8	127.7		72		
	6	C	25/40	.66/.66	27.3/32.8	212.6	69	73.2	56.8	59.8
	7	D	30/50	.66/.66	29.1/32.8	212.3	65.5	74.5	54.7	61.2
	8	E	25/40	.66/.66	29.1/32.8	175.7	67.1	75.5	55.7	61.4
Submodule #3	9	F	30/40	.66/	35/35	163.8	47.4	57	37.9	44.5
	10	G	30/40	.66/	35/35	218.4	50.8	61	39	46
	11*	G	30/40	.66/	35/35	218.4				
	12	G	30/40	.66/	29/32.8	195.9	47.7		41.6	
Submodule #3M	13**	G	30/40		35/40	195.9	50.4	54.8	38.7	41.7
	14	G	30/40		35/35	195.9	55.2	57.3	45.5	46.8
	15***	G	30/40		35/35	195.9	64.5	65.9	52.5	53.4
	16	G	30/40		35/35	93.2	69.4	72.2	59.3	61.3
Submodule #3M	17	H	30/40	.83/1	30/33	240.3	60.4	61.4	52.6	53.57
	18	H	30/40	.83/1	30/33	240.3	61.3	62.6	53.3	54.1
	19	H	30/40	.83/1	30/33	193.99	60.1	61.8	52.2	53.5
	20	H	30/40	.83/1	30/33	240.3	59.6	61.0	51.4	52.5
	21	H	30/40	.83/1	30/33	244.9	55.4	61.2	48.0	52.3
	22	H	30/40	.83/1	30/33	127	69.1	71.4	60.8	61.4
	23	H	30/40	.83/1	30/33	127	64.1	67.5	54.1	56.7
	24	H	30/40	.83/1	30/33	103.4	68.6	71.0	58.9	60.6
	25	I	30/40	.83/1	30/33	139.7	70.1	72.6	60.6	62.4
	26	I	30/40	.83/1	30/33	152.8	70.2	72.1	59.1	60.4

*Zinc plates of cells #8 and #9 were peeled off for weight distribution analysis.

**Submodule modification: Interchange between combs #9 and #10.

***Submodule modification: Replacement of combs #3 and #4 with new combs.

A standard load-leveling cycle regime was run for all tests in this Phase I program. A typical voltage profile for the 7-hour charge and the 5-hour discharge is shown in Figure 24-7.

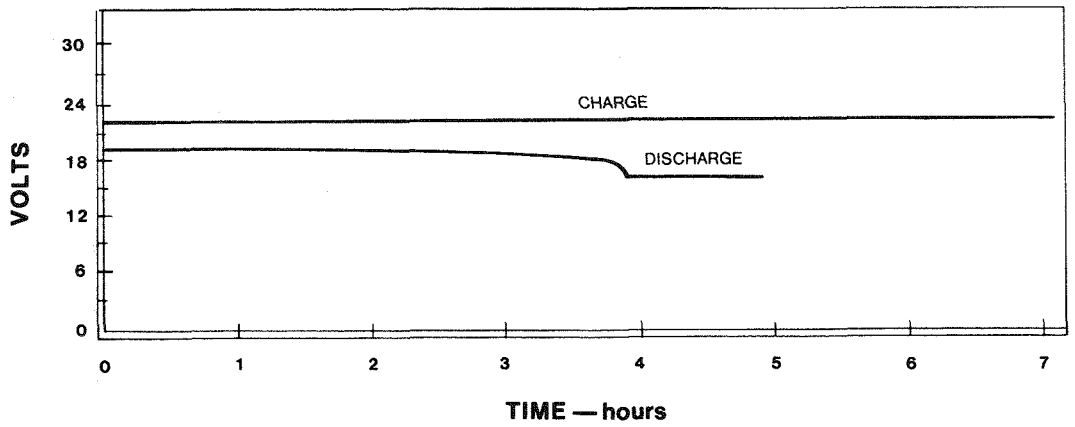

Figure 24-7. Typical voltage-time profile under standard load-leveling cycle regime.

Coulombic and Energy Efficiencies

The performance efficiencies at "full power" and "usable" for all test cycles are displayed in Table 24-1. Early in the program, high levels of hydrogen evolution were encountered. Considerable effort was directed at reducing this gas formation so that very limited useful information was obtained from tests of submodule #1.

Submodule #2 yielded the highest efficiencies recorded during the entire Phase I testing program. Cycles 6-8 showed an average usable coulombic efficiency of 74.4% ($s = 1.2$) with an average charge capacity at the targeted 200mAh/cm^2 despite several variations in operating conditions and electrolyte composition. Usable energy efficiencies close to 60% were recorded. While it is considered likely that some dendriting occurs near the end of charge on all cycles, only cycle 8 was terminated short of the 200mAh/cm^2 objective due to major dendrites.

The various formulations used for testing submodule #2 contained little or no supporting electrolytes. It is expected that further improvements in energy efficiency can be achieved when an optimum electrolyte is employed. For instance, an increase in voltaic efficiency from 80% to 90% during cycle #8 would raise the usable energy efficiency to 68%.

Submodule #3, which replaced #2 in the test stand late in November, proved to be a less-than-optimum performer. Originally run as received from inventory stock under similar conditions, this assembly yielded only 59% usable coulombic and 45% usable energy efficiency averages. Efforts to analyze this weakness and to improve this submodule were made during cycles 11, 13, and 15. Reports on this work are given later in this section. These efforts improved the performance of submodule #3 as modified (#3M) but the efficiency levels of #2 were not attained.

Near the end of this program in March, a coordinated program was initiated to test the 45kWh load-leveling battery module and the 8.3kWh submodule at the same time under identical conditions. Cycles 17 through 21 were conducted using submodule #3M with electrolyte from the 45kWh module and under pressures, temperatures, and current densities the same as in the full size battery. These five cycles yielded very consistent results, achieving full charge capacity but operating at an average usable coulombic efficiency of only 61.6%. The average usable energy efficiency of 53.2% is well below the program objective of 65%. It should be noted that these data from cycles 17-21 can be directly compared with the data accumulated during ten parallel test runs of the 45kWh module reported in Part III, Section 20 of this report.

Cycles 22-26 were undertaken in an attempt to determine if the operating efficiencies were the same for all parts of the cycle regime. By shortening cycles 22, 23, and 24 so that the charge time is reduced to 50%, 63%, and 70% while holding all other parameters constant, data for the final half of a complete full-cycle regime was obtained. This work yielded nearly a 10% improvement in coulombic efficiency to 70% and in usable energy efficiency to 59.6%. Cycles 25 and 26 were repeated under identical conditions except that a more fundamental electrolyte composition was used. The usable coulombic and energy efficiencies were improved further to 72.4% and 61.4%, respectively.

The actual delivered energy taken from the submodules during these specific runs is plotted against charge time in Figure 24-8. Normally the energy delivered would be expected to be directly proportional to time of charge. As can be seen this was only true for charges less than 5-1/2 hours. After 6 hours the energy delivered falls off markedly in proportion to the length of charge. The poorer performance on the longer cycles is presently thought to be caused by current losses brought about by undetectable dendrites. More work is needed to verify this assumption.

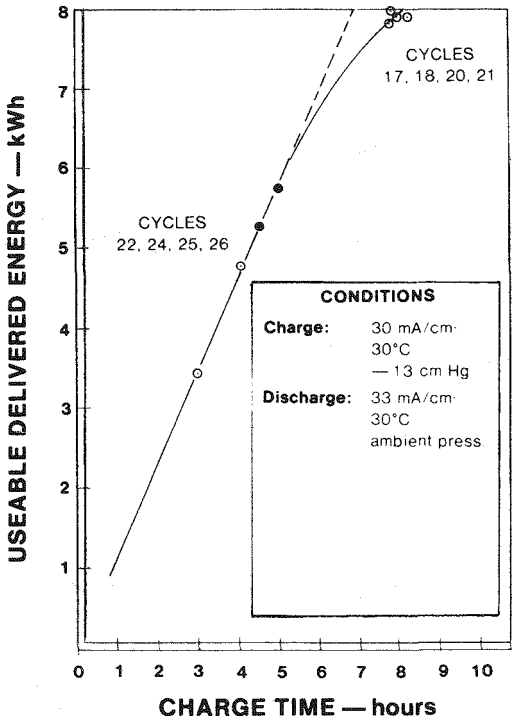

Figure 24-8. Effect of charge time at constant current on delivered energy.

Submodule Qualification

One of the objectives of the program was to qualify individual submodules as they were completed for use in a larger 45kWh battery stack assembly. It was learned early that there was marked variation in the performance of individual submodules. This was shown to be caused by variation in the electrochemical performance of the separate unit cells within the submodules. It is expected that this is due to the handcrafted technology currently used to assemble the units. In order to optimize the performance of a submodule it is essential to minimize this variation in performance among its individual cells. The voltage-time profiles, obtained by monitoring each unit cell voltage during charge and discharge, are a convenient means of identifying cells performing below average.

It may be noted from Table 24-1 that submodule #2 operated with a usable coulombic efficiency of 75%. There was very little variation in the individual members of this assembly and it can be considered to represent the characteristics of a good, well-balanced submodule.

On the other hand, submodule #3 offered low usable coulombic efficiencies. There was found to be considerable variation in performance between the individual unit cells in this assembly. One cell was completely used up only halfway through the discharge cycle. This unexpected early loss of zinc was found to be caused by low charge efficiencies. Charge efficiencies were investigated by an analysis of the actual weight of zinc deposited throughout the submodule at full charge. This investigation is reported in a following subsection. In summary it can be said here that there was found to be considerable difference in the weight of zinc stripped from various unit cells, although the distribution of weight within the unit cells was observed to be quite uniform.

In an effort to improve the efficiency of submodule #3, it was modified in two different ways. First the positions of substandard unit cells was exchanged with those that operated well. The performance of a unit cell was found not to be associated with its location -- it performed the same no matter where installed. Next, three substandard unit cells were removed and replaced with new comb elements. The average usable coulombic efficiency was raised to 62% with a corresponding increase in energy efficiency to 51% average. This was still below the performance levels of submodule #2.

Effects of Temperature and Pressure

During charge of a $ZnCl_2$ battery, molecular chlorine is formed at the chlorine electrode. Much of this becomes dissolved in the electrolyte surrounding the stack structure. This dissolved chlorine is then able to attack the metallic zinc plating out at the zinc electrode. The metal thus dissolved is no longer available for electrochemical reaction during the discharge cycle. This results in coulombic losses, reduces the usable energy efficiency of the battery, and leads to interest in the chlorine concentration in electrolytes.

For any given electrolyte formulation, the concentration of dissolved chlorine in the liquid can be lessened by increasing the temperature or reducing the partial pressure of chlorine in the gas phase. Figure 24-9 is a plot of experimental data illustrating the effects of these temperature and pressure parameters. This data was obtained during special charge cycles of the 8.3kWh submodule testing with a fundamental 3M $ZnCl_2$ electrolyte.

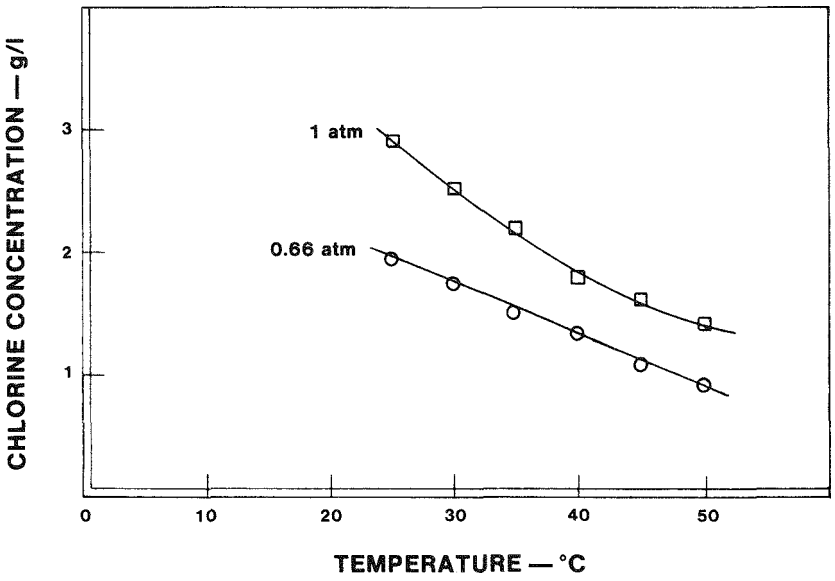

Figure 24-9. Relationship between dissolved chlorine gas and temperature and pressure of system. Test run with 3M $ZnCl_2$ electrolyte.

Another plot of the data at a constant 30°C temperature is shown in Figure 24-10. This clearly indicates the linear relationship between chlorine gas pressure and chlorine solubility in agreement with Henry's Law. Henry's Law can be stated as $p_{Cl_2} = kX_{Cl_2}$; where p_{Cl_2} = partial pressure of chlorine gas in the atmosphere, and X_{Cl_2} = the concentration of dissolved chlorine gas in grams per liter. Definition of the constant is: k for chlorine = 0.39 liter-atmospheres per gram of dissolved gas.

The test cycles run during this Phase I program were made at reduced pressure with the intent of keeping coulombic efficiencies high. It is difficult to find evidence in the experimental data gathered to date (Table 24-1), that the coulombic efficiency is significantly influenced by the chlorine pressure. More cycles with a broader range of temperature and pressure settings will be required to see this effect. Work on this study will continue into the Phase II program.

Another temperature effect, which was observed during the submodule tests, may be of significance. Temperature appears to affect the rate at which molecular hydrogen is liberated from the battery stack. Hydrogen generation was noted to be significantly more during runs at 45/50°C than it was when the electrolyte was held at or below a temperature of 40°C.

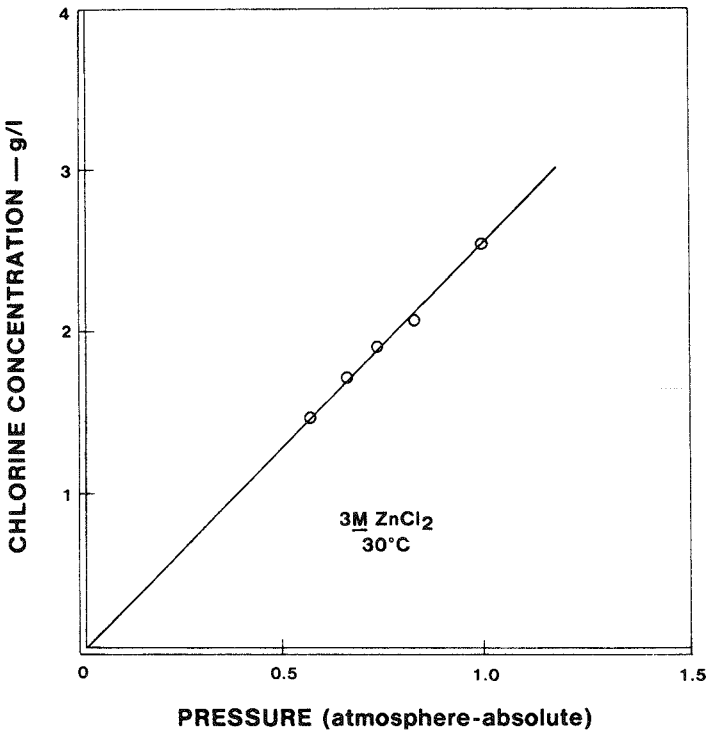

Figure 24-10. Showing constant temperature relationship between dissolved chlorine gas and gas phase pressure. Test made with 3M $ZnCl_2$ electrolyte.

Parasitic and Corrosion Losses

During the early stages of this program it became evident that there were differences in the performance of individual submodule assemblies. It also was apparent that obtainable efficiencies were below the target objectives. Hence it was decided to evaluate the magnitude and possible sources of coulombic losses in the system. Parasitic current measurements were performed on individual unit cells, on pairs of cells, and across the complete battery stack. The measurements were taken at several constant applied voltages below the decomposition potential of $ZnCl_2$ using dechlorinated electrolyte under both flow and non-flow conditions. Described below are four experiments designed to evaluate the following parasitic losses:

- baseline currents (not considered a loss)
- intercell leakage currents
- inlet-manifold parasitic currents
- outlet-flow parasitic currents

The data collected during a number of runs under differing conditions are assembled in Figure 24-11.

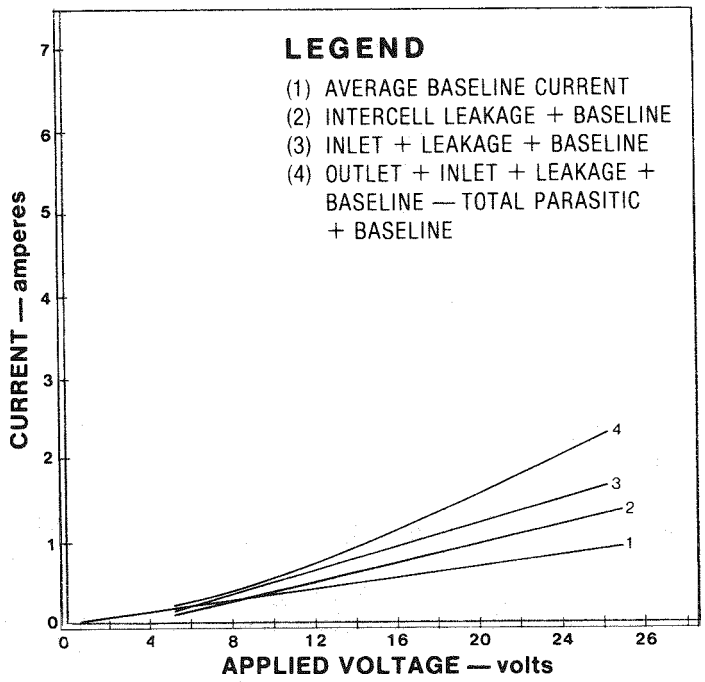

Figure 24-11. Summation of parasitic currents measured in the 8.3kWh submodule tests.

Experiment No. 1. Individual cell baseline currents were measured by applying several constant voltages between 0.5 and 1.9 volts/cell across the unit cell with the stack filled with non-flowing (pump shut off) dechlorinated electrolyte. The steady-state current was recorded. Line 1 of Figure 24-11 is a plot of the average baseline current vs. applied voltage per submodule. (The voltage per cell is one-tenth the applied voltage per submodule.) These data were then extrapolated to the charge and discharge voltages to obtain the predicted baseline currents in an operating stack.

Experiment No. 2. Intercell leakage currents were obtained in a similar manner across individual pairs of cells and across the battery stack in non-chlorinated non-flowing electrolyte. Line 2 of Figure 24-11 is a plot of the obtained data extrapolated to high voltages. Line 2 also contains the baseline current contribution, and the average intercell leakage current is the difference between line 1 and line 2.

Experiment No. 3. The inlet manifold parasitic current was obtained by making similar measurements across the battery stack using a non-chlorinated electrolyte flowing only enough to keep the piping full. These data appear as line 3 in Figure 24-11, and the inlet contribution is the difference between line 2 and 3.

Experiment No. 4. The outlet-flow parasitic current was obtained at the normal rate of supply ($\sim$2ml/cm^2-min) of non-chlorinated electrolyte to the cells. This filled the return-flow channel system with the proper amount of liquid to produce the current paths to the sump found in an operating battery. Line 4 of Figure 24-11 is a plot of these data, and the outlet contribution is the difference between line 3 and 4.

Extrapolation of these data to 19.3 volts per submodule (1.93 volts/cell) and 22.0 volts per submodule (2.20 volts/cell) permitted determination of the projected values for these contributions during discharge and charge, respectively. Table 24-2 summarizes the projected values.

The total parasitic current is taken as the sum of the leakage, inlet, and outlet currents. These data were obtained in 3M $ZnCl_2$ at 45°C. Table 24-3 summarizes the projected capacity losses in the submodule caused by these parasitic currents. The 64Ah loss on charge accounts for a 1.7% projected coulombic efficiency loss, while the 38Ah loss on discharge accounts for another 0.7% projected coulombic efficiency loss due to parasitic currents flowing in the stack.

Corrosion current measurements were performed in the same manner as the total parasitic and baseline currents, i.e. across the submodule utilizing the normal flow-rate of electrolyte to the cells. The measurements were made however, using chlorinated electrolyte. Figure 24-12 contains plots of the corrosion current data obtained using 3M $ZnCl_2$ at 30°C for chlorine concentrations of 0, 1.0, 1.5, and 2.0 g/ℓ. The data without chlorine (line A) was taken as a measure of the total parasitic plus baseline current and can be compared with line 4 of Figure 24-11. The projected corrosion currents are calculated from the differences between the data with chlorine and data without chlorine extrapolated to the charge and discharge voltages. From the shape of these curves, it can be deduced that mass diffusion of dissolved chlorine is controlling and limits the current at the operating

Table 24-2

PARASITIC CURRENTS IN 8.3kWh SUBMODULE

	Current (Amperes)	
	Discharge	Charge
Type	@ 19.3 v/submodule	@ 22.0 v/submodule
Baseline	0.65	0.74
Leakage	0.28	0.35
Inlet	0.22	0.26
Outlet	0.26	0.30
Total Parasitic	0.76	0.91

Table 24-3

CALCULATED LOSSES IN 8.3kWh SUBMODULE
DUE TO PARASITIC CURRENTS

	Charge	Discharge	Total
Parasitic Current (amperes)	0.91	0.76	--
Time (hours)	7.00	5.00	12.00
Capacity Loss/Cell (ampere-hours)	6.40	3.80	10.20
Capacity Loss/Submodule (ampere-hours)	64.00	38.00	102.00

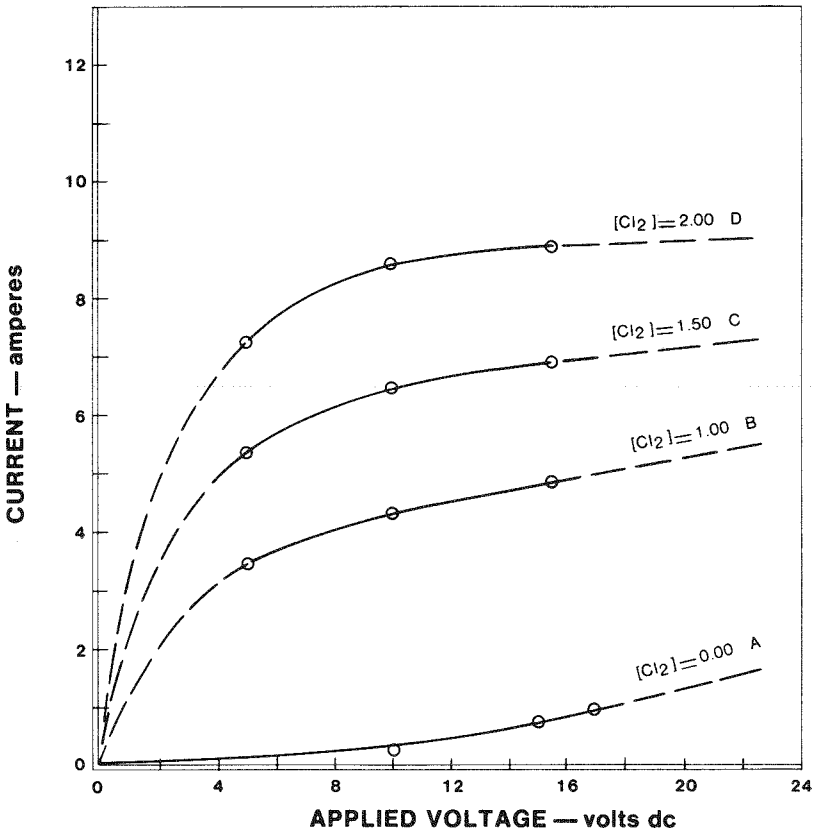

Figure 24-12. Plot of corrosion current measurements made on 8.3kWh submodule test stand at various chlorine concentrations. Note: Test conducted with 3M $ZnCl_2$ at 30°C.

voltages. Furthermore, both charge and discharge corrosion currents will be the same for the same chlorine concentration. These diffusion-limited currents at 1.0, 1.5, and 2.0g/ℓ chlorine concentration are plotted in Figure 24-13. Based on the electrode area per unit cell and the slope of this line, the calculated corrosion current density under these conditions is 1.31mA/cm^2/g/ℓ. This value is approximately half the value of 2.36mA/cm^2/g/ℓ projected by extrapolating zinc weight-loss data obtained on rotating hemispheres (24-1). These values, acquired by different measuring techniques, were obtained in different electrolytes having different pH values, and at different temperatures. Also the surface roughness of the zinc during the weight-loss measurements could have increased turbulence in the diffusion layer causing a somewhat higher value for the corrosion current.

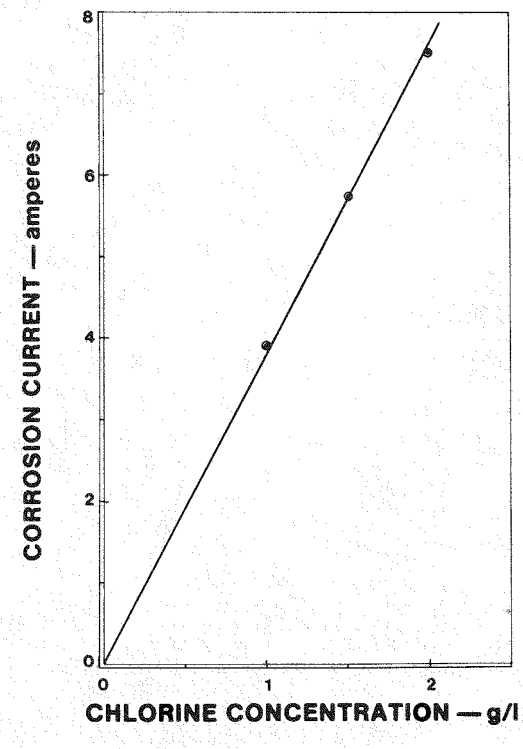

Figure 24-13. Experimentally determined corrosion rate of zinc by dissolved chlorine as a function of chlorine concentration. Note: Test conduted with 3M $ZnCl_2$ electrolyte at 30°C.

The corrosion current values were utilized to predict coulombic losses while charging and discharge at 1.5g/ℓ and 1.5g/ℓ chlorine concentrations, respectively, in the cell gap. The percentage losses are based on a theoretical charge capacity density of 196mAh/cm^2. Summation of the corrosion current and parasitic current data predicts a round-trip coulombic efficiency of 87.3% or 78.6% depending upon the normalized value of the corrosion current used, i.e. either (1.31mA/cm^2)/g/ℓ or (2.36mA/cm^2)/g/ℓ.

Weight Distribution of Zinc Deposit

From the beginning, the performance efficiencies of submodule #3 were below expectations. Voltage monitoring revealed that there was a spread in the efficiencies of each of the ten unit cells in this submodule. Cell number 9 showed the lowest

performance; developing approximately 45% round-trip coulombic efficiency. Two successive cycles gave very similar results -- substandard cells pulling the submodule down to a round-trip usable coulombic efficiency of 59% average and a usable energy efficiency of 45.3% average. At this point a special test was conducted to determine whether the coulombic losses in cell 9 were occurring during charge or discharge. The submoduel was cycled to the normal full-charge condition. The battery was then flushed and unit cells 8, 9, and 10 disassembled. The zinc plating was carefully peeled from the 23 electrode substrates of combs from unit cell 8, a good performer, and unit cell 9, the lowest performer. The zinc plates were then each weighed, tabulated, and the totals and distributions analyzed. The results of this work are shown in Table 24-4. The coulombic efficiency on charge for cell 8 calculates to 85% while it is only 55% for cell 9. This is strong evidence that the excessive coulombic losses during cycling of the submodule are occurring during the charge portion of the cycle.

The 5% deviation in weight among all zinc plates in an individual unit cell shows very satisfactory uniformity throughout the cell. The causes for a 30% deviation in zinc weight from one unit cell to another are not fully understood. Such a difference could be caused by dendritic short circuits, by intercell parasitic leakage currents, or by some bus or chlorine electrode related phenomenon. Visual inspection of the stack structure before and during disassembly revealed no dendrites that could have shorted-out any cells. A later test during cycle #13 eliminated further consideration of parasitic leakage losses. The comb assembly from cell 9 was interchanged with the comb from the zinc terminal end, cell 10. During the next cycle test, it was found that the same previous loss of coulombic efficiency was now transferred to cell 10. This would seem to be strong evidence that these losses are related to the comb structure of the electrode array, but at present the mechanism of such a loss is not understood. During rehabilitation of submodule #3, the presumably faulty comb assembly from cell 9 was saved for future evaluation.

DISCUSSION

The special submodule test stand constructed for this program has proven to be an effective tool for meeting the first objective -- evaluating and comparing the 8.3kWh building blocks of the 45/50kWh EPRI load-leveling battery stack. It incorporates capabilities and features which allow thorough diagnostics of individual unit cells and individual submodule assemblies. It affords a means to study the effects of

Table 24-4

DISTRIBUTION OF ZINC WEIGHTS
FROM UNIT CELLS OF 8.3kWh SUBMODULE

	Zinc Plate Weights (grams)	
Electrode #	Cell #8	Cell #9
1	13.6468 (end)	7.2685 (end)
2	28.0757	17.0259
3	27.8820	17.9400
4	28.4718	18.0822
5	30.3156	16.8853
6	28.7521	19.2915
7	27.0489	18.8659
8	30.4272	19.1810
9	29.0691	18.5671
10	28.7192	19.5950
11	30.0874	19.0557
12	29.5332	18.5914
13	28.8581	17.9492
14	28.1379	18.5068
15	28.8460	19.1830
16	27.4006	20.7862
17	26.9760	18.4570
18	27.5397	18.4772
19	25.9478	18.5289
20	25.5406	18.3768
21	28.6951	18.8319
22	28.4177	17.1977
23	13.4636 (end)	8.2323 (end)
TOTAL	621.8521	404.8765
MEAN	28.2660	18.4035
σ	1.28317	1.082866
% DEVIATION	4.54%	5.88%
CHARGE EFFICIENCY	85%	55%

varied operational parameters and of selected electrolyte formulations under carefully controlled conditions. In its ability to simulate conditions existing in the full-size 45kWh module, it provides an important link between "single" cells and the larger complete integrated battery.

Test cycles on a selection of different submodules operated under a variety of conditions has shown that there is a wide variation in the performance of these assemblies. It also has shown that there exists a large variation in the performance of individual unit cells within some submodules. This is detrimental to performance, but no satisfactory explanation is available at present to account for these variations.

The second objective of this program -- establishing conditions for a full 200mAh/cm^2 capacity cycle at 65% or better round-trip usable energy efficiency -- was not reached. The differences in unit cells of submodules tested and the restrictions on test conditions created problems that could not be overcome in time. All cycle testing during this Phase I program was purposefully restricted to operating conditions that could be duplicated in the 45kWh battery module without system modifications. These limitations were:

- Initial electrolyte concentration between 2.9- and 3.0-molar $ZnCl_2$.
- Electrolyte volumes of approximately 36 liters. This generates a large swing in Zn^{++} concentration during a full-charge cycle.
- System pressure reduction limited to 5 psi maximum.
- Current densities no higher than 40mA/cm^2.

Operating within these limits it was not possible to reach a dendrite-free charge capacity of 200mAh/cm^2 with coulombic efficiencies over 65% no matter what other parameters were varied, and regardless of the electrolyte composition tried.

Some work towards the third objective was successful, and some should be carried on into Phase II in order to arrive at satisfactory conclusions. From the measurements made on shunt and corrosion currents in the stack, round-trip coulombic efficiencies in the range of 79% to 87% may be predicted. However, the technique used to determine corrosion current establishes only the lower limit of the corrosion current. Therefore, such measurements may not accurately predict battery performance.

Measurements on the solubility of chlorine in $ZnCl_2$ electrolyte at various pressures and temperatures support the general theories very well. However, any verification of the assumed improvement in stack performance with reduced chlorine concentration is difficult to find in the test data. Perhaps it is masked by other prominent variables. Special experiments employing a wider range of vacuum and temperature will be conducted during Phase II to test the assumption that chlorine concentration does affect the rate of corrosion of zinc plate, and thus the coulombic efficiency of a cell.

In summary, the significant results of the submodule test program can be highlighted as follows:

- There is wide variation in performance of unit cells in any submodule stack. This variation is not consistent and is detrimental to submodule performance.
- The restrictions on operating parameters and on electrolyte concentration swing were too severe to achieve the specified charge capacity at an acceptable efficiency.
- Coulombic charge inefficiencies vary with time, being much higher with longer cycles.
- Improvements in coulombic efficiency by operating at reduced pressure (and thus at reduced chlorine concentrations) could not be demonstrated by the data collected to date.

REFERENCE

24-1. Jung Kim and Jacob Jorne. "Mass Transfer of Dissolved Chlorine to a Rotating-Zinc Hemisphere in $ZnCl_2$ Solution". J. Electrochem. Soc., January, 1978, p. 125.

Section 25

CYCLE TESTING OF 1.7kWh BATTERY SYSTEM

INTRODUCTION

The cycling objectives for the 1.7kWh system are to:

- determine the electrochemical life of the electrodes
- verify the adequacy of the electrode to bus contact
- cycle system continuously in a controlled test regime
- collect data to fully characterize system

In April of 1976, the 1.7kWh system was first cycled. A detailed description of the results was published in an earlier report (25-1). A delivery of 1.7kWh with an average electrochemical energy efficiency of 64% was recorded for the 54 cycles acquired during 1976.

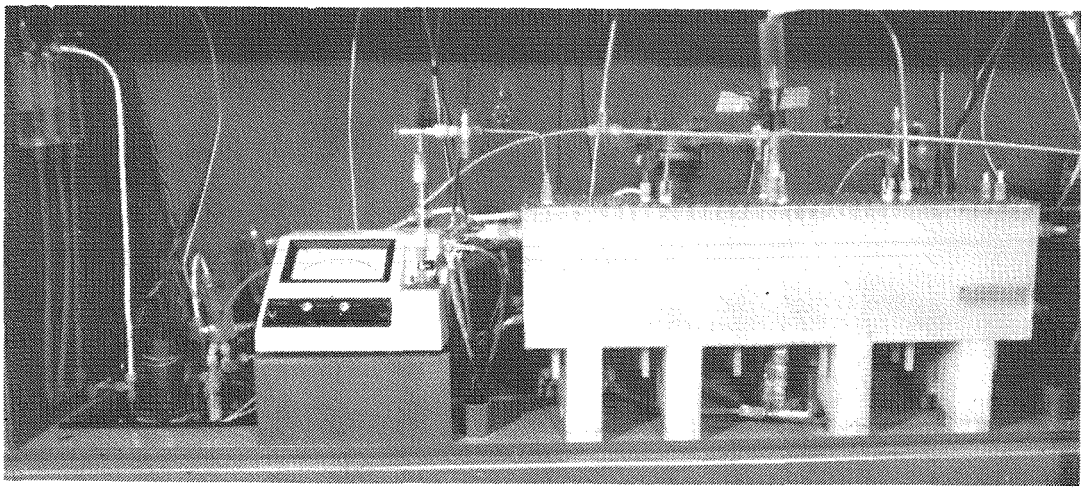

Figure 25-1. Photograph of 1.7kWh Battery System Installed in Laboratory Hood

This system is shown in Figure 25-1. On January 12, 1977, it was interfaced to the microprocessor-based control unit, shown in Figure 25-2. Twenty-four hour attended cycling began February 28. Unattended cycling began two days later and continued thereafter. Four hundred forty-six (446) cycles were accumulated during Phase I (cycle numbers 55-500). System output during these cycles was approximately 1.6kWh with an average electrochemical energy efficiency of 63.8%.

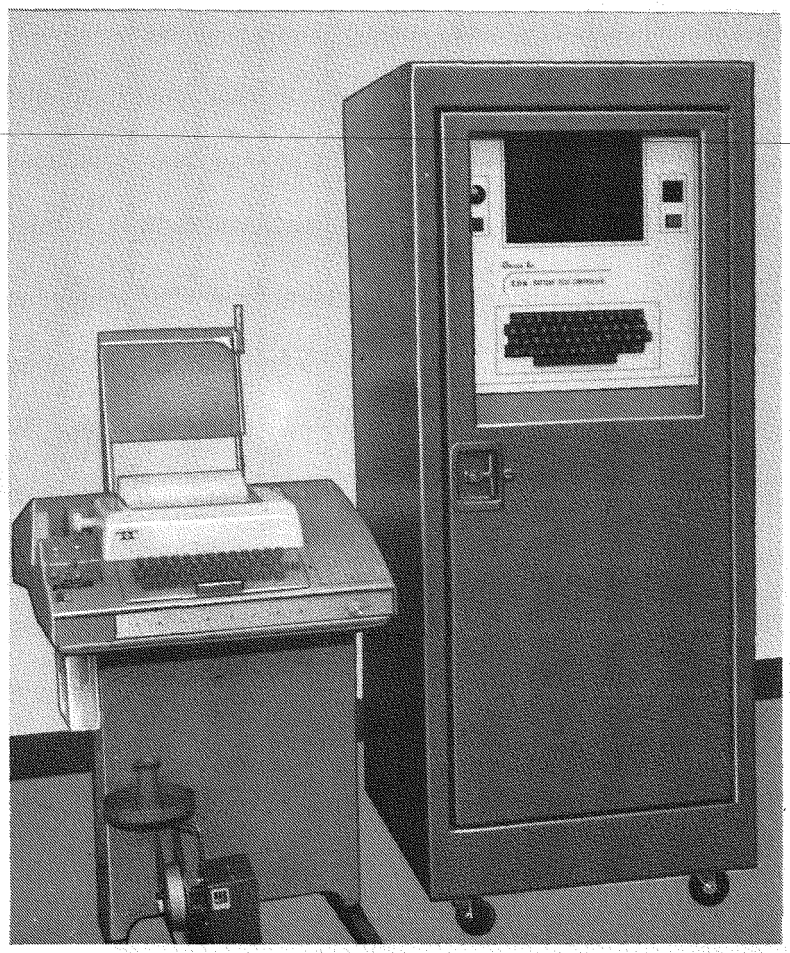

Figure 25-2. Microprocessor-based automatic controller and standard teletypewriter data printout device for the 1.7kWh battery system.

SYSTEM DESCRIPTION

The stack of this system (an enlarged detail presented in Figure 25-3) utilizes monopolar comb construction. Briefly, each chlorine electrode pair has one (1)

electrolyte feeder tube and a single gas vent in the top. The chlorine electrode area is 64.52cm^2. The zinc electrodes are all double-sided (except the two ends which are single-sided). There is a 0.120" gap between the zinc and chlorine electrodes. Masking in this system aids in maintaining the gap.

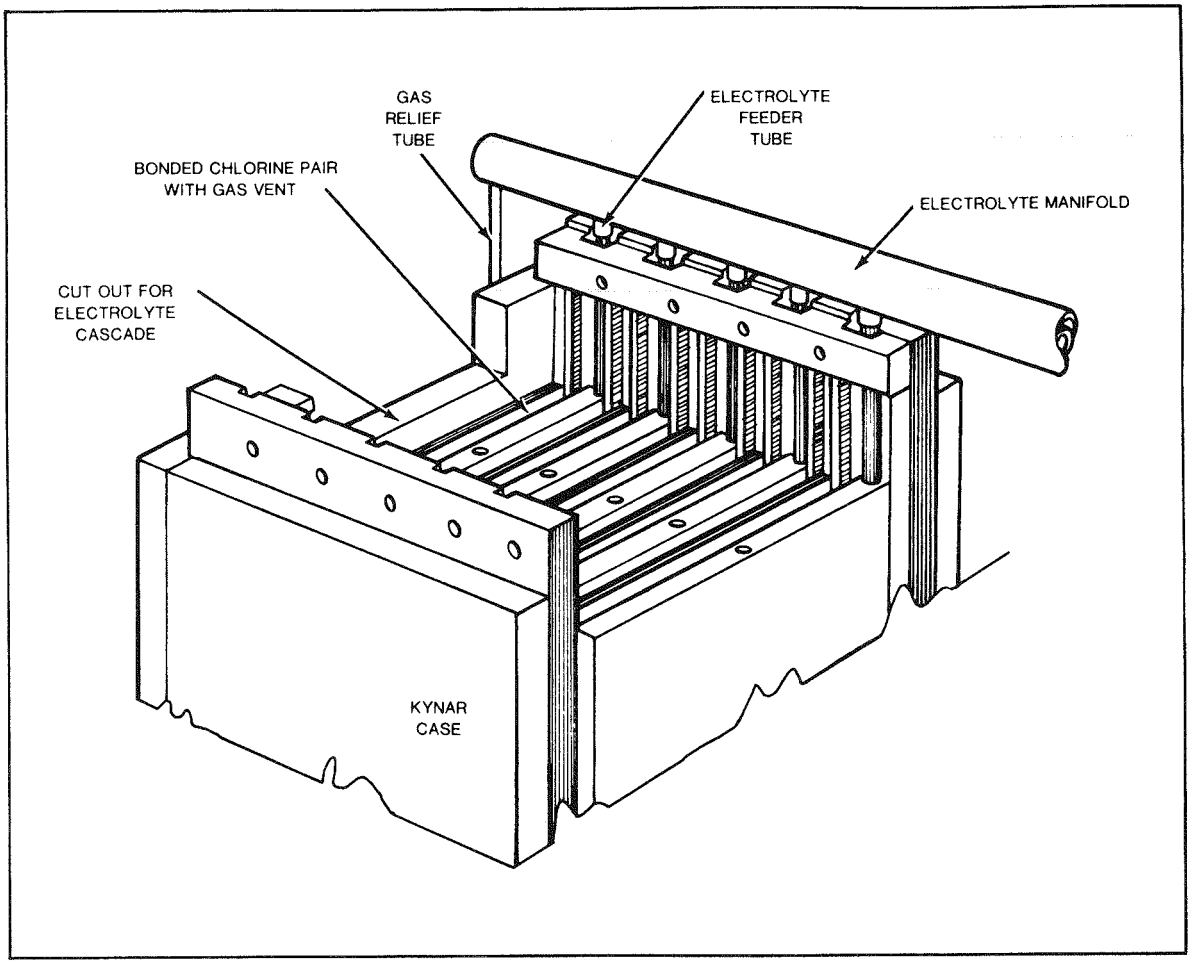

Figure 25-3. Section of 1.7kWh battery showing construction details. Chlorine outlet-bus with provision for electrolyte feed tubes as shown; remainder of secondary outlet busing removed for clarity.

An overview of the stack (Figure 25-4) shows two units paralleled through common secondary buses. The monopolar array of 48 chlorine and 25 zinc (23 double-sides, 2 end single-sided) electrodes per unit totals to 96 parallel cells having a total area of 6194cm^2.

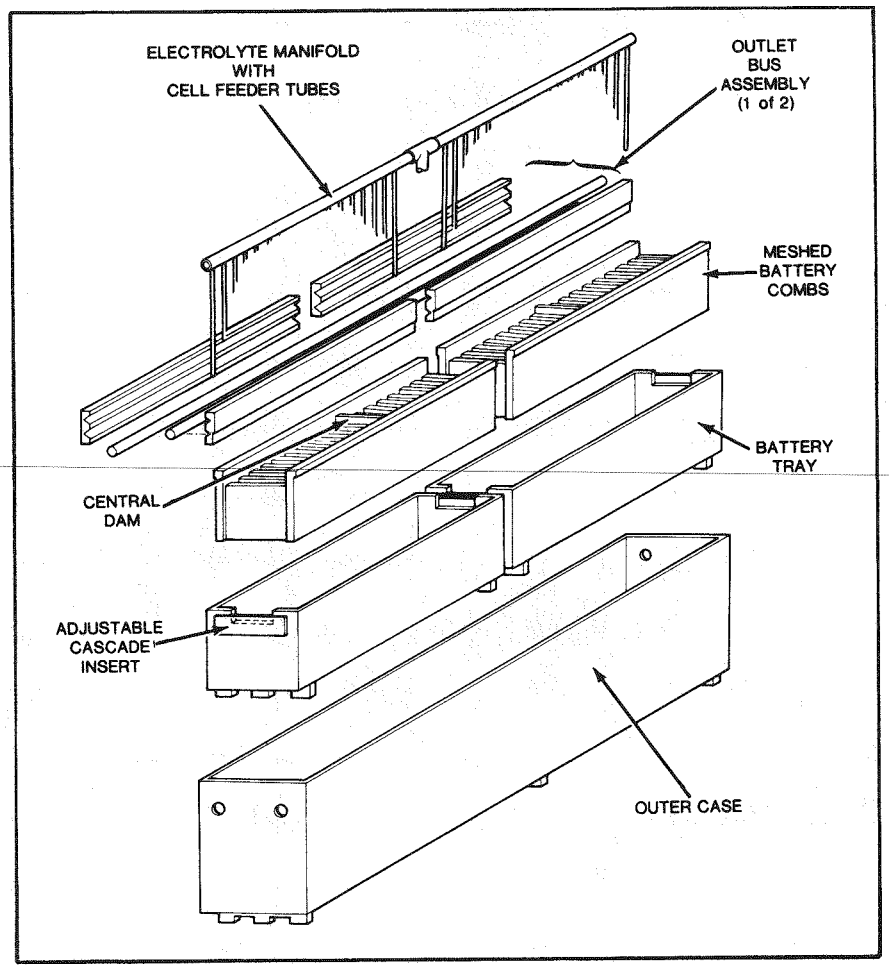

Figure 25-4. 1.7kWh stack unit. Outer case serves as electrolyte sump, and defines major gas space in system. Outer case cover not shown.

The overall system including stack, which is diagrammed in Figure 25-5, consists of four main loops: the electrolyte loop, the gas space loop, the hydrogen recombination loop, and the chlorine storage loop. A more complete description can be found in the EPRI EM-711 Interim Report (25-1).

Loop 1

The main electrolyte loop begins at the bottom of the case, flows out of the sump through a heat exchanger to establish isothermal flow, and, during discharge only, has chlorine gas injected into the stream by a micropump. The flow then enters a

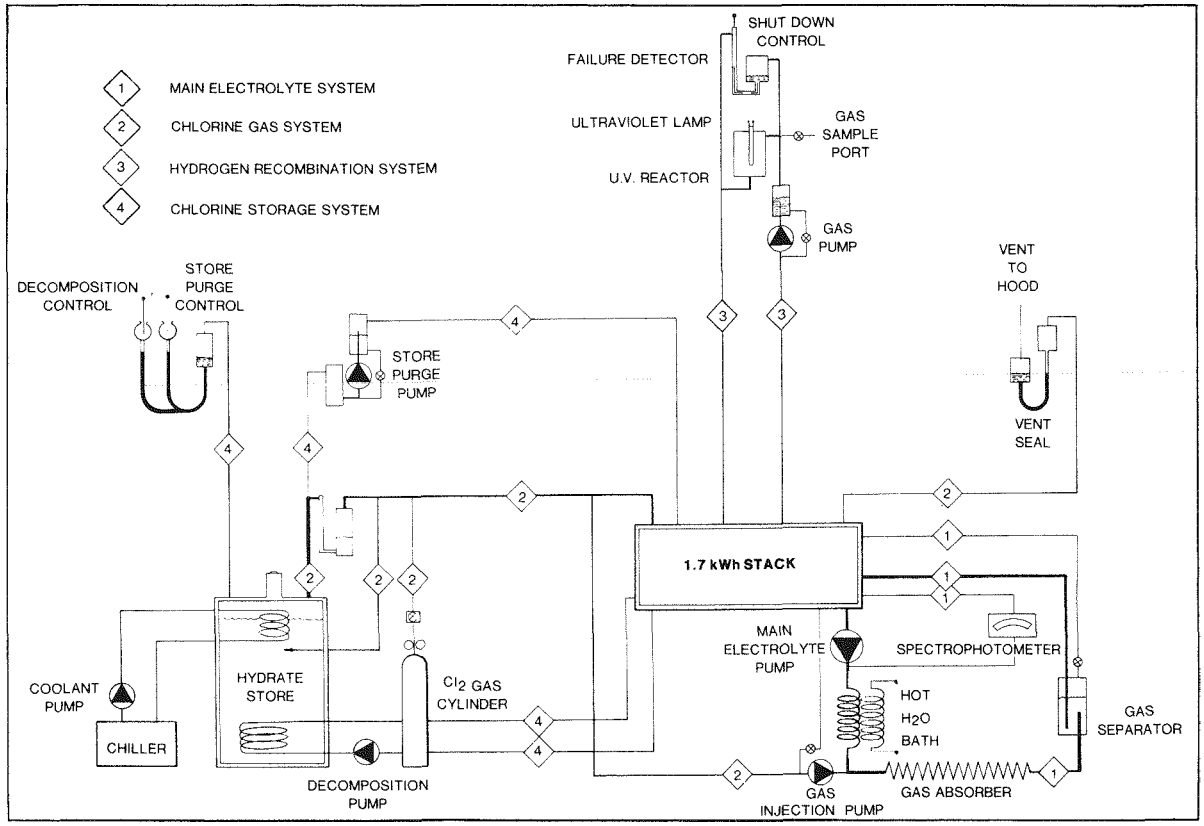

Figure 25-5. Schematic diagram of the 1.7kWh battery test system. Note the four numbered component subsystems and the failure detectors as shutdown controls.

mixer to chlorinate the electrolyte and passes through a gas separator removing excess Cl_2 which returns to the stack gas space. The chlorinated electrolyte re-enters the battery case directly into the manifold. A small amount of electrolyte is continuously pumped through a spectrophotometer. The battery electrolyte capacity for a five-hour charge is 15 liters. The electrolyte flow rate is 1.86ml/min/cm^2 (12ℓ/min).

Loop 2

Only one gas line interconnects the store and the battery. During charge, gas leaves the top of the battery and, directed by a differential manometer, flows into the store via the inlet tube located below liquid level. On discharge, Cl_2 leaves through the upper exit tube, through the differential manometer, and back into the gas space, where it is removed by the gas injection pump. The auxiliary Cl_2 tank is tied directly into this gas line for use in discharge when hydrate is no longer available.

A differential manometer is connected to the battery gas space to prevent the possibility of excessive pressurization of the battery box. The total gas volume is 18 liters.

Loop 3

The gas recirculation loop exits the battery case from the gas space enters a micropump that pumps it through a chamber containing two ultra-violet lights. This serves to recombine any free hydrogen with the chlorine. A small amount of gas bypasses the ultra-violet light chamber and passes through a manometer that acts as a failure detector. The flow rate of gas through this loop is 10ℓ/min.

Loop 4

Chlorine is stored during charge by forming chlorine hydrate in the store. Hydrate is formed by cooling the water in the store to 5°C (the temperature at which hydrate readily forms) by pumping cooled ethylene glycol through the heat exchanger in the store. The Cl_2 gas enters a heated inlet tube above an agitator which mixes the water and chlorine. The precipitated hydrate settles to the bottom of the store as it is formed. On discharge, warm electrolyte from the battery is circulated through a coil in the bottom of the store by a micropump to decompose the hydrate. The control manometers for the vent pump and decomposition pump are connected directly to the gas space. The store vent pump is turned on during charge when the store pressure is high. The decomposition pump comes on in discharge when store pressure is low.

CONTROLLER DESCRIPTION

Objectively, the task of cycle testing the 1.7kWh battery required a completely hands-off, automatic control system. This meant repeatedly stepping the battery system through each charge/discharge cycle while controlling the auxiliary subsystems as well as monitoring various battery operating parameters. There must be a provision for detecting the failure of a battery component or subsystem and safely terminating the test upon such occurrence. Also necessary, are data acquisition and visual display of battery parameters.

The Cycle Controlling Regime consists of seven phases:

- Cooldown - the store is lowered to the temperature range for hydrate formation.

- Constant Current Charge - zinc is deposited on the graphite electrode and chlorine is evolved on a porous graphite electrode. This phase is 5 hours in length at 220 amps with a current density of 35.5mA/cm^2.

- Turnaround - starts decomposition of chlorine hydrate in the store to assure an adequate supply of chlorine during the initial stages of discharge.

- Constant Current Discharge - current is maintained at 190 amps regardless of voltage fluctuations.

- Variable Current Discharge - when voltage falls below 1.7 volts, current is stepped down incrementally.

- Cleanout - remaining zinc is stripped from the electrodes via a resistor switched across the battery terminals. At the end of this timed phase, the system returns to the cooldown phase to begin a new cycle.

- Standby - upon initial power up, the control system enters the STANDBY mode. In an idle state, battery cycling is not initiated until manually switched to another phase in the cycle, or entered after a failure has been detected.

Data Display

Data for display, printout, and control are read and stored in memory by the central processing unit of the computer. Status of battery parameters and calculated performance data are displayed on the cathode-ray tube screen. Hardcopy printout of this information is available on the teletypewriter. By keying in the appropriate parameter description, a printout of displayed data can be obtained (Figure 25-6).

Table 4-1 lists the battery data symbols displayed, their meaning and when they are printed.

Failure Detection

As the microprocessor control system is controlling the battery cycle, it recognizes symptoms of battery or auxiliary unit malfunctions. Data read by the computer is compared against preset system limits. If a limit is exceeded, an audible alarm sounds, a warning lamp is illuminated and an error message is displayed on the CRT screen.

To prevent unnecessary shutdown due to transient conditions, no further action is taken by the controller for a short period of time. Subsequently, if data indicates that the faulty conditions still exist, then the controller terminates the test cycle by reverting to STANDBY, or other appropriate, predesignated course of action to prevent damage to the battery system.

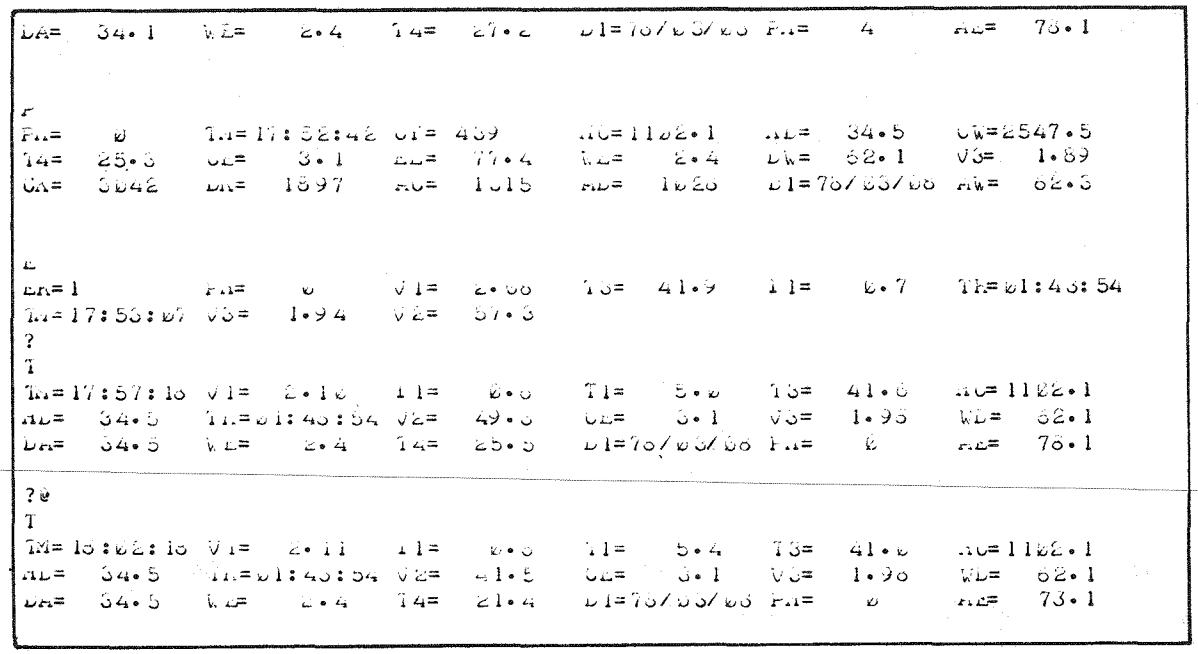

Figure 25-6. Sample Copy of Typical Data Printout from 1.7kWh Battery System

Table 25-1

SYMBOLS USED FOR DATA PRINTOUT

SYMBOL	DESCRIPTION	ENTERED ON DATA RECORD DURING — TIMED PRINTOUT	PHASE CHANGE PRINTOUT	ERROR LINE PRINTOUT
V1	Battery Terminal Voltage	X		X
V2	Spectrophotometer (percent transmittance)	X		X
V3	Ultraviolet Lamp Voltage	X	X	X
T1	Store Temperature	X		
T3	Sump Temperature	X		X
T4	Ultraviolet Lamp Cylinder Temperature	X	X	
I1	Battery Current	X		X
HC	Current Cycle Charge Ah ($\Sigma I\Delta t$)	X	X	
HD	Current Cycle Discharge Ah	X	X	
DA	Ampere Hours (Current Cycle, Charge or Discharge)	X		
CY	Cycle Count		X	
PH	Phase	X	X	X
TM	Time of Day	X	X	X
TR	Time Remaining in Phase	X		X
ER	Error Number			X
D1	Date	X	X	
CE	Current Cycle Amp-Hour Efficiency (HD/HC x 100%)	X	X	
EE	Current Cycle Voltaic Efficiency (WE/CE x 100%)		X	
WE	Current Cycle Energy Efficiency (DW/CW x 100%)	X	X	
WD	Watt Hours (Current Cycle, Charge or Discharge)	X		
AC	Accumulated Charge kAh		X	
AD	Accumulated Discharge kAh		X	
CW	Current Cycle Charge Wh ($\Sigma VI\Delta t$)		X	
DW	Current Cycle Discharge Wh		X	
CK	Accumulated Charge kWh		X	
DK	Accumulated Discharge kWh		X	
AE	Accumulated Voltaic Efficiency	X		
AW	Accumulated Energy Efficiency		X	

TEST DATA

Currently a cycle is defined as a charge duration of greater than 4 hours, with a normal charge being 5 hours, and an energy efficiency equal to or greater than 60%.

The test conditions for this cell are:

- charge current = 220 amps
- charge current density = 35.5mA/cm^2
- constant current discharge current = 190 amps
- constant current discharge current density = 30.8mA/cm^2
- electrolyte flow rate = 1.86ml/min/cm^2 or 12ℓ/min
- dissolved Cl_2 levels = 1.4g/ℓ discharge
- temperature = 40°C

A failure of this system could be one of two types, cycle failure or battery failure. Cycle failure refers to the concept of cycling being interrupted. There are two known causes of this, control equipment or auxiliary hardware breakdown. Control equipment failure could disrupt cycling (1) by sensing an error that does not exist and switching the system to standby, (2) by switching to the wrong phase or switching an auxiliary on or off at the wrong time and thus sensing a real error and shutting the system down, or (3) by losing power and dumping accumulated data. Auxiliary hardware includes pumps (seals, shafts, etc.) motors, solenoids, thermocouples, and manometers. Battery failure is defined as an inability to cycle due to the battery itself. This includes a loss in battery capacity (ability to charge for 5 hours at 35.5mA/cm^2), failure to discharge properly (system totally unable to maintain a 190 amp discharge), or a large loss in efficiency (if mechanical and flow problems could all be dismissed, then this would indicate electrode deterioration). The 127 failures that occurred during the 15 month test program of Phase I are classified and tabulated in Table 25-2. To aid analysis and discussion, the individual failures, identified by the preceding cycle number, are grouped into discrete time periods (cycle intervals).

Cycles 55-100

Cycle number 55 (2-3-77) was the first automated cycle. On February 28, 1977, (cycle number 58) attended 24-hour cycling began. On March 2, 1977, (cycle number 63)

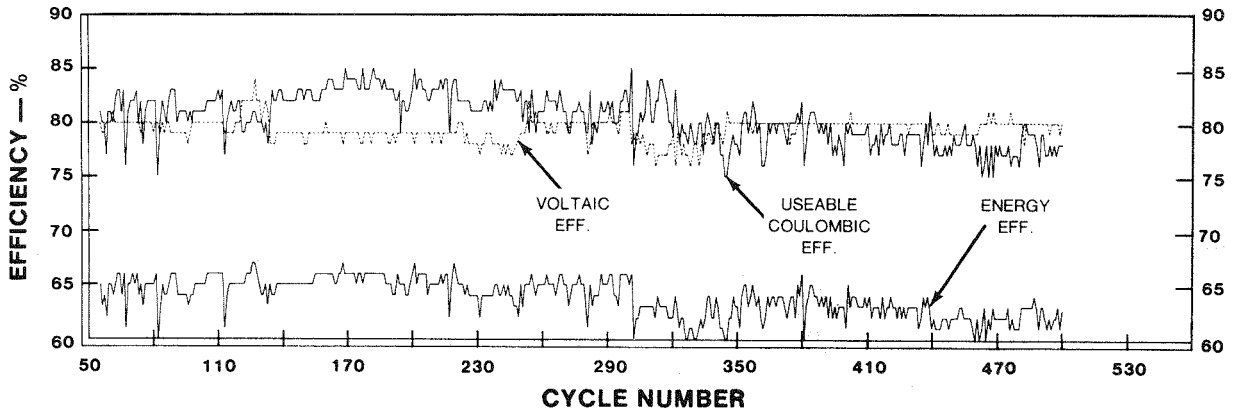

Figure 25-7. Performance efficiencies of the 1.7kWh battery system plotted against cycle number.

Table 25-2

FAILURE TABLE
FOR 1.7kWh BATTERY

Component	Failure Reference Number	Type of Failure	Cycle Number Preceding Failure — Cycle Interval 55-100	101-200	201-300	301-400	401-500	Total Failures of Each Type
PUMPS:								
Gas recirculation	1	Seal leakage		120,156	295			3
	2	Worn gears and shaft		120				1
Gas injection	3	Worn pump head				332,340		2
	4	Loss of motor efficiency				332		1
	5	Pump decoupled from motor	61	136,192				3
Main electrolyte	6	Seal leakage	98		250	340		3
Store purge	7	Loss of motor efficiency				301		1
STORE:								
Agitator	8	Impeller decoupled from motor		189	206	350	455,459	5
	9	Worn brushes				302,398(5)*		6
Coolant loop	10	Motor turned off			294			1
	11	Cooling inefficiently		130,134(2)				3
Decomposition loop	12	Loss of pump motor efficiency			224		438	2
	13	Line blockage		164	297(2)			3
	14	Motor control not working efficiently		113	224		437,438	4
Miscellaneous	15	Thermocouple not working properly			295			1
	16	Fluid exchange between store and battery		112		301(2) 303(2)		5
DATA ACQUISITION SYSTEM:								
Microprocessor based control unit	17	Memory loss		192	217,220 222,224(2) 226			7
	18	Electrical noise causing control problems				327(2)		2
	19	Inlet tube heater not turned on				301(4)		4
	20	Controller put system in charge prematurely			217,277 280			3
	21	Miscellaneous			295	301,302 319(2),320(3) 322,381	492,493 495,497 499	15
Teletype	22	Inoperative			220,229			2
MISCELLANEOUS:	23	Power outage in building		115	284,295	302,373		5
	24	No auxiliary chlorine		100		320	499	3
Low energy efficiency	25	Plugged vent holes				320(15) 303(4),320(3) 344(4),350(4)		30
	26	Unknown reason					452,456 463	3
INDETERMINATE REASON:								
Charge	27	Low voltage			224	320		2
	28	Low current			217			1
Discharge	29	Low chlorine concentration			230	301,344(2)		4
	30	Low voltage			249	320		2
		TOTAL FAILURES IN EACH INTERVAL	2	15	27	69	14	127

*Number in parenthesis indicates number of times this failure occurred.

unattended 24-hour cycling began. Two and a half-days of attended cycling preceded the unattended cycling to ensure that the system would control properly in the continuous cycling mode. The three cycles that preceded cycle number 58 illustrated that the cycle control of the system was working properly. Once established that it could control continuous cycling, the system was allowed to cycle without monitoring.

The average energy efficiency of cycles 55-100 was 64.5% with a standard deviation of 1.3%. The standard deviation of the preceding 54 cycles was 2.0. By this and also by visual inspection of Figure 25-7, it can be seen that the automation of the system produced more consistent levels of battery performance (usable coulombic efficiency and voltaic efficiency).

The two cycle failures experienced were both maintenance related (Table 25-2). The interfacing of the system to a microprocessor-based control unit and the few cycling failures resulted in dramatically increasing the number of cycles run per month as depicted in Figure 25-8. Each plateau on Figure 25-8 signifies when the system was not running, whereas a steady upward climb signifies continuous cycling. The plateau at cycle number 55 was related to control debugging. The previous 54 cycles took almost five months to complete. These 46 cycles took only 1.5 months.

There were two electrolyte changes. The first was after 46 cycles (55-90) in order to test a new electrolyte composition. The second after eight cycles (91-98) was caused by a leaking seal on the main electrolyte pump.

Cycles 101-200

The average energy efficiency of these cycles was 65.3%. The standard deviation was 0.8%. By visual inspection of Figure 25-7, it is evident that the efficiencies have remained quite consistent.

There were 15 failures during these 100 cycles (Table 25-2). Ten of these could be classified as routine auxiliary (maintenance type) problems. Three failures were attributable to the coolant bath not working properly. This problem was solved by putting a new coolant bath unit in place of the old one. One failure was due to a fluid exchange between the store and battery. The cause of this isolated failure was then unknown, therefore no attempt was made to prevent its reoccurrence. Another failure was due to the controller losing power to memory and shutting down the system.

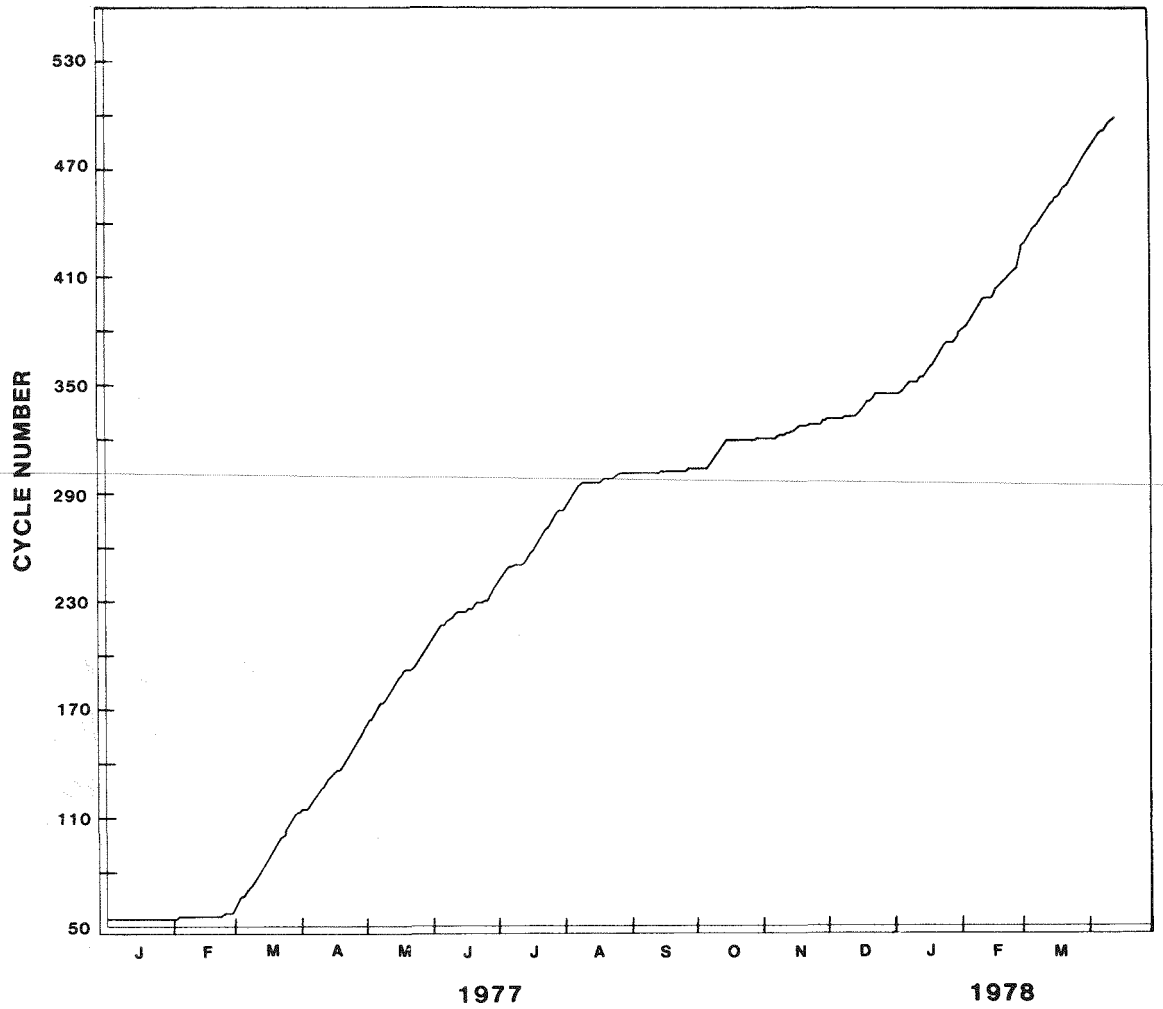

Figure 25-8. Showing the number of test cycles accumulated with the passage of time during Phase I testing of the 1.7kWh battery system.

This also was an isolated failure whose cause was not discovered. Nine cycling days were lost (Figure 25-8) due to these failures. This 100 cycles took a little over two months to complete. An electrolyte change after 14 cycles (99-112) was required as the result of a fluid exchange between battery and store.

Cycles 200-300

The average energy efficiency of these cycles was 64.7%. Standard deviation was

1.14. That is a relatively small variation and by inspecting Figure 25-7 we can see the efficiencies are fairly consistent.

There were 27 failures during these 100 cycles. Thirteen were classified as routine auxiliary problems. Four were types that could not be specifically explained. Ten were directly attributable to the controller. Six of these ten failures were due to low power in the memory unit wiping out previous cycle information. This problem was thought to be caused by either low voltage on line from power company or weak power supply in the unit itself. This problem was corrected finally by putting on a sola transformer to regulate line voltage and replacing the 5V power supply in the controller. This problem has not reoccurred. Three of these failures were associated with the controller allowing the system to start charging before the cooldown exit temperature was reached, resulting in a failure on charge and system shutdown. This problem has not reoccurred. One failure was due to new controller board debugging (see discussion in next 100 cycle section). Thirty cycle days were lost (Figure 25-8). This 100 cycles took about three months to complete.

There was one electrolyte change after 138 cycles (113-250). The electrolyte was lost due to seal on main electrolyte pump.

Cycles 301-400

The average energy efficiency of these cycles was 62.8%. The standard deviation was 1.21. The deviation was somewhat larger than the previous 100 cycles but was still acceptable. The scatter was much greater than for previous cycles (Figure 25-7). There were many experimental problems during this 100 cycles.

There were 67 failures during these 100 cycles. Twenty-four could be classified as routine auxiliary problems. Five of these, on hindsight, proved to be agitator failures due to worn motor brushes. The four liquid exchanges were due to the controller malfunctioning four times and not activating the inlet heater, resulting in the tube freezing up. This was corrected. The nine miscellaneous controller failures and one from the previous 100 cycles, were due to changes being made in the software and the debugging involved. Thirty of these failures were due to low energy efficiencies caused by blockage of chlorine vent holes by wax-like deposits. These problems started in late August and several remedies were tried to remove them. Finally in mid-January, the battery top was removed and the deposits were noted and removed. The vent holes were enlarged to prevent this from reoccurring. The chlorine electrodes were gas-locking (the ones with deposits) and the zinc electrodes

across from them could not discharge as quickly as the ones that could get chlorine. This problem has not reoccurred. One hundred and eight cycling days were lost due to the failures. Almost six months elapsed during accumulation of these 100 cycles.

There were seven electrolyte changes: one after 51 cycles (251-301) due to fluid exchange with store; after two cycles (302-303) due to fluid exchange; after no cycles (after 303) due to another fluid exchange; after 28 cycles (304-331) due to attempts to improve battery performance; after nine cycles (332-340) due to main electrolyte pump seal failure; after four (341-344) cycles, electrolyte too dilute after adding water; after 17 (345-361) cycles to improve performance (after deposits found).

Cycles 401-500

The average energy efficiency of these cycles was 62.3%. The standard deviation was 1.05. This is a smaller deviation than for the previous 200 cycles. There were fourteen failures during these 100 cycles (see Table 25-2). Five of these failures could be classified as routine auxiliary problems. Three of these failures were due to low energy efficiencies; there was no apparent reason for them. Five of these failures were due to miscellaneous problems in the controller, thought to be due to electrical noise getting into system. Only one cycling day was lost (Figure 25-8). This was due to failure #21. Approximately two months elapsed during accumulation of these 100 cycles.

There were two electrolyte changes: one after 100 cycles (362-461) due to suspected electrolyte contamination; one after 17 cycles (462-478) due to unexplained variations in electrolyte composition.

CONCLUSIONS AND RECOMMENDATIONS

The 1.7kWh battery, constructed according to a very early monopolar-comb design, represents the first entry of porous-graphite chlorine electrodes into the EDA peak-shaving battery program. Even though there are known deficiencies in the design, this stack has developed into a consistent and reliable performer. After some eighteen months of continuous charge/discharge cycling following the expected peak-shaving regime, the battery continues to operate at full-charge capacity (220 amperes for 5 hours). It discharges normally, delivering an average of 1.6kWh. The average round-trip usable energy efficiency developed for all 446 complete cycles is close

to 64%. The slight drop in performance late in the program can be traced to variables in operating conditions rather than to any inherent changes in the battery stack. Once all parameters affecting energy efficiency (electrolyte formulation, pH, chlorine concentration, temperatures, pressures, flow rates, etc.) are optimized, the system can be expected to cycle continuously with great consistency. Logic changes were incorporated into the microprocessor, the heart of the automatic controller, late in December. These apparently have corrected many control problems and the system is now performing according to specification.

It is intended that this system should continue to cycle automatically and unattended for some time to come. Experience indicates that this objective would be more easily reached if reliability improvements can be made to the peripheral equipment. It is recommended that each auxiliary component be examined and, as time permits, modified to this end. It has been suggested that some testing with this system be done more closely approximating the current peak-shaving duty sequence. This would incorporate extended "stand" times between charge and discharge. There is a need to examine the physical and electrochemical characteristics of zinc plates after 3 to 7 hours of inactivity. Also to be evaluated would be effect of stand time on H_2 evolution rates and efficiency.

REFERENCE

25-1 Development of High-Efficiency, Cost-Effective, Zinc-Chlorine Batteries for Utility Peak-Shaving -- 1976. Palo Alto, Calif.: Electric Power Research Institute, March 1978. EM-711.

Section 26

CYCLE TESTING OF THE 1.4kWh BATTERY SYSTEM

INTRODUCTION

The cycling objectives for the 1.4kWh system are to:

- determine electrochemical life of ruthenized titanium chlorine electrodes
- cycle system continuously in a controlled regime
- collect data to fully characterize system

The ruthenized-titanium chlorine electrodes that were cycled 100 times in 1975 in the 1.0kWh battery system are currently undergoing life testing in the 1.4kWh system. The 1.4kWh battery was put on line in April of 1976. It was first cycled in May, 1976. The hard-wired logic for this system was first interfaced to it in mid-August, 1976, followed at the end of August by the first automatically controlled cycle. In early November, 1976, attended 24-hour cycling began. Seven days later unattended cycling began and continued thereafter. A detailed description of the testing, through 1976, was published in the EPRI EM-711 Interim Report (26-1). Briefly, 135 cycles were acquired in 1976 each delivering an average of 1.4kWh with an average electrochemical energy efficiency of 67.0%.

In 1977 one hundred eighty-eight (188) cycles were accumulated during Phase I (cycle numbers 136-323). These cycles delivered 1.4kWh, on the average, with an average electrochemical energy efficiency of 66.5%.

SYSTEM DESCRIPTION

A complete description of the 1.4kWh battery system can be found in EPRI EM-711 Interim Report (26-1). It can best be described by visualizing four distinct loops

(Figure 26-1): the electrolyte loop, the gas space loop, the hydrogen recombination loop, and the chlorine storage loop.

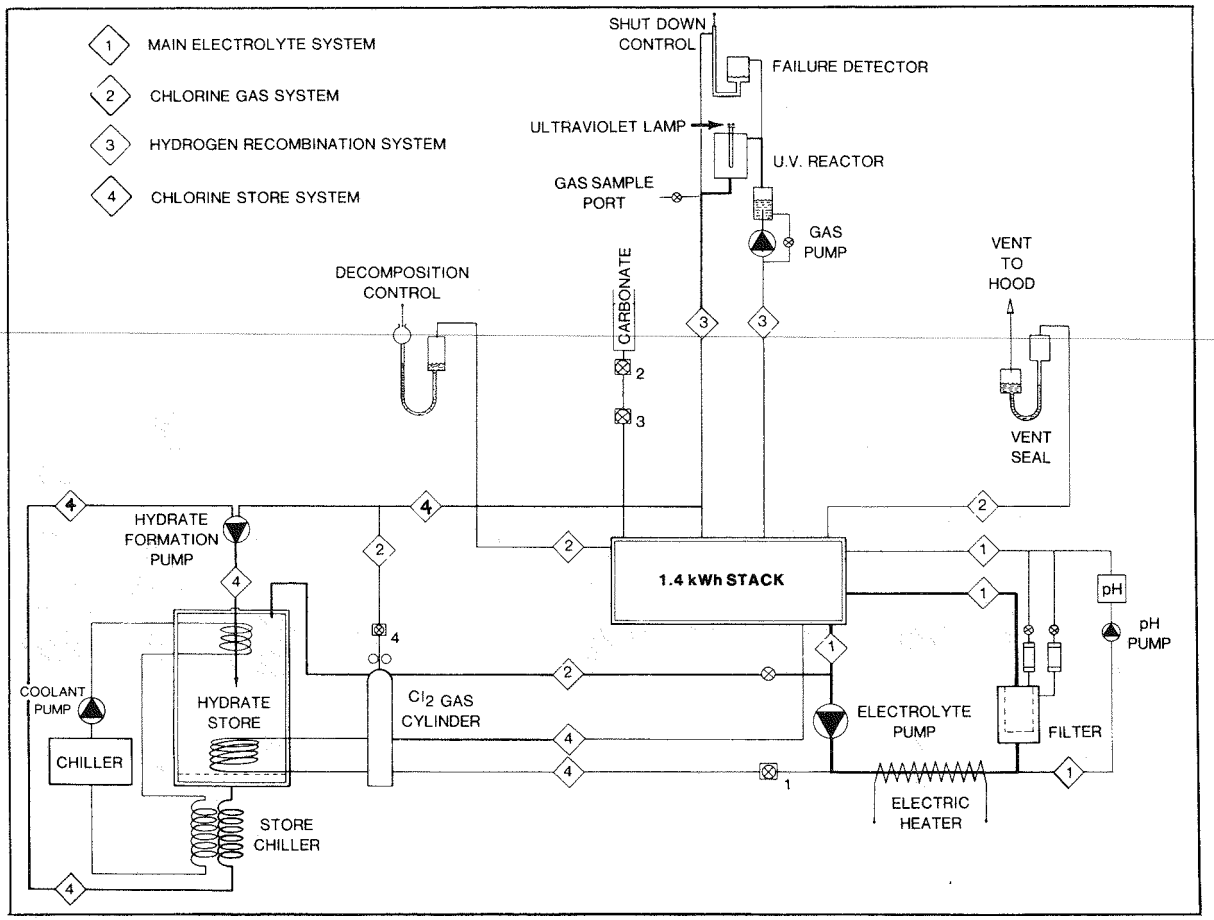

Figure 26-1. Schematic of 1.4kWh battery test system. Note the four principle subsystems or loops into which the system is divided.

Loop 1. The main electrolyte loop begins at the battery sump. From there it goes into a heat exchanger, through a filter, back into the battery box, and then it drains back into the sump. A side loop goes into a flow-through pH meter. The electrolyte capacity of this system is 12 liters.

Loop 2. The gas loop consists of two lines. One line brings the chlorine from the top of the battery to the hydrate pump on charge. The other line returns the chlorine from the store back to the battery on discharge. The auxiliary chlorine tank

and the control manometer for the decomposition pump are both located along the latter line.

Loop 3. The gas recirculation loop is made up of a gear pump and a chamber containing two ultra-violet lights. As the name implies the gas from the battery case is being constantly recirculated through the ultra-violet light chamber. This serves to allow recombination of any free hydrogen with chlorine. A pressure sensing manometer is used as a failure detector on this system.

Loop 4. Chlorine is stored during charge by forming chlorine hydrate in the store. Water flows from the bottom of the store through a heat exchanger to cool it and then into a gear pump. The hydrate forms at the exit side of the pump and enters the store and accumulates on a filter cloth at the bottom of the store. Coolant is also pumped through a coil in the store to maintain its temperature during charge. On discharge warm electrolyte from the battery circulates in a coil at the bottom of the store to decompose the hydrate.

CONTROLLER DESCRIPTION

This section describes the automatic control (shown in Figure 26-2) and data acquisition system (shown in Figure (26-3) as applied to the 1.4kWh titanium battery. The primary task was to provide the necessary circuitry to step the battery through a predetermined test profile. This included control of the test cycle and the various battery auxiliaries. The second, but equally important, requirement was to provide the monitoring and logic necessary to protect the battery from damage due to the failure of either a battery component or an auxiliary function. A third task was to provide for the logging of various battery data in a form that would allow immediate access and long term data analysis.

Automation Sequence

The battery test profile describes the orderly sequence of events that occur during the charge and discharge cycle of the battery. The cycle controller phases are as follows:

- STANDBY - Upon initial power, the control system enters the STANDBY mode. In an idle state, battery cycling is not initiated until manually switched to another phase in the cycle.
- COOLDOWN - During COOLDOWN, the first step in cycle testing, the store is cooled to operating temperature.

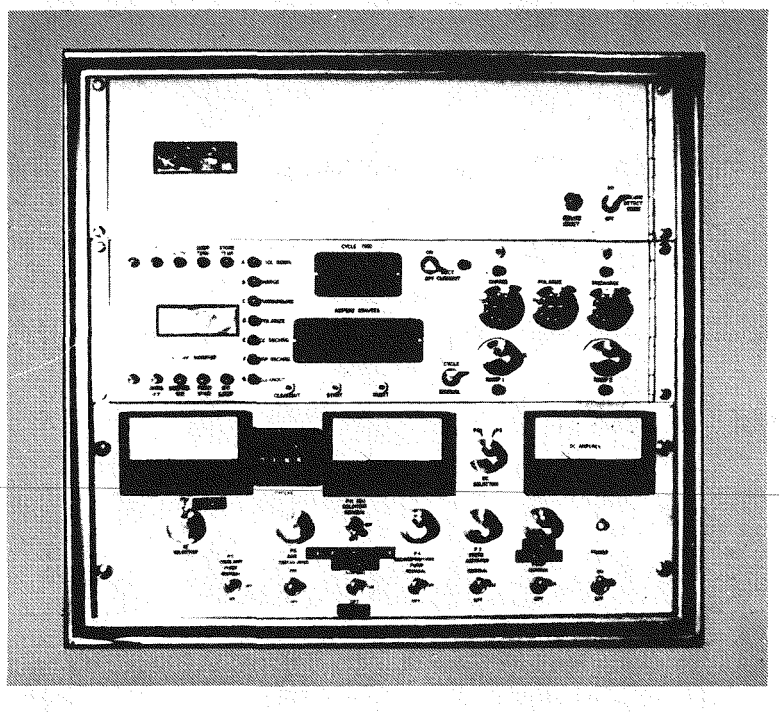

Figure 26-2. Front panel of automatic cycle controller for 1.4kWh battery system.

- CONSTANT CURRENT CHARGE - A timed phase, the CONSTANT CURRENT CHARGE mode, entered when the store reaches operating temperature, controls power rectifier current flow at a preset level.

- TURNAROUND - A short timed mode, TURNAROUND set, the period between CHARGE and DISCHARGE modes to allow chlorination of the electrolyte.

- POLARIZE - The main electrolyte pump turned off, rectifier on to 1/2 normal current. The battery drops to a low limit voltage due to lack of Cl_2. At the limit, the main electrolyte pump is turned on to a predetermined speed.

- CONSTANT CURRENT DISCHARGE - This mode is a timed phase during which current is held at a preset level.

- VARIABLE DISCHARGE - This phase removes all useful charge from the battery. Constant current flow is maintained until the battery can no longer support the normal output voltage level. As voltage drops, the current is incremented toward zero current flow and the test cycle automatically proceeds to the CLEANOUT phase.

- CLEANOUT - Any zinc remaining on the electrodes is stripped from the battery stack by circulating electrolyte and a "short" (load resistors) connected across the battery terminals during this timed phase. Then, control returns to COOLDOWN and the test cycle is repeated.

Figure 26-3. Photograph of data monitoring and acquisition equipment. Note the use of a standard teletypewriter for data printout.

Failure Monitors

The Battery Automation System enables the battery to be operated continuously on a 24-hour basis without human intervention. The control logic and associated interfaces accomplish this. However, the need exists for a safety or failure monitor capable of determining if a component failure has occurred or if the battery is operative in an abnormal manner requiring termination of the test cycle. The known failure modes were identified from previous battery experience. Additional possible failure modes were also identified. These determined the battery parameters that needed to be monitored. The failure monitor design insures that if a critical

parameter exceeds a preset limit, a signal is sent to the control logic circuit. When the control receives the failure signal, it causes the battery test to abort into a standby mode.

Data Acquisition

The continuous unattended cycling of the battery requires a means of recording test data for evaluation. In 1974-1975 a data logging system was designed and built in-house for the purpose of continuous data logging of battery cell tests. It was decided that this system would be used for data logging.

The data logger is being used to record data on the 1.4kWh battery. Battery test parameters are read out and recorded on the teletypewriters (see Figure 26-4). At 5-minute intervals the time of day, battery terminal voltage, battery current, ampere minutes of charge, store temperature and pH in volts (10 volts - 14pH) are recorded.

```
+ 01410;0;+ 03874;0;+ 00362;0;+ 02286;1;+ 00473;1;+ 00923;1;
+ 01415;0;+ 04054;0;+ 00362;0;+ 02286;1;+ 00540;1;+ 00929;1;
+ 01420;0;+ 04235;0;+ 00362;0;+ 02287;1;+ 00591;1;+ 00955;1;
+ 01425;0;+ 04415;0;+ 00362;0;+ 02286;1;+ 00490;1;+ 00966;1;
+ 01430;0;+ 04595;0;+ 00362;0;+ 02287;1;+ 00560;1;+ 00966;1;
+ 01435;0;+ 04763;0;+ 00362;0;+ 02287;1;+ 00579;1;+ 00980;1;
+ 01440;0;+ 04943;0;+ 00362;0;+ 02287;1;+ 00519;1;+ 00998;1;
+ 01445;0;+ 05123;0;+ 00362;0;+ 02287;1;+ 00561;1;+ 01048;1;
+ 01450;0;+ 05303;0;+ 00362;0;+ 02287;1;+ 00470;1;+ 01041;1;
+ 01455;0;+ 05483;0;+ 00362;0;+ 02287;1;+ 00550;1;+ 00992;1;
+ 01500;0;+ 05664;0;+ 00362;0;+ 02288;1;+ 00603;1;+ 00985;1;
+ 01505;0;+ 05831;0;+ 00362;0;+ 02288;1;+ 00492;1;+ 00986;1;
+ 01510;0;+ 06011;0;+ 00362;0;+ 02288;1;+ 00565;1;+ 00998;1;
+ 01515;0;+ 06191;0;+ 00362;0;+ 02287;1;+ 00473;1;+ 00993;1;
+ 01520;0;+ 06371;0;+ 00362;0;+ 02289;1;+ 00543;1;+ 00965;1;
+ 01525;0;+ 06552;0;+ 00362;0;+ 02290;1;+ 00595;1;+ 00982;1;
+ 01530;0;+ 06732;0;+ 00362;0;+ 02290;1;+ 00501;1;+ 00974;1;
+ 01535;0;+ 06912;0;+ 00362;0;+ 02290;1;+ 00581;1;+ 00971;1;
+ 01540;0;+ 07092;0;+ 00362;0;+ 02290;1;+ 00498;1;+ 00971;1;
+ 01545;0;+ 07272;0;+ 00362;0;+ 02290;1;+ 00566;1;+ 00954;1;
+ 01550;0;+ 07440;0;+ 00362;0;+ 02290;1;+ 00458;1;+ 00971;1;
```

Figure 26-4. Sample of printout recorded regularly during all test cycling of 1.4kWh battery system.

TEST RESULTS

A cycle is currently defined as a charge duration of 4 hours or greater and an energy efficiency greater than or equal to 60%.

There are two types of failure, cycle failure and battery failure. A cycle failure is a control failure, consisting of controller problems or auxiliary hardware failure, including routine maintenance and breakdowns. The other type is battery failure. This includes inability of system to charge at 180 amps for 5 hours (charge capacity), or if the system was unable to discharge in the normal manner, i.e. rate of discharge, length of discharge, and discharge profile in agreement with other cycles. Or, if there was a large efficiency loss (that could not be accounted for by cycle failure) over an extended period of time.

The test conditions for this cell are:

- Charge current = 180 amps
- Charge current density = $37mA/cm^2$
- Constant current discharge current = 160 amps
- Constant current discharge current density = $33mA/cm^2$
- Temperature = 40°C

Cycles 136-200

As this year began the interfacing of the hard-wired logic controller had been completed (approximately August 30, 1976, cycle #53), substantially debugged (November 1, 1978, cycle #85), and continous (24-hour) cycling was underway (since November 8, 1976, cycle #90). Thus the automated cycle was well established. The average energy efficiency of these cycles was 66.9%. The average energy efficiency of the previous 135 cycles was 68.3%. As can be seen, the energy efficiency for cycles 136-200 was somewhat lower due to the use of different measuring shunts and instruments on the controller and also the elimination of human error. The apparent slight performance (energy efficiency) deterioration is not real (Figure 26-5).

There were 24 failures during this 65 cycles (Table 26-1). Of these, six were maintenance related (normal mechanical problems); four were due to iron contamination in the electrolyte; nine were controller related (the problem was found and corrected); five were due to discharge U.V., the actual cause was not known. Sixty-seven cycling days were lost (Figure 26-6). This 65 cycles took almost 4 months to complete.

There were three electrolyte changes: one after five cycles (136-140) to try a new electrolyte composition, one after 44 cycles (141-184), and another after two cycles (185-186). These changes were due to iron contamination in electrolyte.

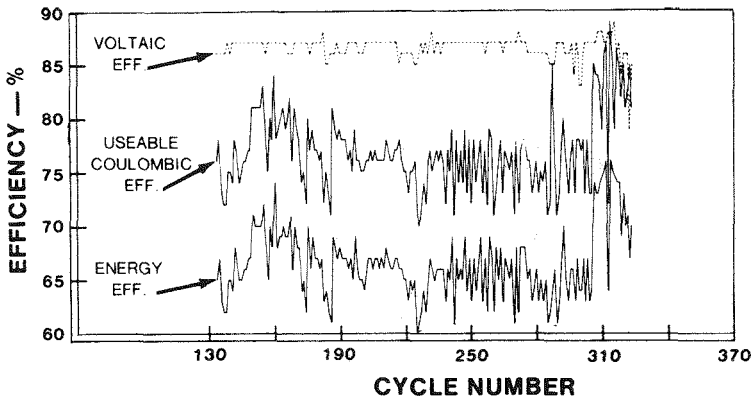

Figure 26-5. Efficiencies of 1.4kWh battery system plotted against cycle number.

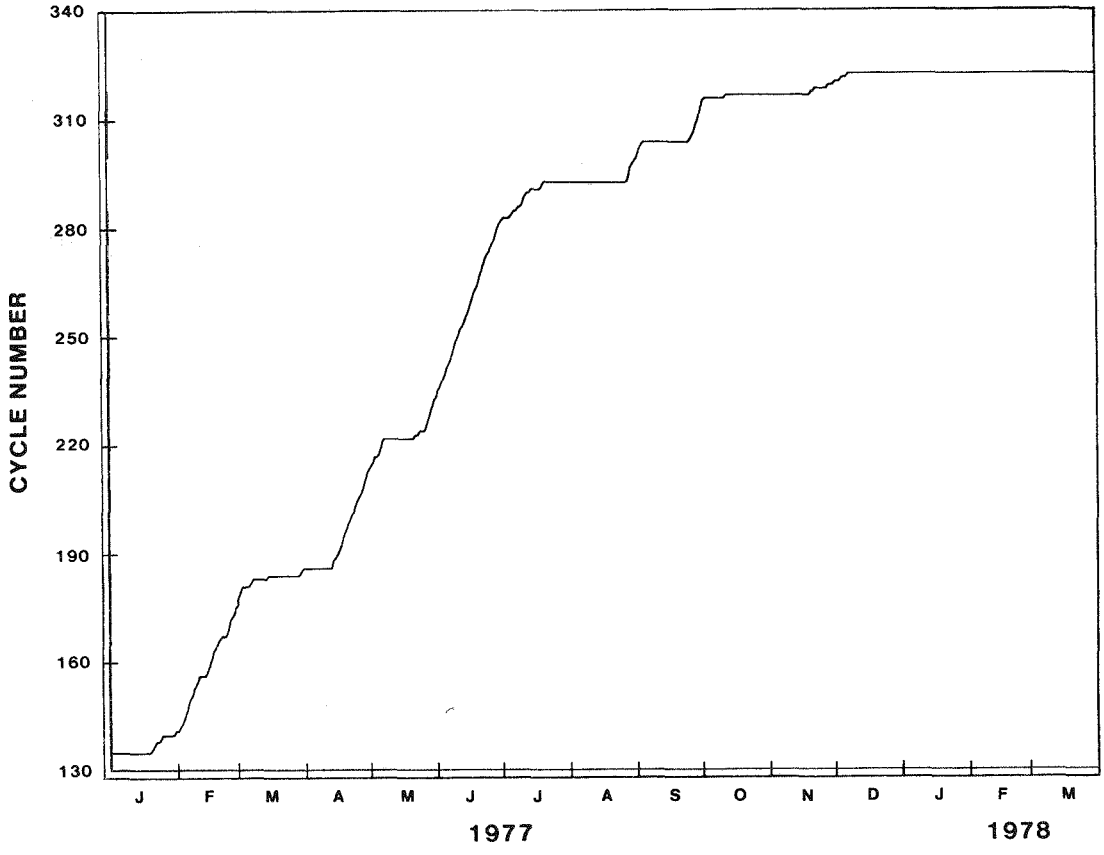

Figure 26-6. Showing the number of test cycles accumulated with the passage of time during Phase I testing of the 1.4kWh battery system.

Table 26-1

FAILURE TABLE
FOR 1.4kWh BATTERY

Component	Failure Reference Number	Type of Failure	Cycle Number Preceding Failure: Cycle Interval 136-200	201-300	301-323	Total Failures of Each Type
PUMPS:						
Gas recirculation	1	Seal leakage		224,293	304	3
	2	Worn gears		224		1
	3	Worn shaft		224	304	2
	4	Liquid seal leakage		253	304	2
	5	Worn bearings		240	304	2
Main electrolyte	6	Seal leakage	181	217,293	304,318 320	6
	7	Worn shaft		222		1
STORE:						
Agitator	8	Impeller decoupled from motor	153	291,292 293(5)*		8
	9	Loss of motor efficiency	167	293		2
	10	Worn shaft		293	317	2
	11	Worn bearings	177	293(2)		3
Coolant loop	12	Cooling inefficiently	189,198	214,274 284		5
Decomposition loop	13	Loss of motor efficiency			304	1
	14	Motor control not working		293		1
Miscellaneous	15	Inlet tube to store blocked		222		1
	16	Fluid exchanged between store and battery		222(2) 293	316	4
	17	System failure (replaced store)		293	317	2
DATA ACQUISITION SYSTEM:						
Logic controller	18	Skipped cleanout phase		287,291 293(2)	303,304(2) 305	8
	19	Elapsed time from detecting failure to system shutdown too short	138,141 143,156 166,177 181			7
	20	Miscellaneous	183,184	285,290	316	5
	21	Controller did not adjust pH		293		1
Teletype	22	Inoperative		222,293		2
MISCELLANEOUS:	23	No auxiliary Cl_2		283		1
	24	Power outage in building		293		1
	25	Inoperative solenoids			304,318	2
	26	Sump temperature elevated		206		1
	27	Contamination of electrolyte	184,186		304	3
	28	Valve on auxiliary Cl_2 tank set improperly (low flow rate)		236		1
	29	System did not cleanout totally	186(2)			2
INDETERMINATE REASONS:						
Charge	30	Low voltage			308	1
Discharge	31	Low voltage	181,183(3) 186	293(3)	308,316	10
	32	Low energy efficiency		298		1
		TOTAL FAILURES IN EACH INTERVAL	24	46	22	92

*Number in parenthesis indicates number of times this failure occurred.

Cycles 201-300

The average energy efficiency of these cycles was 65.3%. By visual inspection of Figure 26-5, we see that the energy efficiencies have become more scattered. This is due to changes in usable coulombic efficiencies as the voltaic has remained fairly consistent through all previous cycling (86-87%).

There were 46 failures during this 100 cycles (Table 26-1). Of these, 22 were maintenance-related. Eight were due to store failure; the store, motor, and agitator assembly were replaced. Four were due to fluid exchange (at least one and possibly all caused by frozen store inlet tube), the system was replumbed hopefully to assure that this would not reoccur. Four were due to the controller skipping cleanout (it reoccurred after cycle 300 and is discussed in section on cycles 300-323); two were due to miscellaneous controller problems (they never reoccurred); six were due to indeterminate reasons; two did not reoccur (sump temperature and low Cl_2 rate); and four discharge undervoltage failures reoccurred after cycle 300 (see section on cycles 301-323). Sixty-six cycling days were lost. This 100 cycles took over four months to complete.

There were seven electrolyte changes: after 36 cycles (187-222) due to iron contamination of electrolyte, after no cycles due to liquid exchange between store and battery, after 63 cycles (223-285) due to iron contamination of electrolyte, after eight cycles (286-293) due to fluid exchange, after no cycles due to loss of electrolyte from seal failure on the main electrolyte pump, after no cycles due to electrolyte contamination.

Cycles 301-323

The average energy efficiency of these cycles was 70.7%. The standard deviation was 4.3 (this is due to the 4 cycles preceding 305). By examination of Figure 26-5, it is apparent that the overall efficiency has increased significantly and that most of this gain has been in coulombic efficiency. From cycle 305 on there was a significant change in performance. There is no apparent reason for this increase, the electrolyte was changed but it was of the same composition as had been in previous use. The system filter was also cleaned. The improved performance has been maintained since then even after prolonged stand times and changes of electrolyte.

There were 22 failures (Table 26-1) during these 23 cycles. Eleven failures were maintenance related (normal mechanical problems), one store failure (new type store put on), one occurrence of fluid exchange between store and battery, six were due to the controller skipping cleanout (this was repaired by the electrical department), one due to contamination of electrolyte, two more were due to occurrences of discharge undervoltage (there is still no explanation for this). Seventy-nine cycle days were lost (Figure 26-6). These 23 cycles took approximately three months to complete.

There were six electrolyte changes. One after eleven cycles (294-304) due to electrolyte contamination, one after no cycles due to seal failure on the main electrolyte pump, one after 12 cycles (305-316) due to fluid exchange between store and battery, one after one cycle (317) due to low electrolyte level, one after one cycle (318) due to seal failure on main electrolyte pump, one after two cycles (319-320) due to seal failure on main electrolyte pump.

CONCLUSIONS AND RECOMMENDATIONS

The 1.4kWh battery with the hard-wired logic controller represents the earliest attempt (1976) to fully automate a zinc-chlorine battery system. Over 300 complete cycles have been accumulated with no loss of capacity and with very consistent voltaic, coulombic and energy efficiencies maintained throughout this period of two years. While the electrochemical performance of the battery has been outstanding, long-term continuous cycling has not been demonstrated. Unattended operation was normal and routine but interrupted cycles due to mechanical and control malfunctions were frequent. Many cycles and many days were lost with repair and upkeep on the unrefined machinery and the unsophisticated control equipment.

Currently this system is running under manual control at designed full charge capacity of 180 amps for 5 hours and discharging normally. It continues to demonstrate average round-trip energy efficiencies in excess of 67%. In fact, the last 23 cycles were at an average 71% energy efficiency with no conclusive explanation for the sudden increase. Because of continuous troubles with faulty components, the logic controller was abandoned in December, 1977. Normal cycling terminated at that time, with cycle number 323.

It is recommended that this system be maintained in a standby condition as a demonstration of the ruthenized-titanium chlorine electrode technology. It can be used for limited testing by manual operation with cylinder chlorine at any time. The system could be returned to the continuous automatic cycling mode only be extensive redesign of the store and pumping elements and by interfacing with a microprocessor-based control system. Such a refurbishing would take several months to implement.

REFERENCES

26-1 Development of High-Efficiency, Cost-Effective, Zinc-Chlorine Batteries for Utility Peak-Shaving -- 1976. Palo Alto, Calif.: Electric Power Research Institute, 1978, EM-711, Part III, Section 2.

Section 27

SINGLE CELL LIFE TESTING

INTRODUCTION

The principle objective of single cell life testing is the determination of the useful life of zinc-chlorine cells operated under continuous charge-discharge cycle conditions. Inherently, it is the life expectancy and permanence of activation of the porous graphite chlorine electrode that are open to question.

Single cell testing for peak-shaving applications has been an on-going program at EDA since 1975. A number of different cells, each reflecting the design state-of-the-art and the operational conditions of its time, have been placed on continuous cycle programs during that period. A detailed description of the test methods and evaluation criteria, is presented in the EPRI EM-711 Interim Report (27-1).

As Phase I began, only two cells (PCS-HB and PCS-MH2) remained on test. No new tests of single cells were begun during this period as emphasis has shifted toward the use of larger multi-cell systems for evaluating electrode life. These have the advantage of testing a large number of electrodes in the same period of time.

RESULTS AND DISCUSSION

The test time accumulated by each of the two cells, expressed as electrochemical operational times in ampere-hours/cm^2, is presented in Table 27-1. Using a figure of 0.2 ampere-hours/cm^2 as a full-charge cycle, cell PCS-MH2 has accumulated, to date, the equivalent of 508 cycles. This cell continues on test. The testing of cell PCS-HB was terminated because of a mechanical failure after having amassed the equivalent of nearly 600 cycles. This failure, as with all previous cells of this design, was occasioned by a loss of contact with the chlorine electrode caused by loose bolts. During an attempt to correct this loss the chlorine electrode was

mechanically damaged. This prevented further testing even though there was no evidence to suggest that the electrode was not functioning routinely when destroyed.

Table 27-1

ELECTROCHEMICAL OPERATIONAL TIME
ACCUMULATED THROUGH PHASE I

Cell Designation	Ampere hours/cm^2*		Present Status
	Charge	Discharge	
PCS-MH-2	101.6	71.1	on test
PCS-HB	119.3	82.1	retired

*Note that low coulombic efficiency calculated using these values is due to zinc-on-zinc cycling mode, and as such does not reflect that achievable under the complete discharge type of cycle planned for peak-shaving.

CONCLUSIONS AND RECOMMENDATIONS

The one remaining single cell continues to cycle under control of relatively unsophisticated equipment. As a result it is being cycled in the zinc-on-zinc mode with considerable manual attention being required. On the other hand, the 1.7kWh battery system described in Section 25 of this report is now cycling 96 chlorine electrodes in a complete load-leveling test regime under fully-automatic control. This later system has, to date, nearly surpassed the accumulated cycles of the single-cell test systems. The larger battery, designed more like a peak-shaving stack, together with its developed auxiliaries and the microprocessor-based controller, provides a superior and more cost-effective method of testing porous-graphite chlorine electrodes. It is recommended that the single-cell testing program be terminated until such time as a meaningful accelerated life test can be developed. In the meantime, the aging of porous-graphite electrodes will continue to be monitored in the 1.7kWh battery system.

REFERENCES

27-1 Development of High-Efficiency, Cost-Effective, Zinc-Chlorine Batteries for Utility Peak-Shaving -- 1976. Palo Alto, Calif.: Electric Power Research Institute, 1978, EM-711, Part II, Section 4.

Section 28

ACCELERATED TESTING OF POROUS-GRAPHITE CHLORINE ELECTRODES

INTRODUCTION

The use of porous-graphite chlorine electrodes has resulted in controversy concerning battery life. Although the low corrosion rate associated with low pH operation is apparently commensurate with the lifespan requirements, the need exists for an accelerated test to demonstrate that these estimates are realistic.

In the past, the documented corrosion levels associated with chlor-alkali diaphragm cells has been a cause of concern when evaluating the potential of the zinc-chlorine battery. Although this concern remains, it has been substantially mitigated by data generated at EDA. The corrosion level demonstrated by the 1.7kWh battery system is thought to be the norm in zinc-chlorine battery operation.

A recent concern is the voltaic stability of the "activated" porous-graphite electrode. Further discussion of this topic follows.

Nature of the Active Chlorine Electrode

Section 34 of Part V presents the concept of an extended, more highly active surface layer of some finite thickness atop a base matrix. This structure is formed as a result of electrode activation. Removal of this more active layer produces a voltaic penalty, although less than possibly expected. The improvement in performance over virgin PG-60 is not solely due to this surface layer, but also to what appears to be a fundamental modification to the inner electrode matrix. Electrode processing has modified and improved wetting of the porous graphite, and this quite likely plays a major role in the performance of the matrix graphite.

Although the study is incomplete, the collected data indicates that cell performance will not be as sensitive to the state of the active layer as previously thought. The option of reactivation electrolytically is always available if necessary. Indeed, the very corrosion which this test program is to evaluate may be "reforming" (or regenerating) this active layer at a rate comparable with its destructive effect to the very same entity.

A Comparison of Chlor-Alkali Diaphragm Cell Corrosion with the Zinc-Chlorine Battery

The consumption of graphite during brine electrolysis in diaphragm cells has been well characterized under conditions employed in chlorine production (28-1). Corrosion leads to two types of corrosion products: oxides of carbon (predominantly CO_2) and particulate graphitic debris.

Zinc-chlorine battery conditions are quite different, however, than those employed in chlor-alkali cells. In Table 28-1 the most pertinent differences are presented.

Table 28-1

COMPARISON OF OPERATIONAL CONDITIONS FOR GRAPHITE ELECTRODES IN CHLOR-ALKALI DIAPHRAGM CELLS AND THOSE LIKELY IN ZINC-CHLORINE BATTERY STACKS

System Parameter	Chlor-Alkali Anode Compartment	Zinc-Chlorine Battery Stack
pH	3 - 4	-0.5 - +0.5
Temperature, °C	90 - 100	20 - 50
Current Density, mA/cm^2	100 - 140	25 - 50
Cl^- Concentration, mole/ℓ	4 - 6	5 - 11

Of these parameters, it is likely that pH is the most important. Current inefficiency in a diaphragm cell (directly proportional to the rate of graphite consumption) is a linear function of the hydroxyl ion concentration -- the discharge of this ion at the anode being principally responsible for current inefficiency in the pH range: 3 to 4. If the mechanism at a pH of 0 were identical and the linear

relationships still held, the rate of graphite consumption would be a factor of 1000 less at this pH (relative to a pH of 3).

The lower temperature of operation for the zinc-chlorine battery also serves to lessen the rate of attack on the graphite substrate. In recent experimentation by EDA, an approximate doubling of CO_2 evolution rate in batteries was observed for a 10°C rise in the range 25-50°C. Thus a reduction in the rate of graphite consumption of between 2^4 and 2^8 may be anticipated for the battery (relative to a diaphragm cell) based on these temperature effects.

The effect of a relatively lower current density in the zinc-chlorine battery on the rate of graphite consumption cannot be estimated even by approximation as was done for the pH and the temperature. Decreased overvoltages, due to a factor of four to six lowering of the current density, are also a factor in the significantly lower consumption rate.

Another factor which must be considered is the anolyte chloride-ion concentration. In a zinc-chlorine battery without supporting electrolyte this is likely to range between 6M chloride ion (fully discharged) and 1M chloride ion (fully charged). As the rate of graphite consumption in a diaphragm cell has been shown to be directly proportional to $1/[Cl^-]^4$, this concentration swing could result in a thousandfold acceleration of the consumption rate through battery charging, if a similar mechanism were in operation. The addition of supporting electrolytes would significantly reduce this effect.

Manifestation of Electrode Corrosion in the Battery System

Corrosion in the zinc-chlorine battery system manifests itself in two ways:

- Carbon oxides - mainly CO_2 - are present in the gas phase.
- Carbonaceous debris may be present (noticed upon visual inspection).

Although all graphite components, and possibly even Kynar to some extent, contribute to their formation and presence, the porous-graphite chlorine-electrode is the primary source.

Monitoring of the gas phase by gas chromatography is a relatively straightforward matter. An evaluation of debris is another, more complicated matter. Its presence cannot be refuted. Note that the amount present in a well worked continuously

operated battery, i.e. the 1.7kWh unit, is insignificant. This observation is based upon visual inspection of filters utilized in this and other battery systems. Although not a quantitative measure, it is based upon repeated observation with consistent results and therefore takes on a meaningful level of significance.

Newly assembled batteries may exhibit significant levels of graphitic debris due to the manufacturing and assembly process. Filtration or a simple electrolyte change serves to handle this situation quite satisfactorily.

When operating continuously, a battery system essentially handles carbonaceous debris "automatically". By this it is meant that the small amount of particulate material being generated is continuously being corroded to CO_2 chemically. This purely chemical corrosion, it would appear, will enable the battery to be "self-cleaning" in this regard so long as operation under proper conditions is maintained. It remains for this study, once underway, to further document this premise.

Estimation of "Acceptable" Corrosion Level

The maximum tolerable steady-state rate of carbon dioxide evolution for a system with chlorine electrodes, 80 mils in thickness, may be calculated approximately as follows:

Total CO_2 evolution possible

$$\frac{(0.08\text{in})\cdot(2.54\text{cm/in})\cdot(1\text{cm}^2)\cdot(1\text{g/cm}^3 \text{ of PG-60})\cdot(24\ell\ CO_2\text{/mole})}{12 \text{ g of graphite/mole}} \simeq$$

$$400\text{ml } CO_2/\text{cm}^2 \text{ of electrode}$$

Presuming that 10% of the electrode can be consumed and converted to CO_2 without causing performance deterioration in 2000 cycles, then each square centimeter of electrode surface could generate

$$(0.1)\cdot(400\text{ml } CO_2)/2000 \text{ cycles} = 0.02\text{ml } CO_2/\text{cycle}$$

The amount of chlorine evolved per cm^2 during charge of $200mAh/cm^2$ is

$$(0.2\text{Ah})\cdot(1.32\text{g } Cl_2/\text{Ah})\cdot(24\ell/\text{mole})/(71\text{g } Cl_2/\text{mole}) = 89\text{ml } Cl_2/\text{cycle}$$

Thus, the maximum tolerable steady-state concentration of Cl_2 in the evolved gas is

(0.02ml)/(89ml)

or approximately 0.02%.

This calculation admittedly assumed no CO_2 is evolved on discharge and ignores debris formation. On the other hand it is conservative in that it is predicated upon an electrode consumption level of 10%, and data is available which demonstrates that as much as 50% (40 mils) could be lost and still allow adequate performance.

Typical System Carbon Dioxide Levels

The available data for various systems are admittedly quite variable. This is undoubtedly due to the incomplete control of various factors, and possibly to the age of a given unit.

For example, the following charge levels have been documented:

System	Electrolyte $[Cl^-]$	Temperature °C	pH	mA/cm^2	Vol. % CO_2
1.7kWh	8M	40	0.2	∿35	.01 - 0.04
8.3kWh	8M	35	0.2	∿30	.04 - .06
20kWh	8M	50	0.6	∿42	0.1 - 0.2

As the 1.7kWh system is the oldest, and as a result has well-aged electrodes, its CO_2 rates can be considered more meaningful than that of the latter two units.

Recently data from the 8.3kWh unit has shown that the discharge CO_2 rate is 1/4 to 1/5 that found on charge. Using this ratio and the tabulated CO_2 charge levels, this translates into approximately $0.0012g/cm^2$ of carbon lost in 1,000 hours of operation for the 1.7kWh battery unit.

Activated PG-60 electrodes 0.080in thick have an initial weight of approximately $0.22g/cm^2$. Assuming 100% chlorine "efficiency", we can approximate as follows:

Weight loss:	10%	25%
Grams lost/cm^2:	0.022	0.055
Hours @ 0.002g/1000 hrs:	18,333	45,833
No. cycles (12 hr/cycle):	1,528	3,819

These observations, although encouraging, are speculative. It is necessary for this and other on-going studies to provide more definitive data upon which final conclusions may be based.

RAMIFICATIONS OF CHLORINE ELECTRODE DEGRADATION

Corrosive degradation of the porous-graphite chlorine electrode can result in cell failure in numerous ways. Those considered of major significance are detailed in Table 28-2.

Table 28-2

POSSIBLE CHLORINE ELECTRODE FAILURE MODES

Failure	Cause	Manifested as:
1. "Bowing" of electrode	Corrosive weakening	Lowered capacity due to decreased gap. (Shorting possible).
2. Crack (or rupture)	Corrosive weakening	Decreased voltaic performance (no longer "flow-through). Shorting may occur. Zinc corrosion.
3. Loss of "active" surface	Corrosion, or corrosive undercutting	Decreased voltaic performance.
4. Electrode-to-bus contact deterioration	Corrosion	Decreased voltaic performance.
5. Non-uniform electrolyte flow	Uneven corrosion	Deterioration in discharge voltage profile.
6. Non-uniform electrolyte flow	Plugging of electrode back-side with debris.	Deterioration in discharge voltage profile.

For discussion purposes two "types" of failure are categorized as follows:

- Loss of physical integrity (1 and 2) of the electrode plate due to corrosion resulting in what can be total failure of a cell.
- Decreases in voltaic performance (3 through 6) which will be gradual and of varying degree.

THE ACCELERATED TEST PROGRAM

A chlorine-chlorine test cell instead of a zinc-chlorine cell will be employed in the study for the following reasons:

- A doubling of electrode data.
- Gas phase will be more stable, since H_2/Cl_2 recombination will not be a factor.
- Ease of cell operation since zinc-plate dendrite problems are avoided.
- Electrolyte pH may be employed as a measure of electrode corrosion.

By using this type of a cell, however, it will obviously not be possible to monitor directly capacity losses or discharge-voltage profile decay. The advantages would, however, appear to warrant this approach initially.

Parameters to be Monitored

Graphite Corrosion Products. Graphite corrosion products will be monitored routinely. Gas phase makeup will be followed with a "dedicated" gas chromatograph. Debris generated will be collected and weighed. A correlation between electrode weight change (which will be determined) and the CO_2 and debris generated may exist. Inter-electrode gap will be large enough to allow inspection of the electrode face for flatness during operation. Structural integrity, although not directly measured via cell capacity, will therefore still be monitorable.

Voltaic Performance. The operating cell voltage will be employed as a figure of merit in this case. Additionally, provision has been made for the employment of reference electrode probes which will be utilized to monitor each electrode individually.

Proposed Cell and System for Accelerated Testing

The test system presently being assembled is shown in Figure 28-1. Provision has been made for both the collection of debris in a determinable (weighable) manner and for gas sampling.

A more detailed drawing of the upper cell compartment proper is shown in Figure 28-2. The use of glass allows for ease of inspection while operating. The large 0.6in inter-electrode gap facilitates insertion of reference probes and the inspection mentioned.

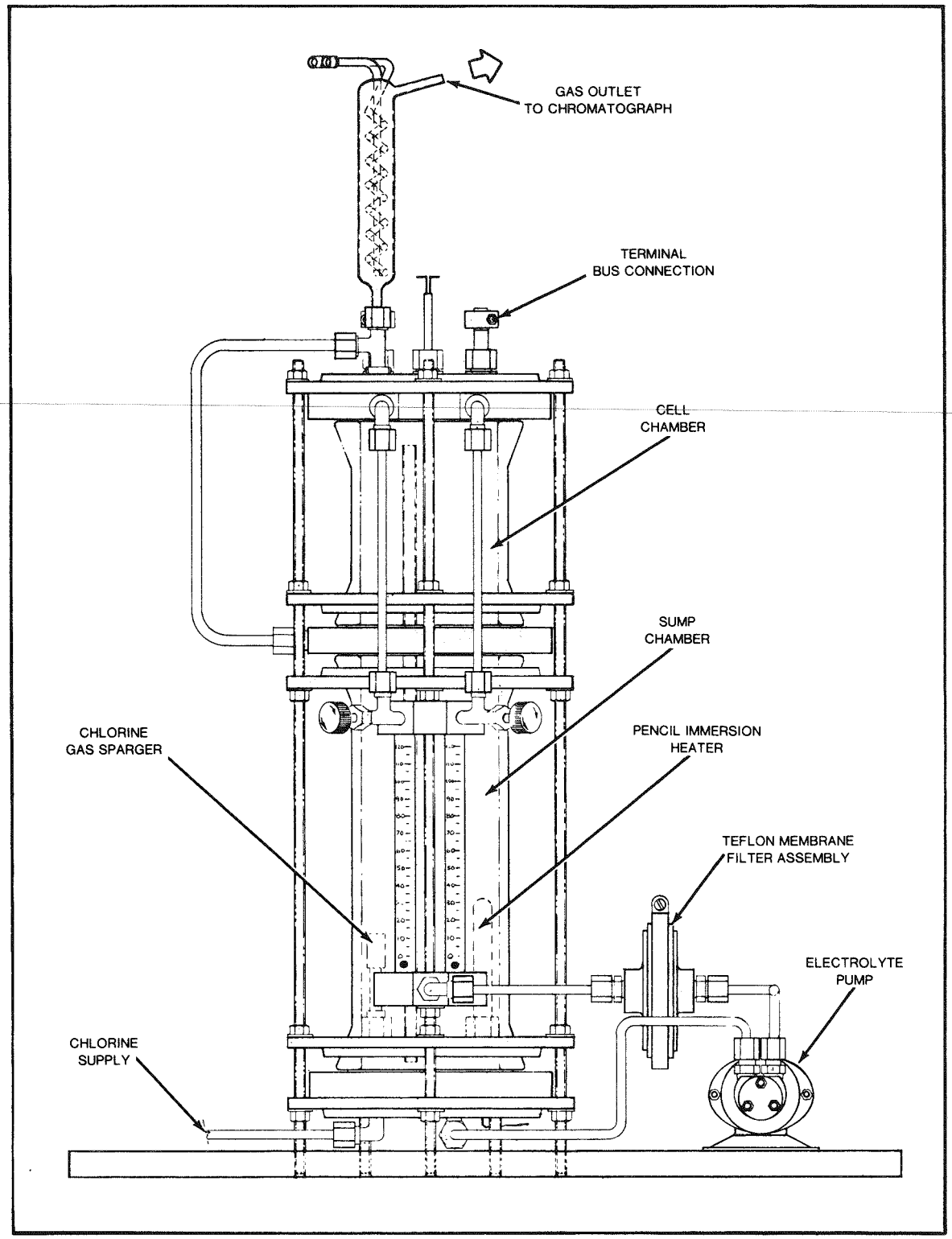

Figure 28-1. System proposed for accelerated life test program. The upper Teflon bulkhead unit is employed in manifolding electrolyte feed to the two test electrodes.

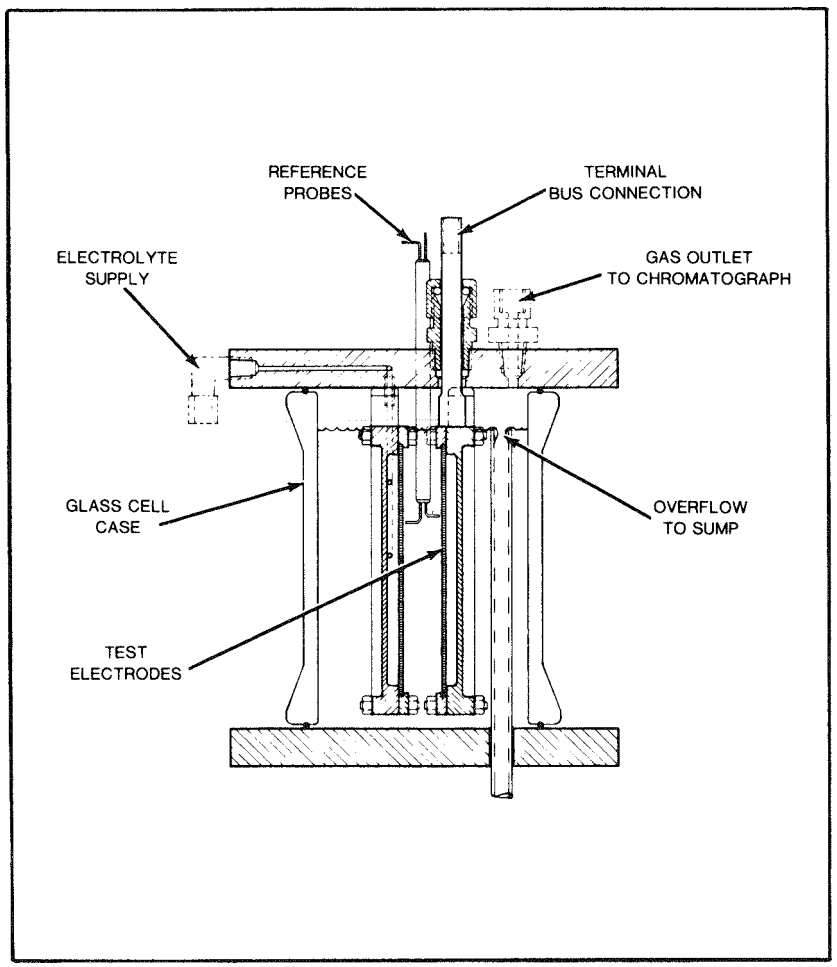

Figure 28-2. Detailed drawing of proposed accelerated life test cell. By utilizing the chlorine-chlorine cell approach, the potential of simultaneously testing two porous electrodes is made possible.

By using a "busing" or contact arrangement equivalent to current practices (see Figure 28-3) it is possible to also monitor the stability of this most important design feature. As currently envisaged current interruption techniques would be required to separate voltaic losses due to changes in this contact from those of the electrode proper.

Initially the cell concept will be tested and evaluated. After the implementation of any necessary modifications, accelerated testing proper will commence.

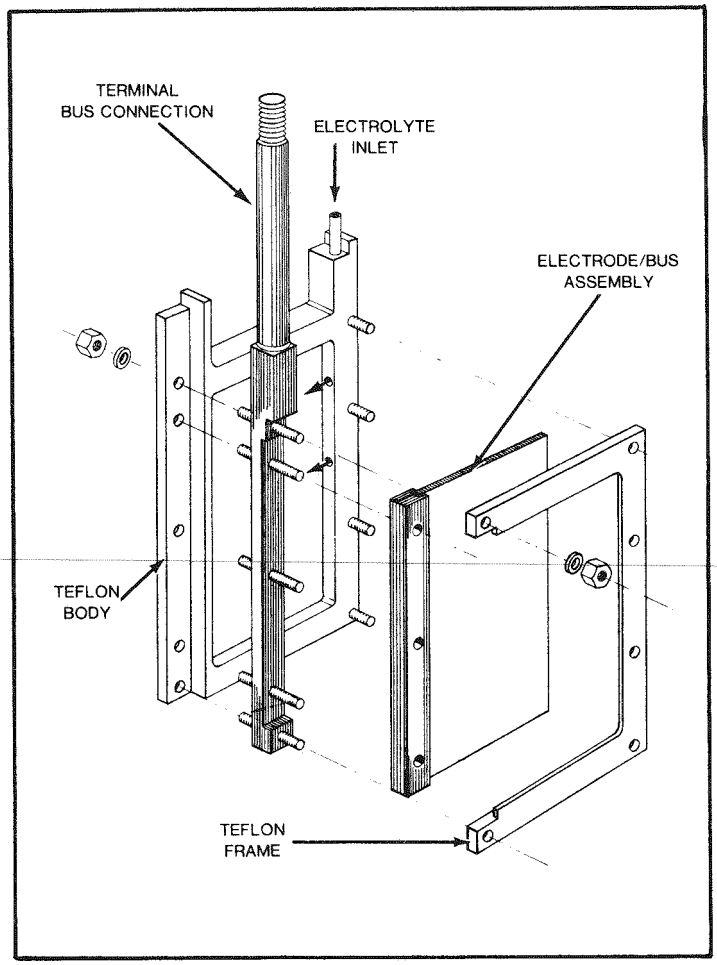

Figure 28-3. Demountable electrode assembly. Two identical units are employed. Note that electrode/bus assembly is easily weighed.

Proposed Experimental Approach

A two-level factorial approach in three variables as detailed in Table 28-3 will be employed. The third "paired" variable is admittedly a concession to the use of a chlorine-chlorine cell, and reflects the pH and chloride-concentration swing associated with battery operation.

Temperature and current density levels specified should ensure a 10-20 fold range in corrosion. When obtained as a function of electrolyte swing, the data generated should allow definitive judgements as to any limitations which may exist and, in addition, provide direction as to any required corrective measures which must be undertaken.

Table 28-3

VARIABLES IN PROPOSED 2^3 FACTORIAL
CHLORINE-ELECTRODE LIFE STUDY

Current density, mA/cm^2:	30, ∿90
Temperature, °C:	30, 80
Electrolyte:	
Chloride M	3.2, 8
pH	0.5, 0.0

CONCLUSIONS AND SUMMARY

Although actual accelerated testing has not as yet begun, a firm basis has been laid for its initiation. The more basic and fundamental understanding of the processed electrode's voltaic performance resulting from the joint EPRI-EDA Phase I program has provided needed direction to the effort, and will result in a more cost-effective program.

REFERENCES

28-1 J.S. Sconce. Chlorine: Its Manufacture, Properties and Uses. ACS Monograph, Reinholt Publishing Corp., 1962, pp. 81-126.

PART V

DEVELOPMENT PROGRAMS

Section 29

INTRODUCTION TO PART V

The overall objective of the joint EPRI-EDA project is the commercialization of a high-efficiency, cost-effective, zinc-chlorine battery for peak-shaving applications. Extensive development is required to meet this objective. Analytical and experimental work performed during Phase I is reported here as Part V of this report. Generally, the work reported here was directed toward improved electrode performance, higher electrochemical efficiencies, and development of alternative cost-effective construction materials. Following these introductory pages of Section 29, there are eight separate sections, each dealing with a particular phase of this development work.

Section 30 reports on an investigation into the volumetric changes and the acidity properties of zinc chloride electrolytes under certain conditions. This, together with the work reported in Section 37, is important in formulating an optimum electrolyte for maximum battery performance and efficiency.

Together, Section 31 and 32 report on fundamental studies that seek to optimize electrode size. The proper width for a chlorine electrode in a comb-type bipolar cell is influenced by the effects that current distributions across the face have on cell performance. The proper height for an electrode in this type cell is influenced by a complex interaction of hydraulic and chemical-corrosion parameters. The work reported in these two sections will not only help establish the maximum size of flat-plate type electrodes to be used in future cells but will assist in improving the mathematical models used to study cell-efficiency parameters.

Sections 33 and 34 report on continuing efforts to qualify improved materials of construction for the zinc-chlorine battery system. Large quantities of plastics and graphite will be needed in commercial-sized batteries. Section 33 describes the work done to identify low-cost plastic compounds to replace expensive fluorine-based polymers used in laboratory systems. A number of different plastics are needed that can be economically processed and will withstand the corrosive effects of the chlorinated electrolyte without releasing contaminants that adversely affect

system performance. Specific formulations have been identified that have passed screening and electrochemical tests. These have been tentatively released for use in future construction.

In Section 34, the work that achieved a successful method for in-situ activation of the porous-graphite chlorine electrode is described. This electrochemical process results in voltaic performance at least equaling that obtained by the thermochemical process employed in the past. Most importantly, the ability to achieve these results consistently in an assembled stack greatly simplifies production procedures and undoubtedly will show marked cost benefits. A repeatable and scalable technique has been demonstrated.

Considerable amounts of porous graphite, approximately 50 tons, are required to produce the quantity of chlorine electrodes needed in a full-size (100MWh) peak-shaving battery plant. Section 35 tells of the work being done to select and qualify alternates to the Union Carbide PG-60 material used in prototype cells to date. This is important to ensure that cost-effective materials are available for future production and that there exists a competitive source of supply. Progress on qualifying other graphite materials is reported but this program has not yet been completed.

Section 36 addresses the subject of inert gas rejection from the battery. Carbon dioxide, hydrogen, and oxygen are byproduct gases of chemical and electrochemical reactions taking place in the battery stack. Undesirable quantities of these will accumulate in the closed battery system unless a rejection device is provided. Four possible techniques for separating these gases from chlorine (which must not be rejected) and concentrating them for removal are analyzed in this report. A combination approach is recommended for the battery module and a development program leading to some commercial device is suggested.

In Section 37, experiments to verify the mechanisms that generate undesirable hydrogen in a zinc-chlorine cell are reported. The results of a metallic impurity testing program and tests to confirm suspected contamination from the chlorine electrode are obtained using a zinc-transfer plating cell. This work, when completed, will provide the understanding necessary to upgrade battery performance and to set realistic impurity standards for electrolyte production.

As would be expected, these development programs, carried out during the fifteen months of Phase I, have not all reached final conclusions. Important progress has been made. Characteristically, as original questions are answered, new ones are raised. The work completed to date in electrolyte analysis, the studies of cell-current distribution, and investigations of chlorine-electrode activation provide the fundamental background for continued refinement of the theoretical cell model. This model will be used during Phase II to investigate means of increasing battery efficiency. In like manner, continued progress toward commercial batteries will rely heavily on continuing the work in materials and process investigations.

Section 30

ELECTROLYTE CHARACTERIZATION STUDIES -- ACIDITY AND PARTIAL MOLAL VOLUMES

INTRODUCTION

Zinc-chlorine battery efficiency is largely determined by the coulombic efficiency of the zinc electrode in a cell. Both battery energy efficiency and the longevity of the chlorine electrode, in turn, are directly dependent upon the pH of the electrolyte. Increased acidity causes a small, but measurable decrease in the efficiency of zinc deposition because of the codeposition of hydrogen. Conversely, the chlorine electrode becomes more stable as acidity increases. Selection of electrolyte pH therefore must be a compromise between electrode stability and efficiency.

The present battery design indicates that about 2.5 moles per liter of zinc chloride will be removed from the electrolyte while the battery is charging. This zinc chloride concentration change will produce measurable changes in the pH of the electrolyte and will also cause the electrolyte volume to contract. The pH change will occur because the zinc ion, through hydrolytic reactions, behaves as a moderately strong acid and therefore makes appreciable contributions to the acidity of the electrolyte. Volume changes in the electrolyte during a battery cycle are associated with the removal or addition of zinc chloride from or to the electrolyte. Both the pH changes and volume change influence the design and operation of the battery.

Measured pH is a function of the zinc chloride concentration, the free acidity, and the presence of potassium or sodium chloride. This section examines in detail the pH effects of hydrochloric acid, zinc-chloride, sodium chloride, and potassium chloride. From the results, no changes in pH of the electrolyte throughout a charge-discharge cycle may be predicted.

Volume expansion and contraction during a battery cycle make it necessary to use correction terms when electrolyte analyses are made. For example, volume contraction during the charge cycle, due to zinc chloride removal, has the effect of increasing the molar concentration of the supporting electrolyte.

Experimental results for the partial molal volumes of zinc chloride, potassium chloride, and sodium chloride are included in this section. These results are compared to literature values for aqueous solutions and the magnitude of the electrolyte volume change is evaluated.

PREPARATION OF STANDARD ZINC CHLORIDE SOLUTIONS

Concentrated zinc chloride solutions are prepared at EDA from the reaction of zinc metal with an aqueous chlorine solution. The concentrate is generally about 5 molar in zinc ion. Standard zinc-chloride solutions approximating 1, 2, 3, and 4 molar were prepared by careful dilution of the zinc chloride concentrate. Distilled or deionized water was used for all the experimental work.

The zinc concentration in each of the solutions was determined potentiometrically using ferrocyanide as the titrant and is based on the ferro-ferricyanide couple. Details of the titration procedure are found in Instrumental Methods of Analysis (30-1). End points were determined by double differentiation of the titration curves.

The analyzed zinc concentrations in the prepared standard solutions are given in Table 30-1.

Table 30-1

$ZnCl_2$ SOLUTIONS AT 24 ± 2°C

Solution	Zinc Conc. (mol/ℓ)
1	1.010
2	1.996
3	3.002
4	3.990

ACIDITY OF STOICHIOMETRIC ZINC CHLORIDE SOLUTIONS

The zinc chloride produced at EDA usually contains a small amount of zinc hydroxide. Experimentally, it has been determined that the zinc hydroxide may be titrated to a stoichiometric end-point as shown in Figure 30-1. The pH at the end point, which corresponds to a stoichiometric zinc chloride solution, is dependent on the zinc chloride concentration. The pH of zinc chloride solutions as determined using this technique is shown graphically in Figure 30-2.

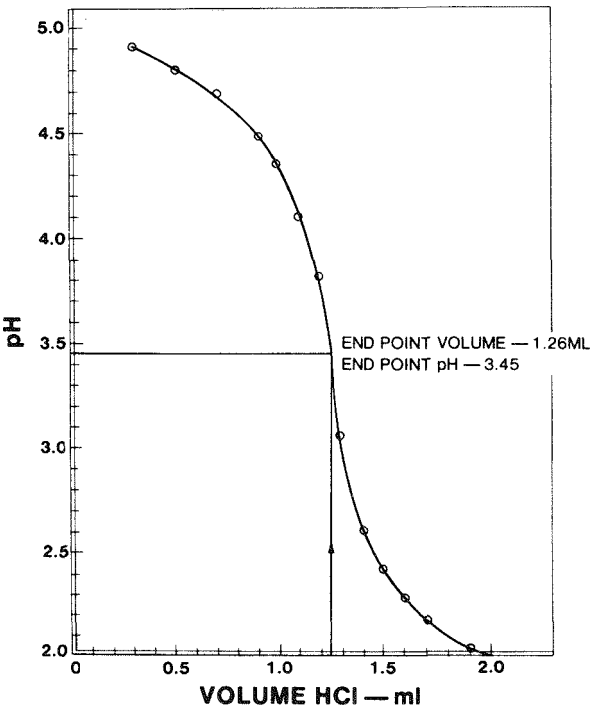

Figure 30-1. Titration curve of 1.0 molar $ZnCl_2$ solution containing a trace of $Zn(OH)_2$ with dilute HCl.

MEASURED ACIDITIES OF ELECTROLYTE-HYDROCHLORIC ACID SOLUTIONS

The measured pH of zinc chloride solutions containing hydrochloric acid is a function of both the zinc chloride concentration and the free acid concentration. Zinc chloride behaves as a weak acid due to hydrolysis and the addition of a strong acid to concentrated zinc chloride solutions is somewhat analogous to the addition of a strong acid to a weak acid, such as acetic acid. Therefore, as the zinc chloride

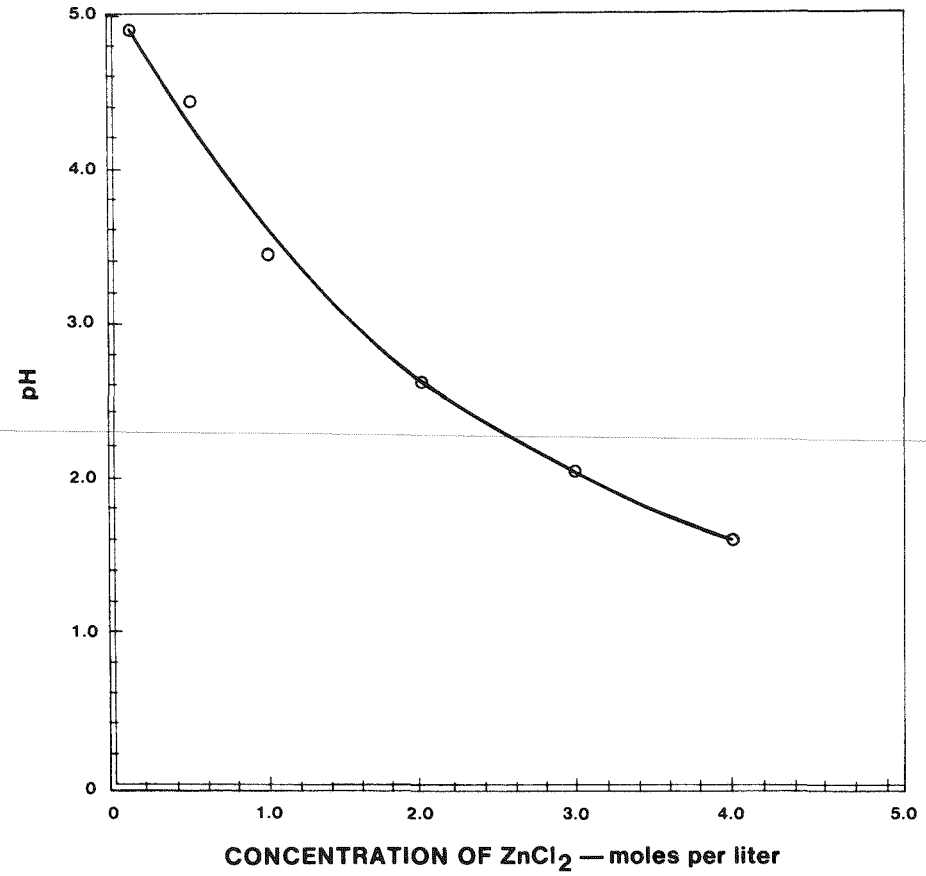

Figure 30-2. Curve showing the pH vs. the molarity of $ZnCl_2$ solutions.

concentration is increased, a lesser amount of strong acid is required to adjust the solution to a given pH.

Measured volumes of the zinc chloride stock solutions were carefully adjusted stoichiometrically in accordance with the techniques presented above. Then, hydrochloric acid was added incrementally and the pH was measured after each addition. Volume corrections, when required, were made to obtain the actual molarity of hydrochloric acid. The experimental results are shown in Figure 30-3. A pH versus molarity curve for hydrochloric acid in water is shown as a reference curve. Note that all the curves, except A, have the same slope within experimental accuracty.

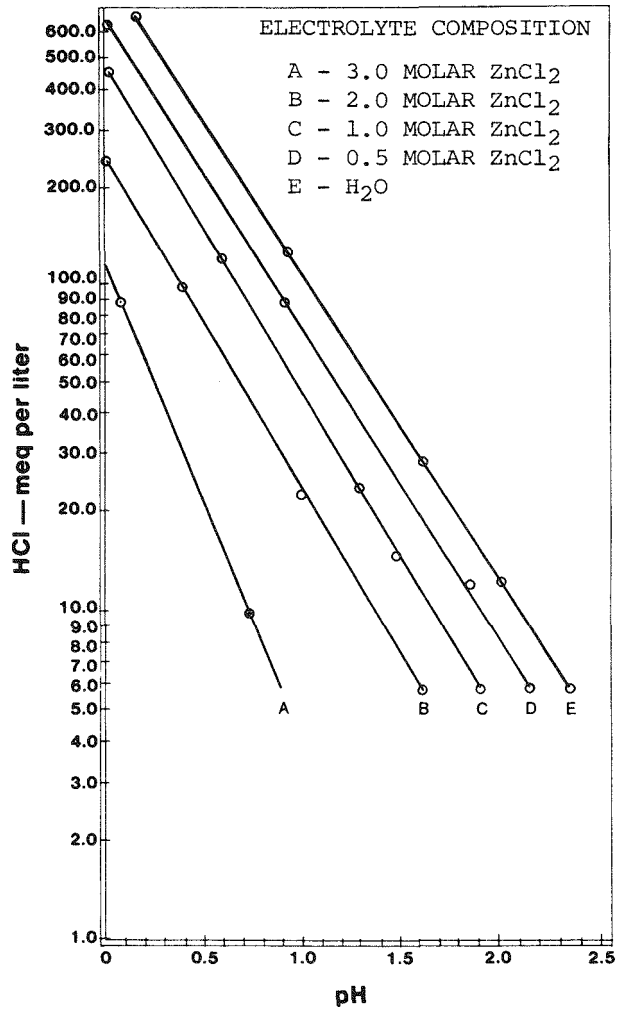

Figure 30-3. pH of $ZnCl_2$ solutions as a function of the free acid concentration.

pH Effects of NaCl and KCl in $ZnCl_2$ Solutions

To evaluate the pH effects of sodium chloride and potassium chloride the following procedure was used. A stock solution of 2-molar zinc chloride was carefully adjusted to its stoichiometric pH. Three 50ml aliquots of this solution were then placed in 150ml beakers. The first beaker served as a control and 0.15 moles of NaCl were added to the second beaker. To the third beaker, 0.15 moles of KCl were added. Thus, the molality of zinc chloride (moles $ZnCl_2$/kg H_2O) was the same in each beaker. Also, the second and third beaker each contained 3.17 molal additional salt.

The pH change of the three solutions was recorded as 6M HCl was added in small increments. The use of 6M HCl was dictated by the desire to minimize volume expansion. The pH curves for these three solutions are shown in Figure 30-4.

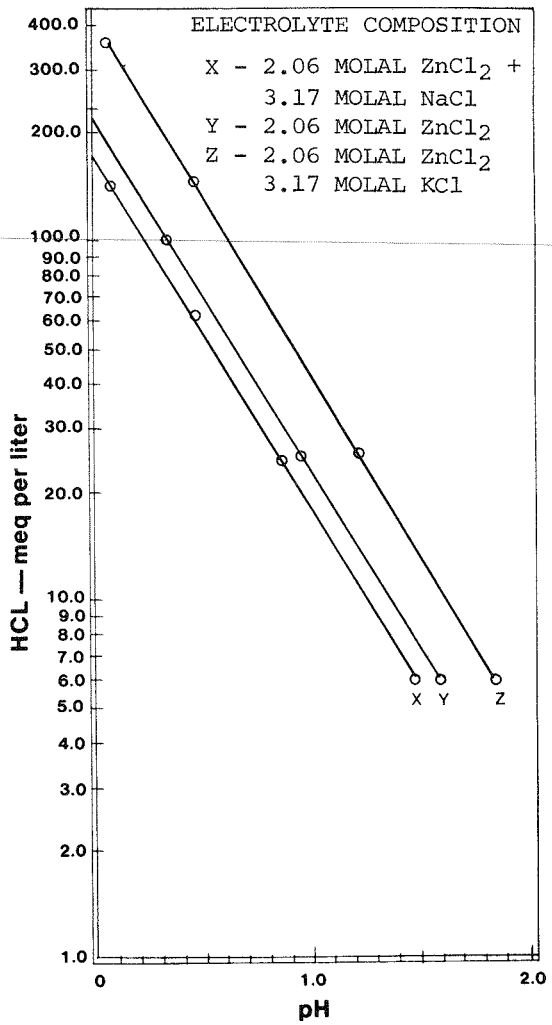

Figure 30-4. Plot of pH of $ZnCl_2$ solutions as a function of free acid concentration in the presence of a supporting electrolyte.

DISCUSSION

Solutions of zinc chloride are acidic due to the hydrolysis of the zinc ion. Biederman (30-2), Schorsch (30-3), and Perrin (30-4) have evaluated the hydrolysis of zinc

chloride for concentrations less than 0.2 molar. Their findings are listed in Table 30-2. Perrin unable to detect any polynuclear complexes of zinc. Our findings indicate that the pH of a zinc chloride solution is a reliable indicator of the stoichiometry of the solution. For example, if a solution contains free alkali, OH^-, the equilibria presented in Table 30-2 will shift to the right and exhibit buffering characteristics. Addition of a strong acid to such a solution will produce a titration curve of which the point of inflection will indicate a stoichiometric composition. The pH at which the inflection point occurs is a function of the hydrolytic constants and the zinc-chloride concentration. As shown in Figure 30-1, an analytical end point is obtained as the solution goes from a slight excess of zinc hydroxide to a slight excess of hydrochloric acid. The pH at the end point of the titration is assumed to be the pH of a stoichiometric $ZnCl_2$ solution at that concentration. The assumption appears valid and the difficulty in determining the pH at this point is due to the steepness of the titration curve around the end point. The pH transition range for the solutions used in this work is given in Table 30-3. For comparison, the data points used in Figure 30-2 are also shown.

Table 30-2

LITERATURE VALUES FOR ZINC-CHLORIDE HYDROLYSIS IN SUPPORTING ELECTROLYTES

Investigator/Year	Medium	Hydrolysis	-log K
Biedermann/1964	5M NaCl	$Zn^{+2} + H_2O \gtrless ZnOH^+ + H^+$	10.2 ± .2
		$2Zn^{+2} + H_2O \gtrless Zn_2OH^{+3} + H^+$	8.2 ± .1
Schorsch/1963	2M NaCl	$Zn^{+2} + H_2O \gtrless ZnOH^+ + H^+$	9.01 ± .02
		$2Zn^{+2} + H_2O \gtrless Zn_2OH^{+3} + H^+$	7.2 ± .02
Perrin/1962	KNO_3	$Zn^{+2} + H_2O \gtrless ZnOH^+ + H^+$	9.4

The effects of added sodium chloride and potassium chloride are different. The pH of the 2 molar zinc chloride solution prior to addition of either salt was 2.68. After adding sodium chloride to solution, the pH dropped slightly to 2.64. Upon addition of potassium chloride to a zinc chloride solution, the pH increased to 2.89.

Table 30-3

pH TRANSITION RANGES OF ZINC CHLORIDE SOLUTIONS
AS DETERMINED BY TITRATION

Molarity $ZnCl_2$	Endpoint pH	pH Transition Range
0.101	4.90	4.75 ± 1.05
0.499	4.42	4.04 ± 0.74
1.010	3.45	3.43 ± 1.25
1.996	2.62	2.72 ± 0.78
3.002	2.22	2.05 ± 0.54
3.990	1.60	1.82 ± 0.76

The curves in Figure 30-4 are linear from the initial starting pH. The pH change caused by salt addition is negligible in the case of sodium chloride and could be due to experimental error or a trace of acid in the sodium chloride.

The results from potassium chloride testing appear to exceed experimental error and are believed real. The increase in pH, both initial and in the presence of added hydrochloric acid, may be due to a decrease in the activity of hydrochloric acid. Another possibility is that potassium ions stabilize the various zinc-chloro complexes which would result in less acid-base hydrolysis of the zinc ion. But, it may be argued that sodium chloride should behave in a similar fashion. A third consideration is that the molarity of zinc chloride in each of the three solutions is different. The addition of either KCl or NaCl causes volume expansion which represents a dilution of the zinc concentration on the molarity scale. On the molar scale, potassium chloride, due to its larger partial molal volume, causes a greater dilution than does sodium chloride.

PARTIAL MOLAL VOLUMES OF ZINC CHLORIDE IN ZINC-CHLORINE BATTERY ELECTROLYTES

Although formally defined as a limiting value, in actual practice the partial molal volume may be determined over a small change in composition. The partial molal volume of a solute generally increases as the solute concentration is increased. Therefore, the value of the partial molal volume must be referred to the concentration at which the measurement was made.

For the partial molal volumes of salt solutions shown in Figure 30-5, density vs. composition tables found in the 42nd edition of Handbook of Chemistry and Physics (published by CRC) were used.

Several different techniques may be used to calculate $\bar{v}_2$. In this work, the following equation was used (30-5).

$$\bar{v}_2 = \frac{M_2 - 1000\ (\partial D/\partial c)}{D - c\ (\partial D/\partial c)}$$

where

$\bar{v}_2$ = partial molal volume of the solute

M_2 = molecular weight of the solute

D = density, g/ml

c = concentration in moles/liter

In Figure 30-5, the concentration intervals were about 0.1 molar for zinc chloride while for potassium chloride and sodium chloride, the concentration intervals extended to about 0.3 - 0.5 molar.

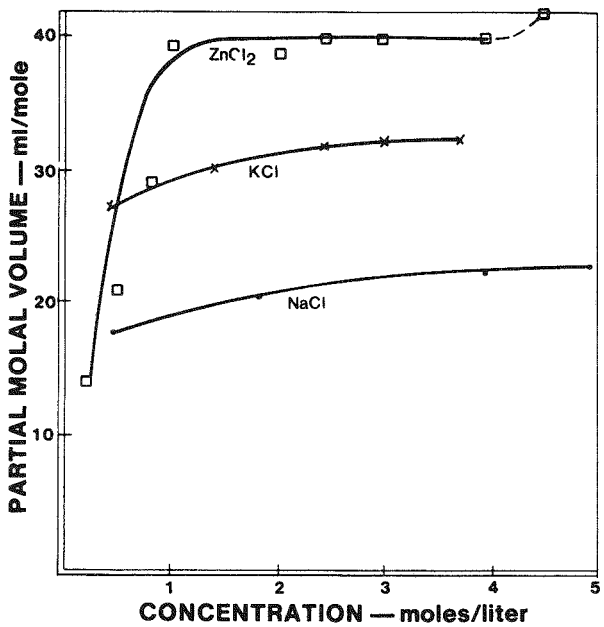

Figure 30-5. Plot of calculated partial molal volumes of battery electrolyte salts.

In Figure 30-5, it is observed that the partial molal volume of zinc chloride shows considerable concentration dependence for solutions less than one molar. For one to four molar solutions, the partial molal volume of $ZnCl_2$ is about 40ml/mole.

For potassium chloride, a more gentle slope is observed, with a value of 32ml/mole around 3 molar. For sodium chloride, a value of 22ml/mole is obtained. Due to the concentration intervals used in calculating the partial molal volumes of these two salts, the volumes for concentrations less than one molar may contain considerable error.

PARTIAL MOLAL VOLUMES OF SALTS IN BATTERY ELECTROLYTES

Experimentally, densities of solutions of known compositions were determined by weighing. The appropriate calculations were then made to determine the partial molal volumes of zinc chloride in water and in 4 molal potassium chloride, and the partial molal volumes of potassium chloride and sodium chloride in 2.14 molal zinc chloride. This data is presented in Table 30-4.

Table 30-4

PARTIAL MOLAL VOLUMES AT 23 ± 2°C

Solute	Medium	Concentration Interval	$\bar{v}_2$ ml/mole
$ZnCl_2$	H_2O	0 - 1.01 molar	23.
$ZnCl_2$	H_2O	1.01 - 1.996 molar	32.
$ZnCl_2$	H_2O	1.996 - 3.002 molar	40.
$ZnCl_2$	H_2	3.002 - 3.990 molar	40.
$ZnCl_2$	4 molal KCl	0 - 0.441 molar	41.
$ZnCl_2$	4 molal KCl	0.441 - 0.878 molar	50.
$ZnCl_2$	4 molal KCl	0.878 - 1.305 molar	45.
$ZnCl_2$	4 molal KCl	1.305 - 1.724 molar	45.
NaCl	2.14 molal $ZnCl_2$	0 - 1.89 molar	27.
NaCl	2.14 molal $ZnCl_2$	1.89 - 3.595 molar	28.
KCl	2.14 molal $ZnCl_2$	0 - 1.86 molar	38.
KCl	2.14 molal $ZnCl_2$	1.86 - 3.43 molar	36.

DISCUSSION

The experimental values for the partial molal volume of zinc chloride in water is about 40ml/mole for concentrations greater than 2 molar. The experimental data yields poor values in dilute solutions due to the large concentration interval. In constructing Figure 30-5 from the handbook values, concentration intervals of 0.1 to 0.2 molar were used as previously described. At high concentrations, the experimental molal volumes for zinc chloride are in good agreement with the calculated values.

The partial molal volumes of zinc chloride in potassium chloride have considerable variance. These are believed to be experimental scatter of data due to the technique used, rather than real variations. It would appear that the partial molal volume of zinc chloride in potassium chloride is about 45ml/mole, and essentially independent of the zinc chloride concentration. This value is observed to be about 5ml/mole higher than the value of zinc chloride in water.

The partial molal volumes of potassium chloride and sodium chloride in zinc chloride medium are also observed to be 5ml/mole larger than their respective aqueous values. This increase in molal volume may be due, in part, to the formation of chloro-zinc complexes. The formation of such complexes would free the water of hydration from the chloride ion and zinc ion as well. Also, the tetra-chloro zinc ion is larger than a tetra-aquo zinc ion (30-6) (30-7). The combination of freeing bound water, formation of the tetra-chloro zinc complex with its low affinity for water, and interionic repulsions in concentrated solutions may account for the constant changes in molal volumes observed in this work.

In summary, the electrolyte pH will change by 0.5 - 0.8 pH units during a battery cycle due to changes in the zinc chloride concentration. Also, the electrolyte volume will contract by about 10% as the battery goes from fully discharged to fully charged. This volume contraction is due to the removal of zinc chloride from the electrolyte.

REFERENCES

30-1 H.H. Willard, L.L. Merritt, Jr., and J.A. Dean. Instrumental Methods of Analysis. 4th ed. New York: D. Van Nostrand Co., Inc., 1965, pp. 568-577.

30-2 G. Biedermann. Proceedings of the International Conference on Coordination Chemistry. 8th. Vienna, 1964, pp. 434-437.

30-3 G. Schorsch, and Bull. Soc. Shim. France, 7, 1964, pp. 1449-1455.

30-4 D.D. Perrin. Journal of the Chemical Society. 1962, pp. 4500-4502.

30-5 I.M. Klotz. Chemical Thermodynamics. New York: W.A. Benjamin, Inc., 1964, pp. 241-268.

30-6 D.L. Wertz, and J.R. Bell. Journal of Inorganic and Nuclear Chemistry. 35, 1973, pp. 137-143.

30-7 Ibid, pp. 861-868.

Section 31

CURRENT DISTRIBUTION IN ZINC-CHLORINE BATTERIES

INTRODUCTION

The heart of the zinc-chlorine battery system, as presently envisioned, is the comb-type bipolar battery stack shown schematically in Figure 31-1. The intercell bus bar, fabricated of graphite, serves not only to electrically connect adjacent unit cells but also to separate the individual cell electrolytes. Zinc-electrode substrates, also fabricated of graphite, are fitted into grooves on one side of the bus bar. Similarly, pairs of chlorine-electrode substrates are fitted into grooves on the other side of the bus bar. During charge and discharge, electrolyte is pumped through the chlorine-electrode substrates, which are fabricated of porous graphite. This comb assembly of chlorine-electrode substrates, bus bar, and zinc-electrode substrates is replicated to form the series-connected stack shown in Figure 31-1. Stack termination is accomplished, as shown, by use of a bus

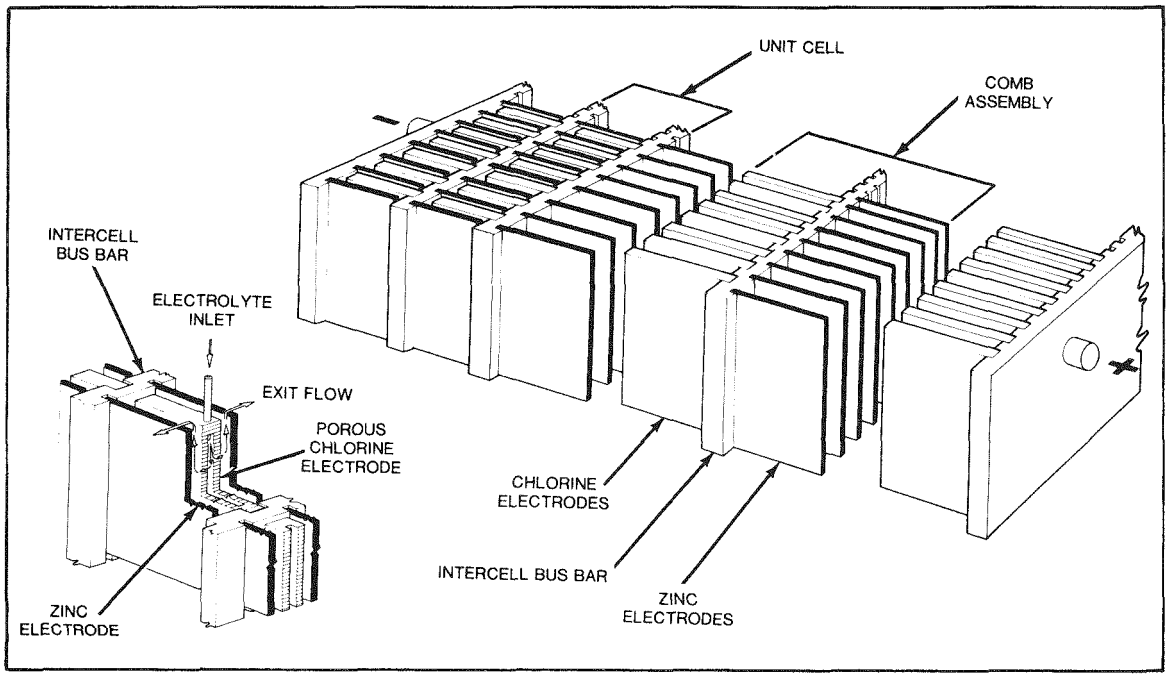

Figure 31-1. Comb-type bipolar arrangement of electrodes in a zinc-chlorine battery.

bar with one type of electrode. It should be noted that in this concept both faces of each zinc electrode are plated, while only the two outside faces of each chlorine-electrode pair are active.

Each unit cell is comprised of multiple single cells, i.e. one side of a zinc-electrode substrate facing a chlorine-electrode substrate. A schematic of a single cell is shown in Figure 31-2. Immediately after initiation of charge, the current density is approximately uniform because of the similarity of the sheet resistance of both graphite substrates. However, in the early stages of charge, the current-density distribution becomes more asymmetrical because of the electrodeposition of conductive zinc. At the end of charge, the zinc film is consequently thickest near the chlorine-electrode bus-bar. This tends to increase the probability of edge-dendrite formation. Zinc-dendrite formation is favored at this location because of the higher local current density.

The distribution of current density across the zinc and chlorine electrodes is a function of the chlorine-electrode substrate width, thickness, conductivity, the electrolyte resistivity, the inter-electrode gap, the apparent current density, and the non-ohmic ("IR-free") cell polarization; i.e. the total cell polarization less the ohmic polarization components. Research and development on cell technology have resulted in: (a) lowering of chlorine-electrode polarization by improved activation techniques, (b) reduction of the electrolyte resistivity by use of supporting electrolytes and an increased temperature of cell operation, (c) qualification of a more conductive porous graphite, and (d) increased charge and discharge apparent current densities by use of zinc-plate leveling agents. Developments (a), (b), and (c) have led to improved voltaic efficiencies. Development (d) not only improved coulombic efficiency but also raised the stack energy density, thereby reducing the specific cost ($/kWh) of the stack. However, such changes also affect the distribution of current density, as described in this paper.

Initially, a circuit model is developed for the single cell. A differential segment of this circuit is then integrated over the width of the cell, and an expression for the current-density distribution is derived. The current-density distribution is calculated for a "standard case", considered to represent present technology. Current-density distributions are presented also for changes in cell width, electrode polarizations, chlorine-electrode resistivity and thickness, inter-electrode gap, and electrolyte resistivity. Next, the calculated zinc-deposit

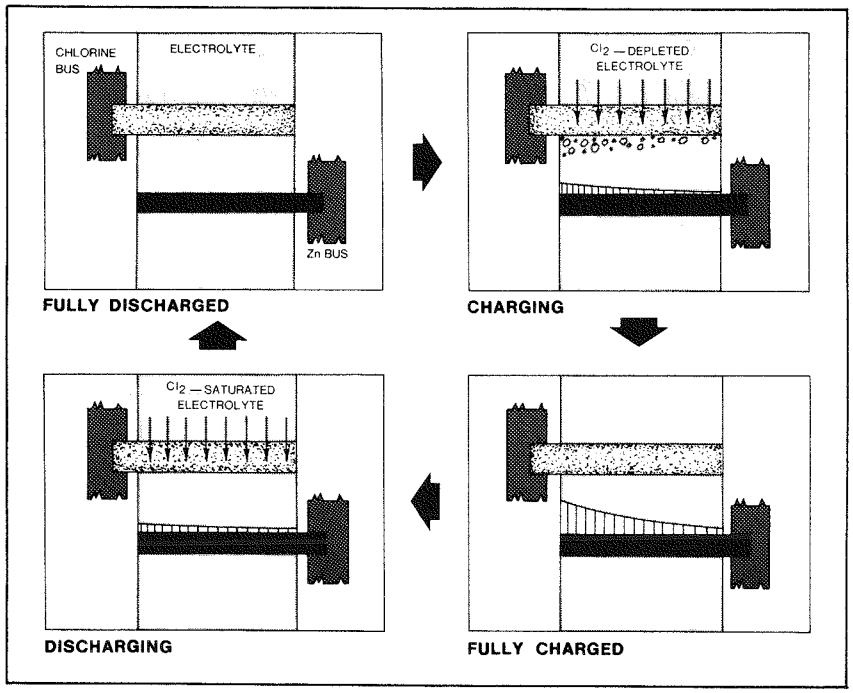

Figure 31-2. Sequence of schematics showing the distribution of zinc on the zinc-electrode substrate during a full-charge-discharge cycle.

thickness distribution after a seven-hour charge under standard case conditions is presented. The result of these calculations are then contrasted with each other and with experimental data on weight distribution across the width of the zinc electrodes.

CELL MODEL

The comb-type bipolar unit cell is comprised of a number of single cells connected in parallel. This repetition allows for the development of the electrical-circuit model of the cell from a single-cell section. First, a discussion of the voltaic losses in the single cell and the assumptions made regarding these losses is presented. The terminology used in this discussion and throughout the paper is shown in Table 31-1.

Figure 31-3 illustrates a top view of the single-cell section of a unit cell. The various voltage losses are identified. A voltage loss in the bus bar, V_b, is found on each side of the cell, as the current enters and exits the cell. From symmetry

Table 31-1

TERMINOLOGY

English

A	Constant, equation 32
B	Constant, equation 28
H	Cell height
i	Current in a differential element
I	Total cell current
J	Current density
k	Constant, equation 5
m	Constant, equation 26
R	Resistance
v	Voltage in a differential element
V	Voltage
W	Cell width

Greek

δ	Thickness
Δ	Differential element
ρ	Resistivity

Subscripts

b	Bus (Cl_2 or Zn)
c	Charge (voltage)
d	Zinc deposit
e	Inter-electrode gap
f	Cl_2 electrode-bus contact
g	Cl_2 electrode
k	IR-free (polarization)
o	Zn-electrode (polarization)
p	Cl_2-electrode (polarization)
r	Reversible (voltage)
s	Zn-electrode substrate
t	Defined by equations 6 and 7
x	Zn electrode-bus contact
y	Distance from Cl_2-bus along cell width
z	Zn electrode

considerations, these losses are assumed to be equal. Each chlorine and zinc electrode has a voltage loss, V_f and V_x respectively, associated with a constant resistance between the electrodes and the bus bars. It is assumed that these contact and bus-bar resistances are constant along the height of the cell. Since the electrodes are anchored to the bus bars continuously along the cell height, a current-density variation along the cell height is assumed to be negligible.

The uneven distribution of current across the cell is the result of the difference in the voltage drops across the chlorine and zinc electrodes, V_g and V_z respectively, over the active width of the cell. The electrode resistances are similar at the initiation of charge, as both the chlorine- and zinc-electrode substrates

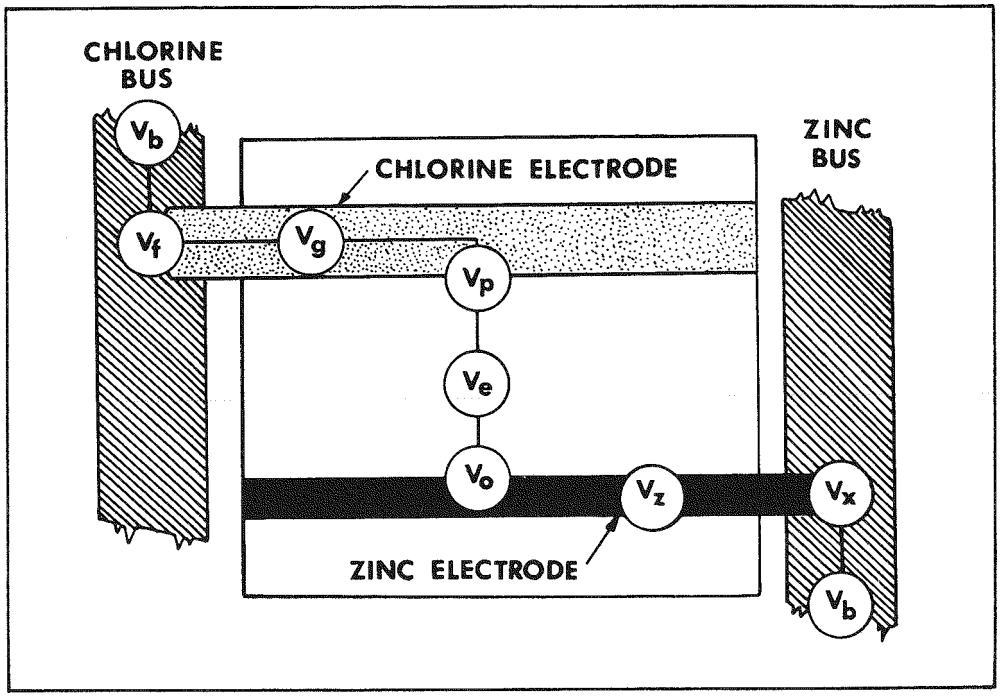

Figure 31-3. Schematic illustration of voltage drops in a zinc-chlorine cell, showing ohmic polarizations in the buses (V_b), electrode-bus contacts (V_f and V_x), electrodes (V_g and V_z), and the electrolyte (V_e). The zinc- and chlorine-electrode polarizations are V_o and V_p, respectively.

are fabricated of graphite. However, within minutes after the initiation of charge, the zinc-electrode resistance decreases significantly. This is due to the electrodeposition of highly-conductive zinc on this electrode. Consequently, the zinc electrode is assumed to be an equipotential surface.

The IR-free polarizations at the chlorine and zinc electrodes are represented by V_p and V_o, respectively. The voltage loss in the electrolyte across the inter-electrode gap is represented by V_e. For modeling purposes, all three polarizations are fused into one resistive component. The necessary assumption is that the IR-free polarizations conform to Ohm's law. Figure 31-4, a typical cell-polarization plot, illustrates the validity of this assumption.

The IR-free polarization is represented as the difference between the total and ohmic polarization curves. It may be observed that the ohmic polarization curve is linear with an intercept at 2.12 volts, the open-circuit voltage (O.C.V.) of

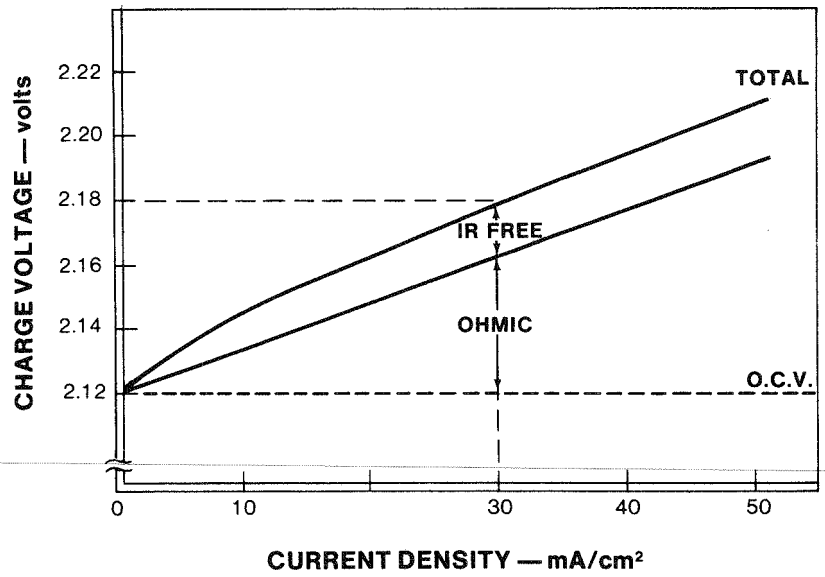

Figure 31-4. A typical current-voltage curve for a zinc-chlorine cell during charge. The separation into ohmic and IR-free components was achieved by a current-interruption technique.

the cell. The combination of the ohmic and IR-free polarizations is also essentially linear over the current density range of interest, 20-50mA/cm^2. This assumption may be expressed mathematically. The voltage loss due to the ohmic polarization in the electrolyte and the IR-free polarization is

$$V_t = V_p + V_e + V_o \quad (1)$$

and may be arranged to give

$$V_t = (V_p + V_o) + V_e \quad (2)$$

By applying Ohm's law, V_t may be expressed as

$$V_t = k \cdot J_t + \rho_e \cdot \delta_e \cdot J_t \quad (3)$$

where J_t is the current density in the electrolyte across the inter-electrode gap, ρ_e is the electrolyte resistivity, δ_e is the inter-electrode gap, and k is a constant. This expression for V_e is derived as follows:

$$V_e = R_e \cdot I_t$$

$$= \left(\frac{\rho_e \cdot \delta_e}{H \cdot W}\right) \cdot (J_t \cdot H \cdot W)$$

$$= \rho_e \cdot \delta_e \cdot J_t \qquad (4)$$

Both the constant, k, and $\rho_e \cdot \delta_e$ have units of $\Omega \cdot cm^2$. These are the units of the slopes of the polarization curves in Figure 31-4. In order to combine these terms, it is assumed that

$$k = \rho_k \cdot \delta_e \qquad (5)$$

Equation 1 may now be expressed as

$$V_t = (\rho_k + \rho_e) \cdot \delta_e \cdot J_t \qquad (6)$$

For convenience, ρ_k and ρ_e are expressed as one term, ρ_t. Therefore, equation 1 may be written:

$$V_t = \rho_t \cdot \delta_e \cdot J_t \qquad (7)$$

where $\rho_t \cdot \delta_e$ is defined as the compound resistivity-gap product.

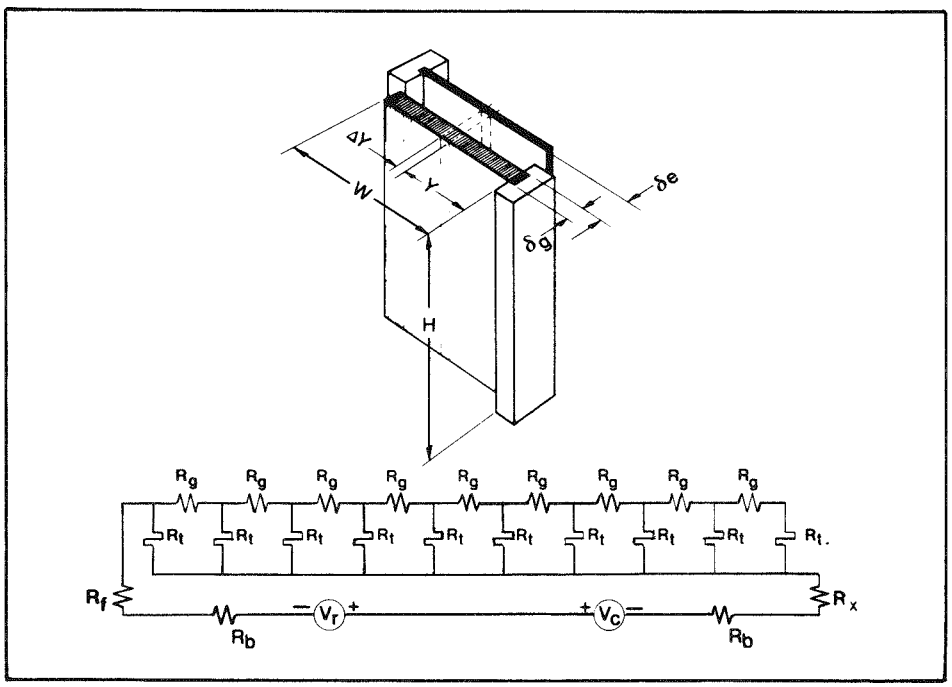

Figure 5. Perspective drawing and the corresponding ten-segment circuit model for a single cell.

The ten-segment circuit model for the single cell is shown in Figure 31-5. The resistors across the top of the circuit, R_g, represent the chlorine-electrode resistance, while R_t represents the combined resistance in the electrolyte. This combination refers to the fusion of the IR-free polarizations and ohmic polarization in the electrolyte into one term. The series connection of the chlorine-electrode resistances and the parallel connections of the electrolyte resistances reflect the direction of current flow in the cell. The zinc electrode is represented as a short-circuit connected across the R_t resistors. This is because the zinc electrode was assumed to be an equipotential surface. The bus bar, R_b, and contact resistances R_f and R_x, are connected at the end of the respective electrodes. Finally, a charging condition is modeled by the reversible cell voltage, V_r, being opposed by the charge cell voltage V_c. The difference between these two voltage sources represents the total voltage loss across the cell.

The equations which determine the chlorine-electrode resistance, R_g, and the combined resistances in the electrolyte, R_t, are given by:

$$R_g = \frac{\rho_g \cdot \Delta y}{\delta_g \cdot H} \tag{8}$$

$$R_t = \frac{\rho_t \cdot \delta_e}{H \cdot \Delta y} \tag{9}$$

These equations are based on the standard resistance formula of path length multiplied by resistivity and divided by the cross-sectional area. In the case of the chlorine electrode, the path length is designated as Δy, and represents a unit distance across the active width of the cell. In the calculation of the combined electrolyte resistance, the path length is the inter-electrode gap, δ_e.

The magnitudes of these resistors were calculated from a set of parameter values, defined as the "standard case". This set of cell-parameter values, represents present technology in comb-type bipolar cells, and is shown in Table 31-2. The chlorine-electrode and combined-electrolyte resistances were calculated to be:

$$R_g = 0.0009 \text{ ohm}$$

$$R_t = 0.2 \text{ ohm}$$

It should be noted that it is the difference between these two resistance values which determine the distribution of current across the cell. If the resistance presented by the electrolyte is much greater than the chlorine-electrode resistance, the distribution tends to become uniform across the cell.

Table 31-2

SELECTED CELL PARAMETERS AND THEIR STANDARD-CASE VALUES

Parameter	Title	Standard-Case Values
W	Cell width	6 cm
H	Cell height	10 cm
δ_e	Inter-electrode gap	0.2 cm
ρ_e	Electrolyte resistivity	3 ohm-cm
$V_o + V_p$	IR-free polarization	0.018 V
ρ_t	Compound resistivity	6 ohm-cm
δ_g	Cl_2-electrode thickness	0.2 cm
ρ_g	Cl_2-electrode resistivity	0.003 ohm-cm
V_r	Reversible cell voltage	2.12 V
V_c	Charge cell voltage	2.18 V
I	Charge cell current	1.8 A

The current distribution across the cell may be calculated from this circuit model. However, this must be considered as an approximate analysis, because of the discrete nature of the ladder circuit. The accuracy of the calculation is dependent upon the number of sections chosen for the circuit. The extreme case would be to take a section of this circuit, define it as a differential segment, and integrate it over the width of the cell. This in essence is the basis of the following analysis.

CALCULATION OF CURRENT-DENSITY DISTRIBUTION

By integrating a differential segment of the circuit model over the cell width, an expression in terms of current density was derived. This expression allowed for the current density to be calculated at any point across the cell width.

Figure 6 shows a differential circuit element of the single cell. This element is simply one segment of the circuit model used in the approximate treatment. The element is located a distance (y) from the chlorine bus, and extends a distance (Δy) along the width of the cell.

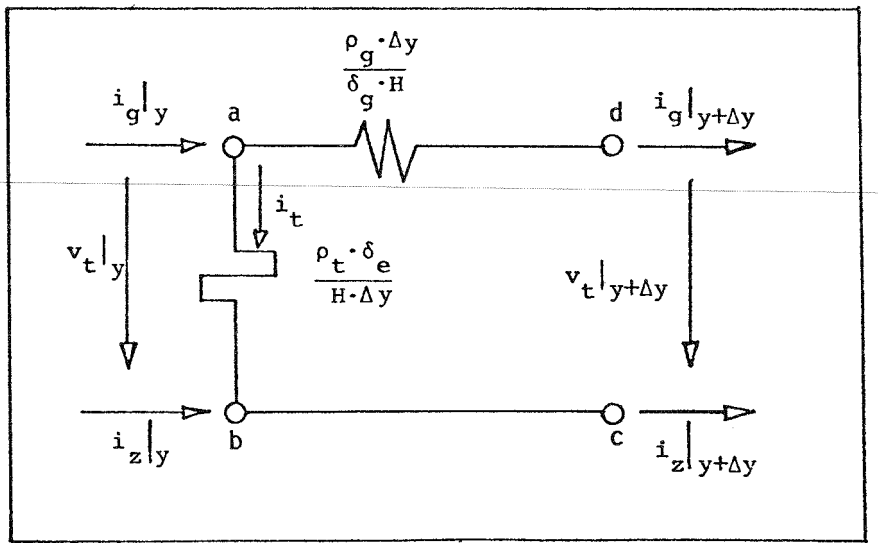

Figure 6. Differential circuit element of a single cell.

This differential element was found to be quite similar to the differential elements in cooling fins (1) and fuel cells (2). With rectangular cooling fins, the heat transfer along the fin is analogous to the distribution of current along the chlorine electrode. In both situations, the distributions are a function of the width direction alone. Also, the assumption that the zinc electrode is an equipotential surface is the same as assuming that the air around a cooling fin is at constant temperature. In the case of fuel cells, the only difference in the circuit elements rests in the assumption that significant resistance is present in the fuel electrode. The fuel electrode in the fuel cell is equivalent to the zinc electrode in the zinc chlorine cell. As stated previously, the resistance presented by the zinc electrode is so small that the zinc electrode may be treated as an equipotential surface. Due to the similarity between these situations, the integration technique used for the zinc chlorine cell is an adaptation of the other integration procedures.

In the steady state, one current balance for the differential circuit element is given by

$$i_g|_{y+\Delta y} - i_g|_y + i_t|_y = 0 \tag{10}$$

where

$$i_t|_y = \frac{v_t|_y}{\left[\frac{\rho_t \cdot \delta_e}{H \cdot \Delta y}\right]} \tag{11}$$

Upon substitution of $i_t|y$ into equation 10, and taking the limit of equation 10 as Δy approaches 0,

$$\frac{di_g|}{dy}_y = \frac{-H}{\rho_t \cdot \delta_e} \cdot v_t|_y \tag{12}$$

Kirchoff's law for the voltage balance around the closed loop abcd gives

$$v_t|_y - v_t|_{y+\Delta y} - \frac{\rho_g \cdot \Delta y}{\delta_g \cdot H} \cdot i_g|_{y+\Delta y} = 0 \tag{13}$$

In the limit as Δy approaches 0,

$$\frac{dv_t|}{dy}_y = \frac{-\rho_g}{\delta_g \cdot H} \cdot i_g|y \tag{14}$$

The two differential equations (equations 12 and 14) may be combined by taking the second differential of equation 14, and substituting equation 12 into it. Differentiating equation 14,

$$\frac{d^2v_t}{dy^2}|_y = \frac{-\rho_g}{\delta_g \cdot H} \cdot \frac{di_g}{dy}|_y \tag{15}$$

and combining this equation with equation 12 gives

$$\frac{d^2v_t}{dy^2} = \left[\frac{\rho_g}{\delta_g \cdot \rho_t \cdot \delta_e}\right] \cdot v_t \tag{16}$$

This differential equation defines the voltage drop in the electrolyte at any distance along the width, and may be related to the current density in the electrolyte by the following equation.

$$J_t = \frac{i_t}{H \cdot \Delta y} \tag{17}$$

where

$$i_t = \frac{H \cdot \Delta y}{\rho_t \cdot \delta_e} \cdot v_t \tag{18}$$

Therefore,

$$J_t = \frac{v_t}{\rho_t \cdot \delta_e} \tag{19}$$

Before equation 16 may be solved, two boundary conditions must be defined. The boundary conditions are:

$$I = \int_{y=0}^{y=W} i_t dy = \frac{H}{\rho_t \cdot \delta_e} \int_{y=0}^{y=W} v_t dy \tag{20}$$

$$\left.\frac{dv_t}{dy}\right|_{y=0} = \frac{-\rho_g}{\delta_g \cdot H} \cdot I \tag{21}$$

The first boundary condition (equation 20) was realized from the fact that the sum of all the differential currents in the electrolyte must be equal to the total cell current (I). The second boundary condition (equation 21) reflects the fact that the total cell current is carried in the chlorine electrode at y=0.

The solution for the second order differential equation of the circuit element (equation 16) is in the general form of

$$v_t = A \cdot \cosh(my) + B \cdot \sinh(my). \tag{22}$$

The constant m may be solved for by substituting the general form into equation 16. Differentiating the general form yields

$$\frac{dv_t}{dy} = A \cdot m \cdot \sinh(my) + B \cdot m \cdot \cosh(my) \tag{23}$$

and

$$\frac{d^2 v_t}{dy} = A \cdot m^2 \cdot \cosh(my) + B \cdot m^2 \cdot \sinh(my) \tag{24}$$

and substituting into equation 16 gives

$$A \cdot m^2 \cdot \cosh(my) + B \cdot m^2 \cdot \sinh(my) = \left[\frac{\rho_g}{\delta_g \cdot \rho_t \cdot \delta_e}\right]\left[A \cdot \cosh(my) + B \cdot \sinh(my)\right] \quad (25)$$

Therefore,

$$m^2 = \frac{\rho_g}{\delta_g \cdot \rho_t \cdot \delta_e} \quad (26)$$

The constant B may be solved for by substituting equation 23 into the second boundary condition:

$$A \cdot m \cdot \sinh(my)\Big|_{y=0} + B \cdot m \cdot \cosh(my)\Big|_{y=0} = \frac{-\rho_g}{\delta_g \cdot H} \cdot I, \quad (27)$$

where $\sinh(0) = 0$

$\cosh(0) = 1.$

Therefore,

$$B = \frac{-\rho_g \cdot I}{\delta_g \cdot H \cdot m} \quad (28)$$

The constant A may be solved for by substituting the general form into the first boundary condition:

$$I = \frac{H}{\rho_t \cdot \delta_e} \cdot \int_{y=0}^{y=W} \left(A \cdot \cosh(my) + B \cdot \sinh(my)\right) dy \quad (29)$$

$$I = \frac{H \cdot A}{\rho_t \cdot \delta_e} \cdot \left[\frac{\sinh(my)}{my}\right]_{y=0}^{y=W} + \frac{H \cdot B}{\rho_t \cdot \delta_e}\left[\frac{\cosh(my)}{m}\right]_{y=0}^{y=W} \quad (30)$$

$$I = \frac{H \cdot A}{\rho_t \cdot \delta_e \cdot m}\left[\sinh(mW)\right] + \frac{H \cdot B}{\rho_t \cdot \delta_e \cdot m}\left[\left(\cosh(mW)\right) - 1\right] \quad (31)$$

Therefore,

$$A = \frac{\frac{\rho_t \cdot \delta_e \cdot m \cdot I}{H} - \frac{\rho_g \cdot I}{\delta_g \cdot H \cdot m}\left[1 - \cosh(mW)\right]}{\sinh(mW)} \quad (32)$$

The solution for equation 16 may then be written

$$v_t = \left[\frac{\frac{\rho_t \cdot \delta_e \cdot m \cdot I}{H} - \frac{\rho_g \cdot I}{\delta_g \cdot H \cdot m}\left(1 - \cosh(mW)\right)}{\sinh(mW)}\right] \cdot \cosh(my) - \left[\frac{\rho_g \cdot I}{\delta_g \cdot H \cdot m}\right] \cdot \sinh(my) \quad (33)$$

However, this somewhat unwieldy equation may be reduced significantly by dividing both sides of the equation by m, and substituting for m^2. Dividing through by m yields

$$\frac{v_t}{m} = \left[\frac{\frac{\rho_t \cdot \delta_e \cdot I}{H} - \frac{\rho_g \cdot I}{\delta_g \cdot H \cdot m^2}\left(1 - \cosh(mW)\right)}{\sinh(mW)}\right] \cdot \cosh(my) - \left[\frac{\rho_g \cdot I}{\delta_g \cdot H \cdot m^2}\right] \cdot \sinh(my) \quad (34)$$

where

$$m^2 = \frac{\rho_g}{\delta_g \cdot \rho_t \cdot \delta_e} \quad (35)$$

Upon substitution of m^2 into equation 34

$$\frac{v_t}{m} = \left[\frac{\frac{\rho_t \cdot \delta_e \cdot I}{H} - \frac{\rho_t \cdot \delta_e \cdot I}{H}\quad 1 - \cosh(mW)}{\sinh(mW)}\right] \cdot \cosh(my) - \left[\frac{\rho_t \cdot \delta_e \cdot I}{H}\right] \cdot \sinh(my) \quad (36)$$

$$\frac{v_t}{m} = \frac{\rho_t \cdot \delta_e \cdot I}{H}\left[1 - \frac{\left(1 - \cosh(mW)\right)}{\sinh(mW)} \cosh(my) - \sinh(my)\right] \quad (37)$$

$$v_t = \frac{m \cdot \rho_t \cdot \delta_e \cdot I}{H} \quad \frac{\cosh(mW)}{\sinh(mW)} \cdot \cosh(my) - \sinh(my) \quad (38)$$

This equation may be further reduced by using a trigonometric formula, once the term sinh(mW) is made the denominator for the complete equation. This is illustrated in the following development:

$$v_t = \frac{m \cdot \rho_t \cdot \delta_e \cdot I}{H} \left[\frac{\cosh(mW)}{\sinh(mW)} \cdot \cosh(my) - \frac{\sinh(mW)}{\sinh(mW)} \cdot \sinh(my)\right] \quad (39)$$

$$v_t = \frac{m \cdot \rho_t \cdot \delta_e \cdot I}{H} \left[\frac{\cosh(mW) \cdot \cosh(my) - \sinh(mW) \cdot \sinh(my)}{\sinh(mW)}\right] \quad (40)$$

$$v_t = \frac{m \cdot \rho_t \cdot \delta_e \cdot I}{H} \left[\frac{\cosh(mW - my)}{\sinh(mW)}\right] \quad (41)$$

From equation 19, this equation defined in terms of the current density in the electrolyte is

$$J_t = \frac{m\ I}{H}\ \frac{\cosh(mW-my)}{\sinh(mW)} \qquad (42)$$

The standard-case values for the cell parameters were substituted into the current-density distribution equation. A graph of the results is shown in Figure 31-7. The broken line across the graph represents the average current density. The curve illustrates the distribution of current density across the width of the cell. The point of maximum current density is found at the side of the cell where the chlorine electrode is anchored into the bus bar. This will be referred to as the "chlorine-bus" side. Similarly, the minimum current density is located at the "zinc-bus" side of the cell. It should be noted that the deviation of the curve from the average current density at the chlorine bus is approximately twice the magnitude of the deviation at the zinc bus. The change in current density across the total cell width is found to be 18.9%.

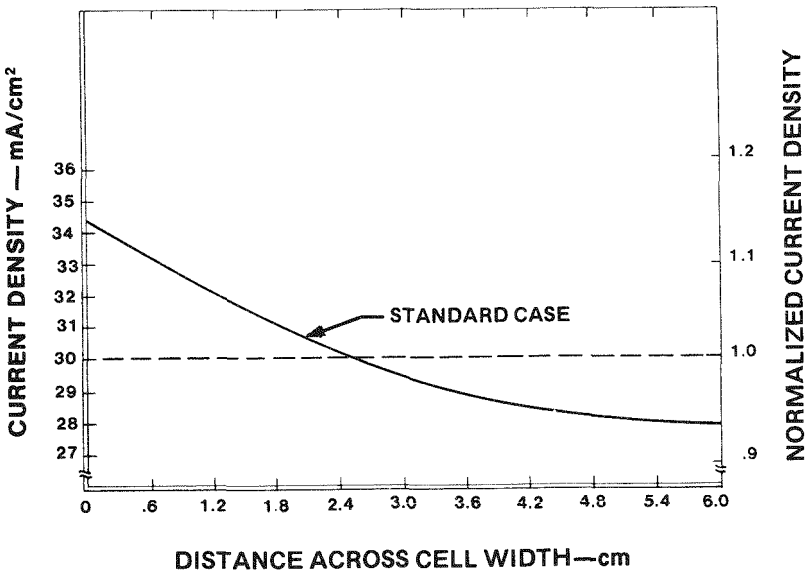

Figure 31-7. The standard-case current-density distribution. Note that the current density is highest on the chlorine-bus end of the zinc electrode.

A normalized current density axis is also shown, as the value of the cell current does not affect the slope of the current-distribution curve. This allows for changes in the cell current to be readily calculated. For example, if the cell current is increased to 3 amps, corresponding to an average current density of 50mA/cm^2, the

current density at the chlorine bus would be 57.3mA/cm^2 and 46.4mA/cm^2 at the zinc bus.

The voltage losses in the cell were also calculated. The total voltage loss across the chlorine electrode was found to be 7.8mV. The total loss due to the electrode polarizations and electrolyte resistivity was 33.4mV. This left a total of 18.8mV available for losses in the contacts and bus bars, as 2.18V was the standard case value for the charging voltage.

The sensitivity of the current-density distribution to changes from the standard-case values is explored by analyzing the effects of variation of the five major active-cell parameters, as shown in Table 31-3.

Table 31-3

CELL PARAMETERS INVESTIGAGED

Parameter	Title
W	Cell width
$\rho_t \cdot \delta_e$	Compound resistivity - gap product
ρ_g/δ_g	Chlorine electrode resistivity - thickness ratio

Some of the cell parameters are combined to avoid duplication in presenting the results. For instance, a change in the value of the chlorine-electrode resistivity-thickness ratio, ρ_g/δ_g, may also be considered as a change in the chlorine-electrode resistivity, ρ_g, when the chlorine-electrode thickness, δ_g, is held constant, and vice versa.

Figure 31-8 illustrates the current-density curves for changes in the cell width, W. The curve denoted "6cm" represents the standard case, and only the width parameter was varied from the standard case to obtain the other curves. The effect of the cell width on current-density distribution is more evident in Figure 31-9. This curve represents the current density calculated at the chlorine bus -- the maximum current density in the cell -- as a function of cell width. This curve is parabolic in nature, and indicates the sensitivity of current density to increases in the cell width.

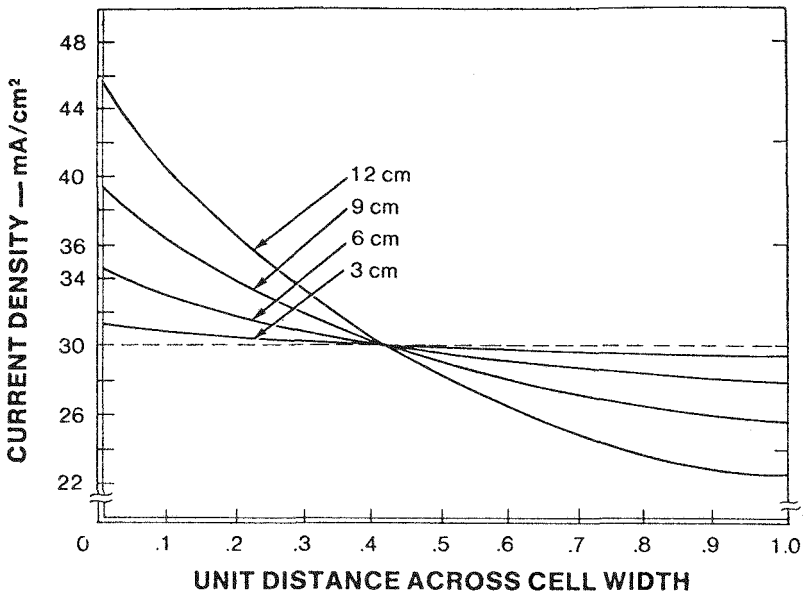

Figure 31-8. Current-density distribution as a function of cell width. Note that a width of 6cm is the standard-case value.

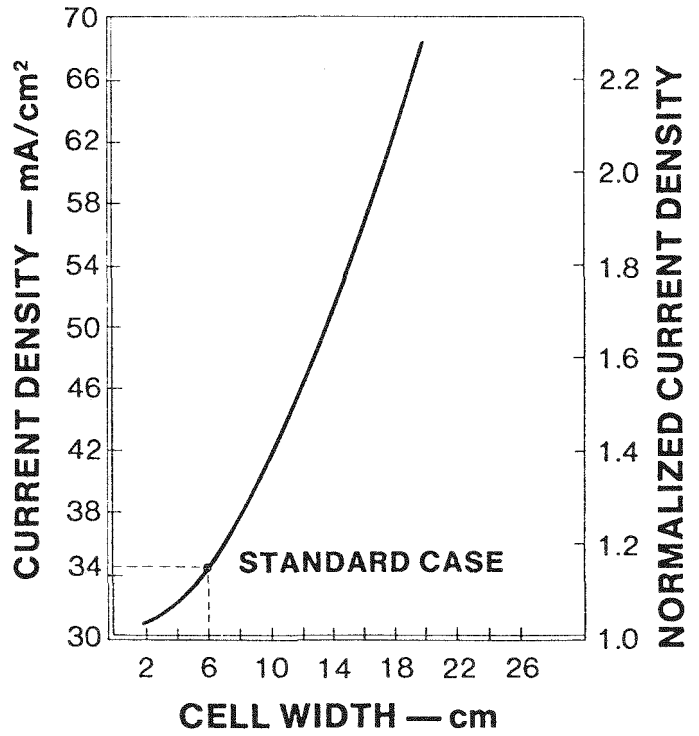

Figure 31-9. Active cell current density adjacent to the chlorine electrode bus as a function of cell width.

Figure 31-10 illustrates the effect of variations in the chlorine-electrode resistivity-thickness ratio on current density. Again, the zinc-electrode current density at the chlorine bus is used as a reference, as it serves to indicate the sensitivity of the parameter variations on current density. The graph reveals that an essentially linear relationship exists between the current density at the chlorine bus and the chlorine-electrode resistivity-thickness ratio.

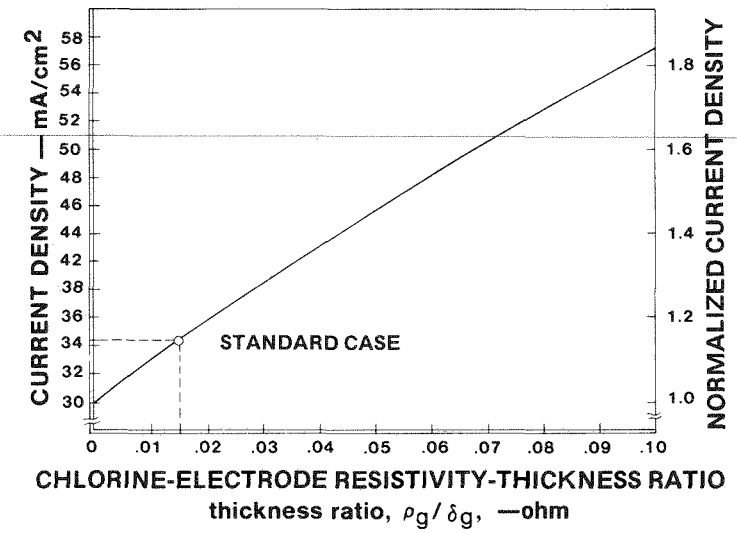

Figure 31-10. Active cell current density adjacent to the chlorine electrode bus as a function of the chlorine-electrode resistivity-thickness ratio.

Figure 31-11 shows the effect of the compound resistivity-gap product on current density at the chlorine bus. It is clear from this curve that the effect of this parameter on the current-density distribution is significant. This parameter is of course the most susceptible to physical variation. Even a simple temperature change in the electrolyte will cause a change in the compound resistivity, ρ_t. Although the current-density distribution curve in Figure 31-7 may be smoothed or leveled by an increase in $\rho_t \cdot \delta_e$, this will also increase the voltaic losses in the

cell. These losses must be minimized to optimize the electrochemical energy efficiency of the battery. Consequently, as cell operation becomes electrochemically more efficient, the tendency will be to increase the variation in current density.

CALCULATION OF ZINC-DEPOSIT DISTRIBUTION

The current-density distribution equation provides a continuous analysis of current density across the width of the cell. By applying Faraday's law, an instantaneous zinc-deposit weight distribution may be found directly from the current-density distribution. However, the magnitude of the inter-electrode gap will change as

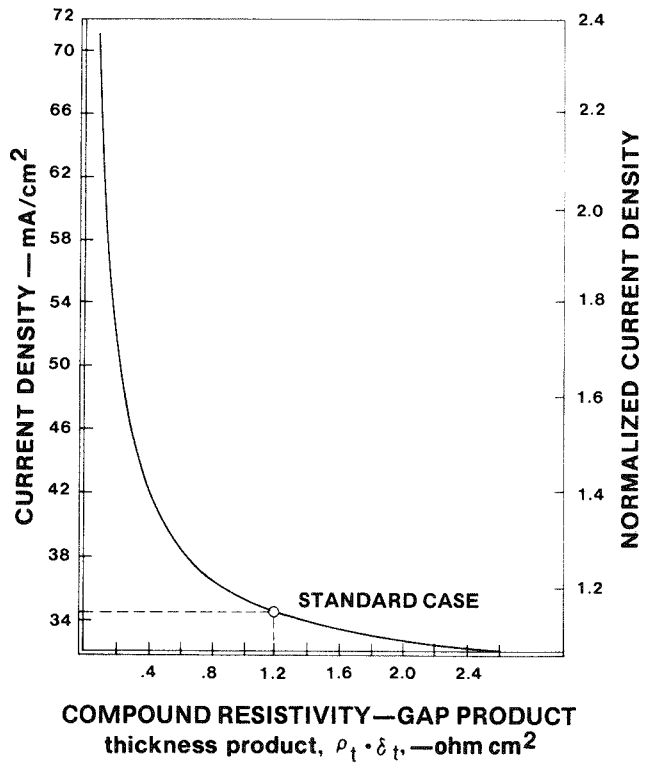

Figure 31-11. Active cell current density adjacent to the chlorine electrode bus as a function of the product of compound resistivity and the inter-electrode gap.

the zinc is plated on the graphite substrate of the zinc electrode. As the charge continues the deposit becomes thicker, and the distance between the zinc and chlorine electrodes effectively decreases. This causes a decrease in the compound resistivity-gap product, $\rho_t \cdot \delta_e$. As a result, the variation of current density across the cell increases, as well as the variation in zinc-deposit thickness and weight.

Another factor which tends to increase the variation of current density across the cell is the corrosion of electrodepositing zinc by chlorine dissolved in the electrolyte. The corrosion current density is essentially constant over the surface of the electrode. In other words, the rate of corrosion is independent of changes in current density across the cell. When a fixed corrosion current density is subtracted from the charge current density from each side of the cell, the result is an increase in the percentage variation of charge current density across the cell.

Current density may be related to the thickness of zinc deposit and the charge time. From Faraday's Law:

$$\text{Weight of zinc deposited (g)} = \frac{I(\text{amp}) \cdot \text{time(h)}}{26.8(\text{amp} \cdot \text{h})} \cdot \frac{\text{Molecular weight of zinc}}{2 \text{ electrons transferred}} \qquad (43)$$

The thickness of the zinc deposit may in turn be found from the weight of the deposit.

$$\text{Thickness of deposit} = \delta_d = \frac{\text{Weight of zinc deposited}}{\text{Density of deposit} \cdot \text{Active area of cell}} \qquad (44)$$

By substituting equation 43 into 44,

$$\delta_d = (1.22) \cdot \frac{I(\text{amp})}{\text{Active area of cell}} \cdot \frac{\text{time(h)}}{\text{Density of deposit}} \qquad (45)$$

which may be reduced to

$$\delta_d(\text{cm}) = \frac{(1.22) \cdot J_t \cdot \text{time(h)}}{\text{Density of deposit}} \qquad (46)$$

The density of zinc metal as given in textbooks is 7.14 g/cm^3. However, for purposes of this paper, a density of 6.3 g/cm^3 is used. This value corresponds to an experimental determination based on the weight and average thickness of zinc deposits peeled from nine different single cells. Therefore, the expression relating the thickness of the zinc deposit to the current-density distribution and the charge time is:

$$\delta_d(\text{cm}) = (0.194) \cdot J_t \cdot \text{time(h)} \qquad (47)$$

This expression was used to determine the distribution of zinc across the cell for the standard case. However, two calculations are presented. In the first calculation, the assumption that the zinc electrode is an equipotential surface is again utilized. In the second, the resistance of the zinc electrode is included, because this resistance is significant at the initiation of charge.

An expression defined as the zinc-electrode resistivity-thickness ratio, is derived to provide for the inclusion of a zinc-electrode resistance term in the distributed parameter equations. This expression which represents the parallel combination of the electrode-substrate resistance and the zinc-deposit resistance is

$$\frac{\rho_z}{\delta_z} = \frac{\rho_s \cdot \rho_d}{\delta_d \cdot \rho_s + \delta_s \cdot \rho_d} \tag{48}$$

The title and standard-case values for these parameters are listed in Table 31-4.

Table 31-4

ZINC-ELECTRODE RESISTIVITY-THICKNESS RATIO PARAMETERS

Parameter	Title	Standard-Case Value
ρ_s	electrode-substrate resistivity	1.0mΩ-cm
δ_s	electrode-substrate thickness	0.05cm
ρ_d	zinc-deposit resistivity	0.012mΩ-cm
δ_d	zinc-deposit thickness	initially 0

The standard-case value of the zinc-deposit resistivity is approximately twice that of the theoretical resistivity of zinc metal. The standard-case value was determined from laboratory measurements made on several zinc deposits which were peeled from test cells.

By substituting the zinc-electrode resistive component into the differential circuit model of the single cell (Figure 31-6), the resulting equations remain essentially the same. The only change from equation 26 is the expression for m^2. The new

expression is:

$$m^2 = \frac{1}{\rho_t \cdot \delta_e}\left[\frac{\rho_z}{\delta_z} + \frac{\rho_g}{\delta_g}\right] \qquad (49)$$

The expression for v_t is the same as equation 25, although it is not reduced to the more simplified, previous expression.

The use of equation 46 to determine the zinc-deposit distribution involved an iterative process. The time used for each iteration was 10 minutes, and the total charge time was set at seven hours. Due to the number of iterations involved, a programmable calculator (3) was used to perform the calculation. The method of calculation was

- The current density, J_t, was calculated at 11 points across the width of the cell, as in previous calculations.
- The deposit thickness, δ_d, was then calculated at these 11 points.
- The deposit thicknesses were then subtracted from the inter-electrode gap, which was initially constant across the width of the cell.
- These numbers provided the new inter-electrode gap across the cell for the next time iteration.
- The zinc-electrode resistivity-thickness ratio, ρ_z/δ_z, was calculated in the case where the resistance presented by the zinc electrode was included.
- This process was repeated until a total charge time of seven hours was accumulated.

The resulting zinc-deposit distribution for the case where the equipotential zinc electrode surface is assumed is shown in Figure 31-12. The thickness variation across the cell was found to be 20.9%. As expected, the variation in zinc thickness was greater than the instantaneous current-density distribution, 18.9%, calculated previously. Upon investigation of the last 10 minutes of the seven-hour charge, the current-density distribution was found to be 23.1%. This represents a 22.2% increase in the current-density variation over the charge period.

The growth rate of zinc deposition was also investigated. The growth rate at the chlorine-bus side of the cell as a function of time is shown in Figure 31-13. This represents the worst case, as the zinc-deposit thickness is greatest at this point. As indicated from the graph, the change in the zinc-deposit growth rate with time is substantially linear.

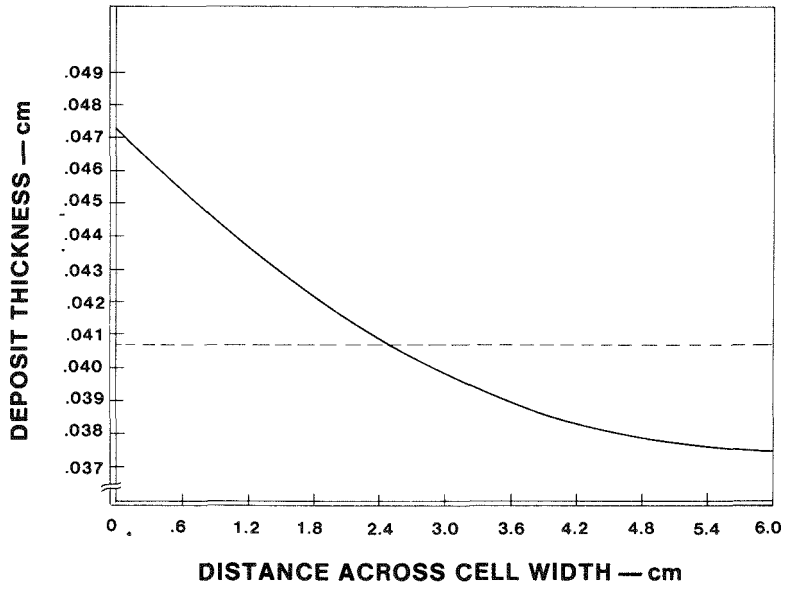

Figure 31-12. Zinc-deposit thickness distribution for the standard case after a seven-hour charge.

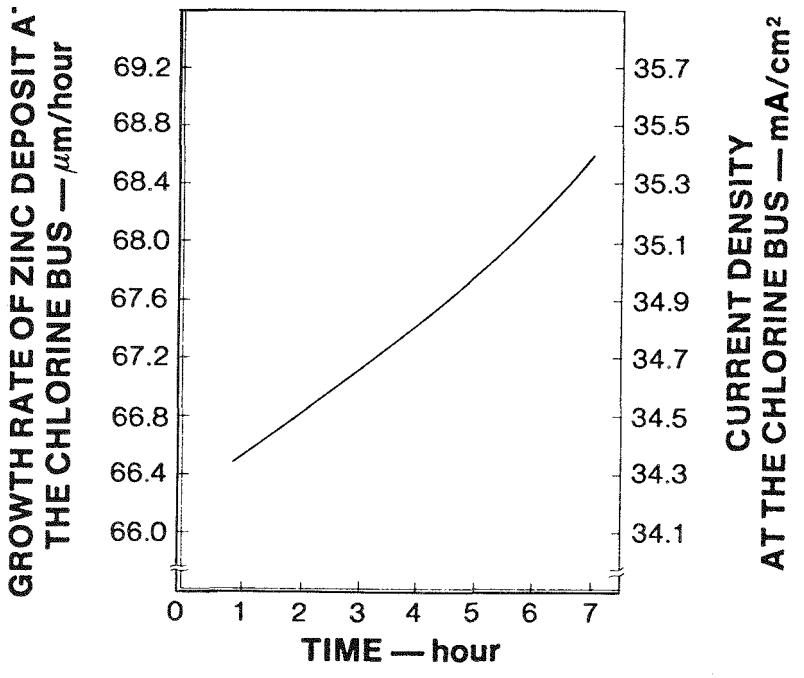

Figure 31-13. Growth rate of zinc deposition adjacent to the chlorine bus for the standard case as a function of charge time at 30mA/cm^2.

The zinc-deposit distribution was then calculated for the standard case where the resistance presented by the zinc electrode was included in the analysis. The zinc-deposit thickness variation was found to be 20.2% across the total width of the cell, i.e. a negligible decrease when compared to the 20.9% variation found when the zinc electrode was assumed to be an equipotential surface. Further, it was found that by the end of the first 10 minutes of charge, the resistance presented by the zinc electrode had decreased to a value one order of magnitude less than that of the chlorine electrode. Consequently, the assumption of an equipotential zinc surface did not significantly affect the accuracy of the analysis.

EXPERIMENTAL INVESTIGATIONS

In addition to the zinc-deposit resistivity and density measurements already noted, other measurements were made to confirm the calculated zinc-deposit thickness distribution. All of these measurements were conducted on nine zinc deposits peeled off in unbroken plates from test-cell substrates. These cells were charged for seven hours under substantially the same conditions as the standard -case parameter values.

Micrometer measurements on the plates revealed that the zinc deposits consistently were thicker at the chlorine-bus side of the cell than at the zinc-bus side. However, the surface roughness of the zinc did not allow accurate measurement. Weight measurements were therefore employed. Discs, 0.25 in. diameter, were punched on each side of the plates. Figure 31-14 indicates the position of the discs with respect to the plates. The center-line distance between the discs represents approximately 80% of active cell width. Results of the weight measurements are shown in Table 31-5. The average weight variation across the width of the plates is 17.7% $\pm$ 3.8%.

DISCUSSION

In the previous section an analytical technique was developed which may be used to calculate the variation in current density across the width of zinc-chlorine cells. This technique was then modified to calculate the effect of the current-density distribution on zinc electrodeposition. Experiments were also performed to determine the accuracy of these calculations.

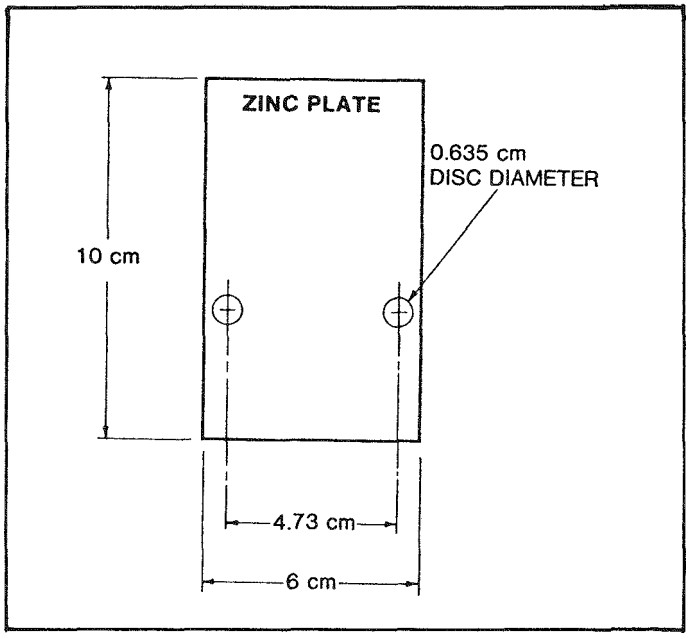

Figure 31-14. The position of the discs used to determine the variation in weight of zinc deposited on nine electrodes after a seven-hour full-capacity charge.

Table 31-5

EXPERIMENTAL WEIGHT VARIATIONS ACROSS 80% OF CELL WIDTH

Disc A Chlorine-Bus Side (mg)	Disc B Zinc-Bus Side (mg)	Difference in Weight (A-B)	Variation (%)
8.60	7.17	1.43	16.6
8.14	6.74	1.40	17.2
7.73	6.02	1.71	22.0
7.85	6.35	1.50	19.1
8.23	6.84	1.39	16.9
7.77	6.67	1.10	14.2
8.52	7.45	1.07	12.6
7.43	5.58	1.85	24.8
7.87	6.61	1.26	16.0

Table 31-6 compares the experimental average of 17.7% with values calculated across 80% of the zinc-electrode width. Three calculated values are shown. The first and second values are variations calculated on the basis of an equipotential and a finite, but decreasing, resistance zinc surface. The third value is computed on the basis of an average corrosion current density of 6mA/cm^2 during charge. This corresponds closely to the average fractional coulombic inefficiency of 0.20 which was experimentally observed for the nine zinc electrodes. The value of 20.3% is in good agreement with the experimental value of 17.7% particularly in view of the fact that secondary effects in the cell; e.g. gas bubbles, and hydrodynamic effects, are not considered.

This analytical technique is a powerful tool in the design of zinc-chlorine battery stacks, based upon the comb-type bipolar concept. It facilitates the determination of optimum cell dimensions. As electrode technology is improved, yielding more active electrodes and higher capacity densities (mAh/cm^2), this technique has provided a method whereby these and other future parameter changes may be evaluated. Properly used, this design tool will help to provide the cost-effective, efficient, and reliable zinc-chlorine battery stacks of the future.

Table 31-6

COMPARISON OF CALCULATED AND EXPERIMENTAL THICKNESS/WEIGHT VARIATIONS

	Percent variation over 80% of cell width
Thickness calculated with equipotential surface assumption for Zn-electrode	17.2
Thickness calculated with Zn-electrode resistance included	16.6
Thickness calculated with Zn-electrode resistance included and at 80% electrodeposition efficiency	20.3
Weight experimentally determined	17.7

REFERENCES

1. R. B. Bird, W. E. Stewart, and E. N. Lightfoot. Transport Phenomena. New York: J. Wiley & Sons, 1966, pp. 288-290.

2. E. F. Sverdrup, C. J. Warde, and R. L. Eback. "Design of High-Temperature Solid-Electrolyte Fuel-Cell Batteries for Maximum Power Output per Unit Volume." Energy Conversion, 13, 129-141.

3. Texas Instruments Programmable Calculator 59 with the PC-100A Print/Security Cradle.

Section 32

EFFECTS OF ELECTRODE HEIGHT AND ELECTROLYTE STATIC HEAD ON CELL PERFORMANCE

INTRODUCTION

Each comb-type unit cell of present design contains 44 pairs of electrode faces. Each pair, in turn, is comprised of one PG-60 porous-graphite chlorine-electrode face and one ATJ dense-graphite zinc-electrode face. Electrolyte enters from the bottom and flows upward and is uniformly released through each pair of profiled porous-graphite electrodes. The electrolyte accumulating above the submerged electrodes is semi-quiescent in nature and will be hereafter referred to as the electrolyte "static" head.

The operation of a zinc-chlorine cell requires the minimum static head height necessary to ensure full immersion of the electrodes. At a given electrolyte flow rate, the liquid height of this static head determines the horizontal flow velocity of the electrolyte across the top of the submerged electrode comb. For this reason the static head level may influence the fluid dynamic pattern of the electrolyte between pairs of electrodes, thereby affecting the corrosion rate of the zinc electrodes. Optimum coulombic performance of zinc-chlorine batteries requires evaluation of the significance of this effect.

In the present peak-shaving battery design, the desired voltage and current from a battery module is achieved by arranging the required number of submodules in parallel. Possible performance variations within any submodule would, of course, affect the total usable energy of that battery module. These variations could be minimized through quality control and/or reducing the number of submodules. Increasing the electrode area within the unit cells of the submodule is one method of reducing the number of parallel-connected submodules required to obtain the same energy capacity

battery module. Simultaneously, the graphite machining cost per battery module would be significantly reduced.

With the objective of minimizing performance variations and reducing the electrode machining cost, EDA is pursuing the development of larger electrodes. Previous work at this laboratory has shown that significant IR drops exist across the width of the chlorine electrode due to its high resistivity (3.05×10^{-3} ohm-cm). The present chlorine electrode of 2.563" appears to be close to the optimal width. The alternate method of increasing the electrode area is to increase the electrode height. For example, the use of a 6 " high electrode would represent a 50% increase in electrode area compared to the present 4" electrode.

It is generally theorized that an increase in electrode height could increase the rate of corrosion of zinc at the top of the zinc electrodes due to the higher electrolyte velocity at the top. The extent to which the electrode height can be increased was experimentally evaluated. The objectives of this study are to determine:

- the effect of electrolyte-static head
- the minimum electrolyte-static head for the current battery
- the maximum possible height of the electrode with acceptable coulombic and voltaic performances

The results from this investigation will be applied to future peak-shaving battery designs.

EXPERIMENTAL APPROACH

The effect of the electrolyte-static head on the electrochemical performance of zinc-chlorine cells was examined in a typical EDA test system (Figure 32-1). Electrolyte of 2M $ZnCl_2$ from the sump was circulated through a constant temperature water bath and a filter using a micropump. The flow was monitored by a flowmeter and the temperature was controlled at 30°C-35°C. Chlorination of the electrolyte on discharge was achieved by use of a gas sparging tube located in the sump.

The cell enclosure (case) is an integration of a sump and a test cell (Figure 32-2). The test cell contains two pairs of profiled chlorine electrodes (PG-60) and two pairs of zinc electrodes (ATJ). These electrodes were assembled according to the bipolar comb-type design.

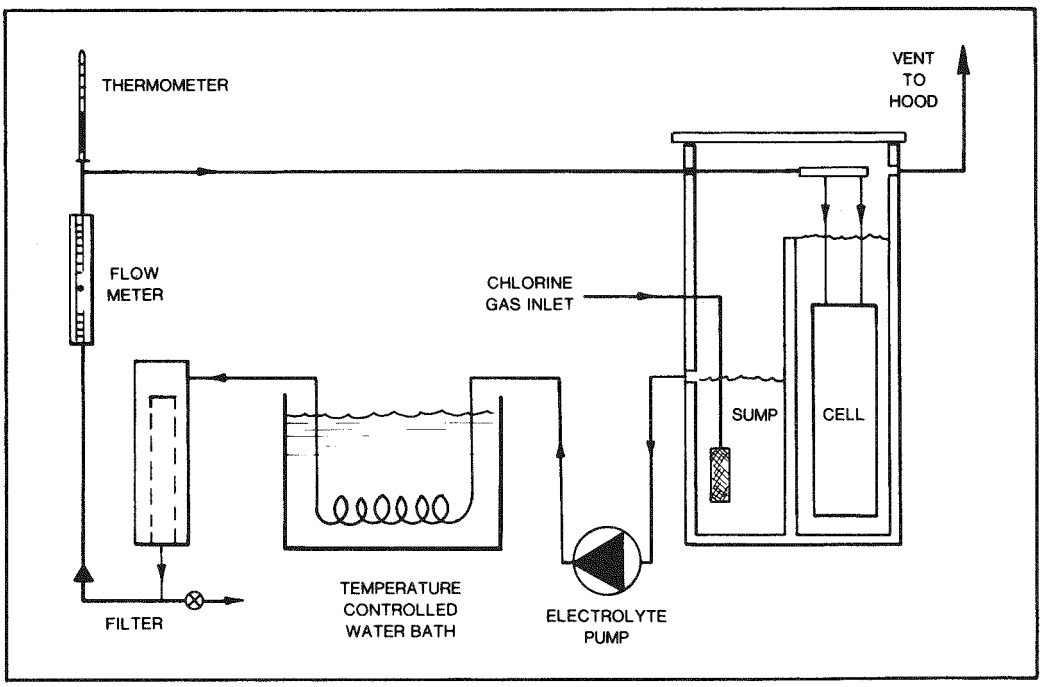

Figure 32-1. Schematic of test system for studying the electrolyte-static head and electrode-height effects.

Electrodes of three different heights (4", 6", and 8") were used to examine the electrode-height and the static-head effects on the electrochemical performance. Chlorine electrodes if sizes 4.000" x 2.625" x 0.080" and zinc electrodes of sizes 4.000" x 2.625" x 0.039" were used as the standard electrode size for comparison. The dimensions and structure of the 6" and 8" high electrodes are similar to the 4" high electrode with the obvious exception of being larger in the height dimension.

Referring to Figure 32-2, a fixed partition of 3.9", separating the sump and the test cell compartment serves to develop a 0.1" high overflow on the 4" high electrode. To regulate the electrolyte-static head as desired, an adjustable partition was added to the fixed partition to develop the overflow required. Experimentally, the exact height of the static head was measured by a scale made of titanium. Six static head heights, ranging from a low of 0.1" to a maximum of 4.1", were selected for evaluation.

All experiments were conducted under the standard test conditions as listed in Table 32-1. In order to minimize the experimental variables, supporting electrolyte

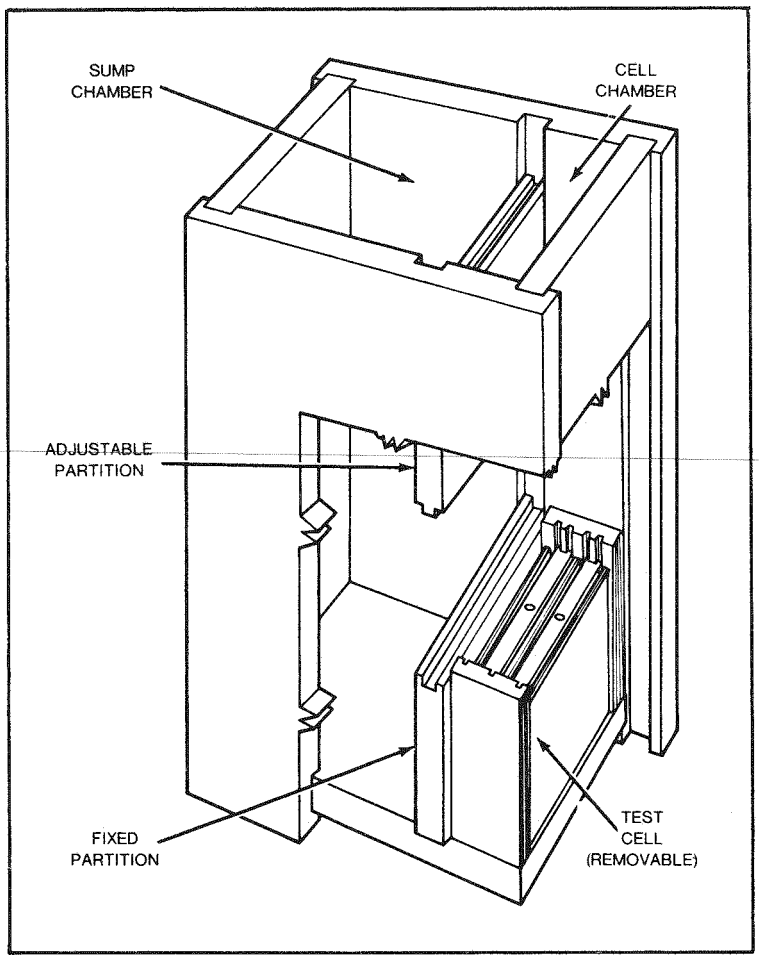

Figure 32-2. Test case showing the test cell, sump, and the use of an adjustable partition to develop the desired electrolyte-static head.

was not employed and the chlorine concentration was controlled at 2.4-2.5mg/ℓ during charge and 2.1-2.2g/ℓ during discharge by controlling the electrolyte temperature at 30°C ± 0.5°C. To ensure the height of the static head as the only variable parameter, all experiments were conducted using the same electrodes, the same electrolyte, and under controlled replicate operating conditions.

The shape of the voltage-time discharge profile and the round-trip coulombic efficiency at three current steps are used as the criteria for evaluating the effect of static head height.

Table 32-1

STANDARD OPERATING CONDITIONS

Charge:	4 hours at $30mA/cm^2$
Discharge:	a) One step discharge: to 0 volts at $30mA/cm^2$
	b) Three step discharge:
	1st step: $30mA/cm^2$ until $\Delta V_{dischg} = 60mV$
	2nd step: $20mA/cm^2$ until $\Delta V_{dischg} = 110mV$
	3rd step: $10mA/cm^2$ until $\Delta V_{dischg} = 0$
Chlorine Electrode Area:	4" electrode: $260cm^2$
	6" electrode: $390cm^2$
	8" electrode: $520cm^2$
Electrolyte:	Before charge: 2M $ZnCl_2$ (SpG = 1.21)
	After charge: 1.5M $ZnCl_2$ (SpG = 1.15-1.16)
	Total volume of electrolyte: approximately 1.5ℓ
pH:	Before charge: 0.20 ± 0.02
Temperature:	30°C ± 0.5°C
Flow rate:	$2ml/cm^2/min$
Cl_2 concentration:	Charge: 2.4 - 2.5g/ℓ
	Discharge: 2.1 - 2.2 g/ℓ

For the electrode heights of 4", 6", and 8", the voltage-time profiles and the round-trip coulombic efficiencies were measured with various static head heights. A three current step discharge process was employed for examining the static head effects on a 4" electrode. The first step discharge was held at $30mA/cm^2$. The discharge current was stepped down to $20mA/cm^2$ after reaching a voltage decline of 60mV, and stepped down further to $10mA/cm^2$ while reaching a voltage decline of 110mV. The cut-off voltage for the third step was set at zero volt. The discharge capacity (amp-min) was monitored using a digital coulometer and recorded at each step. Cell probe voltages were measured with a digital voltmeter and recorded on a strip chart recorder.

RESULTS

Effect of Electrolyte Static Head

Voltage-Time Profile vs. Static Head. The effect of electrolyte static head on the voltage-time profile was studied extensively in a 4" electrode cell employing static heads of 0.10", 0.30", 0.80", 1.80", 3.10", and 4.10". Figure 32-3 compares the three-step discharge profiles for static heads of 0.50" and 4.1". These profiles are identical in shape, indicating that the effect of static head on the shape of the voltage-time profile is not significant.

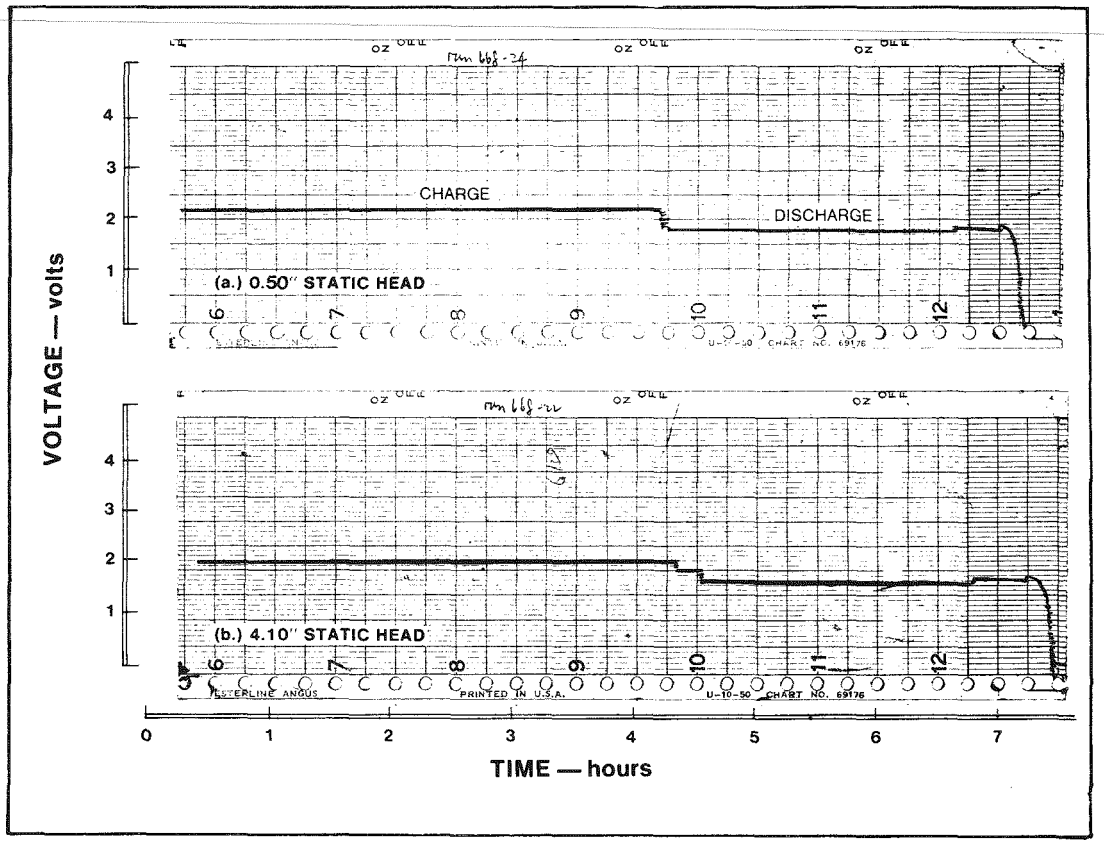

Figure 32-3. Voltage-Time Profile for 4" Electrode

For the 6" and 8" electrode cells, the static head effect was evaluated in constant current discharge mode, i.e. 30mA/cm^2. A comparison of the discharge profiles for a 0.38" static head and a 4.25" static head on a 6" electrode cell again shows no

effect due to static-head height. Similar results were obtained in an 8" electrode test cell.

Coulombic Efficiency vs. Static Head. The normalized coulombic efficiencies (defined as the accumulated coulombs at each discharge step to the total discharge coulombs) at the three discharged steps, i.e. 30mA/cm^2, 20mA/cm^2, and 10mA/cm^2, over a wide range of static head heights for a 4" electrode are tabulated in Table 32-2. With the chlorine concentration of 2.4-2.5g/ℓ during charge and 2.1-2.2g/ℓ during discharge, the total coulombic efficiencies are approximately 67%, independent of the static head height, and the effect of electrolyte-static head on the coulombic efficiency is insignificant. The normalized coulombic efficiency at each discharge step was also found to be independent of the electrolyte static-head height, within experimental error. The normalized coulombic efficiency at the third discharge step, i.e. 10mA/cm^2, is equivalent to the total coulombic efficiency.

Table 32-2

COULOMBIC EFFICIENCY VS. ELECTROLYTE-STATIC HEAD
FOR THE 4" ELECTRODE CELL

Electrolyte Static Head (inch)	Total Coulombic Efficiency (%)	Normalized Coulombic Efficiency (%)* at discharge step of: 30mA/cm^2	20mA/cm^2	10mA/cm^2
0.10	66.1	86.8	97.9	100
0.30	67.2	91	97.4	100
0.50	67.06	91	97.8	100
0.50	67.4	89	97.8	100
0.80	66.5	90.5	97.5	100
1.8	66.8	91.8	97.8	100
3.1	66.8	93	98.4	100
4.1	66.0	86.8	97.9	100
4.1	65.8	86	97.4	100

*Defined as the accumulated coulombs at the respective discharge step over the total coulombs.

Table 32-3

COULOMBIC EFFICIENCY VS. ELECTROLYTE-STATIC HEAD
FOR THE 4", 6", AND 8" ELECTRODE CELLS

Electrode Height (inch)	Electrolyte-Static Head (inch)	Total Coulombic Efficiency (%) at One Step Discharge 30mA/cm^2
4	0.30	67
4	0.30	67
6	0.38	67
6	0.38	67
6	4.25	67
8	0.38	68
8	0.60	66
8	2.50	66

Table 32-3 shows the total coulombic efficiencies obtained during constant current discharges, i.e. 30mA/cm^2, using various static head heights for the 4", 6", and 8" electrode cells. The effect of static head height on the coulombic efficiency was found to be insignificant at any of the three electrode heights.

Charge Capacity vs. Static Head. The effect of static head on the maximum charge capacity was determined for a 4" electrode cell. Under the conditions tested, the maximum capacity obtained lies in the neighborhood of 190mAh/cm^2, i.e. 6 hours charge at 30mA/cm^2, independent of the static heads of 0.10" and 4.10" tested.

Effect of Electrode Height

Voltage-Time Profile vs. Electrode Height. Generally, a voltage-time profile provides a good measure of the gross effect of electrode-height on the cell performance. Figure 32-4 compares the one step discharge profile for the 4", 6", and 8" high electrode cells. The discharge profile for a 4" electrode cell with a 0.30" static head is used as a standard for comparison. The discharge profiles for the 6" and 8" electrode cells show the usual characteristics of flat plateau and sharp tailing at the termination of discharge, and are essentially identical to that of the 4" electrode cell. These results indicate that an increase of electrode-height from the basic 4" to 6" and 8", i.e. a 50-100% area increase, causes neither a significant loss in voltaic performance nor maldistribution of current density.

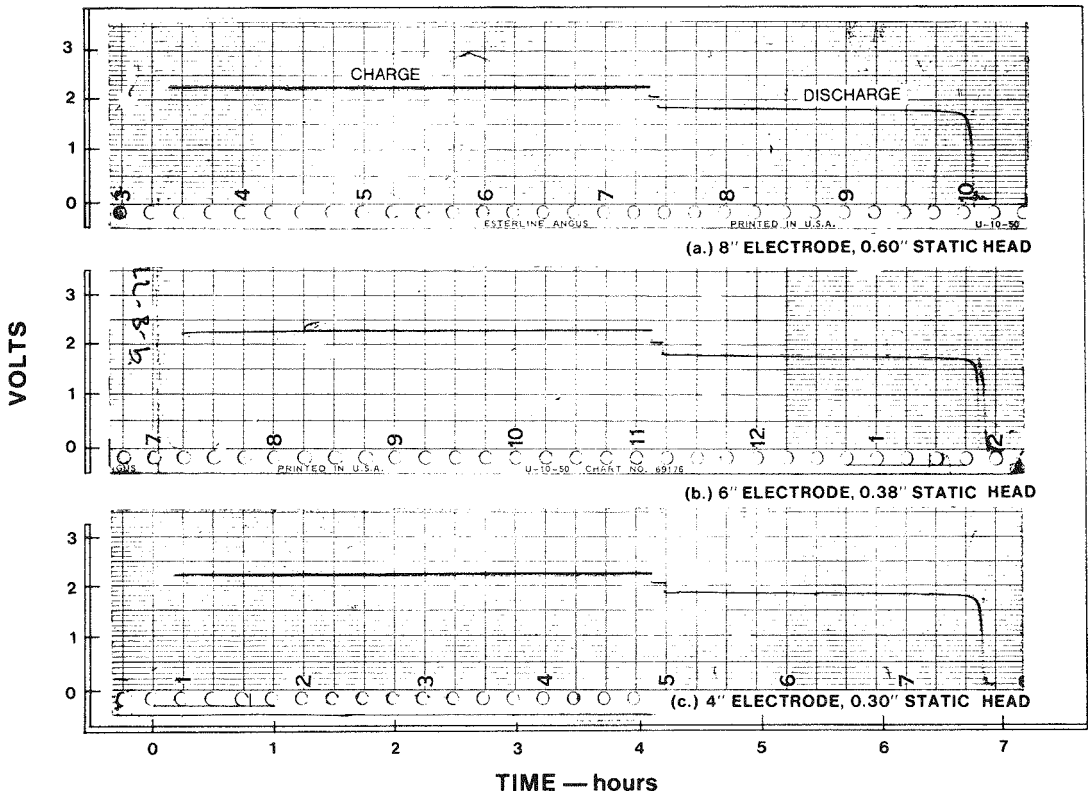

Figure 32-4. Voltage-Time Profile for Various Electrode Heights

Coulombic Efficiency vs. Electrode Height. The electrode-height effect on cell performance was also evaluated by comparing the coulombic performance of the 6" and 8" electrode cells to the basic 4" electrode cell. Table 32-3 compares the coulombic efficiencies of the 8", 6", and 4" electrode cells. The 8" and 6" electrode cells offer an average coulombic efficiency of 67%, which is similar to that offered by the 4" electrode cell. Within experimental error, it is concluded that no significant loss in coulombic performance is indicated up to an electrode height of 8".

Weight Distribution of Zinc Deposit

Under the standard test conditions, i.e. 2M $ZnCl_2$; 30mA/cm^2; T = 30°C; and 2.4-2.5g/ℓ of chlorine concentration, the zinc plates of the 4", 6", and 8" electrodes at a charge capacity of 120mAh/cm^2, i.e. 4 hour charge, were peeled from the substrates for weight analysis. Table 32-4 shows the weight of each zinc plate from the 6" electrode cell and the statistical analysis with reference to the electrode

Table 32-4

WEIGHT OF ZINC PLATE AT A CHARGE CAPACITY OF 46.66Ah

Plate No.	Weight (grams) 6" electrode
1_L (end plate)	10.360
1_R	10.7228
2_L	11.4147
2_R (end plate)	11.3321
Total weight	43.7756
Mean	10.9439
σ	0.5254
$\%\sigma$	4.8
Charge eff. (%)	77

The test cell had this electrode arrangement:

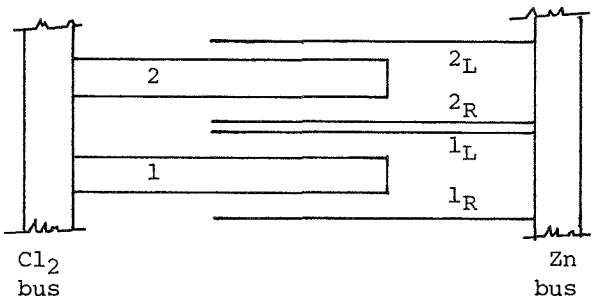

arrangement as shown. Based on the weight of four zinc plates, the percentage of the standard deviation is calculated to be 4.8. Figure 32-5 shows the weight distribution of 1/2"diameter zinc disks punched from 15 locations. The weight of the disks at the top plate appears to be slightly heavier than those at the bottom. This is probably due to the IR drops at the zinc bus as the current was introduced from the top. However, no corrosion loss of zinc at the top due to the expected higher electrolyte velocity was indicated. The weight distribution is identical to the 4" electrode, and is considered to be satisfactorily uniform. The corresponding zinc weight distributions for the four plates in the 4" and 8" electrode cells indicated respective standard deviations of 13.3% and 6.1%.

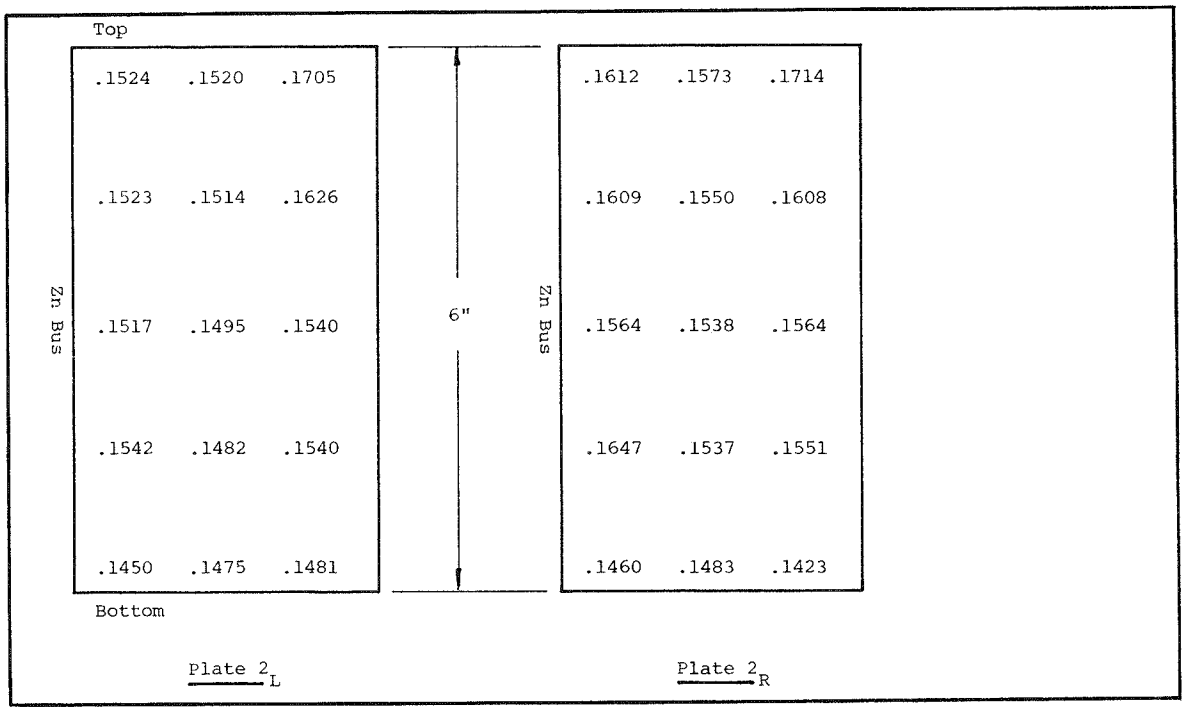

Figure 32-5. Weight of 1/2" Zinc Disk (grams) for a 6" Electrode

DISCUSSION

Electrolyte-Static Head Effect

In the operation of the zinc-chlorine cell, electrolyte flowing through the porous-graphite chlorine electrode is recirculated at a constant rate with the use of an electrolyte pump. Thus, electrolyte injected into the cavity of the porous-graphite chlorine electrode is forced to flow through the porous matrix due to the line pressure developed by the electrolyte pump. Flowing through a porous matrix is analogous to flowing through an orifice in which a pressure drop develops due to the flow resistance along the pore. The uniform resistance of the pores enables electrolyte to flow uniformly through the entire electrode. The uniformity of the flow distribution through the chlorine electrode is primarily controlled by the characteristics of the pores and, from this point of view, static head should not affect cell performance by influencing flow distribution uniformity.

However, the static head height can affect the flow pattern at the top of the electrodes. Under the present stack design, the up-flowing electrolyte, accumulated as a semi-quiescent liquid, changes direction and flows horizontally towards the drain cup leading to the sump. If the static head is too small, i.e. under-size, a significant amount of turbulence could develop at the top of the electrodes causing

additional chemical corrosion of zinc at the top plate. For larger static heads, the up-flowing electrolyte, mixing with the more quiescent fluid, will cause less turbulence which could result in less chemical corrosion of zinc at the top plate.

From the results, it is concluded that the effect of electrolyte static head on cell performance is not important. The operation of zinc-chlorine cells requires very little static head. However, the presence of a small static head is essential to ensure that the electrodes are fully immersed in the electrolyte.

Electrode-Height Effect

In the operation of zinc-chlorine cells, the electrolyte flow rate per unit area of electrode is kept constant. The liquid head pressures caused by increased electrode heights are insignificant in comparison to the pressure drop in the feeder tubes and pressure drop through the electrodes. Increasing the electrode height increases the electrolyte velocity at the top of electrodes. Even doubling this velocity by doubling the height from 4" to 8" did not appear to affect the electrochemical performance. Cells with 6" and 8" high electrodes offered similar coulombic efficiencies and similar voltage time discharge profiles as compared to the 4" electrode cells.

For a given chlorine concentration (g/ℓ), the chlorine flux ($g/min\text{-}cm^2$) is higher at the top plate than the bottom due to an electrolyte velocity difference. It is generally accepted that chemical corrosion at the zinc plate is due to the attack of dissolved Cl_2. Since the rate of chemical corrosion of zinc is a function of the chlorine flux, the corrosion rate at the top of an 8" electrode is expected to be higher than that of a 4" electrode. However, this behavior was not observed experimentally. Under the operating Cl_2 concentration of 2.4-2.5g/ℓ, the distribution of deposited zinc at a 6" and 8" electrode are satisfactorily uniform indicating no baring of zinc at the top plates, and is essentially identical with the 4" electrode.

One possible explanation is that doubling the average electrolyte velocity in the inter-electrode gap, by doubling the electrode height, does not significantly alter the diffusion layer thickness adjacent to the zinc electrode. This diffusion layer thickness being essentially unaffected will result in similar corrosion rates and coulombic efficiencies for all three test cells.

Section 33

SELECTION AND QUALIFICATION OF PLASTICS

INTRODUCTION

Plastics are used in the zinc-chlorine ($ZnCl_2$) battery system for the battery case, electrode frames, pipes, masks, and manifold components. Continuing efforts are being made to specify materials that resist the corrosive chlorine environment and that do not release detrimental contaminants into the battery electrolyte. The criterion for qualifying plastics materials for use in battery fabrication is based on three primary factors:

1. The chemical properties of the material, i.e. additives, elemental analysis
2. The physical properties of the material, i.e. flexural and tensile strengths
3. The economics, i.e. material and fabrication costs to produce end-item components for the battery system

During 1977, areas of study were channeled into the evaluation and specification of explicit generic groups. Extensive work was performed to develop a stable polyvinyl-chloride formulation. In fact, two polyvinyl-chloride compounds have been found which appear inert in a chlorinated zinc chloride environment. Presently, both are undergoing electrochemical evaluation for extensive use in battery fabrication. Several advantages could be gained by using polyvinyl-chloride (PVC) instead of the Kynar (polyvinylidene fluoride) currently used. Of utmost importance is the drastic reduction in material cost. This factor is reinforced by the fact that PVC can be solvent-bonded very satisfactorily, machines much more easily than Kynar, and exhibits less cold flow characteristics.

Numerous polyester formulations have been evaluated. A specific resin with specified glass components was found to be stable in the screening test system. The specified polyester formulation presently is being electrochemically evaluated in the materials cycling cells, but results are not conclusive yet. The development

group has constructed an 8.3kWh module case from this polyester to evaluate the material, per se, in direct contact with the zinc chloride electrolyte and hydrate in an operating battery.

Eighteen polyethylene samples have been screened. Polyethylenes are easily injection-molded and low in cost. This makes them suitable for fabrication of the frames, masks, and manifold components. A high density compound appears more stable than lower density formulations, however blistering is still observed. Various formulations have been evaluated in hopes of finding one which does not blister but, as of yet, none have fully met this requirement.

Viton, an elastomeric material, has great application as a gasket material in the battery. Vitons are normally cured with metal-oxides which could lead to possible contamination of the electrolyte. Studies are being conducted to determine the stability of double peroxide-cured Vitons which would eliminate the formulation of metal oxides. Perfluoroelastomer compounds were also evaluated for gasket applications.

A variety of other materials were evaluated for possible application in the battery. A Nylon tubing and three flexible lined-PVC tubings were evaluated and all were found unsuitable. Polyethersulfones and several polypropylene formulations also were unstable in chlorinated zinc chloride. A number of Armalons* and possible substitutes were evaluated for use as the filter materials. An Armalon formulation, presently used in operating systems, shows a distinct color change upon exposure to the hydrate and/or zinc chloride. A lower-cost alternate was qualified during Phase I.

TESTING METHODS

In order to make the zinc-chlorine battery commercially feasible, low-cost plastics must be qualified for use as the battery casing and for component parts. These plastics must not only resist the corrosive effects of zinc chloride saturated with dissolved chlorine gas, but also they must not release contaminants into the battery electrolyte which would adversely affect efficient battery operation. Thus a development and specification program was organized to find suitable materials for this application. A program to screen numerous materials in a chlorinated zinc chloride environment was prepared according to ASTM D543, Test for Resistance of

---

*DuPont tradename

Plastics to Chemical Reagents. If a material was satisfactorily inert in this initial test, electrochemical evaluation was pursued within an electrochemical cell. An outline of the screening test and the electrochemical test follows.

Screening Tests

The American Standard Testing Method D543, Test for Resistance of Plastics to Chemical Reagents, was used as a model in setting up a system to screen a large number of materials. A set of test parameters was selected and maintained throughout this degradation testing in order to produce comparable data. Screening tests were performed using the system shown in Figure 33-1.

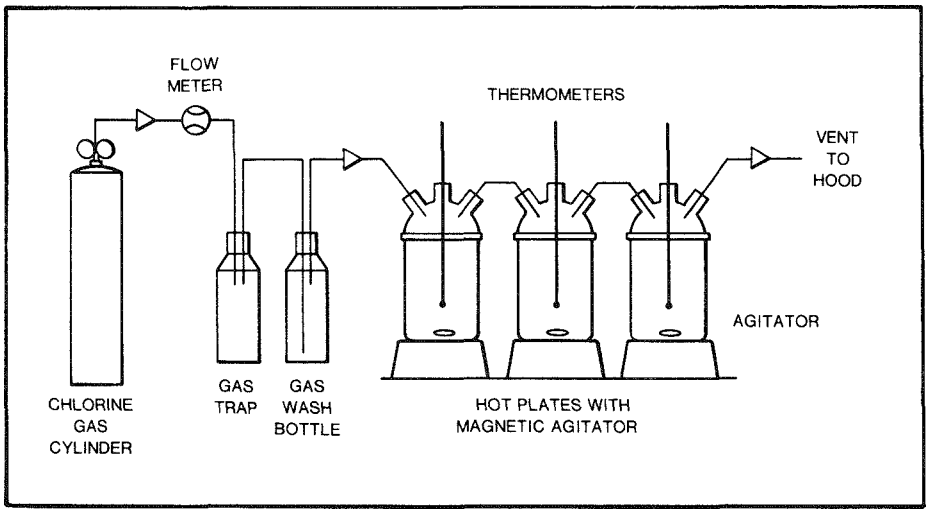

Figure 33-1. Diagram of laboratory system used for initial chemical screening tests. Note that sample bottles are arranged in series.

Standard testing parameters were selected with regard to the various conditions of battery operation. All plastics were viewed microscopically and photographed prior to any degradation studies. Initially, all test specimens were exposed to chlorinated zinc chloride (30% solution, pH 1.0) for ∿30 days at ambient temperature. Whenever the specimens and their test solutions appeared unaffected by this initial exposure, the temperature was increased to 50°C and the tests continued for an extended period of time.

Selected measurements were made on each test material and the test solution to determine any degradation. These physical measurements included weight and dimensional changes, blisters/mm^2, surface area, and blister diameter for each test specimen. Changes in the specific gravity and pH of the zinc chloride also were recorded. An atomic absorption analysis of the test solutions was made to check for any leached-out components. Total organic carbon analyses were performed on some test solutions of promising materials to determine the occurrence of any breakdown of the carbon chains. If samples appeared inert in these screening tests at 25°C and 50°C, each was electrochemically evaluated.

Some testing also was conducted in wet chlorine gas and chlorinated water. A program which monitors the change in pH of distilled water, aqueous zinc chloride, and acidic water in relation to the absence and presence of materials also was pursued using the same test system. Further studies in this area are to be conducted during 1978.

Electrochemical Tests

The purpose of the electrochemical evaluation program is to qualify a material for use in the battery. Materials that are evaluated in this program already have undergone extensive screening in chemical tests and are believed suitable. The electrochemical test is the final evaluation made on a material prior to its more widespread use as a battery construction material.

The critical nature of this work demands that extreme care be taken in the operation of the test cells. The introduction of external impurities cannot be tolerated. Test results alone may well determine the acceptance or rejection of a material. For this reason, testing must be an accurate measure of the behavior of the material.

Figure 33-2 illustrates a typical standard test cell used for electrochemical evaluation. These cells were operated until "normal" cycles could be achieved using the following cycling parameters.

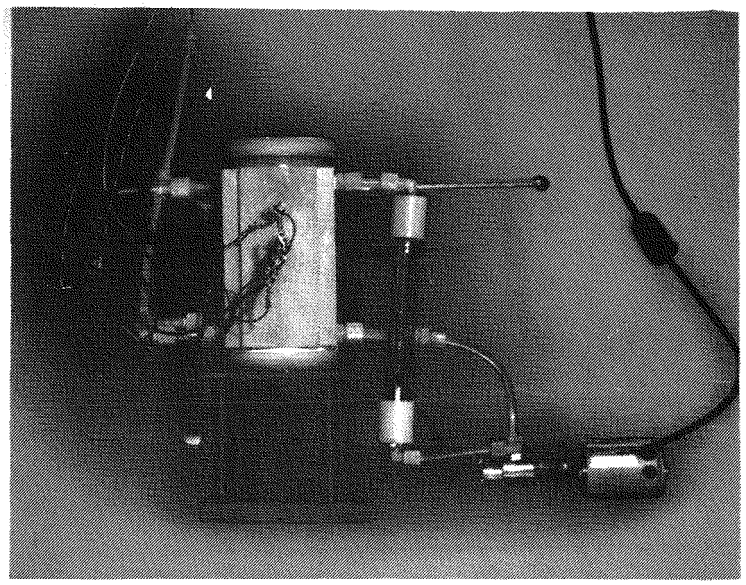

Figure 33-2. Typical electrochemical cell system for use in materials evaluation.

A. Electrolyte
   - 3M $ZnCl_2$ + KCl + NaCl
   - specific gravity: 1.40 ± .02
   - pH: 0.00 - 0.10
   - ∿500ml volume per cell

B. Charge
   - 7.1 amps for 4 hours (28.4mA/cm^2)
   - 2.19 ± 0.02 volts
   - ambient temperature and pressure
   - no chlorine introduced

C. Discharge
   - $ZnCl_2$ saturated with chlorine ∿3 minutes prior to starting discharge
   - 6.9 amps (27.6mA/cm^2) until cell voltage drops to 500 millivolts
   - ambient temperature and pressure

D. Overnight
   - battery shorted following discharge
   - slow chlorine flow rate
   - add ∿100-150ml distilled water to compensate for evaporation

After "debugging" the cells, fresh electrolyte was put into each cell. Extreme care was taken to minimize contamination of the electrolyte and cells. The electrolyte was circulated over zinc rods to remove any metal impurities. Samples were retained for atomic absorption analysis. The cells were then cycled daily and data recorded until relatively stable cycles again could be achieved, then various test materials were placed into the cells for evaluation. Records specifying the plastic parts in each cell, made from materials other than Kynar and Teflon, were recorded together with cycling data. One of five cells was retained as a control. The cycling data from this cell, constructed entirely from Kynar and Teflon, was used as the base line for comparison with cells containing test materials. Initial electrochemical evaluation consists of cycling the test cell with spacers and electrode masks made from the materials to be evaluated. The spacers provide a large surface area for exposure to the electrolyte in close proximity to the chlorine sparger and heating element. The masks serve to expose the material to the most active electrochemical treatment within the cells. This is illustrated in Figure 33-3. Gas analysis for N_2, O_2, H_2, and CO_2 is taken daily during charge cycles as is the pH variation. Any adjustments made to the electrolyte are recorded. Usable coulombic efficiencies for each cell are plotted against cycle number. Atomic absorption and total organic carbon analysis are made periodically to determine leaching and to indicate possible breakdown of the polymer chains. If cell cycling data does not deviate extensively from the control baseline after a test material has been implemented as masks and spacers, an entire cell is constructed from the material and is cycled for 100 data cycles using the same parameters.

Final conclusive qualification of any new material is difficult because of the many interrelated operating factors within a battery. Time-in-service is the only true test. During the Phase II program all data will be analyzed pertaining to those materials that have successfully completed the screening and the electrochemical test. This statistical and numerical analysis together with careful interpretation should permit identification of commercially acceptable battery construction materials.

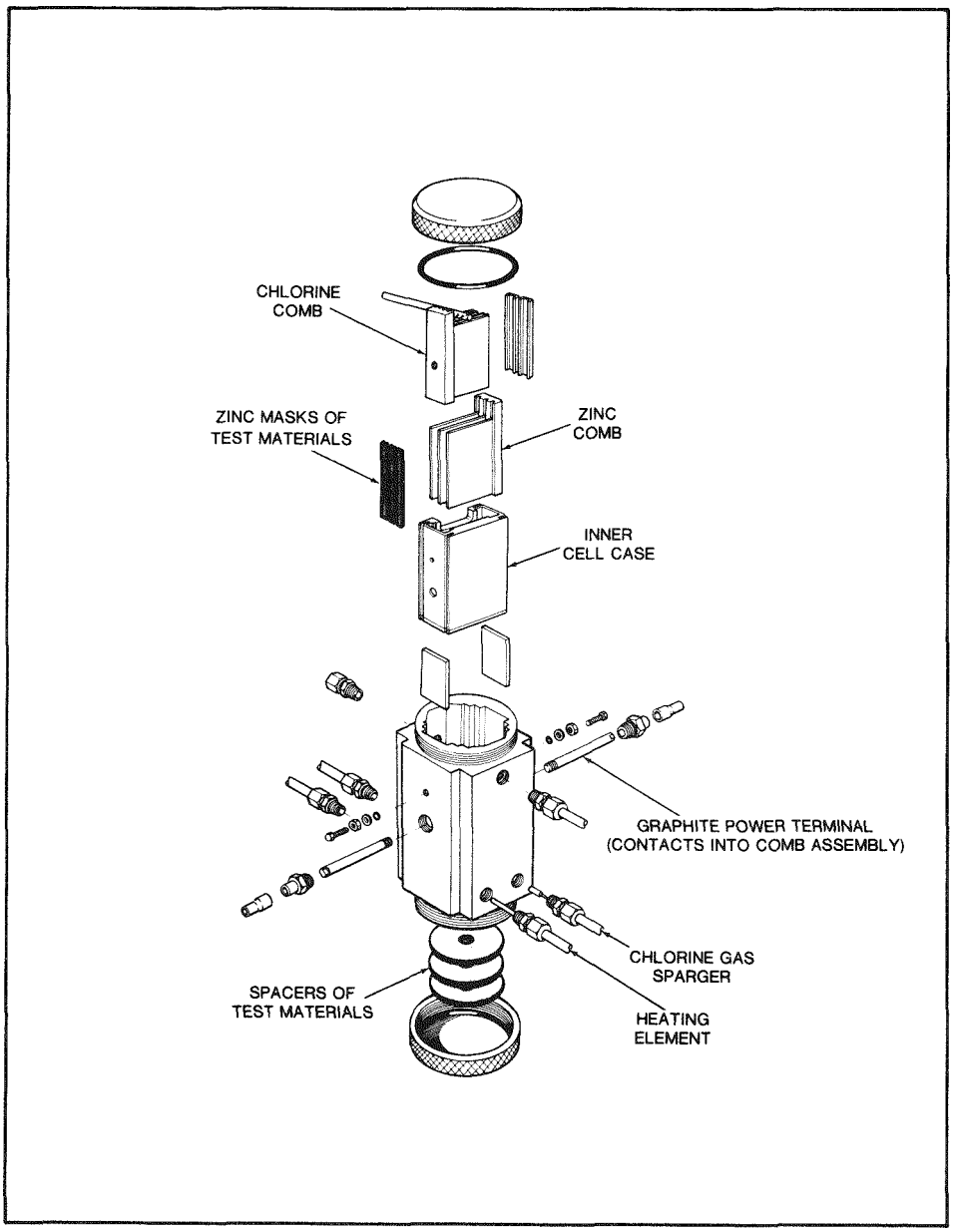

Figure 33-3. Exploded view of test cell used for electrochemical evaluation of materials. Note location of spacers and masks fabricated from test material.

POLYVINYL CHLORIDE

Two polyvinyl chloride (PVC) compounds which are stable in the chemical environment of the zinc-chlorine battery have been specified. Presently both are being electrochemically evaluated. Many different PVC formulations are possible by virtue of the various additives. Because of the large number of PVC samples evaluated, the screening test results are discussed below in general terms.

Polyvinyl chlorides are thermoplastics derived from vinyl monomers (CH_2-CHCl). These resins are produced by free radical-polymerization in bulk, suspension, emulsion, or solution systems. Two of these polymerization methods were evaluated in the PVC samples screened. It was determined that the stability of the resin was affected simultaneously by mode of polymerization and subsequent formulation. Different additives for a bulk-and suspension-prepared resin are required for stability in the $ZnCl_2$ system. A CPVC resin was also considered, but processing difficulties and instability in zinc chloride made further development unnecessary.

Polymerization temperature is the primary control used to vary resin molecular weight, which in turn affects processing. Polyvinyl chlorides require stabilizers (i.e. metal soaps of Pb, Cd, Ba, Ca, Zn, Sn) to prevent heat degradation during this processing. Lubricants are added to facilitate melt flow during processing by internal reduction of intermolecular forces between polymer chains, and/or external reduction or adhesion to metal surfaces of processing equipment. Processing aides, fillers (i.e. TiO_2, $CaCo_3$, carbon), mold release agents, and plasticizers may also be added to polyvinyl chlorides.

The initial screening tests of the two specified polyvinyl chlorides at both 25°C and 50°C showed no blistering whatsoever. Atomic absorption analysis indicated no contamination coming from the PVC compounds. Therefore, electrochemical evaluation was made on both PVC compounds. Cells were assembled which contained specified surface areas of both PVC compounds as spacers and masks. During the test program routine measurements of gas evolution (CO_2 and H_2), electrolyte pH, and specific gravity, temperatures, and cell-operating voltaic and coulombic efficiencies are recorded. Near the end of this Phase I program the data from one of the two test cells appeared no different from data acquired with the baseline established with an all-Kynar cell. Therefore, an entire cell was constructed of this specific PVC material and was placed in operation. A number of PVC components also were installed in development cells of other programs. To date, no problems have been encountered which can be attributed to these materials. However, at this

time, insufficient consistent data has been obtained to form firm conclusions. No definite baselines can be yet established for the control, thus it is not possible to attribute day-to-day variations in cell operations to any one of the materials in test.

In order to account for future commercial needs for the zinc-chlorine battery, injection-molding and vacuum-forming compounds of this same PVC formulation have been ordered. An increase in the stabilizer and an addition of lubricant to the formulation will be necessary for an injection-molded compound. Necessary injection-molding data has been requested. Extruded test samples of this slightly different material have been requested and received. Welding rod for bonding and Schedule 80 pipe (1" and 2") and fittings are available in-house. In order to assure proper fabrication of injection-molded and vacuum-formed parts, manufacturer's representatives will be asked to supervise initial fabrication efforts.

POLYESTER

Glass-reinforced polyester is another low cost material that has been developed. Numerous resin types, including vinyl esters, were evaluated. A corrosion-resistant resin was found to be the most stable polyester in the battery environment. The importance of the glass-reinforcing component is also recognized. Various glasses have been examined to determine their physical and chemical resistance characteristics. From the screening test and electrochemical test data acquired to date, a specified polyester resin and glass composite has been formulated.

Due to the unique composition of glass and resin in a polyester laminate, different modes of degradation were observed in these compounds. There are five main corrosion mechanisms seen in polyester formulations:

1) Blistering - polyester resins usually exhibit macroscopic raises in the surface unlike the microscopic blistering observed in most other generic resin types.
2) Delamination - separation of resin and glass layers.
3) Discoloration - a brown or charred-black discoloration is most common; may be a thermal or chemical reaction.
4) Wicking - flaking of resin due to seepage of water molecules into the resin along the fibers; appears as microscopic pin holes on the surface with flaking in the generalized area.
5) Resin attack - physical breakdown of resin; may appear as tiny blisters.

Three physical faults also may be observed in a polyester compound as a result of improper fabrication technique and poor quality raw materials:

1) Jack strawing - the resin pulls away from the glass during the curing process, thus leaving exposed glass and voids for the migration of the zinc chloride solution into the test sample. This fault can be attributed to a) poor glass quality, b) inconsistency of silane sizing agents on the glass, or c) incompatibility of the resin with the glass.

2) Initial air inclusions in the cured polyester - often used as a basis for accepting or rejecting a shipment. These air inclusions can encourage other forms of degradation. The presence of air inclusions could occur due to poor quality glass or improper fabrication techniques, i.e. room temperature too cool. This problem can be remedied by the addition of 2-3% styrene to the resin and/or slight warming of the resin.

3) Air inhibition - appears as a whitish surface haze. If an already cured polyester laminate is recoated with resin on the inner mold surface following initial lay-up of the form, this defect may be observed. Adding a 1% additive to the resin of 5% paraffins in styrene followed by post curing can prevent this.

Fabrication techniques for the battery components have been considered in the evaluation of polyesters. Polyesters can be injection-molded provided changes are made in the glass reinforcement. Vacuum-molding techniques are possible using the same composition as the EDA test material. A bulk molding compound would be developed for compression-molded parts. Chopped glass fibers and specific fillers would be used. Hand lay-up techniques also could use the same polyester formulation being tested at EDA. This technique was recommended for fabrication of the manifold pipe so that a veil could be used to line the interior wall. Larger diameter pipe could be filament-wound using the same formulas. Pulltursion is another available fabrication method. It would not be possible to use a veil with this method, however.

Polyesters can be machined using carbide cutting tools and saw blades. Large machined areas to be exposed to the zinc chloride soltuions should be masked with a resin layer and cured prior to service use. This technique would minimize contamination from any exposed glass. Polyester bonding techniques also have been studied. As a general rule such bonds are not reliable and should be engineered out of the construction.

There is, at present, an on-going electrochemical testing program to evaluate the glass-reinforced polyester compound. An 8.3kWh submodule battery case and related store components were built of this material. Data from operation of this system will be used to reach a decision on the acceptance of polyesters.

POLYETHYLENES

Another compound showing promise for use as the battery case material is a high density polyethylene. Such compounds are prepared by a coordination catalyst method under low pressure, <1500 psi, polymerizations. This produces a linear product with very few side chains, and densities of 0.955 to 0.970 g/cc. The greater stability of the high density polyethylenes is attributed to the decreased branching and thus decreased availability of ethyl and butyl groups for reaction. The main polymer structural features which influence the properties of polyethylene are: degree of branching in polymer, average molecular weight, and molecular weight distribution. The increase in density improves the tensile strength, hardness, and chemical resistance; as well as lowering permeability of the compound to liquids and gases. Higher molecular weight compounds also have improved chemical and impact resistance. However, they are harder to process because of their higher melt viscosities. A polyethylene compound could be used most easily for injection-molding. Its low cost and mechanical properties, particularly weldability, make it an attractive alternate to Kynar.

Studies to date, using an extruded polyethylene formulation, continue to show some occurrences of blistering. Through the cooperation of the manufacturer, testing is planned for a formulation using higher levels of a single stabilizer of low volatility. Various other possible causes of this blistering have been pursued.

VITONS AND PERFLUOROELASTOMERS

The major effort in the area of materials has been directed toward the development and qualification of the rigid plastic components in the battery. There are, of course, non-rigid components to be considered as well. These include the gasket and filter materials, and flexible tubing. Viton* fluoroelastomers are presently being used in the laboratory for gasketing. Two types of Viton are available: Type A and Type B. Viton A is a copolymer of vinylidene fluoride and hexafluoropropylene. Viton B is a terpolymer of vinylidene fluoride, hexafluoropropylene,

*DuPont Trademark

and tetrafluoroethylene (TFE).

There also has been some interest in the perfluoroelastomers (Kalrez) which are, in essence, low temperature Vitons. Kalrez compounds are terpolymers of tetrafluorinated ethylenes, perfluoromethyl vinyl ether (PVME), and PVME groupings. However, these are very expensive materials at present and this factor has influenced further development of the Vitons over perfluoroelastomers.

Initial evaluations of Viton O-rings in service in the zinc-chlorine battery have shown a loss in elasticity and stress cracks in the elastomer. Also of concern is the fact that most Vitons are amine and/or metal oxide cured, indicating the possible leaching of metals. Nine various Viton and Kalrez formulations were evaluated in the screening tests. Table 33-1 summarizes this test data arranged in ascending order of reactivity.

OTHER MATERIALS

Numerous other materials have been screened besides those mentioned above. These materials include three epoxy compounds. A graphite fiber-filled epoxy compound was investigated for reinforced-case material applications and the epoxy severely degraded. However, the graphite fiber cloth appeared stable. Physical degradation also occurred in two epoxy pH electrode assemblies. Thermoplastic polyamide resin, (Nylon) and polyurethane were evaluated and both were found to be completely unstable in the zinc-chlorine environment. Further studies of polyimides were not pursued during this past year due to their high costs. Although polysulfones previously had been studied and found unstable, a modified polyethersulfone was tested and it reacted with chlorinated zinc chloride in much the same manner as other polyethersulfone, but with more heavy metal contamination.

The low cost and moldability of polypropylenes encouraged further investigation of this generic group. High-density and glass-filled compounds were evaluated for casing and frame applications, as well as a TFE film on non-woven polypropylene laminate, for possible use as a filter cloth. All of these formulations reacted in the chlorinated zinc chloride environment. The possibility was considered that impregnating a stable compound into a polypropylene formulation would lend stability to this group. However, a TFE-impregnated polypropylene also showed crazing

Table 33-1

EVALUATION OF FLUOREOLASTOMES

EDA Code	Description	Test Results, Comments
PF 2	Kalrez perfluoreolastomer #1045 - TiO_2 filler with Mg added to improve compound acid resistance.	No apparent physical degradation. Low levels Fe and Ca with higher levels of Ca in solution. This is an expensive compound.
PF 1	Kalrez perfluoroelastomer #1050 - carbon-black filler with Pb added to improve compound acid resistance.	A.A. showed Cu+Fe; and high levels Pb, Mg, Si, and Ca.
V-7	Peroxide cured Viton GH terpolymer.	Fading of color observed but no excessively high levels of elements noted in solution. The pH rose to 3.40.
V-6	Double peroxide cured Viton GH terpolymer.	Fading in color observed, but no excessively high levels of elements noted in solution. The pH rose from 1.0 to 3.28 at 50°C.
V-5	Peroxide cured Viton #VT-R-4590 terpolymer	No apparent physical change and pH stable. High levels of Pb noted in solution.
V-4	Peroxide/metal oxide cured Viton GH #0103-87365 terpolymer.	No apparent physical change observed though high levels of Ca and some Pb noted in solutions. The pH increase of 1.0 4.2 observed at 50°C.
V-3	Fairprene* VT007 (Viton over TFE cloth).	A weight increase of 69.3% was observed at 50°C in chlorinated $ZnCl_2$ along with pronounced expansion of sample. High UNSUITABLE levels of Fe, Mg, Pb, Si, and Ca in solution.
V-2	Litharged Viton copolymer.	Chlorine gas appears to have pitted surface of sample.
V-1	Pink colored Viton.	Viton turned yellow in color. UNSUITABLE.

* Fairprene is a DuPont tradename.

and etching of the surface upon exposure to chlorinated zinc chloride.

Seven more adhesive compounds were evaluated during 1977 with the concept of glued electrodes in mind. None of these new adhesives appeared to be sufficiently more stable in chlorinated zinc chloride than the Lucite adhesive previously evaluated. Some studies were conducted on ceramic-type compounds, but were not pursued to any great extent at this time due to the high-level leaching of numerous elements (Mg, Fe, Si, Pb) into solution.

A graphite fiber cloth (G-16) was tested for use as filler in a polyester resin. This material was in a woven fiber-mat form. There did not appear to be any notable physical degradation of the graphite cloth. A graphite gasket tape material (G-18) also was evaluated. The pressed graphite appeared to bubble up and to expand somewhat. Definite weight increases were noted, but little leached contamination was observed.

The present use of Kynar and Teflon as battery components has made it continually necessary to evaluate various types and compositions of these two relatively stable compounds. Numerous formula variations of each have been evaluated. A Kynar-encapsulated stainless steel rod (K-5) was evaluated but inconsistent data was recorded due to the inability to seal off the exposed stainless steel end. A Kynar-glass laminate showed a definite weight loss and excessive leaching of iron, chromium, magnesium, silicone, and calcium. A Kynar filter screen appeared quite inert in chlorinated zinc chloride, compared to a polypropylene filter screen. Halar (E-CTFE) was considered as a laminate despite its relatively high cost. A Halar film sample (Te-5) was screened extensively at both 25°C and 50°C. These tests indicate that Halar is relatively stable in chlorinated zinc chloride. Only at 50°C did the surface become slightly etched. A Halar coated fiberglass (Te-10) appeared quite stable in the test environment.

Numerous fluorocarbon materials have been evaluated as possible filter cloth materials. Presently Armalon* is being used as a filter material in the hydrate store. Bleaching of the brown color is noted but no ill effects or further degradation have been encountered. Nonetheless, alternates showing no change were pursued. A low-cost substitute for Armalon* was qualified for use as a filter cloth.

DISCUSSION

The plastic materials qualification program of Phase I has added two polyvinyl chlorides (PVC) and a glass-reinforced polyester compound to the list of approved construction materials for zinc-chlorine batteries. These materials continue to

*DuPont Trademark

be electrochemically tested. Their use should now be expanded into fully operational battery systems. Only long term, in-service use of these materials finally can qualify them. However, it is of primary concern that only specified materials be employed and that they are properly fabricated and implemented for the intended use. Records should be maintained of how and where these new materials are introduced into future systems. It is expected that use of these alternate materials will bring about design and engineering changes in the components affected. Table 33-2 was prepared to assist in an orderly changeover. It compares the mechanical and thermal properties of potential compounds with more familiar materials.

Table 33-2

PROPERTIES OF POTENTIAL $ZnCl_2$ BATTERY MATERIALS

	Polyvinylidene fluoride [c] KYNAR®	Tetrafluorindated ethylene TEFLON®	Polyvinylchloride (bulk & suspension resins) PVC	Unsaturated Polyesters (+ 25% glass) FRP	High Density POLYETHYLENE	Elastomer [b] VITON®
APPLICATIONS	Case Material Structural Members	Tubing	Case Material Structural Members	Case Material	Case Material Structural Members Tubing	Gaskets, Seals 'O' Ring
COST $/lb resin [a]	$5.50	$5.00	$0.27	$0.36 (No Glass)	$0.31	$13.00 (Raw Resin)
MECHANICAL PROPERTIES						
Specific Gravity ASTM D-792	1.75 - 1.78	2.14 - 2.20	1.30 - 1.58	1.66 - 2.10	0.95	1.88
Hardness - Shore D ASTM - 785	80	50 - 55	65 - 80	51 (Barcol)	65	80 Shore A
Mold Shrink in/in	0.030	(extruded)	0.001 - 0.005	0.001 - 0.004	0.02 - 0.05	0.025 - 0.035
Tensile Strength ASTM D-638; 36°C; psi	5,500 - 7,400	2,000 - 5,000	6,000 - 7,500	11,500	3,300	>71,200
Flexural Modulus ASTM D-790; 34°C; psi	1.7 x 105		3.7 x 105	8.6 x 105	1.7 x 105	600
Flexural Strength ASTM D-790; psi		Did not break	10 - 16,000	18,000		
Compressive Strength ASTM D-695; 36°C; psi	8,680	1,700	8,000 - 13,000	22,000	2,700 - 3,600	60 ASTM D-575
Izod Impact Resistance ASTM D-256; notched Ft. lb/in.	3.8	3.0	15.0	7.0	2.0	
THERMAL PROPERTIES						
Heat Distortion Temp. ASTM 648; 66 psi	127 - 142°C	118°C	77°C	177 - 236°C (264 psi)	73°C	283°C
Thermal Coefficient of Expansion ASTM D-696 in/in/°C	8.5 x 10-5	10 x 10-5	5 - 10 x 10-5	2.0 x 10-5	12 x 10-5	8.8 x 10-5
Flammability	Self-extinguishing	Non flammable	Self-extinguishing	Flammable	Flammable	Flame resistant
STATUS	In use	In use	Electrochemical Evaluation	Electrochemical Evaluation	Development	Development

SOURCE: Modern Plastics Encyclopedia except as noted

a Chemical Marketing Reporter Feb. 27, 1978

b DuPont

c Pennwalt

Due to large volume applications, the use of polyvinyl chloride and polyester will be important in reducing the cost of battery fabrication. Continued development of polyethylenes will provide another low-cost material for these same frame, mask, and tray applications. The proposed elastomeric compounds for both gasketing and O-ring seals are very similar to commercial materials and will have little effect on the total battery cost.

Section 34

ELECTROLYTIC ACTIVATION OF POROUS-GRAPHITE CHLORINE ELECTRODES

INTRODUCTION

The electrochemical energy efficiency of the zinc-chlorine battery is dependent upon the voltaic efficiency of the battery. Hence, any increase in electrochemical activity of the chlorine electrode will be realized as increased energy efficiency of the entire battery.

Until recently, the electrochemical activity of the chlorine electrode was enhanced or improved by a thermal nitric-acid treatment. In this process, porous-graphite chlorine electrodes are heated in a nitric acid bath at ∿112°C, for 10 to 21 days, depending on the degree of activity required. Although electrodes treated for longer periods of time perform better voltaically, this increase must be weighed against the increased time and cost, and a weakening of the electrode. The degree of weakening depends upon processing time.

Certain inherent weaknesses in this process are apparent. Processing large numbers of electrodes for the larger batteries would necessitate the purchase of processing equipment and facilities. The process also increases probability of damage during battery assembly as handling of the weaker, activated electrodes is necessary.

In light of these facts, it has long been a goal of the EDA-EPRI program and the goal of this project to find an activation process which could be accomplished in an assembled battery. Development of such a process would preclude the large expenditure of capital and the handling of "activated" electrodes. Much work has been directed in recent years toward this end.

The only feasible process to date is electrolysis. This consists of passing an electric current through an electrode (anode) in an appropriate electrolyte. The only applicable electrolyte known prior to this study has been nitric acid.

However, there are certain disadvantages to using nitric acid. Contamination problems associated with filling the battery with nitric acid are obvious. Moreover, the chlorine electrodes are noted to bow; warping to the point of short-circuiting the cell if electrolysis is not terminated at the appropriate time. This warping is due to electrode growth, postulated to be caused by intercalation of a species from the nitric acid into the graphite lattice of the electrode (34-1).

During 1977, a breakthrough in electrolytic activation was accomplished. It was found that if dilute aqueous zinc chloride is used as the electrolyte and if the electrolysis time is increased by an order of magnitude over the nitric acid-electrolytic technique, electrolytic activation is possible which is voltaically equivalent to that using nitric acid. The contamination problems are eliminated. More importantly, very little electrode growth occurs when the dilute $ZnCl_2$ electrolyte is used.

This breakthrough naturally resulted in a more extensive study of electrolytic processing techniques. A relationship between electrode polarization and degree of electrolytic activation (processing expressed in mAh/cm^2) was shown to exist. Other processing baths were shown to be viable alternatives to the dilute zinc chloride initially employed, thereby demonstrating processing flexibility.

After extensive testing in small cells had demonstrated excellent repeatability, scaling-up of the process to a more convincing demonstration-size battery-unit was successfully accomplished. For this exercise a larger single-cell with electrodes of the same design as those of the 50kWh battery program was activated and cycled. The two end combs from an 8.3kWh submodule were used to form a 0.83kWh cell. The voltaic performance of this unit convincingly demonstrated the feasibility and practicality of the process.

Studies into the nature or source of the enhanced voltaic performance of processed electrodes have been an on-going major concern for some time. Obviously a basic understanding of the effect could have major impact on the $ZnCl_2$ battery program. During Phase I a correlation was found between voltaic performance and electrode surface area (by B.E.T. measurements). These electrode treatments, as expected, were thereby shown to be a form of controlled corrosion. Although the study is by no means complete, the data available at present does allow for the first time for definitive judgements to be made about the nature of the active chlorine electrode.

Besides providing needed direction for further study, it has made possible valuable insight into possible limitations of chlorine electrode life.

The experimentation detailed in this section was performed exclusively with Union Carbide Porous Graphite Grade 60. The performance and characteristics of other graphites tested during Phase I are discussed in Section 35.

EXPERIMENTAL PROCEDURES

Test specifics are basically identical to those detailed in the 1976 EPRI report (34-2). They are therefore covered only in sufficient detail as to reflect newer technology or fundamental changes.

Chemicals employed throughout are of ACS Reagent Grade or, as in the case of $ZnCl_2$, are produced at EDA. As voltaic studies do not require the extreme cleanliness required in coulombic evaluations, the methodology of cell cleanup is not detailed other than to note that rinsing on a deionized water line was employed.

Test Cells and Systems Employed

The small cell ($\sim$30Wh) employed during the initial process development stage shown in Figure 34-1 is the same cell employed in 1976. For details about its construction refer to the EPRI report (34-2). The majority of testing reported on was performed with this cell.

During this study the use of a new chlorine-electrode test cell was introduced. This cell, a true "single-cell", is shown in Figure 34-2. Separate voltage measurement and current-carrying leads are naturally employed. Although the primary reason for the construction of the cell was to provide ease of cell assembly, and hence to expedite test turnaround, other features of significance to electrode testing were incorporated. With this cell, gas blockage of the chlorine test plate is avoided by the use of the standpipes indicated. By doing this a flowing vent is avoided, thereby allowing direct and precise measurement of actual electrode flow. Additionally, more uniform current-density distribution is realized by contacting the test electrode along its entire periphery. In these respects the effects of cell design on electrode performance are thereby obviated to some extent.

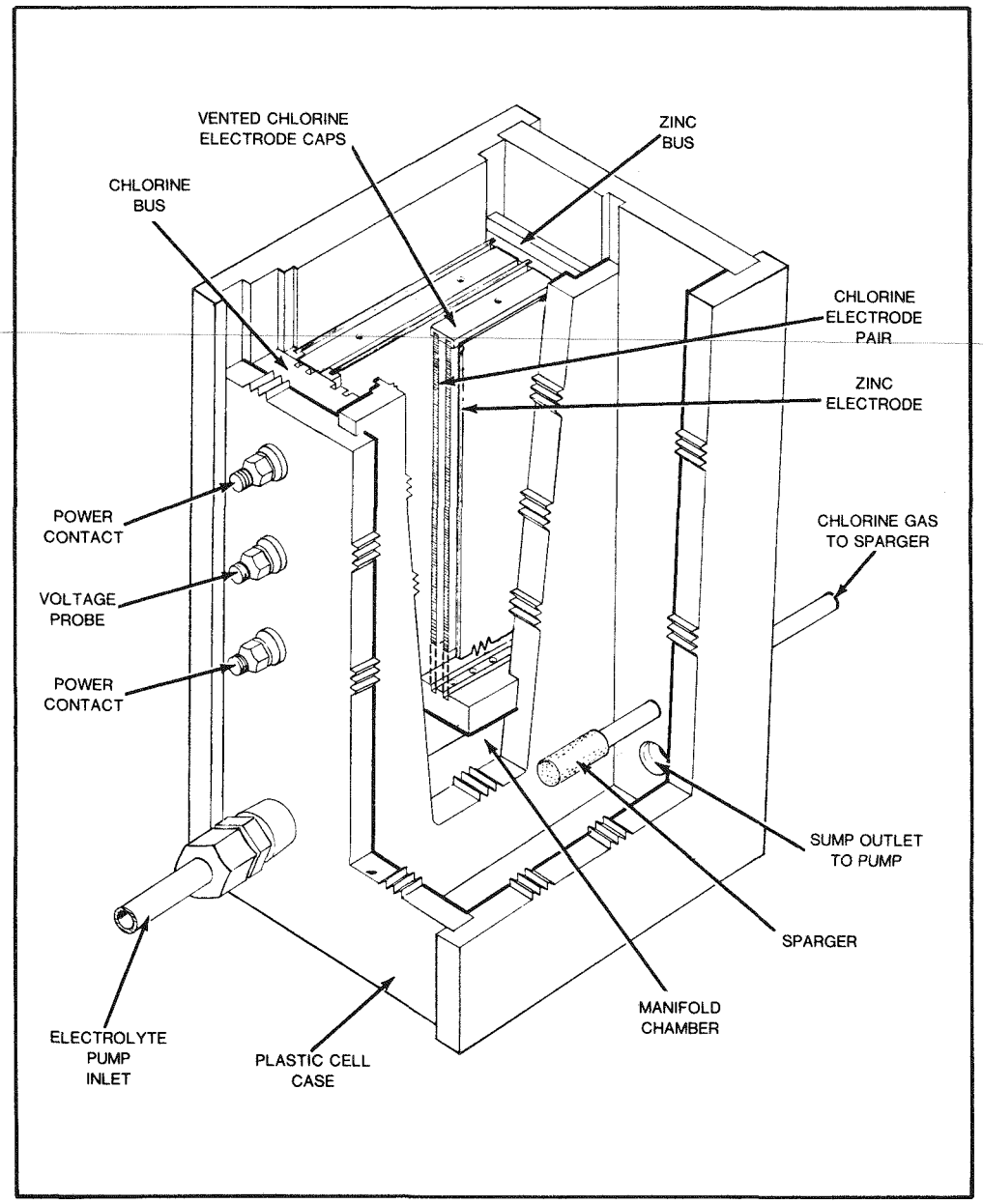

Figure 34-1. Comb-type test cell employed in evaluating voltaic performance of chlorine electrodes. This integral cell/electrolyte-sump design utilizes two chlorine-electrode pairs as indicated, thereby incorporating a central double-sided zinc electrode. Electrode-pair caps employ flowing-vents for gas relief. Electrical contact is via titanium bolts threaded through the Kynar case and into the buses. Inter-electrode gap: 0.150in.

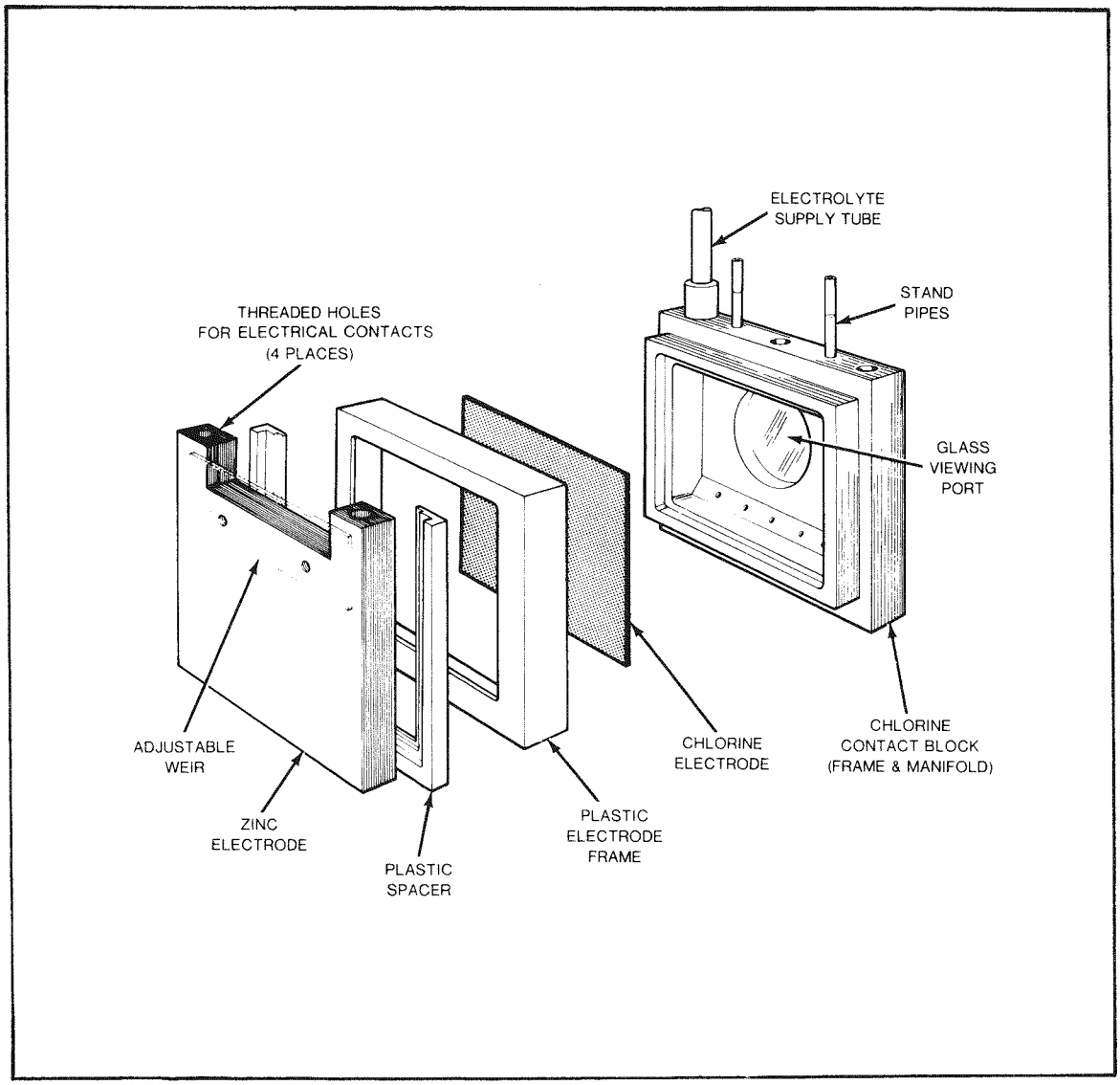

Figure 34-2. Demountable-electrode test cell built specifically for evaluation of chlorine-electrode voltaic performance. Cell was designed for easy turn-around, thereby facilitating testing. Improved current-density distribution is achieved by contacting the chlorine electrode along its entire periphery and by using a thick (1/2") zinc electrode. Standpipes are employed instead of flowing gas-vents; viewing port allows visual determination of gas-blockage. After assembly, cell is clamped together (arrangements not shown), and placed in suitably-sized glass battery jar which acts as electrolyte sump.

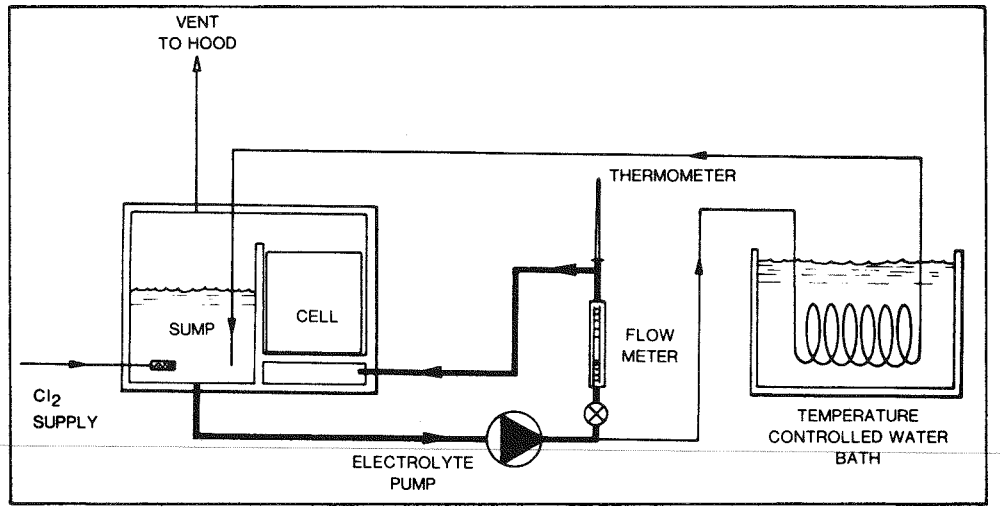

Figure 34-3. Test system used to evaluate voltaic performance of chlorine electrodes. Note use of bypass line for temperature control. Cell shown in the comb-type found in Figure 34-1. With the demountable cell shown in Figure 34-2, a glass battery jar is employed as the electrolyte sump and cell holder.

The operational system employed for both performance evaluation and electrolytic processing is shown in Figure 34-3. Chlorination on discharge was achieved by sparging into the sump. A bypass line/heat exchanger assembly insured precise temperature control. System auxiliaries contacting the electrolyte were exclusively of glass, Kynar, and Teflon with the exception of a rotameter float and micropump shafts of titanium.

Figure 34-4 is a photographic reproduction of the combs employed in scaling up the electrolytic process. These are end combs from an 8.3kWh submodule. They were held together in a Kynar case as shown diagrammatically in Figure 34-5. This was then placed in a glass battery jar. Electrical contact was made to the cell with titanium bus bars bolted down onto the ATJ graphite zinc and chlorine buses.

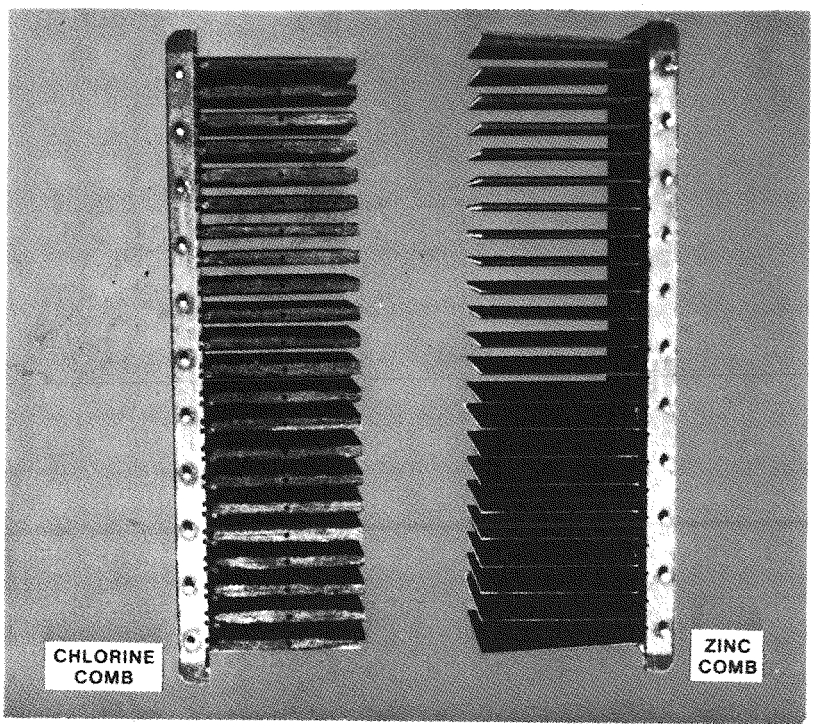

Figure 34-4. Photograph of assembled 0.83kWh zinc and chlorine buses. End combs from an 8.3kWh submodule have been utilized. The meshed combs (with necessary masking) were encased in a Kynar tray for the test unit. Inter-electrode gap is 80mls.

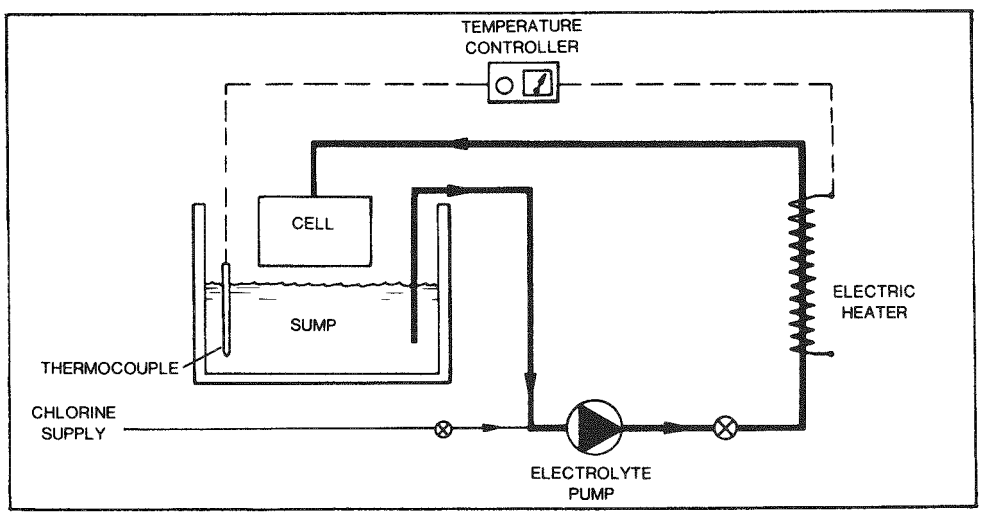

Figure 34-5. Operational system utilized in evaluation of scaled-up 0.83kWh battery unit. Loop used is similar to that employed with some large battery systems. Chlorination on discharge is accomplished by feeding gas to the electrolyte pump inlet. Temperature is controlled in the electrolyte loop proper, and not in a bypass line as with the small-cell study.

Voltage measurements were made with a calibrated DVM. Kynar-coated titanium voltage leads were connected to titanium bolts in the back of the zinc and chlorine buses, as shown in Figure 34-6, to allow for more meaningful voltage measurements. Voltage measurements as reported in polarization curves were made between probes C and 5. Polarization curves were generally taken after 2 hours of charge and 10-15 minutes into discharge.

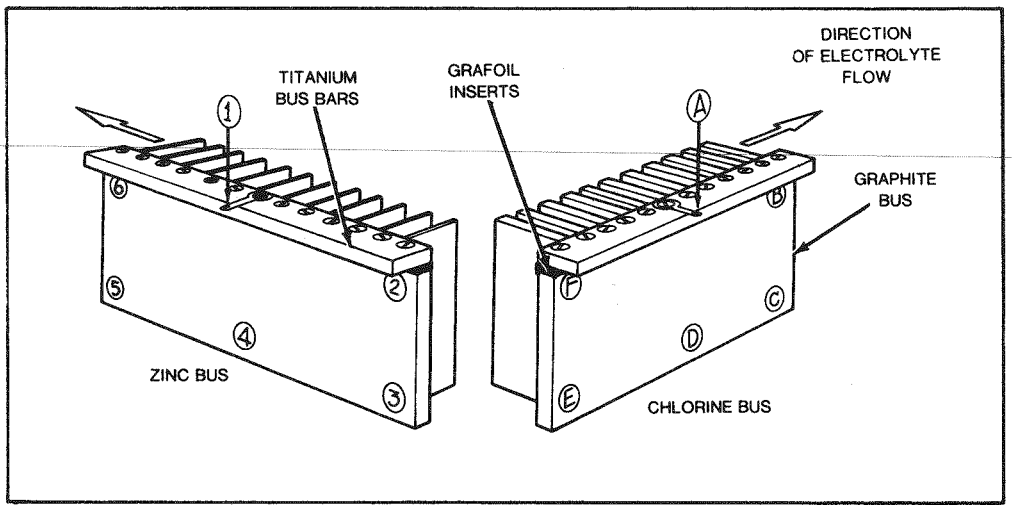

Figure 34-6. Location of voltage probe measurement points. Measurements made allowed detailing of contact and bus resistive losses.

The Activation Process

Electrolytic processing was accomplished on fully assembled cells, and employed the normal test systems. No additional equipment was required. The only variance from routine test operation was that no attempt was made to control system temperature. The following parameters were monitored as a function of time:

- Voltage
- Gas phase composition
- Bath composition

Physical Parameters of Electrode Plates

Measurement of B.E.T. surface area and pore-size distribution were made on selected specimens by Micromeritics, Inc., Norcross, Georgia, 30093. The measurements were made using their Model 2100 Orr Surface-Area Pore-Volume Analyzer. The specific surface area was determined by the standard multipoint B.E.T. technique using Krypton adsorption. Pore-size distributions were measured with a mercury-intrusion porosimeter.

EXPERIMENTAL RESULTS

Electrode Performance as a Function of Electrochemical Processing

Figure 34-7 shows the relationship between voltaic efficiency, charge and discharge voltages for selected current densities, plotted against milliampere-hours/cm^2 of activation. Figure 34-8 shows the polarization curves of various selected electrodes under standard conditions.

As the chlorine electrode becomes electrochemically more active, the side nearest the zinc electrode appears to darken. This effect is maximized somewhere between 300 and 500mAh/cm^2. This is due, perhaps, to the electrode becoming less smooth and hence losing some of its reflective properties. This seems to correspond to the maximum voltaic efficiency attainable with this process.

The performance of these electrolytically activated specimens can be compared to those thermally processed in HNO_3. After approximately 300mAh/cm^2, performance is equivalent to 21-day thermally-processed electrodes. Additionally, there is a corresponding similarity between the two types of electrodes in which the degree of activation is less than complete.

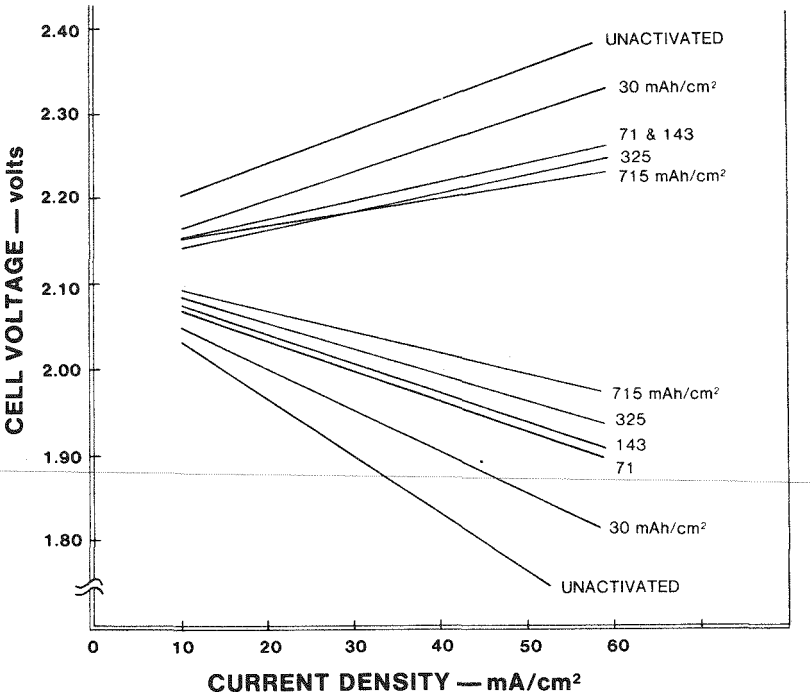

Figure 34-7. Chlorine-electrode voltaic performance as a function of electrochemical activation level (expressed in mAh/cm^2). These test data were generated in the multi-electrode comb-type cell shown in Figure 34-1.

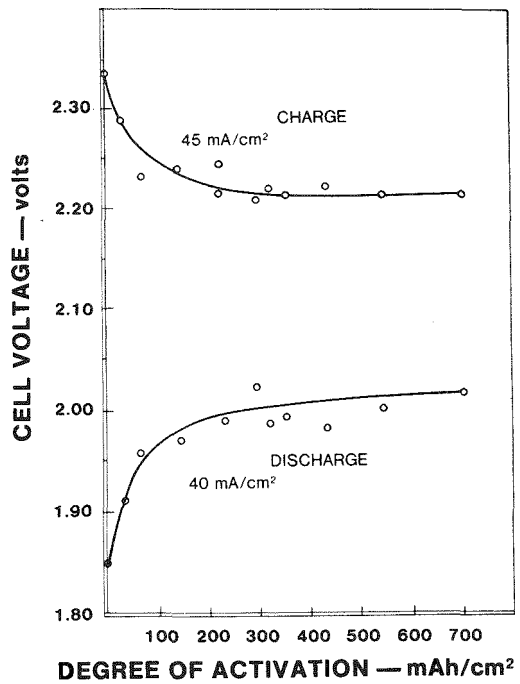

Figure 34-8. Working cell performance as a function of chlorine electrode activity. (Data from the multi-electrode comb-type test cell shown in Figure 34-1).

Voltaic Performance of the 0.83kWh Unit Cell

Figure 34-9 shows a typical set of working-cell polarization curves after activation with the initial "unactivated" curves superimposed. The voltaic performance of the activated unit cell approximates that demonstrated during the above process development in small test cells. After activation the cell was flow-through rinsed on a deionized-water line, i.e. water is forced through the chlorine electrode in the same manner as electrolyte during normal cell operation. Some particulate graphite was evident in the cell. However, less graphite was noted than in the smaller test cells after activation.

The cell was then cycled three times for voltaic evaluation of the electrodes, removed from the sump, and rinsed again. During this rinse more, as much as ten times more, loose graphite was observed in the rinse water than initially after activation. The cell was then cycled for evaluation four more times, rinsing after each cycle. Almost no particulate matter was observed in the rinse water after these cycles.

Polarization curves generated after activation were close, within 20mV at $40mA/cm^2$, to those predicted by tests made in smaller cells. Although the difficulties encountered with system operation may have had some influence on the measured voltaic performance, simple cell experience has shown that the effect would be minimal with activated electrodes.

Charge and discharge polarization curves from Figure 34-9 indicate that the voltaic efficiency of the cell increased from 0.84 before activation to 0.92 after activation, calculated using a charging current density of $45mA/cm^2$ and a discharging current density of $40mA/cm^2$. These efficiencies would naturally be higher at the lower charge and discharge current densities proposed for the 50kWh battery.

After tests were concluded, the cell was dismantled and the electrodes were visually inspected. No physical damage was apparent. The chlorine electrodes were as strong physically as before activation. The only obvious change was the normal darker coloring of the active (unmasked) area of the chlorine electrodes that always accompanies increased electrochemical activity with this electrolytic process.

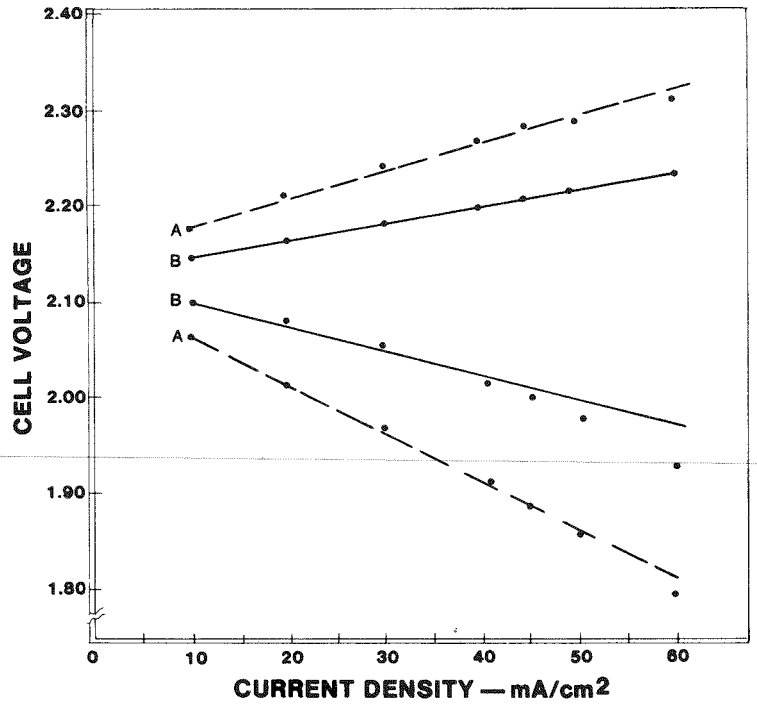

Figure 34-9. Performance of the 0.83kWh test unit before (A) and after (B) electrolytic activation.

The Processed Electrode: Surface Activity Compared with Inner Matrix Performance

When operated at higher current densities (>1A/cm^2) electrodes activated by the thermal nitric-acid process degenerated and lost some portion of their acquired voltaic enhancement. It must be emphasized that this occurs only after operation at unrealistically high currents which are definitely atypical of zinc-chlorine battery operation. Indeed, battery units and the small cells life-tested to date have never exhibited any real losses in voltaic performance while operated at 25-50mA/cm^2.

The above phenomenon led to the hypothesis that the factor which accounts for enhanced voltaic performance could be located on or near the electrode face, and that it had not been generated to the same degree in the bulk matrix. The following experiments were employed in evaluating this concept.

After activating electrolytically and evaluating performance, the electrodes were rinsed, dried, and removed from the cell. The top layers (0.008in) were then carefully removed by end-milling, and the cell was assembled and re-evaluated. The results of these experiments are detailed in Figure 34-10.

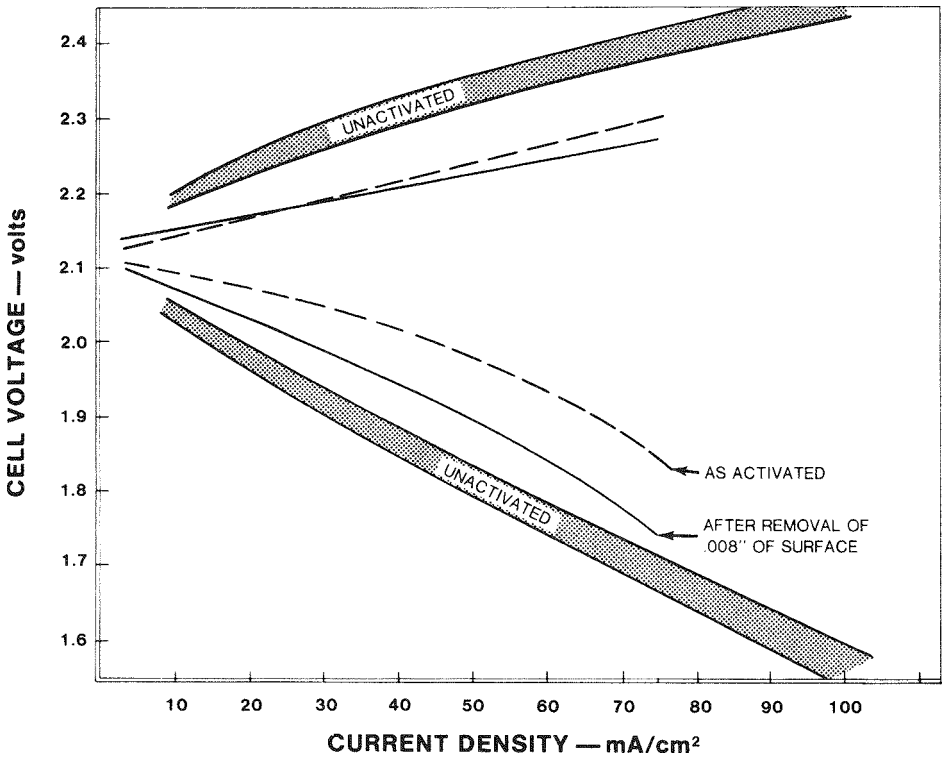

Figure 34-10. Voltaic performance of the inner matrix graphite. After removal of the outer 0.008in of a fully activated electrode, voltaic losses are primarily seen during discharge. These data were obtained with the multi-electrode comb-type test cell shown in Figure 34-1.

Although definitely present, the decrease in voltaic performance is not that great. For example, at 40/45 (mA/cm^2, discharge/charge), a drop of 4% (91 down to 87%) is indicated.

The decrease in performance, although smaller than possibly anticipated, was definitely observable. Electrolytic reactivation was then an obvious step. After reactivation, voltaic performance returned essentially to its original level. The feasibility of reactivation was thereby demonstrated. The experimentation described above was performed with the comb-type cell shown in Figure 34-1.

This led to the question of what would occur if an electrolytically activated electrode were "turned around" and cell performance measured as a function of the "unactivated" side. The results of this investigation are presented in Figure 34-11.

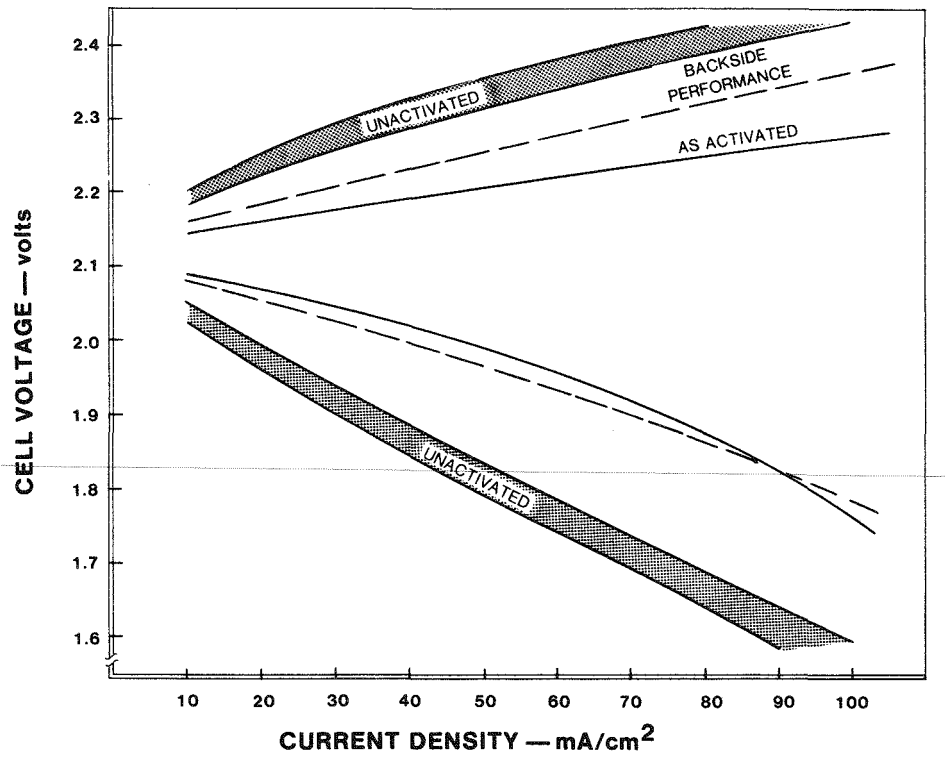

Figure 34-11. Back-side performance of a fully activated (electrolytically) chlorine electrode. The chlorine-electrode test cell shown in Figure 34-2 was employed. The PG-60 plate was electrolytically activated, and its voltaic performance determined. The plate was then flipped over and re-tested.

Performance again drops, but less than for the above case. At 40/45 the penalty was 2.5% (91.9 vs. 89.4%). For this experiment, the chlorine-electrode evaluation cell shown in Figure 34-2 was employed. This cell, which has become the cell of choice for reasons of simplicity and flexibility, has improved current-density distribution due to the method of contact employed in contrast to that of the single-edge buses design.

The Nature of the Active Chlorine Electrode

In searching for the cause of the enhanced voltaic performance realized with porous-graphite chlorine electrodes as a result of these processing techniques, B.E.T. surface area and pore size distribution (by mercury intrusion) measurements were made on selected electrode specimens. The degree to which electrode plates are wetted by the electrolyte was analyzed because it also is considered most significant. These electrode parameters are now discussed in more detail.

B.E.T. Surface Area. Table 34-1 is a listing of the B.E.T. surface area for certain selected electrode samples. As expected from the corrosive nature of processing conditions, surface area increased significantly. The apparent anomaly shown by specimens designated B and C is attributed to differences associated with the two activation processes employed. It is to be expected that modification of surface area would be different due to corrosion as a function of depth into the porous graphite. With electrolytic processing the penetration of current into the porous plate is strongly dependent upon the current density employed. At the current densities preferred (>10mA/cm^2), a "surface layer" effect is expected. With the thermal nitric-acid process, corrosive attack on both electrode faces occurs simultaneously. As the nitric acid is exhausted, the rate of corrosive attack on the graphite tapers off. This decrease leads to an effect similar to the electrolytic process. The interior of the electrode is less affected than the faces, but both faces of the electrode have been modified to some depth. Hence thermally processed electrodes could be expected to show greater B.E.T. surface areas.

Table 34-1

B.E.T. SURFACE AREA FOR POROUS PG-60 GRAPHITE OF VARYING ACTIVITY

Specimen	Treatment	Voltaic Performance	Surface Area (m^2/g)
A	None (baseline)	Poor	0.6 - 0.8
B	Thermal HNO_3 - 11 days	Excellent	2.8
C	Electrolysis in dilute $ZnCl_2$	Excellent	2.0
D	Electrolysis in dilute $ZnCl_2$ (more extensive)	Too weak to test	8.2

Specimen D was weakened to such an extent after activation that a measurement of its voltaic performance was not possible. However, after this excessive amount of activation its surface area is, to a first approximation, taken to be indicative of that present in the more active layer.

Pore Size Distribution. Mercury-intrusion porosimetry measurements show that the pore-size distribution for processed electrodes is similar to that of untreated PG-60 graphite plates. The majority of available pores are in the 20 to 40 micron range, with an average value of 30 microns. There are indications, however, that a significant quantity of smaller pores were formed during the activation of the electrode plate.

Wetting. Wetting of the graphite was found to be sensitive to electrode processing and, to a lesser degree, operational time in the working cell environment. To be more specific, the electrolyte head of a few cm, associated with virgin PG-60 was observed to decrease significantly after processing to less than 1cm. The improvement with time for unprocessed PG-60 has not been monitored carefully, and a precise value is not available. Although improved wetting does result, significant voltaic improvement is not realized.

The Active Chlorine Electrode. These measurements, when viewed in conjunction with improved voltaic performance, have led to the conceptual view of the activated electrode presented in Figure 34-12. The B.E.T. surface area measurements allow the theorization that an increase in surface area has been realized. Although the depth to which the increase occurs is not known precisely, it appears at the least to be limited to the top 10% (<0.008in) for the electrolytic process. After machining off this facial layer, the decrease in performance was not as extensive as might be expected. The improved wetting of the electrode also must be considered a significant contributing factor.

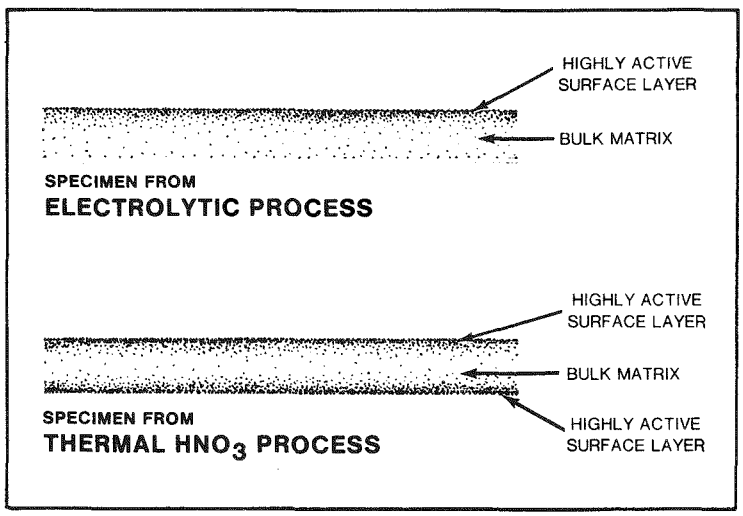

Figure 34-12. A conceptual view of the active-chlorine electrode. With the electrolytic process, the formation of a more active, higher surface-area layer is limited to the electrode-face only.

DISCUSSION

The electrolytic-activation process represents a break-through of major significance in zinc-chlorine battery technology. Its impact on future battery programs may be detailed as follows:

1) Of greatest significance is the fact that it is accomplished on the assembled battery, thereby obviating the capital expense required for and avoiding the handling problems associated with the thermal nitric-acid process.
2) Much shorter processing time is required for electrolytic activation.
3) Process reliability has been demonstrated. The relationship between voltaic performance and the degree of processing (mAh/cm^2) should insure the production of maximum performance with minimum deterioration of the porous-graphite base matrix. This should have major impact on maximizing chlorine electrode life.
4) Reactivation, after artificial removal of the more active surface, has been demonstrated. This feature, in conjunction with point 3, also may have implications for electrode life whereby minimum activation would be employed followed by reactivation when and if needed.

The scaling-up of the process to the 0.83kWh battery unit level convincingly demonstrates the feasibility of the technique. The ease with which this was accomplished bodes well for future larger scale-ups.

Significant insight also has been gained into the nature of these activation processes. This has led to the generation of a conceptual view of the active chlorine electrode which will assist in guiding future chlorine electrode programs. Of greatest significance are the implications this will have on the development of a cost-effective battery electrode.

REFERENCES

34-1. E.B. Barnett, and C.L. Wilson. Inorganic Chemistry. 2nd. ed. London: Longman, Greens & Co., 1957, pp. 308-313.

34-2. Development of High-Performance Cost-Effective Zinc Chloride Batteries for Utility Peak-Shaving -- 1976. Palo Alto, Calif.: Electric Power Research Institute, 1978. EM-711.

Section 35

SELECTION AND QUALIFICATION OF POROUS GRAPHITES

INTRODUCTION

Commercial feasibility of the zinc-chlorine battery is, in part, dependent upon low materials cost and availability. Following the decision to produce an "all-graphite" battery, Union Carbide porous graphite PG-60 was the only electrode material qualified for use in the zinc-chlorine electrochemical cell. However, the steadily rising costs of PG-60 forced a search for an alternative source of porous graphite.

Before any material is qualified for battery system use, it must meet the following requirements:

- Voltaic performance must approach or exceed 90% at operational current densities of 30 to 45mA/cm^2, as received and/or after a reprocessing procedure which enhances activity.
- Cost on the order of $2/lb (1978 dollars) at the projected use level. This includes eventual commercial availability of the required quantities.
- Coulombic performance of the battery must not be adversely affected by organic or inorganic contaminants which may originate from the graphite.
- Resistance to flow (pressure drop) must not be so excessive as to become flow-controlling.
- Material strength must be compatible with the hydraulic forces encountered.

A high priority during Phase I was given to evaluating the voltaic performance of the selected graphites. Routinely monitored parameters included:

- Working cell polarization as a function of current density.
- Voltage vs. electrolyte flow-rate at a given current density.

Additionally, measurements were made to compare the pressure drop developed by flowing electrolyte through each graphite test material with that of PG-60.

The materials chosen for preliminary testing (Table 35-1) are readily available from the manufacturer and either are or could be manufactured on a commercial basis. Experimental material 19C is an exception which, according to the manufacturer, will be made commercially available as a market develops for the zinc-chlorine battery.

The collected data indicates that the voltaic performance of PG-60 is the best of the graphites tested. However, all samples achieved acceptable voltages after some degree of electrolytic activation. Also, all samples achieved acceptable and very similar water permeability values.

Although the effect on coulombic efficiency by contaminants in the graphites remains to be evaluated, vendor-supplied analyses indicate the encountering of few, if any, problems due to inorganic contaminants.

Table 35-1

GRAPHITES SELECTED FOR INITIAL EVALUATION

Material Designation	Status
24A	Commercial
23B	Commercial
19C	Experimental
13D	Commercial

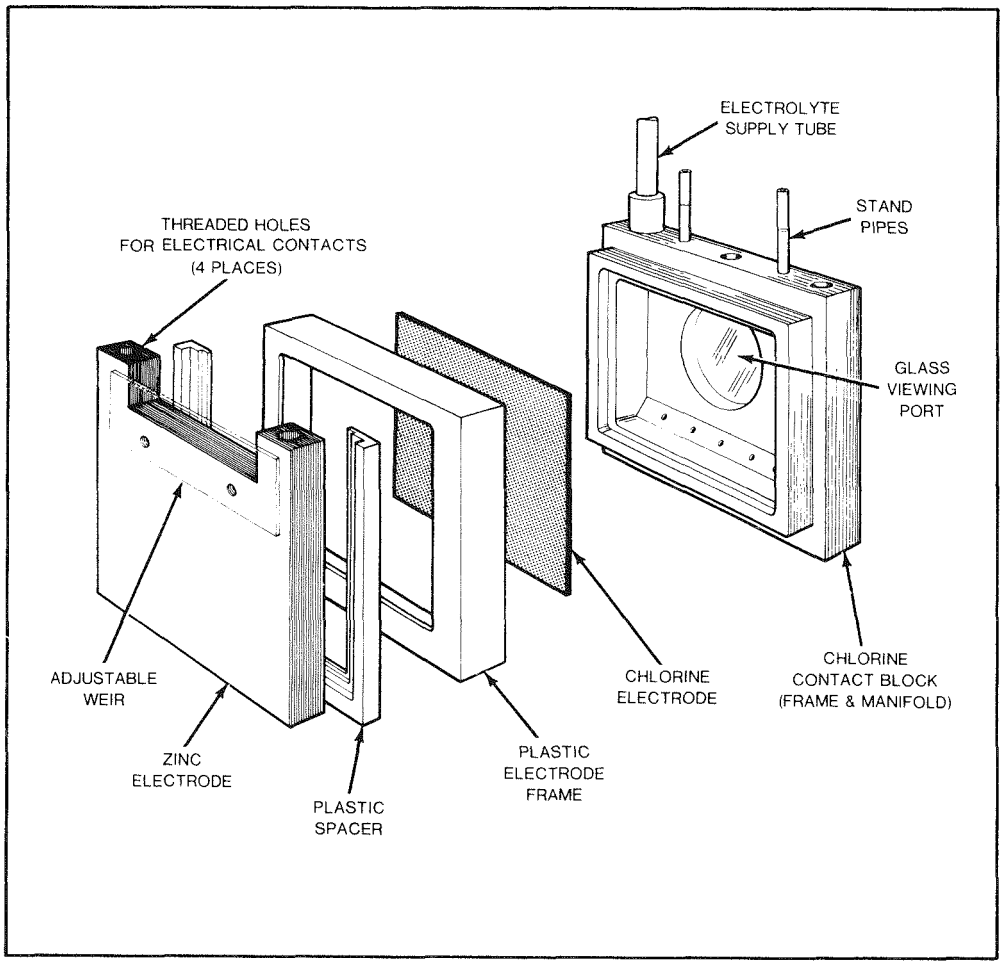

Figure 35-1. Exploded View of the Chlorine Electrode Test Cell

TESTING METHODS

The test cell shown in Figure 35-1 was designed to allow rapid removal and replacement of the chlorine electrode. The conditions selected for testing resemble those employed in the 45kWh battery modules. The test schematic is presented in Figure 35-2. Temperature was maintained at 30°C. In evaluating voltaic performance, higher electrolyte flow rates than with operating systems were employed. This ensures against slight variations in flow and/or dissolved chlorine level materially affecting discharge performance. Tests were made with the electrolyte chlorine-saturated. The electrolyte was 3M $ZnCl_3$ + KCL at a pH = 0.

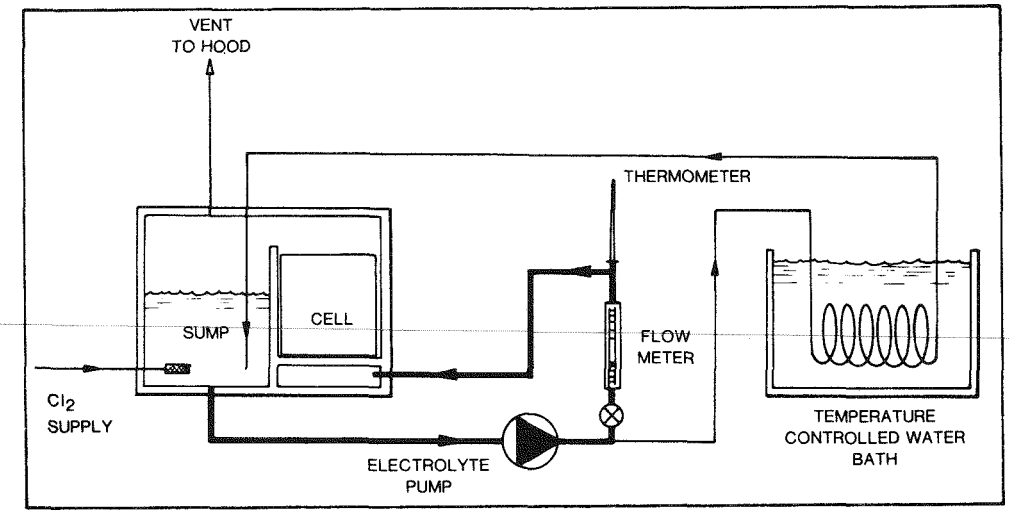

Figure 35-2. Schematic diagram of system for running the chlorine electrode test cell. Electrolyte is maintained at 30°C.

The porous graphite materials being evaluated were activated electrolytically as described in the preceding section. All materials were activated and cycled until leveling of performance with further electrolytic activation was observed. Data reported were thereby obtained with "fully" activated electrodes.

The reservoir height of the water-permeability test system shown in Figure 35-3 was dictated by the pressure necessary to flow through the entire height of the most porous electrode material. A sealant was used to ensure a proper hydraulic seal. Eight hundred milliliters of water were flowed through each electrode, the time required being dependent on the permeability of each sample. Ambient temperature was ∿22°C. Electrode thickness for each was 0.080" (0.20cm).

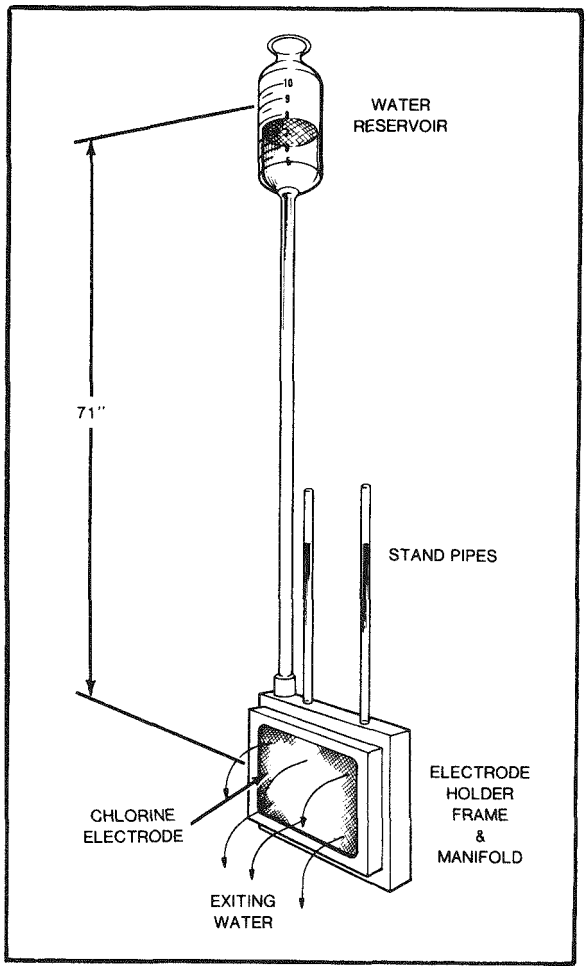

Figure 35-3. Illustration of setup for measuring water-permeability of sample chlorine electrodes.

TEST RESULTS

Voltaic Performance

Working cell polarization data of all graphites tested are presented in Figure 35-4. Although PG-60 curves are superior, all other materials performed reasonably well

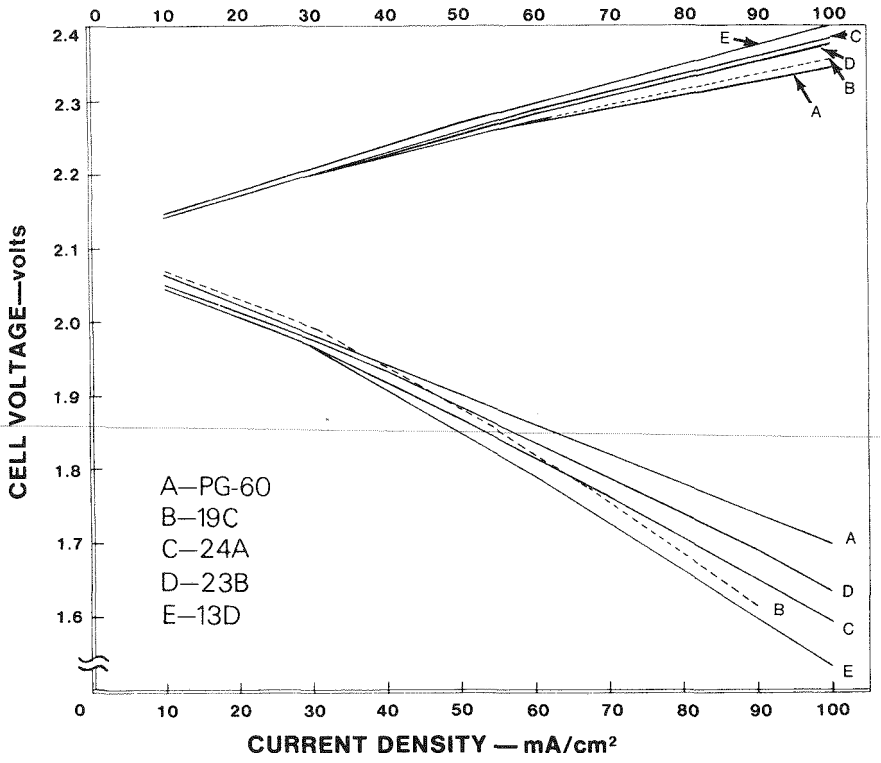

Figure 35-4. Polarization data for various graphites after electrolyte activation.

to a current density of 50mA/cm^2. Graphite 19C performed significantly better in this region than the other candidate materials, but dropped in performance beyond this region. Graphite 23B showed good performance at even greater excursions in current density, remaining nearly linear beyond 50mA/cm^2. Graphite 24A also showed near-linear performance, as did 13D. The latter, however, achieved the lowest voltage values in all regions of current density of all of the materials tested thus far. Charge polarization data seem to indicate very little difference between the various materials. The difference between the lowest charge voltage, of graphite PG-60, and the highest, of 13D, is only 15mV at 50mA/cm^2, whereas it is about 55mV at 100mA/cm^2.

Preliminary pore volume distribution measurements were made on selected material samples. These measurements, shown in Figure 35-5, indicate an average pore diameter of 29 microns for untreated PG-60. Data supplied by the manufacturer of 19C also are presented in Figure 35-5, and show an almost identical average pore diameter. In addition, both sets of data indicate a similar spread in pore volume distribution. In both cases the bulk of the pores are between 20 and 40 microns. However, the major difference in the voltaic performance between the two graphites is thought to be related to the difference in the specific porosity of each. The manufacturer reports the porosity of 19C as being 0.30cc/g, while measurements on PG-60 subcontracted to an outside testing laboratory (Micromeritics Instrument Corporation, 5680 Goshen Springs Rd., Norcross, Georgia 30071) show a porosity of 0.4 - 0.5cc/g. This difference is reflected in the differing mass densities of each graphite; 1.05 for PG-60 vs. 1.35 for 19C. These properties appear to manifest themselves as a decreased voltage on discharge at high current density, while having essentially no effect on charge. Although this property appears to be a disadvantage, its increased density may be capable of extending the electrochemical lifetime of the chlorine electrode or offering certain other benefits.

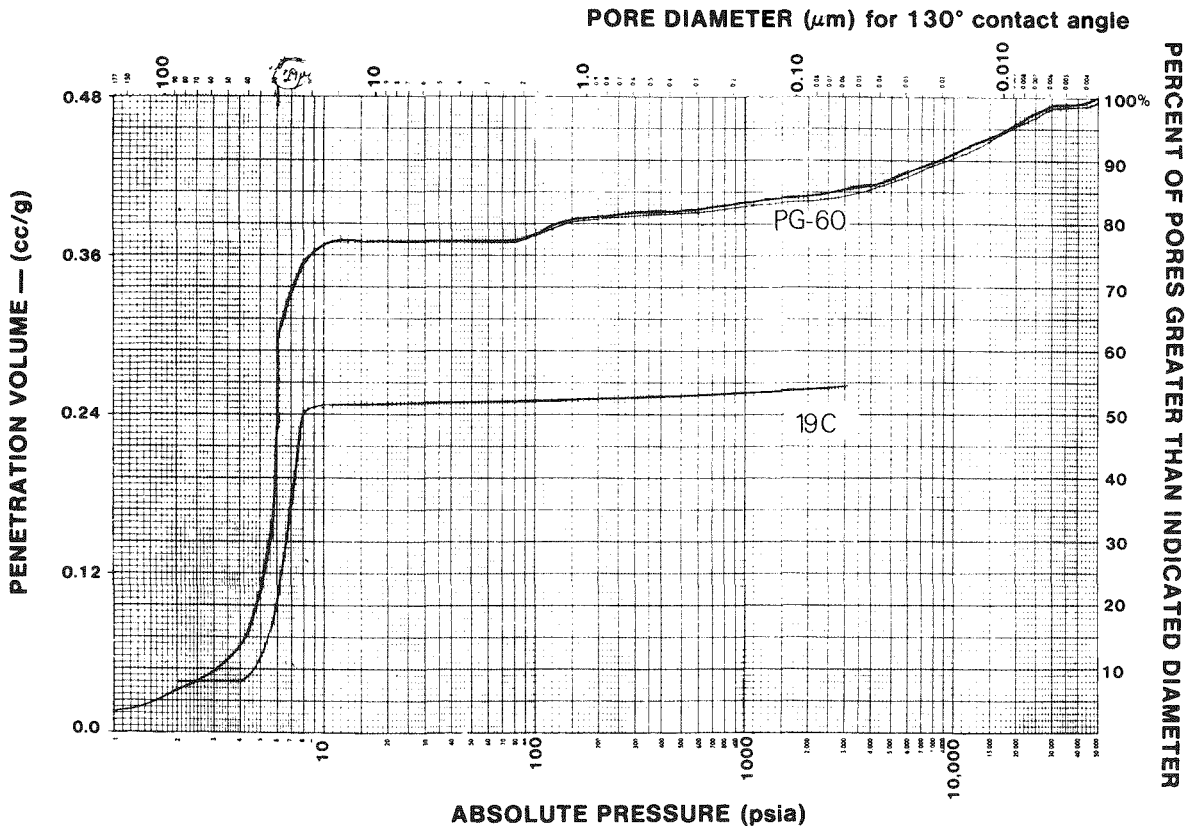

Figure 35-5. Plot of pore size and volume distribution measurements made on selected porous graphite samples.

Cell voltages using each material at a given current density of 40mA/cm^2 vs. electrolyte flow-rate are plotted in Figure 35-6. Very little difference was noted between the various materials. Slight variations in electrolyte composition can cause a shift in the chlorine saturation level. This shifting in saturation level will affect these curves. Because of this fact, slight differences in the curves from material to material are difficult to analyze.

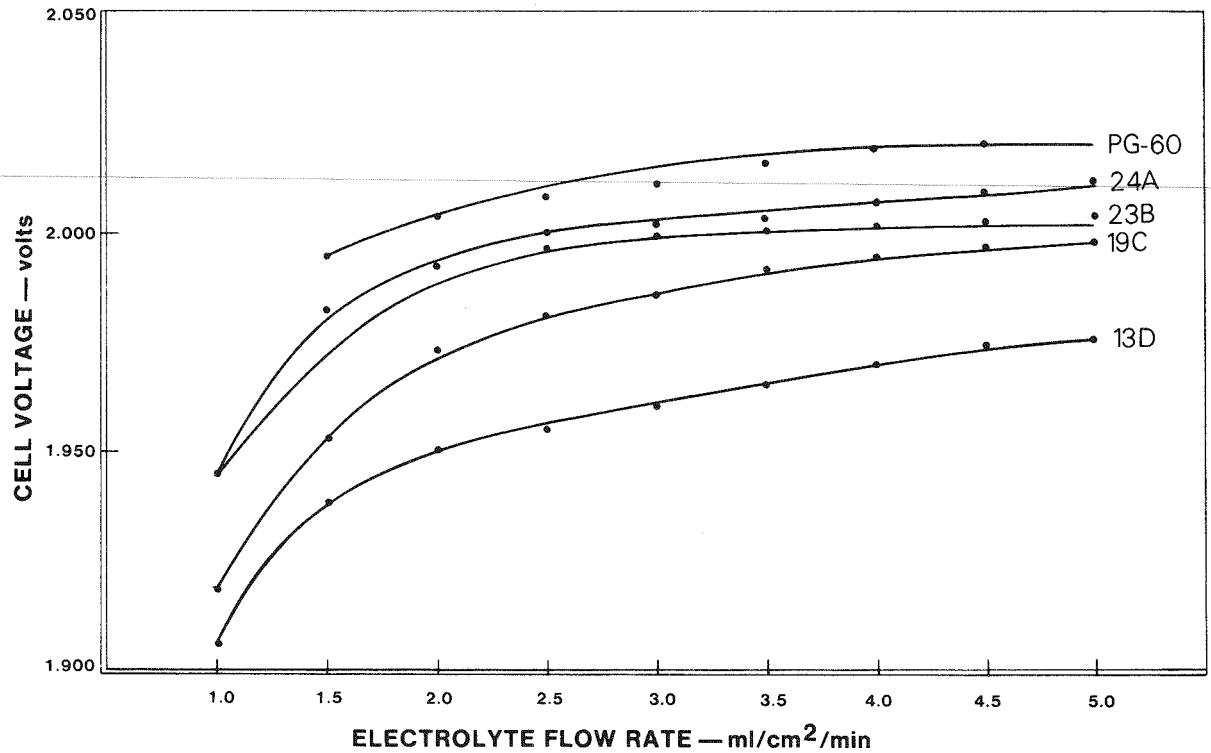

Figure 35-6. Plot of discharge voltage vs. electrolyte flow-rate at a constant current rate of 40mA/cm^2 for several sample electrode materials.

Electrode Permeability

The results from permeability measurements are shown in Table 35-2. The permeability of each material tested differed only slightly from the others, the exception being graphite 19C.

In an operating cell, the pressure of electrolyte behind a PG-60 chlorine electrode is generally about 2cm of electrolyte. These tests indicate that if graphite PG-60 were replaced by graphite 19C, for example, the pressure behind the electrode would be about 1.5 times as great (∿3cm). However, this difference is probably negligible as the flow in the larger battery system is controlled by a much

greater hydraulic resistance in the electrolyte feed tubes.

It should be emphasized that these tests are not absolute measurements of permeability but rather reflect only differences between the various materials. This is due in part to the fact that a wetting time of only one hour was employed. It is not presently known to what extent battery cycling affects wetting or porous graphite. However, it is believed to be significant. The relative contributions of wetting and physical alteration in activated porous graphite to the change in permeability of the material are not known. Minor variations in permeability as mentioned above presently are not thought to be a major consideration that should seriously affect the qualification of a porous graphite material.

Table 35-2

RELATIVE WATER PERMEABILITIES OF THE TEST MATERIALS

Material	Water Permeability ($ml/cm^2/min$)*	Degree of Electrolytic Activation (mAh/cm^2)
PG-60	15.72	none
PG-60	17.76	150
13D	16.74	1,050
23B	18.48	1,350
19C	11.70	518
24A	17.52	750

*Tests made at a water pressure of 0.18 Bar and at $\sim 22^{\circ}C$; plate thickness = 0.080" (0.20cm). Refer to Figure 35-3.

Comparison of Candidate Porous Graphites

After activation each of the graphites tested has demonstrated similar voltaic performance capability at foreseen operating current densities. With the exception of graphite 19C, the electrolyte pressure drops are equivalent to that of graphite PG-60. Although the pressure drop value of 19C is 50% greater than that of PG-60, it remains within the acceptable range.

CONCLUSIONS

Of the porous graphites tested, only graphite 19C approximates the cost criterion. All were capable of acceptable voltaic performance after activation. In short, the voltaic performance of each sample tested is, or can be made, acceptable. Graphite 19C should be qualified coulombically for battery use. Once 19C is qualified, cost reduction of the other materials should result and/or other cost-effective alternatives should be developed due to competition.

Section 36

INERTS REJECTION FROM BATTERY MODULES

INTRODUCTION

Trace amounts of hydrogen, oxygen, and carbon dioxide are by-products of the electrochemical reactions in the zinc-chlorine battery system. These gases are loosely categorized as "inerts" in the system in the sense that the reactions by which they are formed are not reversible in ordinary battery electrochemical processes. In addition, they are inert in the hydrate-formation process whereby chlorine is stored in the battery. Once formed in the closed battery system, they must be removed to prevent accumulation and resultant interference with normal battery operation.

Hydrogen removal is readily accomplished by the ambient temperature photochemical reaction of the hydrogen with chlorine to produce HCl. The HCl is returned to the battery electrolyte with the beneficial effect of maintaining a constant battery pH. This method of hydrogen removal has been used with satisfactory results in the 45 kWh load-leveling system and in a number of previous battery systems.

Oxygen and carbon dioxide, however, are not as easily removed. While hard data is not yet available, it is believed that any photochemical reduction of oxygen with hydrogen under battery conditions is precluded by the hydrogen-chlorine reaction. Catalytic methods of oxygen reduction are precluded by the presence of chlorine, a "poison" for catalysts normally associated with this reaction. Reduction of carbon dioxide in the presence of strongly-oxidizing nascent chlorine is not believed to be feasible by ordinary means at near-ambient temperature. As a result, removal methods predicated upon the separation and venting of these gases are considered as the most practical.

Statement of the Problem

Oxygen production rates at the low pH levels of 0.0 to 0.7 currently used in the zinc-chlorine battery operation have not been accurately determined, but are known to be less than 0.01%. The oxygen is, therefore, not considered a rate-determining inert for definition of the problem. It has been grouped with the CO_2 since it is within the range of uncertainty expected for the production rates of CO_2. The methods selected must be applicable to removal of the O_2 with the CO_2.

Carbon dioxide is evolved during normal operation of the battery system as a by-product of oxidation of the battery graphite. The volumetric rate of CO_2 evolution on charge has been measured as 0.1% of the chlorine rate for a freshly machined "new" graphite cell, and 0.02% to 0.04% of the chlorine rate in cells that have been electrochemically worked for several cycles. The CO_2 rate during discharge has not been well established but is estimated to be 20% to 30% of the rate during charge.

If allowed to accumulate within the battery system, the CO_2 will reach concentrations of 4.3% to 8.6% of the total gas in the projected gas space volumes of 2 ft^3 by the end of the first charge cycle. Concentrations above 2% to 3% interfere with the hydrate formation process during charge, and with chlorine dissolution during discharge. Deleterious effects on battery operation could, therefore, be expected to begin to appear during the first charge cycle. The expected time of appearance is determined by battery design specifics and predicted by mathematical modeling of the system in studies not yet complete. Separation of inerts from the chlorine is considered necessary. This is technically feasible because numerous possible methods are available to separate a purged stream of gases from the battery. The optimum scheme conceivably could utilize more than one method. However, the design of a practical device will require selection of methods which do not consume excessive parasitic power, do not result in excessive chlorine loss, are inherently reliable, and are not excessive in cost. Because compatibility of materials with the nascent chlorine is required for reliability, close attention must be given to the concepts selected from the standpoint of the practicality of device design. Methods requiring high speed rotating parts or difficult valve design, for example, must be considered less desirable from this standpoint than methods which do not.

The gas purge could be conducted on either a steady state or intermittent basis. The purge rate to a removal device necessary to maintain acceptable CO_2 concentrations in the battery can be estimated using the range of expected CO_2 generation rates, the projected gas volumes for future battery systems, and the allowable CO_2

concentration in the battery gas space. On a steady state basis at a CO_2 concentration limit of 1% in the gas space, the purge requirement would be between 0.58 ℓ/m and 1.16 ℓ/m of gas during the charge cycle. Other rates are shown in Table 36-1.

Table 36-1

ESTIMATED CO_2 IN THE BATTERY GAS SPACE -- "AGED" BATTERY

CO_2 Production Rates	Lower Limit	Upper Limit
Moles/charge	0.110	0.220
Moles/discharge	0.022	0.073
Std ml/min charge	5.840	11.600
Std ml/min discharge	1.640	5.380
Cl_2 Removed at 1% CO_2		
Moles/charge	10.900	21.800
Moles/discharge	2.200	7.200
Std ml/min charge	574.000	1147.000
Std ml/min discharge	162.000	530.000

Allowing the gas to accumulate slightly during charge and operating a continuous purge through charge and discharge, the steady state purge requirement would be 0.4 to 0.8 liters of gas per minute, of which 4 ml to 8 ml would be CO_2. Higher concentration limits in the battery gas space would result in correspondingly lower purge rate requirements. Methods of gas separation selected must be fully compatible with these purge rates and offer some flexibility in application to allow for changes which may occur as the battery "ages".

Techniques for Inerts Rejection

The methods for inerts rejection which have been subjected to preliminary evaluation are:

- membrane permeation
- gaseous diffusion
- electrochemical separation of chlorine
- hydrate formation for partial separation of chlorine

It is emphasized that evaluations are preliminary for the purpose of determining general limits in the possible applications. Two or more methods conceivably could be used in a final device if a simpler device resulted. No attempt has been made to finalize possible combinations of devices or to consider design for implementation.

Separation by Membrane Permeation

Membrane permeation techniques utilizing permselectivity, which is the tendency for certain materials to pass one gas more readily than others, were considered briefly as a basis for a separation of CO_2 in a battery system. This process differs from ordinary diffusional processes in that the gases dissolve to a greater or lesser extent in the membrane material, diffuse through, and are released on the outlet side. Membrane permeability separation processes have been used industrially for a variety of gaseous separation processes. Membrane materials used (36-1) include polymers, glass, and metal. The theory for this type of device is well developed.

The principle limitation for application of this type of device to the zinc-chlorine battery system is the need to compress the gas mixture prior to separation to achieve useful separations even in a perfect multi-stage device. This arises because the partial pressure or chemical potential, of the gas on the upstream side of each stage must be at least slightly higher than the gas partial pressure on the downstream side. The maximum pressures expected in the zinc-chlorine battery will be in the hydrate store where pressures of 1.6 atm conceivably would be available. Even with CO_2 concentrations in the store as high as 5%, the CO_2 partial pressure would be only 0.08 atm. At 1% inerts concentration in the store, the partial pressure would be 0.016 atm. Discharging to 1 atm would, therefore, require that the CO_2 partial pressure be increased to 1 atm. Ignoring pressure losses in a membrane separation device, increasing the CO_2 partial pressures to 1 atm would require gas compression from the store pressure to approximately 13 atm when CO_2 concentration is 5% in the store, and 62.5 atm when it is 1%. These compression ratios are not excessively energy consumptive. However, they require the design of a low-volume, high-pressure gas pump compatible with the corrosive chlorine atmosphere. Solution of the attendent materials problems would be required.

Thermal Diffusion

Separation of gases by thermal diffusion is based upon the tendency of components of differing molecular weight in a gas mixture to partially separate when subjected to a temperature gradient. This effect arises as a consequence of conservation of molecular momentum and energy equilibrium relationships in accordance with the kinetic theory of gases. The lighter component moves toward the warm zone at a rate dependent upon the properties of the gases and the temperature differences, thereby establishing a concentration gradient between the warm and cool zones. The concentration gradient results in an ordinary diffusion of the lighter component in the reverse direction at a rate proportional to the "steepness" of the gradient. When the two rates become equal, a steady state condition with a partial separation of components is established.

In usual practice, many stages of separation are combined by situating the warm and cool surfaces vertically so that natural convection produces a relative upward motion of the gas at the warm surface and a downward motion at the cool surface. The upper portion of the column becomes richer in the lighter component, thereby allowing further separation to occur. Figure 36-1 schematically illustrates the temperature, velocity, and concentration profiles which exist in this type of device. Possible configurations of thermal diffusion equipment are presented in Figure 36-2.

A source of comprehensive discussion of the theory for design of thermal diffusion gas separators are references 36-1 through 36-5. The calculation methods for concentration gradients in a thermal diffusion column are given in reference 36-1. Velocity and thermal gradient calculations are treated in reference 36-5.

Concentric-cylinder geometry, or a hot wire in a cylinder, is frequently used because greater economy of materials is obtained. However, for the preliminary calculations used in this program, flat-plate geometry was assumed because the results will be sufficiently close for the "factor of 2" estimates desired and because the heat, mass, and momentum fluxes can more readily be determined.

Other basic assumptions were:

1. Density, viscosity, and the thermal expansion coefficient for chlorine was used for the gas. Again, this assumption is adequate for estimates, and the time-consuming calculation of mixed gas properties was avoided.
2. Plate-end effects were ignored.
3. Effects of concentration on density profiles were ignored.

4. The cold plate was assumed to be at 5°C (500°R), approximately equal to the coolant temperature for hydrate formation in the battery.

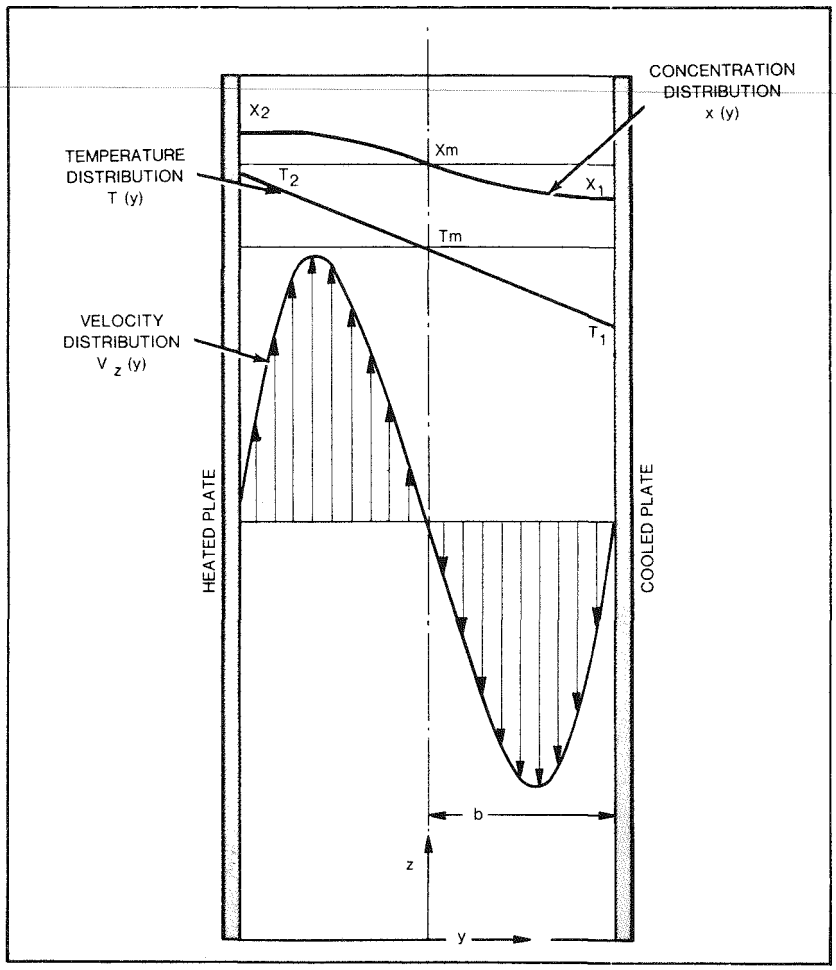

Figure 36-1. Temperature, velocity, and concentration profiles in thermal diffusion column -- flat-plate type.

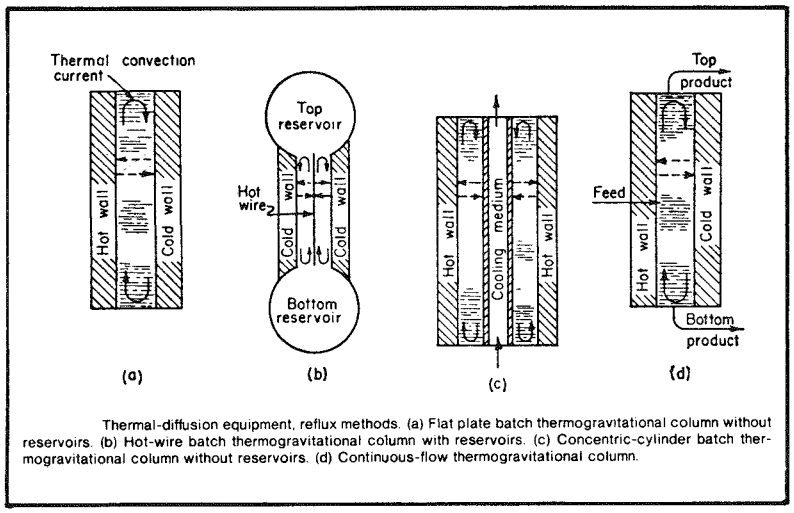

Thermal-diffusion equipment, reflux methods. (a) Flat plate batch thermogravitational column without reservoirs. (b) Hot-wire batch thermogravitational column with reservoirs. (c) Concentric-cylinder batch thermogravitational column without reservoirs. (d) Continuous-flow thermogravitational column.

SOURCE: Chemical Engineers' Handbook, John H. Perry 1963

Figure 36-2. (a-d). Possible Configurations of Thermal Diffusion Equipment

Source: Used with permission of McGraw-Hill Book Company.

The hypothetical flat-plate thermal diffusion column was optimized at first for flow-rate per unit of column width, as shown in Figure 36-3. A 20-stage column was then assumed and the relative area per stage was determined for an increase in CO_2 content in a purged stream from 1% CO_2 from the battery to a 99.9% CO_2 at the outlet. These results are illustrated in Figure 36-4. The area of surface for the total column with two flat plates bounding each channel then was calculated as a function of gap between plates and temperature differences. The area and resulting heat load for convection and radiation is shown in Figure 36-5. Not shown in the figures is the optimum gap width which ranged from 0.10 inches to 0.15 inches, and the column height which totaled less than a foot. The column was short due to the relatively large differences in molecular weight of the separated species, and due to the fact that the column was optimized for length as a first step in the calculation.

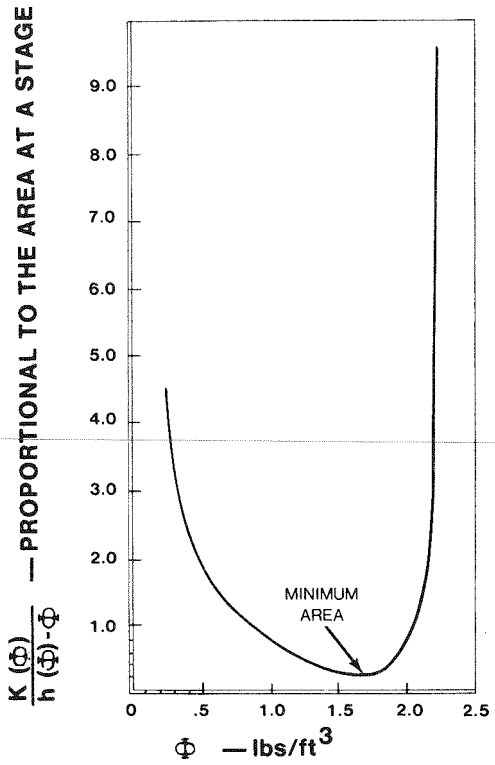

Figure 36-3. Optimum value of convective flow parameter, ∅, for minimum column area.

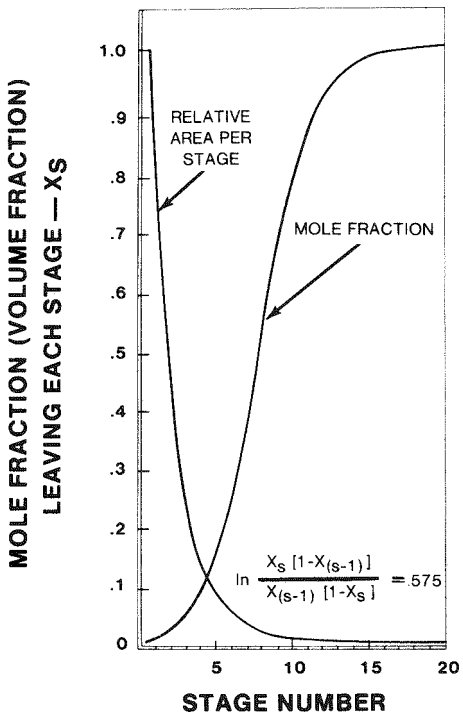

Figure 36-4. Relative Area Per Stage For a 20-stage Thermal Diffusion Column

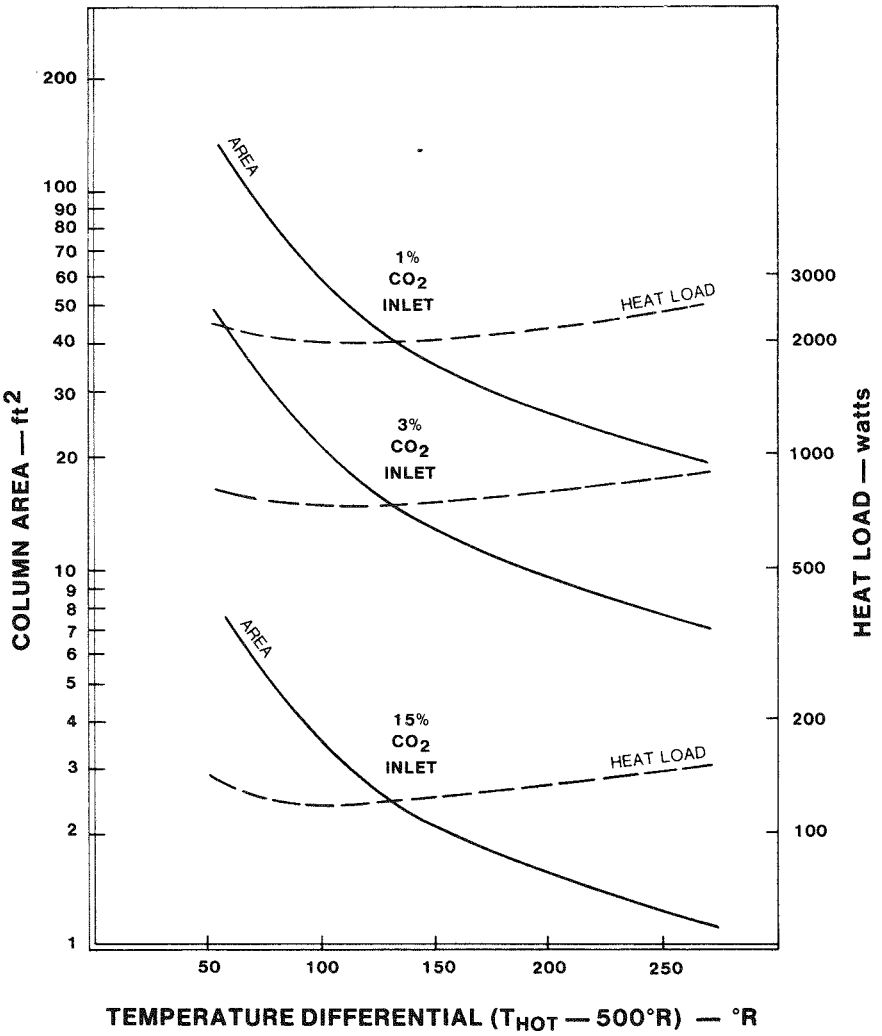

Figure 36-5. Total area of surface and heat load in a thermal diffusion column for optimum gap.

Electrochemical Separation of Chlorine

An "electrowinning" cell was used on an experimental basis to separate chlorine from a mixture of chlorine and inert gas. This type of cell utilizes the chlorine discharge reaction at the cathode to form chloride ion from the chlorine. The chloride ion then diffuses through the electrolyte to the anode where the charge reaction occurs to again form chlorine. In practice, a barrier membrane between the electrodes prevents a recombination of the gases from the cathode and anode sides of the cell. A schematic of this cell is given in Figure 36-6.

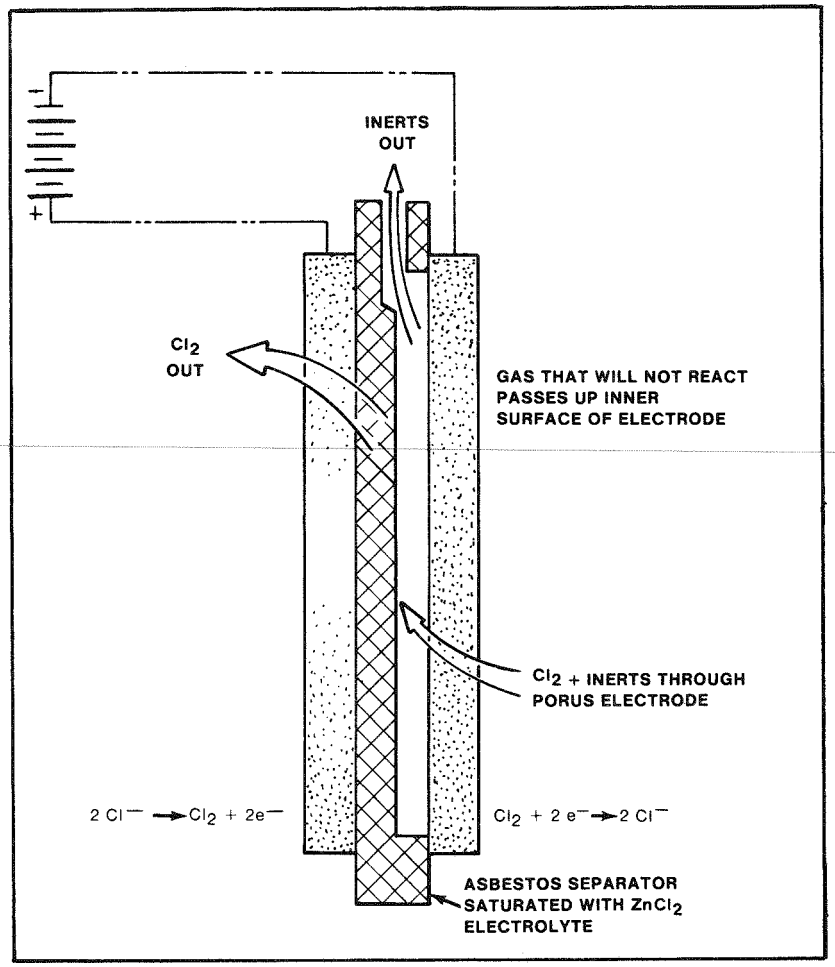

Figure 36-6. Schematic of an Electrowinning Cell

One possible approach to a device design is shown in Figure 36-7. In application the gas phase either would be flowed through or against the cathode with the bypassed gas mixture supplying feed for the next cell in a series-connected arrangement as shown. Electrolyte would not be circulated. The cells would be electrically paralleled at a common voltage and operating at successively lower current densities as chlorine concentration in the gas phase is reduced.

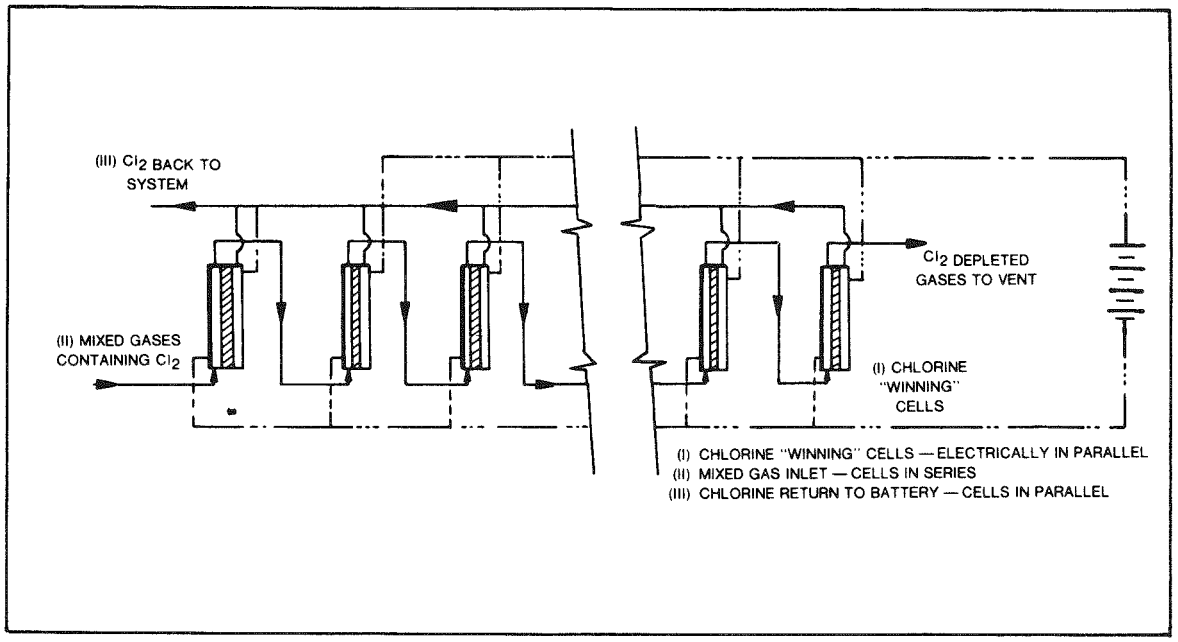

Figure 36-7. Schematic of an Electrochemical Cell System

Estimates for the parasitic power required are given in Table 36-2 for various operating voltages. They are based upon the expected purge rates for maintenance of an average 1% CO_2 concentration in the battery system. The coulombic efficiency for this type of device will closely approach 100%. It may be concluded from the foregoing that the parasitic powers will not be excessive.

Accurate sizing of the device, from estimates of projected electrode area, requires information relating current density, over-potential, and chlorine activity. Best estimates would be predicated upon experience with electrodes from battery testing. Based on battery operating data, the over-potential on the charge side would be small and predictable. Estimates of current densities for the portion of the cell operating in discharge, however, could not be considered reliable except for order of magnitude.

Table 36-2

REMOVAL OF ALL CHLORINE
ASSUMING 1% CO_2 IN PURGE STREAM

Average Power Charge & Discharge	0.3 volts	0.6 volts	1.0 volts
Watts -- Lower CO_2 Rate	17.5 watts	35.0 watts	58.0 watts
Watts -- Upper CO_2 Rate Limit	39.0 watts	78.0 watts	129.0 watts

Accepting limitations, a conservative projection is that, for a good design, the first cell in the series will operate at least 50 mA/cm^2 at 0.6 volts with an outlet concentration 30% of the inlet. Area for this cell would be 821 cm^2 for the lower projected chlorine removal to 1817 cm^2 for the upper limit. At least two additional equivalent stages, operating at lower current densities, conceivably would be required to fully remove the remaining chlorine. Recognizing the limitations of this area projection, it may be concluded that the device would be somewhat bulky, unless methods can be found to increase the current density.

Inert Gas Separation by Hydrate Formation

This section considers the possibility of a properly constructed low-rate auxiliary hydrate former which, in operation at close to equilibrium conditions, would remove sufficient chlorine from a purge stream to concentrate the inerts. This method of CO_2 separation is considered favorable from the standpoint of reducing parasitic power because the energy expenditure is for formation of chlorine hydrate, and is required in any case for the storage of chlorine. It is possible that this device could operate only during charge. During discharge, where CO_2 production rates are lower, inerts would be allowed to accumulate and then be removed at the beginning of the next charge cycle. The equilibrium curve for hydrate formation is illustrated in Figure 36-8 which also shows possible operating temperatures at inlet and outlet.

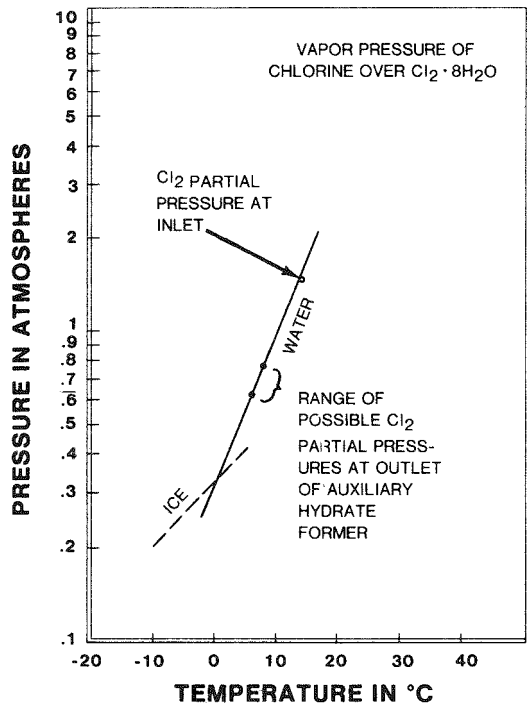

Figure 36-8. Operating points for an auxiliary hydrate former to concentrate inert gases.

Expected inlet pressure from the top of the store during charge is 1.5 atm, Cl_2 partial pressure 1.485 atm with 1% CO_2. With coolant at 5°C, the minimum conceivable equilibrium temperature at the outlet would be 6°C, and the maximum would be 8°C. The associated partial pressures also are shown in Figure 36-8. The effect on the calculated CO_2 concentration at these temperatures is given in Table 36-3 for a charge cycle with CO_2 generated at 0.03% of the Cl_2 rate.

DISCUSSION

Three of the possible methods to remove inerts gas which were considered in preliminary study offer promise for successful application to the load-leveling battery system. The methods are hydrate formation, thermal diffusion, and the electrowinning cell.

Table 36-3

OUTLET CHLORINE CONCENTRATIONS FROM A 1.5 ATM, 1% CO_2 INLET
0.0236 MOLES CO_2/HR

(Diffusional Mixing not Considered)

Temperature at Outlet	6°C	8°C
Total Pressure	≃ 1.5 ATM	≃ 1.5 ATM
Cl_2 Partial Pressure	0.65 ATM	0.81 ATM
Partial Pressure CO_2	0.85 ATM	0.69 ATM
Mol Fraction CO_2	0.57	0.46
Moles Cl_2 removed/cycle	14.8 Mole	16.6 Mole
Coolant Heat Load	51.8 Watts	51.2 watts

Hydrate formation, due to the partial pressure limitation, is applicable to an initial stage of the device to concentrate inerts using available coolant in an auxiliary former. Thermal diffusion, due to large area and parasitic power requirements, could only be used as a final stage in a device with pre-concentrated stream of inerts and chlorine serving as the feed. Because of its low molecular weight, unreacted H_2 present in the system at a concentration of 0.5% to 1.5% will interfere to some extent with the separation of the two heavier gases, CO_2 and Cl_2. The extent of this interference was not investigated in this study, due to the unavailability of relatively simple analytical methods for the three gases.

The electrowinning cell represents a method which is applicable over the entire concentration range and therefore could serve as a basis for a "single method device". Estimated parasitic powere are reasonable, being less than 130 watts in the most conservative assumptions. The technology is known with experimental demonstration of feasibility already completed. The limitation of the method is the relatively large electrode areas projected from the current densities used in present battery technology. With experimental work, however, it is considered probable that current density can be substantially increased.

REFERENCES

36-1. John H. Perry. Chemical Engineer Handbook, 4th ed. New York: McGraw-Hill, 1963, pp. 17-38 to 17-42.

36-2. _____. 5th ed. 1973, pp. 17-45 to 17-47.

36-3. R. Byron Bird, Warren E. Stewart, and Edwin N. Lightfoot. Transport Phenomena. New York: John Wiley & Sons, 1969, pp. 563-576.

36-4. R.C. Clark Jones and W.H. Furry. "The Separation of Isotopes by Thermal Diffusion." Reviews of Modern Physics, April, 1946, pp. 151-224.

36-5. John E. Powers and C.R. Wilkie. "The Separation of Liquids by Thermal Diffusion." American Institute of Chemical Engineers, 3, 1957, pp. 213-222.

Section 37

HYDROGEN EVOLUTION IN ZINC-CHLORINE BATTERIES

INTRODUCTION

Hydrogen evolution is a major concern in the zinc-chlorine battery for several reasons. Its presence causes zinc electrode inefficiency and minor difficulties in battery operation. In previous years, hydrogen evolution has been an intermittent problem in the zinc-chlorine battery. During Phase I, a major effort in the development program was directed toward identifying the major causes of hydrogen evolution on the zinc electrode. A technique using a zinc-to-zinc transfer plating cell was developed for evaluating metallic impurities in the electrolyte. Using this technique, the effects of electrolyte composition are being investigated in a continuing program.

In addition to metallic impurities acting as hydrogen promoters on zinc, chlorine-electrode degradation products were established as a source of electrolyte contamination. Although the degradation products have not been identified, they are believed to be partially-oxidized water-soluble mellitic acid-type by-products of graphite oxidation. The exact conditions leading to the production of these by-products have not been thoroughly investigated but the available information indicates electrolyte pH is the primary factor.

This section describes in detail the behavior of the zinc-transfer plating cell, the results of the metallic impurity testing program, and the experiments which demonstrate electrolyte contamination from the chlorine electrode. The results of this work will enable EDA to specify electrolyte purity to outside suppliers and will help to establish operational controls for the zinc-chlorine battery.

CHARACTERIZATION OF THE ZINC TRANSFER CELL

Impurity Removal Rates as a Function of Rotational Speed

The zinc transfer plating cell shown in Figure 37-1 consists essentially of a constant current power supply, the current monitoring equipment, and the electrodes. The porosity and limited mechanical stability of graphite electrodes precluded its use for gravimetric studies. Instead, titanium was selected for the rotating cylinder electrode because of its chemical stability and durability. However, zinc deposits tend to adhere poorly to titanium. A graphite film in a fluorocarbon binder* was applied to the titanium electrode.

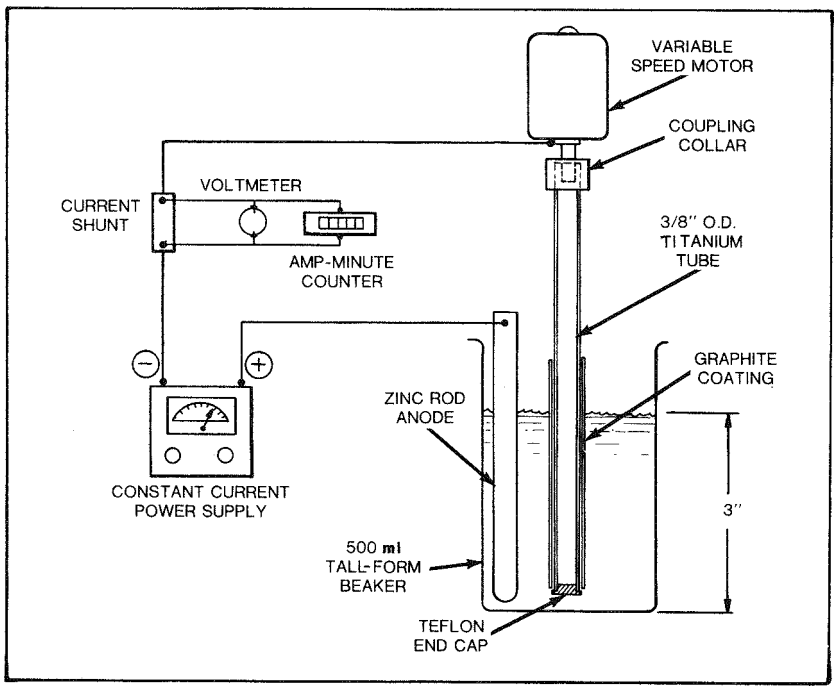

Figure 37-1. Schematic diagram of the zinc-to-zinc transfer plating equipment used to investigate metallic impurities in electrolyte solutions.

The primary function of the system is to evaluate impurity effects on the zinc electrode. The first characteristic evaluated was the impurity removal rate from the electrolyte as a function of the rotational speed. Experimentally, the

* Electroday 502, Acheson Colloids Company

removal rates were evaluated using only the rotating zinc electrode. This was done by placing a preplated rotating electrode into an electrolyte containing three tracer impurities, and adjusting the rotational speed to the desired value. For easily reduced elements, simple displacement reactions occur at the zinc surface and the removal rates depend on both diffusion and agitation. The removal rate was determined by analyzing the solutions at appropriate time intervals. The results, shown in Table 37-1, indicate an essentially linear relationship exists between the removal rate and the rotational speed. The removal rates fit the equation $C = C_o e^{-kt}$ as shown in Figure 37-2, and the half lives, $t_{1/2}$, in Table 37-1, have been derived from the impurity-removal curves.

Table 37-1

IMPURITY REMOVAL RATES AS A FUNCTION OF ROTATIONAL SPEED

rpm	$t_{1/2}$ (minutes)	rpm x $t_{1/2}$ x 10^{-2}
350	12 ± 1	42
500	9 ± 1	45
750	6 ± 1	45

Coulombic Efficiency Tests

The cell shown in Figure 37-1 may be series-connected to other cells to perform multiple tests simultaneously. The test results in Table 37-2 were obtained by using three cells in series to produce triplicate results. The tests were performed at room temperature with an applied current density of about 35mA/cm^2. All tests were conducted using a 2-molar zinc chloride solution. The pH was allowed to vary considerably and the rotational speed of the electrode was 10-30 rpm.

The coulombic efficiencies in Table 37-2 were determined by electrogravimetry. That is, the theoretical weight of zinc deposited was determined by the ampere-hours of charge, and the actual weight of the zinc deposit was determined by weighing. Inefficiencies in the zinc deposition would be primarily due to hydrogen evolution. Under the test conditions, the pH of the electrolyte has no effect on the coulombic efficiency. The results in Table 37-2 indicate the coulombic efficiency

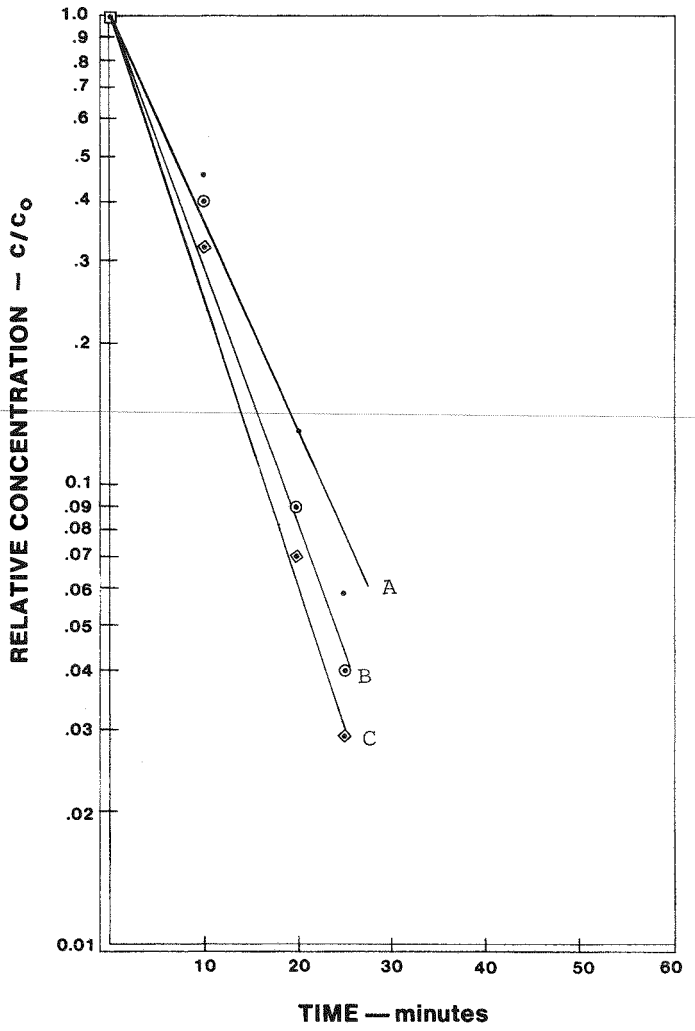

Figure 37-2. Curve showing removal of impurities from solution as a function of time.

of zinc deposition under these conditions is quantitative. Apparently accuracy is limited by the accuracy of the amp-minute counter, which is calibrated to ±0.5% but may drift slightly from day to day.

Analysis of the results shows that the standard deviation of the sets is 0.7 while the standard deviation for a set of test results is considerably less. The preci-

Table 37-2

COULOMBIC EFFICIENCY OF ZINC TRANSFER PLATING CELL

Set	Test	pH	Coulombic Efficiency (%)	Average Efficiency	Standard Deviation
83771	1	0.3	100.5	100.6	0.1
	2	0.3	100.7		
	3	0.3	100.5		
84771	1	0.1	99.2	99.1	0.1
	2	0.1	99.2		
	3	0.1	99.0		
84772	1	0.7	98.9	99.2	0.3
	2	0.7	99.2		
	3	0.7	99.5		
85771	1	1.0	100.1	100.1	0.3
	2	0.5	100.4		
	3	0.05	99.8		
85772*	1	(0.5M HCl)	97.2	97.4	0.9
	2	(0.5M HCl)	98.3		
	3	(0.5M HCl)	96.6		
88771	1	(0.5M HCl)	99.5	99.2	0.2
	2	(0.5M HCl)	99.2		
	3	(0.5M HCl)	99.0		

*Set 85772 rejected from test data by use of 2.5d rule and Q test.

sion of simultaneous testing is much better than day-to-day (sets) reproducibility. Set 85772 is considered an outlying result and is accordingly rejected from the set analysis. The average of the five sets of results is 99.6% efficiency with a standard deviation of 0.7. It is apparent, that to obtain high precision, simultaneous testing is preferred.

Coulombic Efficiencies of Zn Deposition and Zn Dissolution in Zinc Chloride Hydrochloric Acid Solutions

In the preceding section it was concluded that the deposition of zinc from a 2-molar zinc chloride solution was nearly quantitative. Just as important, however, was

that the fifteen test results establish the precision of simultaneous testing and the day-to-day reproducibility of the technique under controlled experimental conditions. In this section, the coulombic effects of varying the zinc chloride concentration and the hydrochloric acid concentration are evaluated from a statistically designed experiment. The rotational speed of the electrode was 15-30 rpm and applied current density was 25-30 mA/cm^2.

The experimental results are shown in Figures 37-3 and 37-4. The coulombic efficiencies for charge are shown as a function of the acid concentration. The data suggests a family of straight lines having the formula y = a + bx where y = efficiency, a = intercept and x = hydrochloric acid concentration. An analysis of variance for the charge coulombic efficiency indicates that the hydrochloric acid concentration is a significant parameter and that the zinc chloride concentration is statistically significant at the F = 0.01 level.

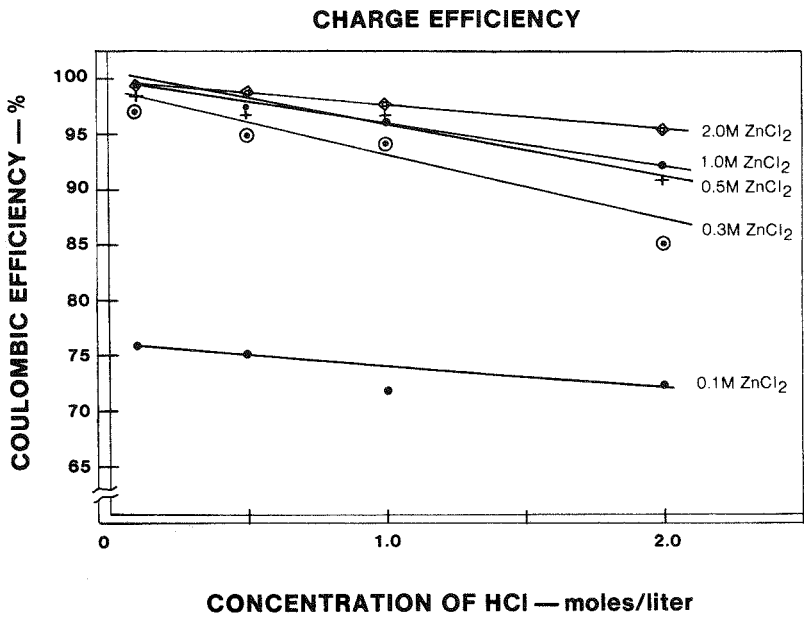

Figure 37-3. Charge coulombic efficiencies of $ZnCl_2$ electrolytes plotted against acid concentration.

Table 37-3 illustrates curve fits for the data shown in Figure 37-3. The average value of "a" for the interval 0.3- to 2.0-molar zinc chloride is 98.9 ± 1.0 and the intercept is considered to be constant within this interval. As the zinc chloride

concentration is decreased, the effect of acid strength increases, as evidenced by the increasing value of "b". The significance of this effect remains to be more fully investigated. At a zinc chloride concentration of 0.1 molar, the intercept becomes 76% and the value of "b" becomes much less significant. A plausible explanation for this is that the limiting current density for zinc deposition has been exceeded and that approximately 25% of the current is going to hydrogen evolution.

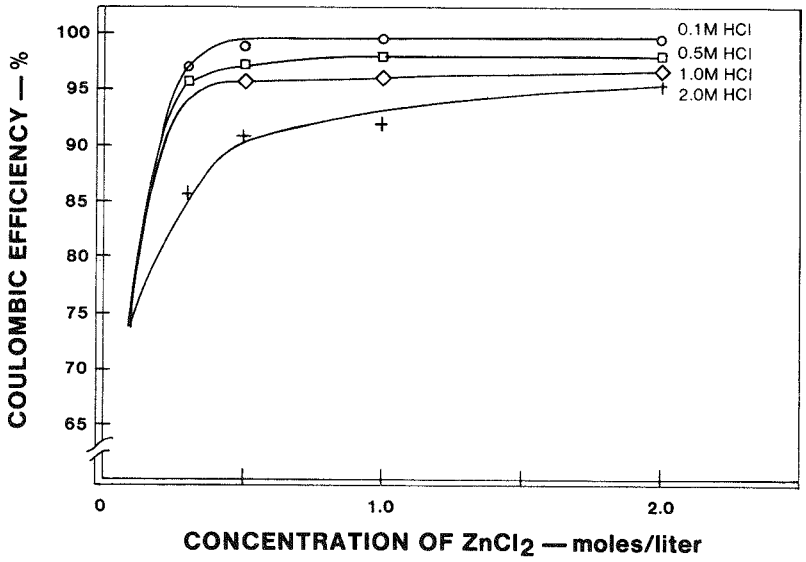

Figure 37-4. Graph showing same data as Figure 37-3 but with axis transposed to show coulombic efficiency as a function of $ZnCl_2$ concentration at constant acid strength.

Table 37-3

LEAST SQUARES FIT FOR DATA IN FIGURE 37-3

$y = a + bx$ a = intercept
y = charge efficiency x = hydrochloric acid concentration

$ZnCl_2$	a	b
2 molar	98.4	-1.46
1 molar	98.0	-3.23
0.5 molar	100.3	-4.90
0.3 molar	98.8	-5.72
0.1 molar	76.4	-1.48

Figure 37-5 shows the discharge efficiencies as a function of the acid concentration. The data is more scattered and may indicate the discharge efficiency is lower than the charge efficiency. If this is true, then the electrode potential cannot be the controlling factor regarding hydrogen evolution. Conclusions based on this single series of experiments are still speculative.

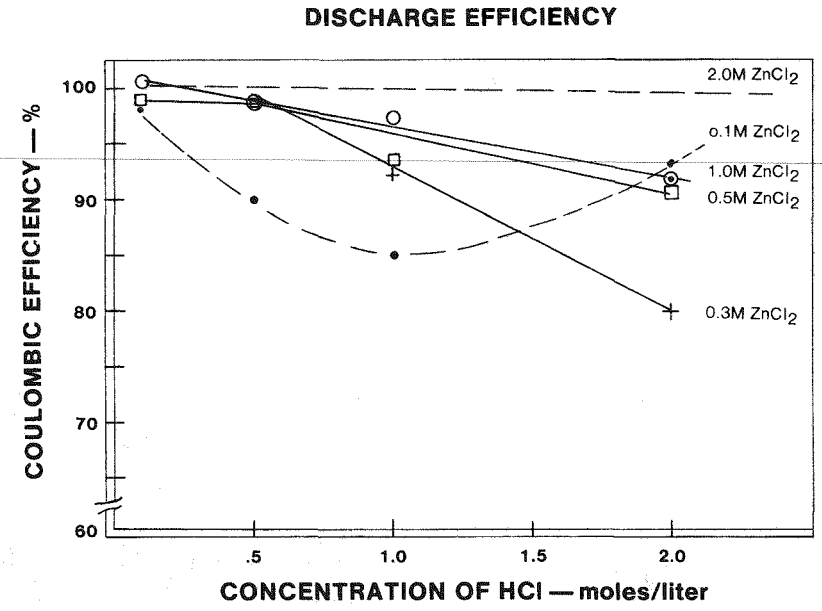

Figure 37-5. Discharge coulombic efficiencies of $ZnCl_2$ electrolytes plotted against acid concentration. Note inconsistency of data compared to charge data of Figure 37-3.

HYDROGEN EVOLUTION

Experimental Conditions for Metallic Impurity Evaluations

The experimental conditions for evaluating hydrogen evolution due to metallic impurities were determined by correlating the behavior of nickel in a test battery to its behavior in a transfer plating cell. The use of nickel was not a random selection. Its behavior in zinc-chlorine batteries has been documented. Although the test results show considerable scatter, all the results demonstrate an extensive loss in the coulombic efficiency which is attributed to the presence of nickel in the electrolyte. The losses in round-trip coulombic efficiencies were determined by the differences in coulombic efficiencies before and after nickel was added to the test cell. The average coulombic loss attributed to nickel was 14%.

The removal of nickel from the electrolyte is very slow when compared to removal of other additives. Typically, additives have a half-life of about one hour while that for nickel is about two hours. The half-life of nickel as determined by its removal rate in the zinc transfer cell produced an unexpected result. In 2-molar zinc chloride, no displacement reaction occurred and the removal rate is zero. Apparently, nickel will slowly co-deposit with zinc, but does not undergo simple displacement reactions with the metal.

The deposition efficiency of zinc from a 2-molar zinc chloride solution containing 2mg/ℓ Ni^{+2} was essentially quantitative as determined by electrogravimetry. This unexpected finding and lack of correlation to battery test results suggest that the electrolyte composition near the zinc electrode was the controlling parameter for the co-deposition of nickel. Nickel removal rates were then evaluated in the zinc transfer cell using solution of 0.10-, 0.50-, and 0.01-molar zinc chloride. In these dilute zinc-chloride solutions, nickel was observed to co-deposit with the zinc, but efficiencies were meaningless because the limiting current density for zinc was exceeded. Further testing in 0.5-molar zinc chloride produced the desired result. A solution containing 2mg/ℓ Ni^{+2} caused a 10% loss in the round trip coulombic efficiency when compared to a control.

The use of nickel to obtain correlation between the zinc transfer cell and battery test results is a rigorous test for duplication of electrode conditions. The use of a 0.5-molar zinc chloride solution in the transfer cell as compared to a 1- to 2-molar zinc chloride solution in the battery is believed to be due to differences in the agitation surrounding the respective electrodes. That is, the electrolyte near the zinc electrode in a battery is more stagnant than the electrolyte surrounding the rotating zinc electrode at 10-30 rpm.

Other aspects of the electrolyte such as the addition of potassium chloride and a pH of 0.3 are consistent with electrolyte typically used in batteries. Also, the use of a leveling agent has been found beneficial to the reproducibility of the testing. Unmodified zinc solutions produce a nodular plate on the hydrophobic graphite while the modified, fine-grained deposits tend to be more uniform.

Impurity Effects on Zinc Deposition-Dissolution Efficiencies

The purpose of this testing was to identify those elements which promote hydrogen evolution from a zinc electrolyte under conditions similar to those in a battery. In addition the magnitude of the effect has been determined by testing the impurities at different concentration levels. With this in mind, only round-trip

efficiencies were determined by charging the rotating electrode with a measured quantity of amp-minutes, and then measuring the amp-minutes required to fully discharge the electrode. The round trip efficiency is then the amp-minutes of discharge divided by the amp-minutes of charge.

During the six-month interval in which the impurities were evaluated, a control test was run 13 times as a check on the technique. The electrolyte for all the tests consisted of 0.5-molar zinc chloride and potassium chloride at a pH of 0.3 $\pm$ 0.1. The tests were conducted at room temperature, 23 $\pm$ 3°C, at an applied current density estimated to be $\pm$ 5 mA/cm^2. The charge time was nominally three hours. The control test results and the date of evaluation are given in Table 37-5.

The table shows the efficiency and reproducibility of the control are similar to other results using this technique. The procedural change instituted on 1-3-78 was made because it was found that when its oxide film is reduced, titanium catalyzes hydrogen evolution at the zinc potential. In most of the previous tests,

Table 37-5

CONTROL RESULTS FOR IMPURITY TESTING
USING ROTATING ZINC ELECTRODE

Date	Initial pH	Coulombic Efficiency (%)
8/15/77	0.30	96.1
8/18/77	0.30	96.9
8/19/77	0.30	94.1
8/24/77	0.30	96.1
8/26/77	0.30	96.2
8/29/77	0.30	96.2
9/1/77	0.30	96.2
10/12/77	0.31	93.8
10/25/77	0.31	96.4
11/1/77	0.30	93.9
1/3/78	0.30	99.1*
1/16/78	0.30	98.8*
1/25/78	0.30	97.9*
	AVERAGE:	96.3
	STANDARD DEVIATION:	1.7

*Procedural changes made using thicker graphite coating.

the titanium was anodized before coating with the graphite. Repeated anodizing was found to be both inconvenient and of limited value. Also, the thin graphite films sometimes contained pinholes or were slowly permeated by the electrolyte which caused the film to lose adherence. No problems have been encountered with the thicker graphite coatings and, as the last three control tests show, the average control efficiency is higher. In addition, the standard deviation is lower for the last three tests. These results indicate less substrate interference and better test reliability. The procedural change does not affect the interpretation of impurity test results prior to the change.

The results for the impurity testing are given in alphabetical order in Table 37-6. Again, the electrolyte composition for all the tests was 0.5-molar zinc chloride and potassium chloride. A round trip coulombic efficiency of less than 94% is considered a positive test for hydrogen promotion on zinc due to the presence of an impurity.

Test results show antimony to be the most detrimental impurity tested. At the 1 mg/ℓ level, Co, Ge, Ni, and Sn also cause considerable hydrogen evolution. Both iron and copper are detrimental at somewhat higher levels. Somewhat surprisingly, arsenic is not observed to be a catalyst for hydrogen evolution on zinc as indicated by some literature references.

Although elements such as chromium, manganese, and vanadium do not affect the zinc coulombic efficiency by hydrogen evolution, their presence in a battery is undesirable. They would cause coulombic inefficiencies because they undergo redox reactions with the dissolved chlorine and the zinc electrode. Although most, if not all, of these impurity effects may be referenced in the literature, their evaluation under the conditions in which a zinc-chlorine battery operates is necessary due to the high acidity and chloride ion strength.

Hydrogen Evolution Due to Graphite Degradation Products

In the previous section, a detailed account was presented about metallic impurity effects on hydrogen evolution at the zinc electrode. Because the design of the technique permits conditions to be rigidly controlled and experiments may be repeated to insure reliability, unequivocal results may be obtained. In this section, it is demonstrated again that reproducible and reliable results are

obtained, but the interpretation of the results is somewhat speculative because the identity of the hydrogen-promoting species has not been proven.

Table 37-6A

ZINC DEPOSITION-DISSOLUTION EFFICIENCY
IN THE PRESENCE OF IMPURITIES

Impurity (mg/ℓ)	pH	Round Trip Coulombic Efficiency (%)
As-100	0.20	96.8
As-100	0.01	96.2
As-50	0.06	96.0
As-10	0.30	96.0
As-5	0.30	95.5
As-1	0.30	94.8
Cd-100	0.30	100.0
Cd-50	0.30	99.1
Cd-10	0.30	97.4
Co-5	0.29	83.8
Co-1	0.30	87.2
Co-0.1	0.30	95.3
Co-0.01	0.29	96.4
Cr-100	0.30	98.3
Cr-50	0.30	99.6
Cr-10	0.30	93.0
Cr-5	0.30	97.2
Cr-1	0.30	96.4
Cu-100	0.30	82.5
Cu-50	0.31	90.3
Cu-10	0.31	94.3
Cu-5	0.30	95.7
Fe-100	0.30	79.7
Fe-50	0.30	90.2
Fe-10	0.29	94.3
Fe-1	0.30	94.9
Ge-10	0.30	19.5
Ge-0.1	0.30	90.4
Ge-0.01	0.29	96.5

Table 37-6B

Impurity (mg/ℓ)	pH	Round-Trip Coulombic Efficiency (%)
In-50	0.30	97.2
In-10	0.30	95.2
In-5	0.29	95.8
Mn-100	0.30	99.0
Mn-50	0.30	99.2
Mn-10	0.30	92.2
Mn-5	0.29	98.1
Mn-0.1	0.25	96.2
Mn-1.0	0.29	94.4
Ni-50	0.30	83.8
Ni-10	0.30	78.8
Ni-5	0.30	85.1
Ni-1	0.30	93.2
Ni-0.1	0.30	92.4
Ni-0.01	0.30	94.2
Sb-1	0.30	25.8
Sb-0.1	0.30	56.9
Sb-0.01	0.22	93.2
Sb-0.5	0.30	55.3
Sn-100	0.28	77.5
Sn-50	0.30	80.2
Sn-25	0.30	82.2
Sn-10	0.30	81.1
Sn-5	0.30	76.3
Sn-1	0.30	82.2
Sn-0.1	0.30	92.4
Sn-0.01	0.30	95.4
V-100	0.30	96.5
V-50	0.30	97.7
V-10	0.30	97.1
V-5	0.30	95.3
V-1	0.30	95.1

Graphite degradation products have been long postulated to be a potential source of electrolyte contamination. In the past, three distinctly different degradation products have been observed. These are carbon dioxide, particulate graphite, and an electrolyte-soluble product which imparts a yellow-orange coloration to the

electrolyte. This third material is believed to be a partially oxidized, relatively low molecular weight substance. It has been observed when batteries have been operated at high pH's for extended time periods. It also has been observed during alkaline cleaning of some poorly performing test cells. All three of these products are formed during electrode activation whether by electrolysis or hot nitric acid treatment.

To evaluate activation by-products, two normally operating cells in the development lab were activated by electrolysis. After electrolysis, the cells were incompletely washed and filled with a standard battery electrolyte at a pH = 0.14. The test cells were then charged at a current density of 30 mA/cm^2 at 40°C. After 1.5 hours of charging, gas samples were found to contain 17% hydrogen and 36% hydrogen, respectively. Following this test, an exhaustive series of washing techniques followed in an attempt to restore the cells to their original behavior. These techniques included extensive dilute NaOH washings, acid washings, water washings, and caustic electrolysis; all followed by battery operation and evaluation of H_2 and CO_2. This extensive testing was performed at 50°C and, although cell performance improved, hydrogen evolution rates were unacceptable.

Further testing included measuring the carbon dioxide evolution rate as a function of temperature. The results are given in Table 37-7. Based on these results, a decision was made to lower the battery temperature to less than 40°C. Washing and continued operation of the batteries at lower temperatures resulted in a rapid disappearance of the high hydrogen evolution.

After the performance of the cells had returned to normal, another test was designed to evaluate the effects of pH on cell performance. In this test three cells were used: two of the cells acting as controls and one cell for the experiment. The electrolyte for the test was a 3-molar zinc chloride solution containing potassium chloride. The pH of the control electrolytes was adjusted to near zero, while the pH of the test cell was adjusted to one. During the charge cycle, gas samples were analyzed periodically to determine the hydrogen and carbon dioxide evolution rates. These results are shown in Table 37-8.

Table 37-7

AVERAGE CARBON DIOXIDE EVOLUTION AS A FUNCTION OF BATTERY TEMPERATURE DURING A THREE-HOUR CHARGE

Conditions: 3M $ZnCl_2$ + KCl + NaCl

Charge: 30mA/cm^2

Cell	Temperature °C	Average % CO_2 in Chlorine Stream
3A	40	0.08
	50	0.15
0	30	0.03
	40	0.07
	50	0.12
1A	30	0.02
	40	0.04
	50	0.13

Table 37-8

HYDROGEN AND CARBON DIOXIDE EVOLUTION IN A ZINC-CHLORINE BATTERY AS A FUNCTION OF ELECTROLYTE pH

Time	Cell 0 pH=0.01		Cell 1A pH-0.0		Cell 3A pH=1.0	
(hours)	%H_2	%CO_2	%H_2	%CO_2	%H_2	%CO_2
0.5	*	0.05	0.6	0.1	0.5	0.3
1	*	0.04	0.3	0.04	0.7	0.2
2	*	0.03	0.2	0.02	0.5	0.4
4	0.03	0.04	0.1	0.03	2.9	0.8
6	0.1	0.06	0.1	0.03	run terminated	

*Hydrogen level too low for accurate measurement.

The same tests were repeated the following day. However, the electrolyte in cell 3A was changed and again the pH was adjusted to one. The performance of cells 0 and 1A remained unchanged while both the carbon dioxide and hydrogen evolution in cell 3A increased.

The results for cell 3A were replicated a third time and the cell was then cycled for three days with a very acidic electrolyte. Following the acidic cycling, the cell was operated under normal conditions and its performance returned to an acceptable level.

The tests demonstrate that the battery may produce its own contaminants. As stated earlier, these contaminants have not been identified but their source is traceable to the chlorine electrode. The results in Table 37-8 suggest an induction period of about 4 hours before the occurrence of significant increases in hydrogen evolution. At about the same time, the carbon dioxide level also increases. No appreciable oxygen evolution was detected. The limited information presented here indicates a reproducible contamination mechanism, but an explanation supported by experimental data is not yet available.

DISCUSSION

The information in this section dealt principally with contaminant effects at the zinc electrode and the efficiency of zinc deposition under various conditions. The zinc transfer plating cell has proven to be a valuable tool for investigating the effects of metallic contaminants. It is expected that this technique with further refinements will be used for fundamental studies, as well as for impurity evaluations. Hydrogen evolution due to the presence of impurities is a readily accepted result. However, hydrogen suppression due to impurities requires detailed experimental proof and, hopefully, a mechanism.

The rotating zinc electrode information will be used to establish a purity specification for the electrolyte. In conjunction with this, analytical procedures and purification techniques are being developed both to detect and remove impurities regarded as detrimental.

The verification of the chlorine electrode as a source of contamination leading to hydrogen evolution confirms an old speculation. The temperature and pH effects have been used to establish operating guidelines to insure stable battery performance.

As proof of the usefulness of this program it should be pointed out that no problems with hydrogen evolution have been encountered since mid-1977.

APPENDIXES

APPENDIX A

THE ZINC-CHLORINE BATTERY: HALF-CELL OVERPOTENTIAL MEASUREMENTS

Jacob Jorné, Jung Taek Kim,* and Dennis Kralik**
Department of Chemical and Metallurgical Engineering
Wayne State University
Detroit, Michigan 48202

ABSTRACT

The voltaic performance of the zinc-chlorine battery was investigated by measuring the individual potentials of the Zn and Cl_2 electrodes vs. a reference electrode. The overpotential at the Zn electrode is very small for both the charging and the discharging, and the use of a flow-through porous Cl_2 electrode is advantageous. Energy efficiency in the range of 65% has been achieved for a complete cycle. Tafel polarization data for both the zinc and the Cl_2/graphite electrodes was obtained using rotating zinc hemisphere and graphite disk electrodes. Exchange current densities and Tafel slopes are reported.

* Present address: Bell Laboratories, Murray Hill, N.J. 07974
** Present address: Diamond Shamrock Company, Painesville, Ohio 44070

INTRODUCTION

The zinc-chlorine battery concept is based upon the electrochemical reaction between zinc, chlorine and $ZnCl_2$ aqueous solution, and the simultaneous chemical reaction between chlorine and water [1]. The overall reactions are:

$$ZnCl_2(aq) \rightleftarrows Zn(s) + Cl_2(g)$$

$$Cl_2(g) + XH_2O \rightleftarrows Cl_2 \cdot XH_2O$$

$$X \simeq 5.9 \cdot$$

The reactions are highly reversible. The emf of a $Zn\text{-}Cl_2$ cell under standard conditions is 2.12 V. During the charging process, the $ZnCl_2$ electrolyte is electrolyzed, yielding a zinc deposit on an inert graphite substrate and Cl_2 evolution on a porous flow through graphite anode. The Cl_2 gas is removed from the cell to another chamber where it is mixed with water at approximately $10^{\circ}C$ and chlorine hydrate is formed.

During the discharging process, chlorine is evolved by heating the chlorine hydrate, mixed with the $ZnCl_2$ electrolyte, and passing it through the porous graphite electrode. Chlorine is consumed electrochemically while zinc dissolves at the other electrode. Coulombic inefficiencies are due mainly to the chemical recombination of zinc with dissolved chlorine. It has been shown by Kim and Jorné [2] that this process is limited by the mass transfer of dissolved chlorine to the zinc electrode. The kinetics and mass transfer of the chlorine electrode on a rotating graphite electrode has been investigated by Kim and Jorné [3] and the kinetic parameters and a kinetic mechanism have been proposed.

In the present communication the voltaic behavior of a single cell is investigated and the individual over-voltages are measured using zinc or calomel reference electrodes. The reference electrode was located in a separate compartment and connected by a tube to the interelectrode space. It is shown that the overpotential on the Cl_2 flow-through graphite electrode is about 200 mV. The ohmic drop can be improved by adding KCl and NaCl as supporting electrodes. Polarization data of the zinc electrode and Cl_2 electrode were obtained using rotating zinc hemisphere and rotating graphite disk electrode, respectively.

EXPERIMENTAL

A single $Zn-Cl_2$ cell was used (EDA, Madison Heights, Michigan). The cell is shown in Figure 1 and consists of a dense graphite electrode (Union Carbide ATJ Graphite) on which zinc is deposited, and a porous flow-through graphite electrode (Union Carbide Porous Graphite Grade 60) on which chlorine is evolved. The thickness of the porous graphite electrode is 0.2 cm and the porosity is 0.52. The gap between the two electrodes is 0.2 cm. The apparent active area of the electrodes was 68 cm^2, the total current was 3 A and the charging process lasted for 1-2 hours.

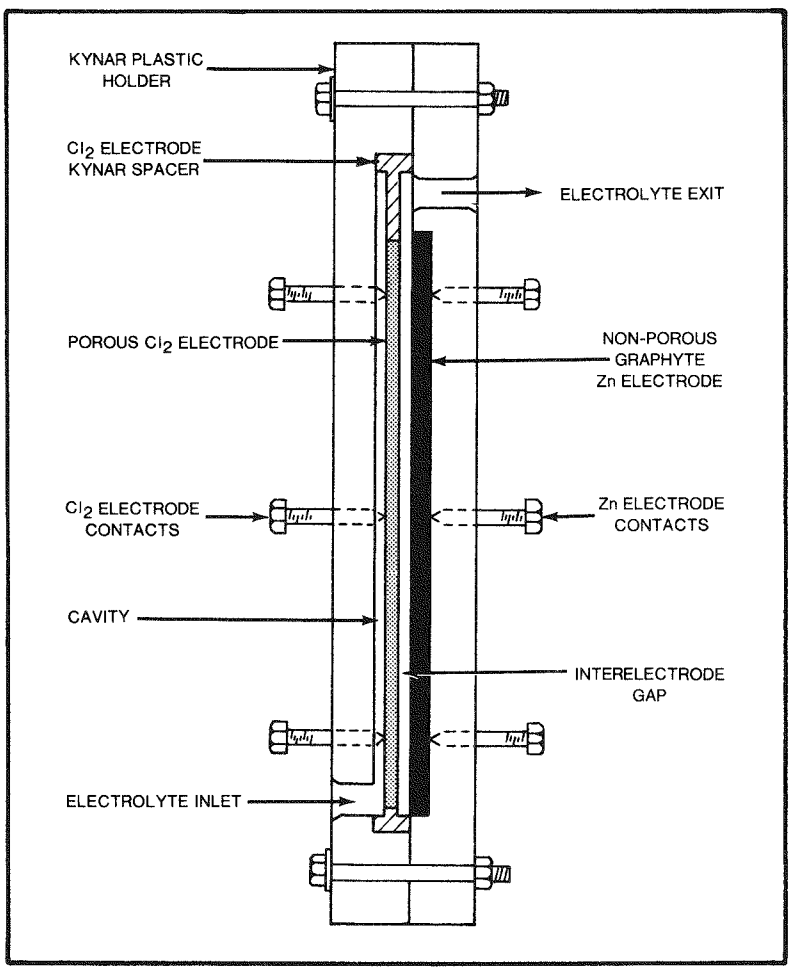

Figure 1. The single cell (cross section).

The experimental setup is shown in Figure 2. A 2.5 liter $ZnCl_2$ (2M) solution was circulated through a flow meter and the cell using a Kynar pump with a teflon gear (EDA modified micropump). The flow rate was 60 ml/min. The evolved Cl_2 was stripped during the charging by nitrogen bubbling throughout the experiment. Prior to each experiment the pH was adjusted by adding HCl and nitrogen was bubbled to remove oxygen and remaining dissolved chlorine. The charging time was adjusted so that the amount of electricity was always the same, 0.080 A Hr/cm^2. The zinc deposits were peeled gently off the graphite substrate, washed thoroughly, dried and weighed. The $ZnCl_2$ concentration was 2M and is some cases KCl and NaCl supporting electrolytes were added in order to reduce the ohmic resistance. In some cases the $ZnCl_2$ concentration was reduced down to 0.5 M.

During the discharging, Cl_2 gas was bubbled through the electrolyte reservoir and fed to the cell with the flowing $ZnCl_2$ solution. The discharging lasted until the cell was completely exhausted and all the Zn deposit was redissolved.

The reference electrode consisted of a Zn rod or SCE placed in a separate compartment filled with the cell's $ZnCl_2$ solution. The reference electrode compartment was connected to the cell by a tube, and by small holes in the interelectrode spacing. The tops of the holes were located in the middle of the gap between the two graphite electrodes. The overpotentials were corrected for ohmic drop using the conductivities of the solutions.

The current was applied by an Udylite PC-10 constant current power supply. The potentials were measured by a Keithley 600 A electrometer and recorded on a multichannel recorder (Honeywell Electronik 194) for the entire charging and discharging of the cell. The amount of electricity passed was measured by an EDA digital coulometer and agreed well with the current-time measurements.

The rotating graphite disk electrode consists of a teflon support rod and a central dense graphite electrode (ATJ Union Carbide). The central graphite electrode was embedded in the teflon rod. The diameter of the graphite electrode was 0.95 cm and the diameter of the teflon rod was 1.9 cm. The rotator was a Pine Instrument ASR rotator with a rotational speed of 0 to 10,000 rpm. The surface of the electrode was polished with waterproof Al_2O_3 paper and a fine paper using the rotator (ω=4,000 rpm).

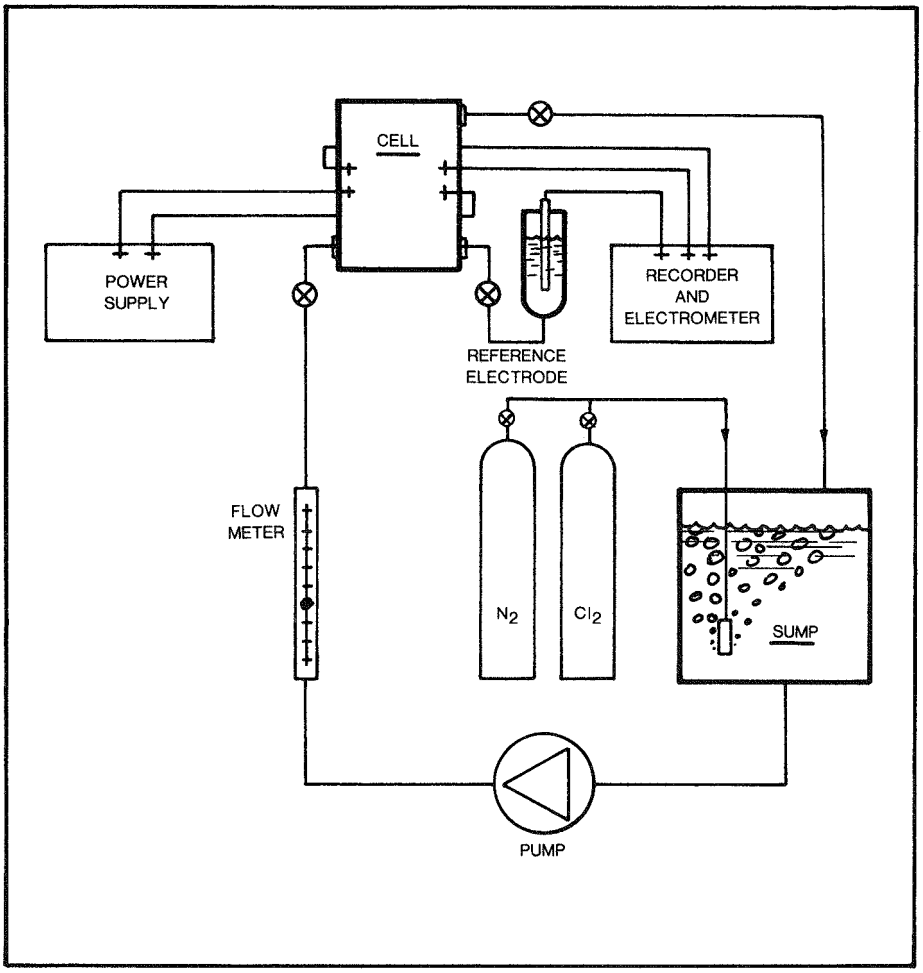

Figure 2. The experimental system.

A 1,000 ml pyrex vessel fitted with a teflon cover was used as the cell container. It was equipped with a 2.25 cm^2 counter platinum electrode compartment connected to the cell by a small glass tube. A saturated calomel electrode (SCE) served as a reference electrode and was placed in a separate reference electrode's compartment connected to the main cell by a capillary extending to the side of the rotating disk electrode. The top of the luggin capillary was located at a distance of 3.5 cm from the center of the disk. The ohmic drops were calculated according to Newman [4].

The potential of the graphite disk electrode was controlled by a Wenking LT 73 potentiostat. A wave form generator (TWG 500) was used in conjunction with the potentiostat in order to sweep the potential of the disk electrode. The potential-current data were recorded on a Houston Instrument 2000 X-Y Recorder.

The $ZnCl_2$ solution was obtained from EDA, Inc. where it was prepared by direct recombination of Cl_2 gas and pure Zn rods (99.999% New Jersey zinc). The $ZnCl_2$ concentration was measured by hydrometer. Cl_2-N_2 gas mixtures were fed into the cell by a gas expenser, and the dissolved Cl_2 concentration was maintained by measuring the Cl_2 and N_2 flow rates. The dissolved Cl_2 concentration was measured by standard titration using 1/100 normal $Na_2S_2O_3 \cdot 5H_2O$. Dissolved oxygen was removed by bubbling N_2 prior to the experiments, and the Cl_2-N_2 gas mixture was bubbled throughout the experiments.

The polarization measurements of the zinc metal in zinc chloride solution were performed on a rotating hemispherical zinc electrode [3]. In order to eliminate the concentration overpotential, the rotational speed of the electrode was ω=3,000 rpm, sufficiently high not to influence the concentration overpotential. Hemispherical electrode was used because its primary current distribution is uniform.

RESULTS AND DISCUSSION

Single Cell

The polarization of the zinc and the chlorine electrodes vs. the zinc reference electrode was measured during the charging and the discharging of the single cell. Typical polarization curves are shown in Figures 3 and 4 for the charging and charging-discharging cycles, respectively.

The upper curves show the Cl_2 - porous graphite electrode potential, and the lower curves represent the Zn electrode potential vs. the reference electrode. The overall cell potential is the difference between the two curves and is 2.30 V during the charging and 1.80 V during the discharging. The individual overvoltage can be read from the drop in the potential after the current is shut off. The main polarization appears to be on the Cl_2 electrode. The overpotential on the

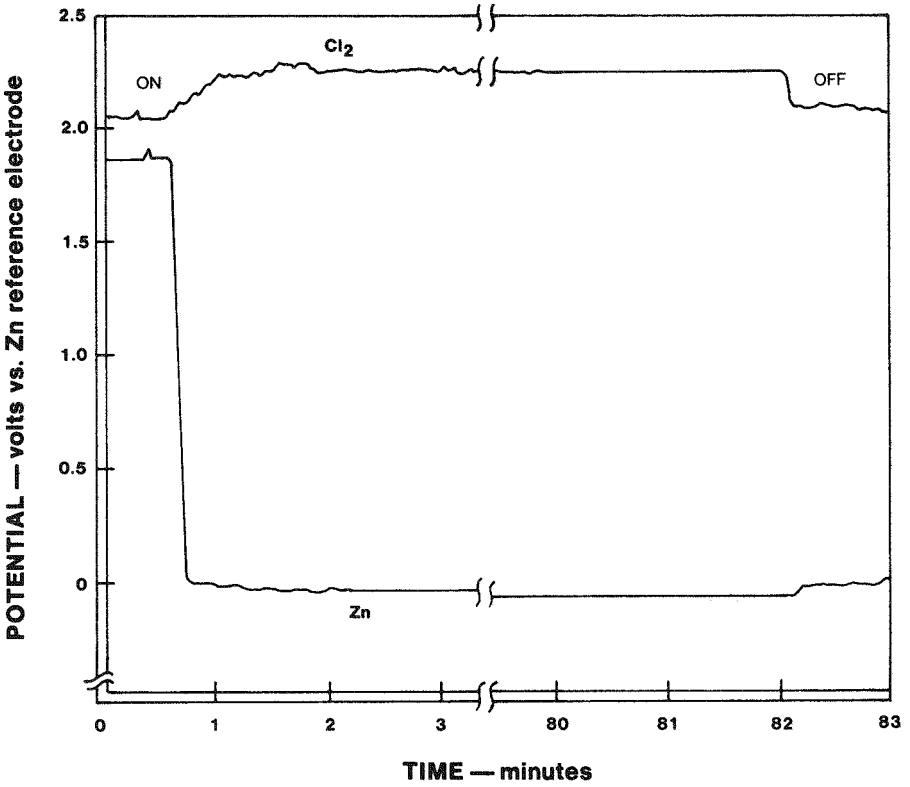

Figure 3. The potentials of the Cl_2 and Zn electrodes vs. the Zn reference electrode during the charging.

Electrolyte:	$ZnCl_2$ (2M)
Temperature:	25°C
Total Current:	3 A
Apparent current density:	44mA/cm^2
Reference electrode:	Zn

Zn electrode is very small, below -50 mV during charging and below +40 mV during discharging. The overpotential on the Cl_2 electrode is +100 mV and -200 mV during charging and discharging, respectively. By adding KCl (2M) and NaCl (2M) as supporting electrolytes, the ohmic drop was reduced significantly and the overall cell potential was reduced to 2.20 V during the charging and increased to 1.90 V during the discharging. The voltaic performance of the cell improved by adding KCl both during charging and discharging; however, the addition of NaCl lowered only the charging voltage, but did not improve the discharging voltage as expected from conductance measurements.

The source of the electrode overpotentials is mostly kinetic. Because of the high Zn^{++} and Cl^- ionic concentrations, mass transfer overpotential is small during the charging process. Mass transfer overpotential can become significant only during the discharging process at the Cl_2 electrode. The solubility of Cl_2 in the solution is on the order of 0.01 M; however, the use of a flow-through porous electrode eliminates the significance of mass transfer overpotential. Kim and Jorné [3] measured the mass transfer and the kinetics of the cathodic reduction of dissolved Cl_2 and showed that the kinetics of the reaction are moderately fast (i_o = 1.1 mA /cm^2). Therefore, using a flow-through porous electrode ensures that mass transfer is not the rate determining step during the discharging process.

A complete cycling of the single cell is shown in Figure 4, where the potentials of the Zn and Cl_2 electrodes were measured vs. SCE. The average charging voltage was 2.3 V and the average discharging voltage was 1.8 V. The voltaic efficiency is given by 1.8/2.3 = 78%. The coulombic efficiency was measured from the total charge passed during the charging and discharging, 6,000 and 5,040 coul, respectively. Hence, the coulombic efficiency is 5,040/6,000 = 84%. The energy efficiency is given by

$$\text{energy efficiency} = (\text{voltaic efficiency}) \times (\text{coulombic efficiency})$$
$$= 0.78 \times 0.84 = 66\%$$

The overpotentials at the Zn electrode are -50 mV and +40 mV for the charging and discharging, respectively. The overpotentials at the Cl_2 electrode are +120 mV and -200 mV for the charging and discharging, respectively. At the end of the discharging process, all of the zinc is removed from the graphite substrate and Cl_2 is evolved and the recorded potential corresponds to that of the anode during the preceding charging process (see Figure 4).

Tafel's Kinetic Parameters

The Tafel polarization data for Cl_2/Cl^- on a dense graphite electrode is shown in Figure 5. The data was corrected for ohmic drop using Newman's method [4]. The apparent exchange current density, i_o = 1.1 mA/cm^2, is obtained from the intercept of the cathodic and anodic polarization branches. The anodic and cathodic Tafel slopes are b_a = 124 and b_c = -120 mV/decade, respectively. The present parameters are in agreement with the results of Hine [5] for NaCl solution

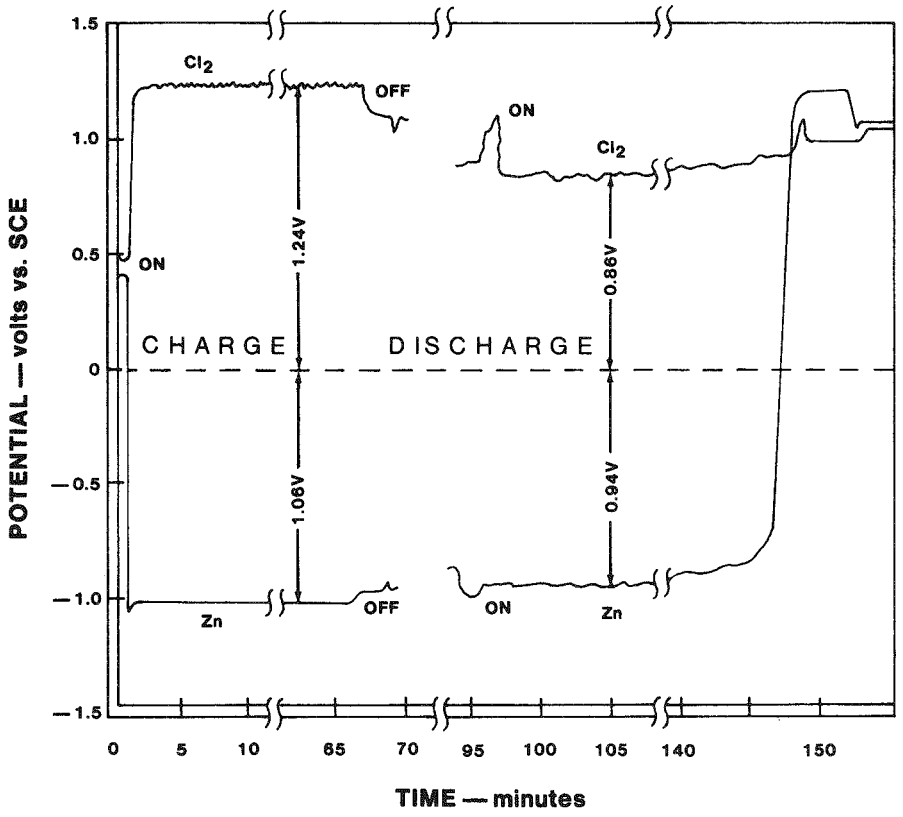

Figure 4. The potentials of the Cl_2 and Zn electrodes vs. SCE reference electrode during the charging and discharging cycle.

Electrolyte:	$ZnCl_2$(2M) + KCl(4M)
Temperature:	25°C, pH = 0.1
Total current:	1.5 A
Apparent current density:	22mA/cm^2
Reference electrode:	SCE
Cl_2 concentration during the discharging:	2.4g/ℓ

(i_o = 1.2 mA/cm^2, $b_a = -b_c$ = 120 mV/decade). The deviation from linearity at the far cathodic potential range E < 0.75 V vs. SCE in Figure 5 is due to mass transfer overpotential. Detailed studies of the kinetics of the Cl_2/graphite electrode in $ZnCl_2$ solution is presented by Kim and Jorné [2].

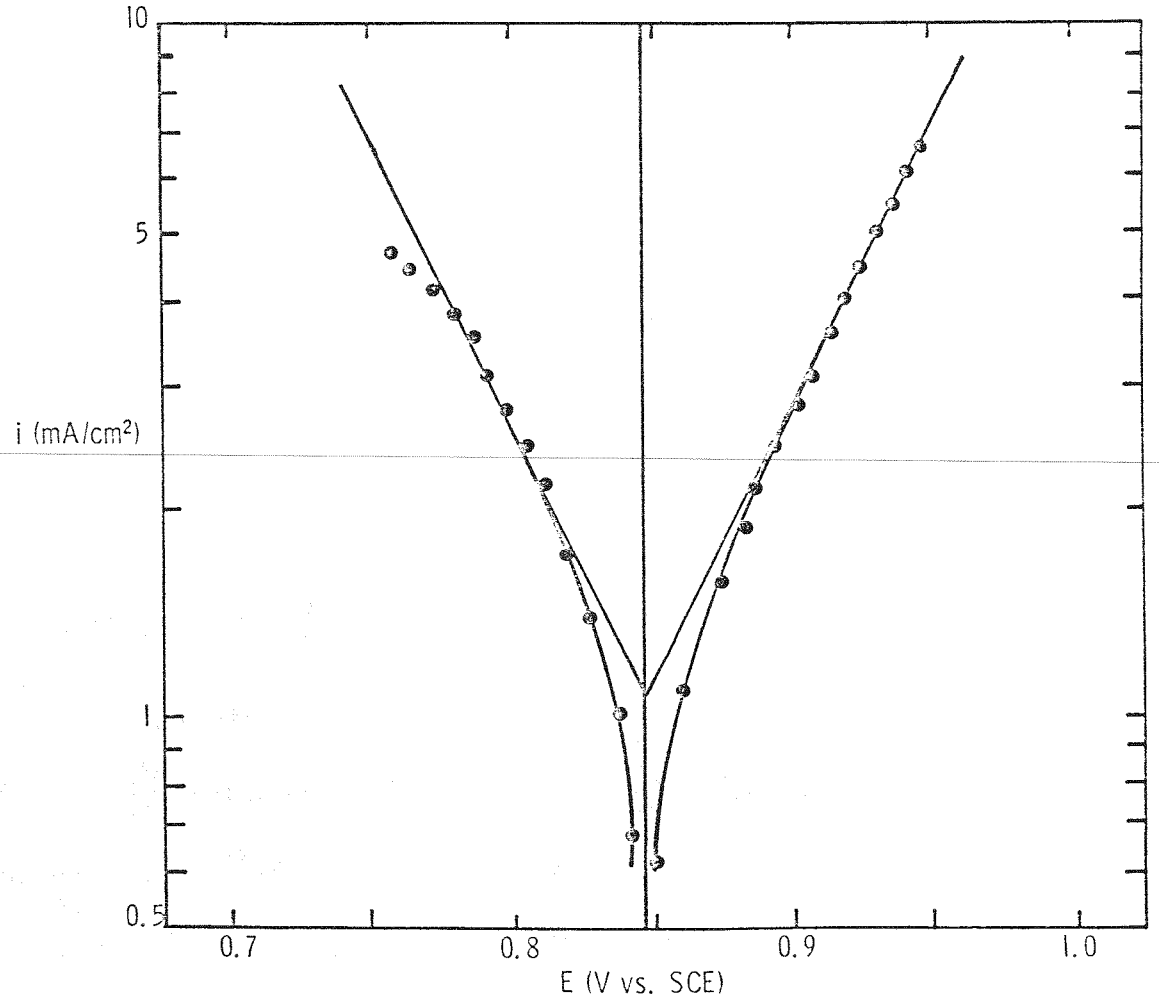

Figure 5 Anodic and cathodic Tafel polarizations of graphite electrode in 37% weight $ZnCl_2$ solution. $[Cl_2]$ = 1.17 g/ℓ; area = 0.713 cm^2; PH = 3.29.

The Tafel polarization curves for the zinc electrode in various $ZnCl_2$ solutions are shown in Figure 6. The data was corrected for ohmic drop using Newman's method [4] for the case where the reference electrode is located far away (3.50 cm):

$$R = \frac{1}{4\pi\kappa r}$$

R is the resistance (Ω), κ is the conductivity ($\Omega^{-1}cm^{-1}$) of the solution and r is the radius of the electrode (cm). The conductivities of the 0.5, 1.0 and 2.0 M $ZnCl_2$ solutions are 0.0820, 0.0943 and 0.0980 $\Omega^{-1}cm^{-1}$, respectively.

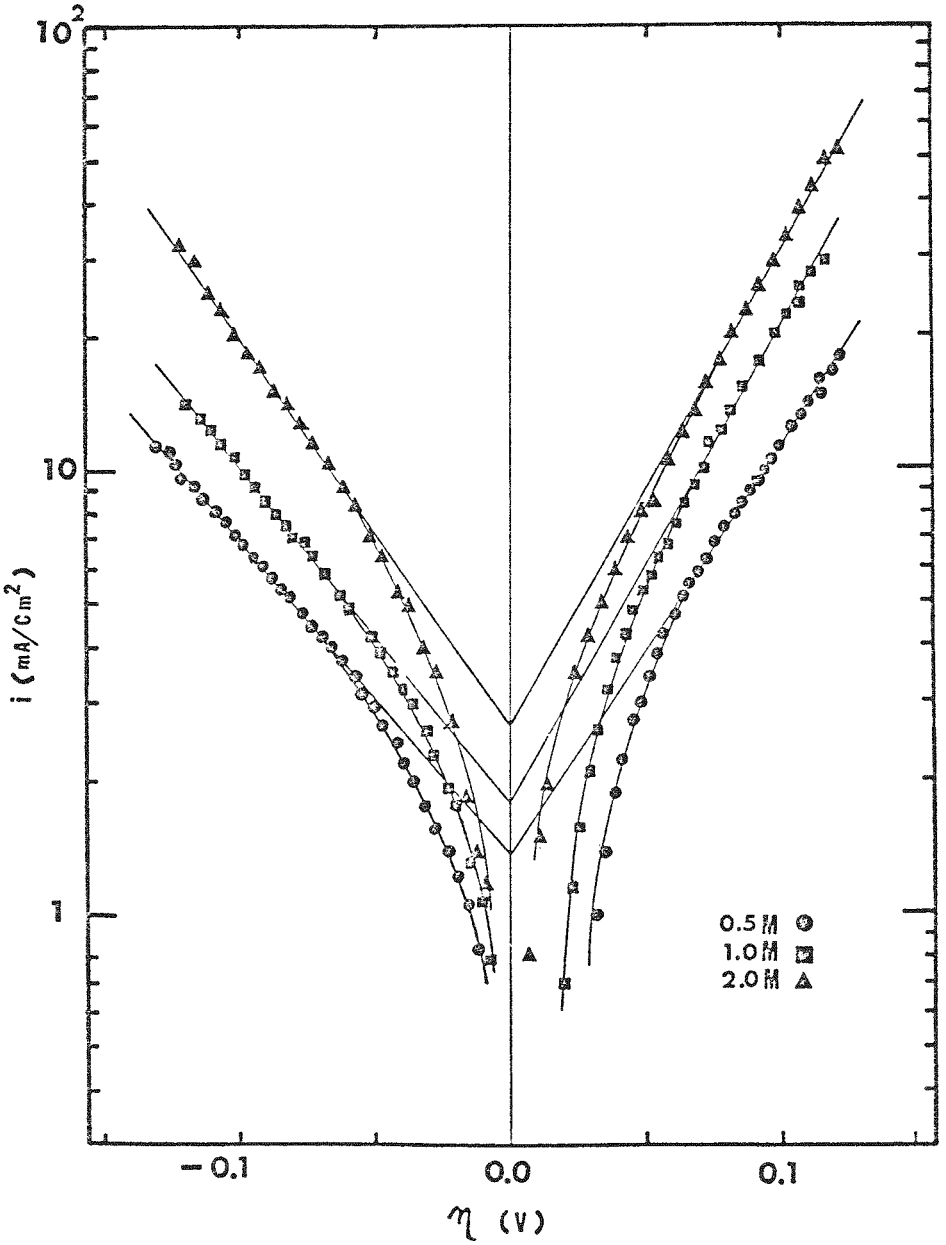

Figure 6 Anodic and cathodic Tafel polarizations of zinc electrode in various $ZnCl_2$ and 1 M KCl solutions ω = 3,000 rpm. Area of zinc electrode 0.752 cm^2.

The obtained exchange current densities and anodic and cathodic Tafel slopes are summarized in Table 1. The theoretical cathodic Tafel slope is $b_c = -[2.3RT/(1-\beta)nF]$. If a symmetric transfer coefficient $\beta = 0.5$ and one electron transfer $n = 1.0$ are assumed, then the Tafel slope is $b_c = -120$ mV. The obtained experimental cathodic Tafel slopes (see Table 1) are in agreement and the theoretical value. Sierra Alcazar and Harrison [6] measured a Tafel slope of 120 mV using an AC impedence technique.

The exchange current density (i_o) was calculated from the intercepts of the anodic and cathodic branches in Figure 6 and the obtained data is also summarized in Table 1. The exchange current density of Zn/Zn^{2+} in KCl is reported by Sierra Alcazar and Harrison [6]: i_o = 0.52 mA/cm^2 for 10^{-2} M $ZnSo_4$ + 1.0 M KCl (pH = 3.5). However, the exchange current also varies with the pH: 1.1 and 0.98 mA/cm^2 in pH of 3 and 1.8, respectively. Detailed kinetics studies and mass transfer of zinc electrode in $ZnCl_2$ solution are given by Kim [7].

Table I

THE KINETIC PARAMETERS OF THE ZINC CHLORIDE SOLUTION (pH = 2.0)

$ZnCl_2$	i_o (mA/cm^2)	b_a (mV)	$-b_c$ (mV)
0.5	1.36	108.5	139.5
1.0	1.75	94.4	131.3
2.0	2.65	90.6	113.7

CONCLUSIONS

The voltaic performance of the Zn-Cl_2 battery was investigated. Flat polarization curves were observed. The main overvoltage was detected on the Cl_2 electrode, while the Zn overvoltage was very low for both the charging and discharging steps. It is believed that most of the Cl_2 electrode overpotential is kinetic in nature due to the relative slowness of Cl_2 reaction on graphite. The ohmic drop can be improved by adding KCl or NaCl supporting electrolytes; however, NaCl was found to be inefficient in improving the discharging cell voltage. It is possible that the additional polarization during the Cl_2 reduction is caused by the salting out effect or complexing ability of NaCl in chlorinated $ZnCl_2$ solution. The use of a porous flow-through graphite electrode is essential because of the low solubility of Cl_2 and the otherwise buildup of mass transfer overpotential during the discharging of the cell. Tafel kinetics has been observed for both chlorine and zinc electrodes and their exchange current densities are in the several mA/cm^2 range.

ACKNOWLEDGMENT

This work was partially supported by Energy Development Associates, Madison Heights, Michigan, and Electric Power Research Institute, Palo Alto, California.

REFERENCES:

1. Symons, P. C. and P. Carr, "Chlorine Electrodes in the Zinc-Chlorine Battery System," Proceedings of the 8th Inter-society Energy Conversion Engineering Conference, Paper No. 739010, pp. 72-77, August (1973).
2. Kim, J. T. and J. Jorné, J. Electrochem. Soc. 124, 1473 (1977).
3. Kim, J. T. and J. Jorné, J. Electrochem. Soc. 125, 89 (1978).
4. Newman, J., J. Electrochem. Soc. 113, 501 (1966).
5. Hine, F. and M. Yasuda, J. Electrochem. Soc. 121, 1289 (1974).
6. Sierra Alcazar, H. B. and J. A. Harrison, Electrochim. Acta 22, 627 (1977).
7. Kim, J. T., "Mass Transfer and Kinetics Studies on Rotating Electrodes," Ph.D. Dissertation, Wayne State University, Detroit, Michigan (1978).

APPENDIX B

AN IMPROVED CONDENSING METHOD FOR REFRIGERATION EQUIPMENT*

Joseph D. Loveley

A Presentation Given at the
Industrial Advisory Committee Meeting
Herric Laboratories, Purdue University
September 16, 1977

---

*Based previously on a paper entitled, "Analysis of Evaporative Cooling and Enhancement of Condenser Efficiency and of Coefficient of Performance", W. Leidenfrost and B. Korenic, accepted for publication in Wärme and Stoffübertragung. See Reference (1).

INTRODUCTION

Well over a year ago the Herrick Labs had been working with an independent industrial laboratory on a load leveling concept for electric utilities. This independent research laboratory with a very specific knowledge benefited from the specialized heat transfer knowledge and capabilities of the Herrick Laboratories. Utilizing the experience of a retired engineering executive to work with Professor Leidenfrost and the two graduate students has been a very rewarding experience to all parties and is an asset in the operation of the Herrick Laboratories.

Energy storage and retrieval is becoming increasingly important in industrialized nations due to increasing costs and the fluctuating demands for electrical power. Peak power demands (essentially daytime power) are increasing faster than the off-hour (late night-early morning) demand. Building base-load power plants does not always offer the best solution for meeting an area's energy requirements. The situation could be improved considerably if base-load equipment could operate at full capacity on a continuous basis. To do this, an energy storage system is required. Ideally, the storage system would absorb all the excess energy delivered by the plant, during periods of low demand, and then return the energy to the system as the demand increases.

An attractive approach to energy storage and retrieval is the use of batteries. Batteries have been in existence for nearly 200 years and their value has long been recognized in low energy applications. The utilization of such devices for load leveling applications is once again receiving considerable attention. To be used for load leveling, the economics, reliability, efficiency, life expectancy, safety and environmental aspects of large battery systems must be competitive with other alternatives. For example, the stored water at Ludington, Michigan owned by Detroit Edison and Consumer Power has an efficiency of 66% power utilization. Present concepts of the battery indicate four major components: the zinc electrode, the chlorine electrode, aqueous zinc chloride electrolyte, and a chlorine storage system where a chiller is required.

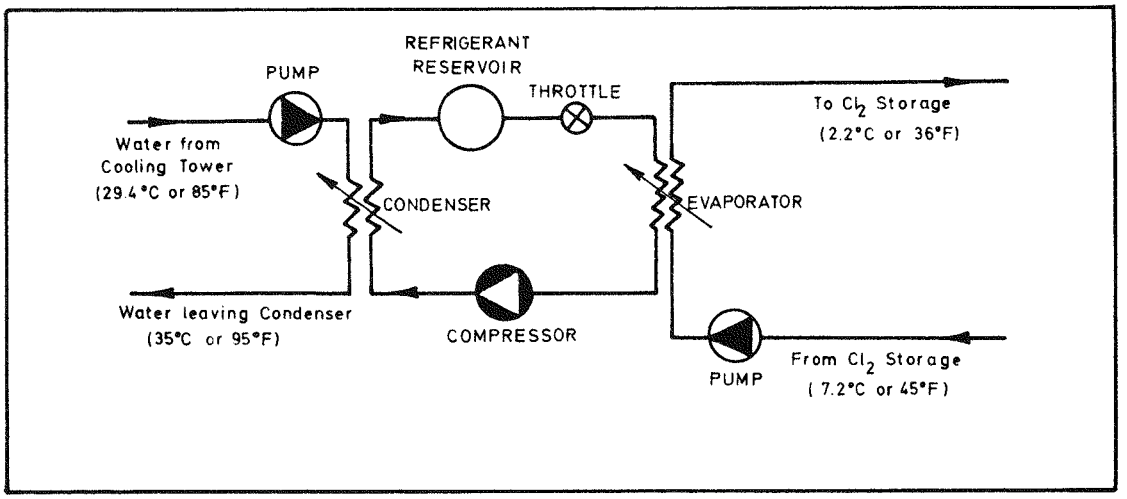

Figure 1. Refrigeration System for Chlorine Storage

A 2 kWh zinc-chloride battery has been constructed and evaluated for 100 cycles to determine the technical feasibility of this battery system for utility application. The battery was tested under operating conditions appropriate to the peaking application - approximately a 4-hour charge, 4-hour discharge cycle.

The battery system uses zinc and chlorine as the active electrode materials, employs an aqueous circulating electrolyte, and is operated at a temperature closely controlled and maintained by a centrifugal refrigeration system. The chlorine is stored external to the battery as chlorine hydrate, a slush-like material.

The 1 kWh test battery, using graphite plates for the zinc electrode and porous, ruthenized (sprayed with ruthenium) titanium for the chlorine electrode, demonstrated an average energy efficiency of 74.6% at a current density of 33 mA/cm^2. The system was operated at 27°C, a chlorine pressure of less than one psig.

The results of this study demonstrate the technical feasibility of the zinc chloride battery for utility application. The high electrochemical energy efficiency is consistent with the goals for this application.

2. PROJECT OBJECTIVES

a) The project required developing and costing out a complete bill of material for a centrifugal chiller system to cool the liquid in the process to conditions that were not ideal as to the maximum efficiency of the cooling equipment (see Figure 1).

b) The project required an investigation of air-cooled vs. water-cooled condensers. Professor Leidenfrost pointed out there were opportunities to improve efficiencies of the condensing operation by lowering condensing temperatures through a more efficient heat transfer. The economic pressures to reduce power-kw/ton or EER forces us to consider an evaporative condenser.

Consideration of an air-cooled condenser had posed many tubing and piping connections that would be hazardous because of their multiplicity. In our judgment we would be pyramiding a development on a development to use anything other than a conventional cooling tower with the water cooled condenser. The Leidenfrost concept of continuously wet heat transfer surfaces would minimize the scale and mineral deposits which are a problem with condensers cooled with cooling tower water on the inside of the condenser tubes. Where cooling towers are to be used, the build-up of scale in the condenser tubes is a continual maintenance problem and dependent upon water conditions can be critical in many areas of the country.

3. ANALYTICAL PROGRAM INITIATED

The opportunity to investigate this imporved heat transfer process is a challenge that, while it may not be available in the initial pilot installation of the load leveling process, it may become a vital part of the installations that would be made later on after the initial phases have been perfected.

4. MODELING OF A TUBE AND PLATE FIN TYPE EVAPORATIVE CONDENSER FOR WETTED, PARTIALLY WETTED AND UNWETTED OPERATION

A "blow-through" type evaporative condenser unit is shown in Figure 2. The heat exchanger consists of a tube and fin coil, 8 fins per inch, through which the refrigerant is channeled. Water is supplied by spray nozzles to the top of the heat exchanger and flows under the action of gravity downwards and is collected in a reservoir. Air enters the bottom of the coil, flows by forces convection upwards and leaves the top of the unit. The water is recirculated and replenished to the amount evaporating during the cooling process.

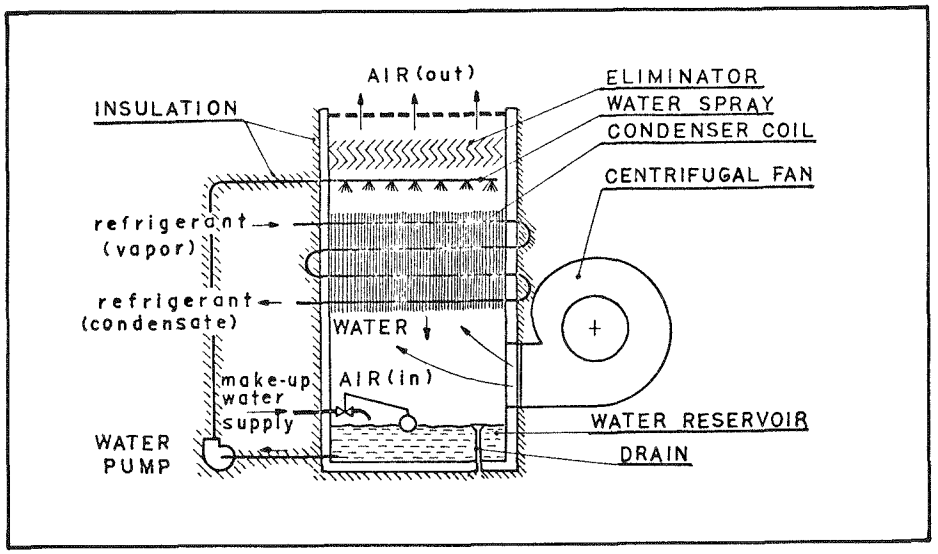

Figure 2. Evaporative Condenser Apparatus

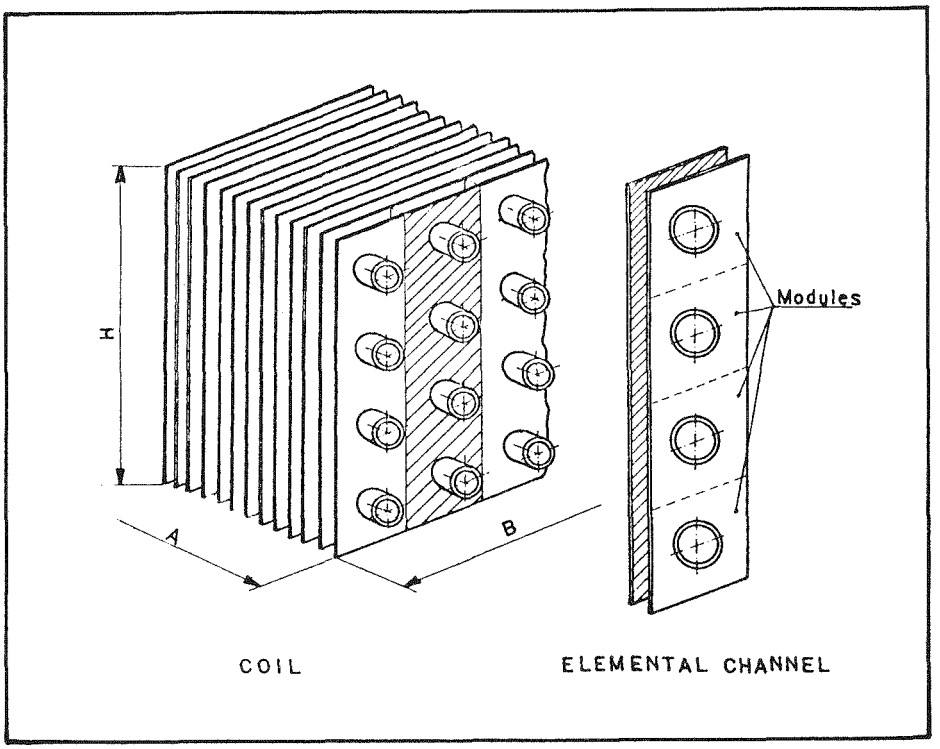

Figure 3. The elemental extended surface and its modules as a part of the evaporative condenser coil.

Figure 3 shows a close-up of the heat exchanger core being composed of identical elemental parallel fins.

Pertinent information of the geometry of one module is given in Figure 4.

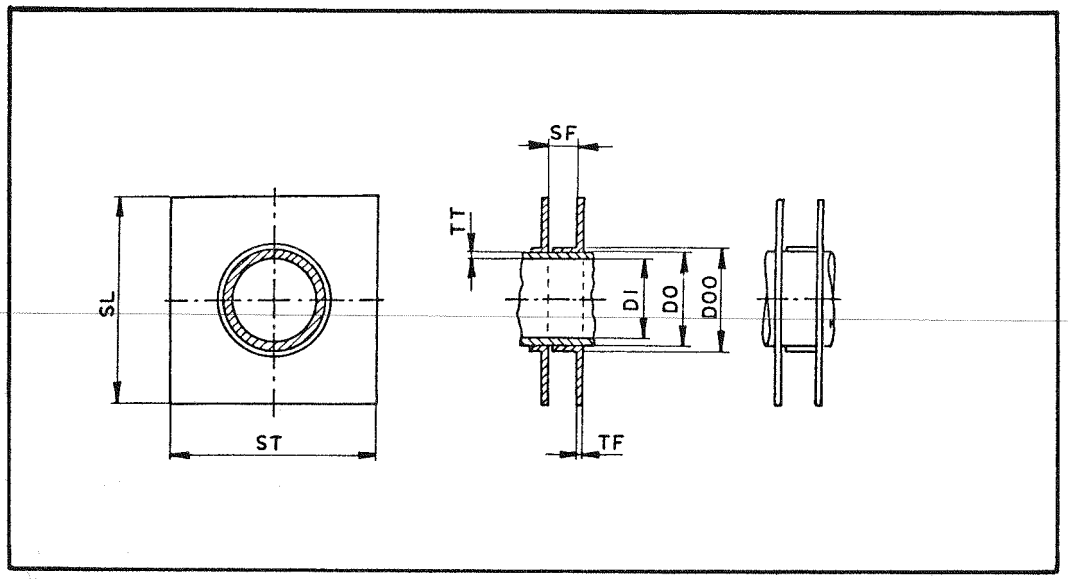

Figure 4. Module of the Plate Heat Exchanger Coil

The increase of heat transfer at the air side can be assumed to be of no influence to the convective heat transfer of the condensing refrigerant and to the conductive heat transfer through the wall. Therefore, the apparent air side convective heat transfer coefficient h_A^* can be determined from U*. h_A^*, the hydraulic diameter of the air passage, and the thermal conductivity of moist air together yield the Nusselt number Nu_A^* and the augmentation of heat transfer can be expressed as

$$\Delta Nu_A = \frac{Nu_A^* - Nu_A}{Nu_A} \qquad (1)$$

Q_{cw} is larger than the required Q_c and in a similar way as discussed above, the heat exchanger area either could be decreased to A_c^* or T_c could be lowered to T_c^* in order to lower LMTD (Log Mean Temperature Difference). This is shown schematically in the T vs. A_c plot of Figure 5.

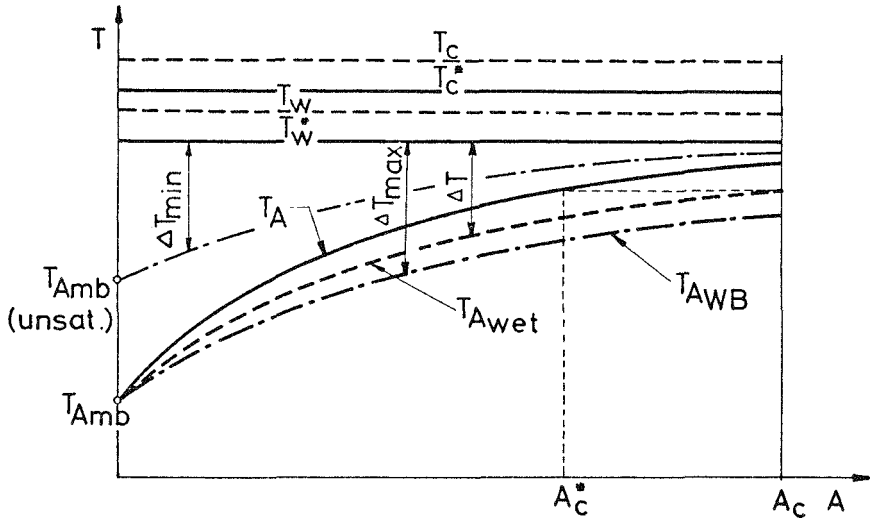

Figure 5. T vs. A_c diagram, wetting of heat exchanger surfaces.

The T-S diagram of Figure 6 demonstrates that lowering the condensing temperature to T_c^* lowers the compressor power by ΔW_{act} and increases the cooling capacity by ΔQ_e.

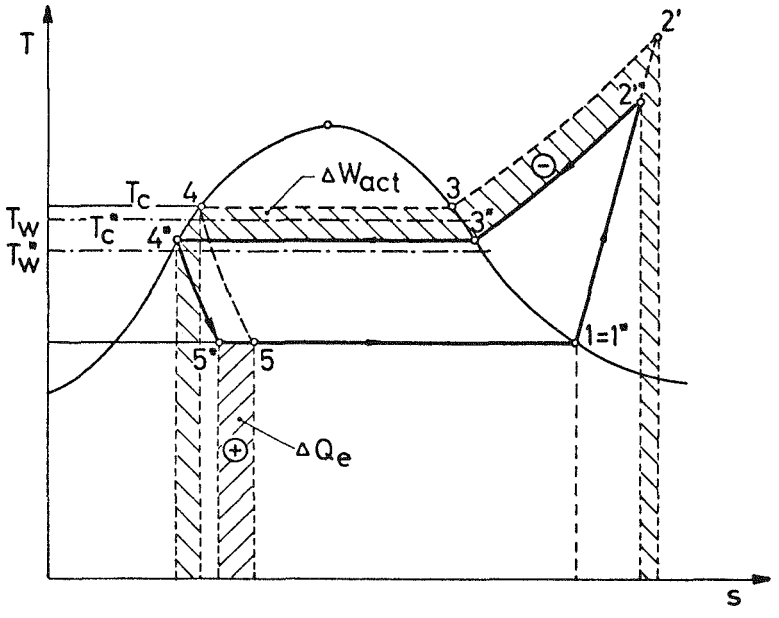

Figure 6. Temperature-entropy diagram, possible decrease of temperature of condensing refrigerant due to evaporative cooling.

The coefficient of performance COP* for the refrigeration system can be expressed as

$$COP^* = \frac{Q_e + \Delta Q_e}{W_{act} - \Delta W_{act}} \qquad (2)$$

and the enhancement of COP for the refrigeration cycle is given by

$$\Delta\%COP = \frac{COP^* - COP}{COP} \times 100 \qquad (3)$$

The above discussion can be extended to a special idealized case. It was demonstrated that $h_A \rightarrow h_A^*$. We assume that $h_A \rightarrow \infty$ resulting in $U \rightarrow U_{max}$.

The plate-fin-tube heat exchanger shown in Figure 2 and of design specified in Figure 3 was selected for the performance analysis. The geometrical parameters of Figure 4 were chosen to be of the following dimensions.

ST = SL = 2.54×10^{-2} [m] = 1" centers
TF = 1.78×10^{-4} [m] = .010" fin stock
TT = 8.89×10^{-4} [m] = .035" tubewall thickness
DO = 1.58×10^{-2} [m] = 5/8" OD

(tube material: copper; fin material: aluminum).

Other parameters were selected to be:

Number of modules per element channel: $n_m = 3$

Number of fins per unit length of tube: FPM = 315 [m^{-1}]; i.e., 8 fpi

Velocity of the refrigerant R-12: $V_R = 1$ [m/s]

Condensing temperature: $T_c = 40$ [C]

Reynolds number of water film: $Re_w = 250$

Coefficient of wetness: $K_w = 1$

Ambient air temperature $T_{A_{in}} = 25$ [C].

All other parameters were considered as variables:

Relative humidity: $\phi A_{in} = 50, 80, 90, 100$ [%]

Velocity of air: $V_A = 1 - 10$ [m/s]

Reynolds number of air: $Re_A = 160 - 1600$.

The results of the computations are presented in Table 1 for six different cases. For various inlet conditions, the following parameters were computed:

$T_{A_{out}}$, $\phi_{A_{out}}$, q_{cw}, $R_{\ell at}$ (percentage of heat load due to evaporation), $T_{w_{av}}$, Ke, T^*_c, ΔNu_A, Δ%COP and ε (heat exchanger effectiveness of unwetted exchanger).

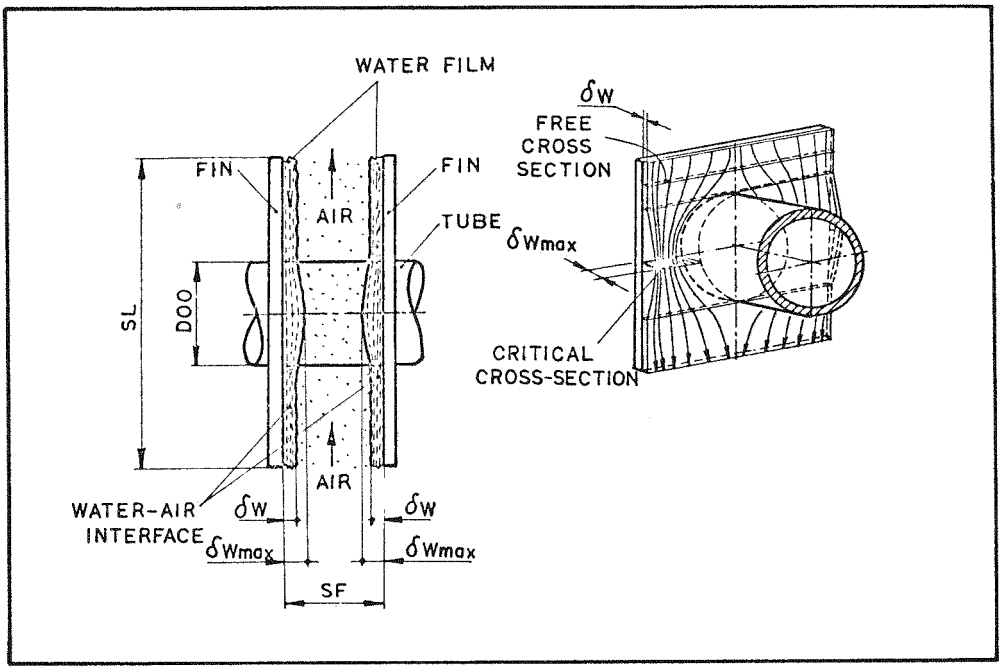

Figure 7. FLow Parameters of the Wetted Modules

The water film is assumed to flow laminarly downward under the influence of gravity. The air passage between the fin is smaller due to the presence of water on both fin surfaces. The passage is smallest where the water flows around the tube. Obviously, the water flow must be selected such that the smallest cross-section is never blocked. This mixing temperature will be lowest when the entering air is saturated and at the wet bulb temperature T_{AWB}. The precooled air will be heated within the exchanger, its temperature difference to the wall of the condenser will be larger everywhere than in the first case and the Log Mean Temperature Difference (LMTD) will be larger. The latter will be beneficial inasfar as the cooling capacity of the refrigeration system is increased and the compressor power decreased. Both will improve the coefficient of performance (see Figure 6).

All these improvements resulted from cooling the air before it enters the condenser. The air moving through the heat exchanger is heated at constant moisture content and becomes unsaturated, therefore further improvement by adding more water is possible up to the point it approaches blocked air flow. Wetting the heat exchanger surface not only increases the heat transfer by mass transfer $U \rightarrow U_w$ but

increases in addition the heat absorbing capacity of the air; i.e., its temperature change will be smaller and $T_m \rightarrow T_{mw}$.

The following basic assumptions were made for the analysis of heat, and mass transfer of the evaporative cooling of the condenser [1], [2].

1. The water is recirculated for use;
2. The temperature of the water at the top of the unit is equal to that at the bottom of the unit; i.e., temperature of the water entering the coil is equal to its temperature at the exit of the coil;
3. The water flow $\dot{m}_W$ is many times the flow which should be sufficient for the complete evaporation. There must be uniform and effective distribution between fins and the deposit of impurities in water between the top and bottom of the coil should be negligible. Therefore, assumption to operate with an excess water quantity is a necessity. Otherwise, fouling and dust collection could be so severe that the condenser performance would deteriorate.
4. Both complete wetting of the fins and incomplete wetting are included in the analysis involving the coefficient of wetness K_w.
5. It is assumed that the wetting of the coil will be in the form of a water film flowing by gravity over the vertical fin.
6. The water film should flow laminarly in order to be thin, of smooth surface, and steady.
7. Calculations are based on the constant temperature of the refrigerant T_C in the condensation process. The values of the thermodynamical properties of the refrigerant R-12 are specified for the temperature of condensation $T_C = 40°C$.

In general, the state of air flowing through the wetted fins approaches gradually the saturation condition and the negative diagram value q_w approaches zero and becomes then increasingly positive and condensation might occur within the fins. The temperature of the water must for the same reason have a maximum somewhere along the spacer fin arrangement. This is shown in Figure 8. Figure 8 shows temperature distribution of water, air and refrigerant for $T_{A_{in}} = 25°C$, $\phi A_{in} = 90\%$, and $v_A = 2$ m/sec. The water temperature is practically constant. Air dry bulb temperature increases as shown and wet bulb temperature increases until equal at saturation temperatures.

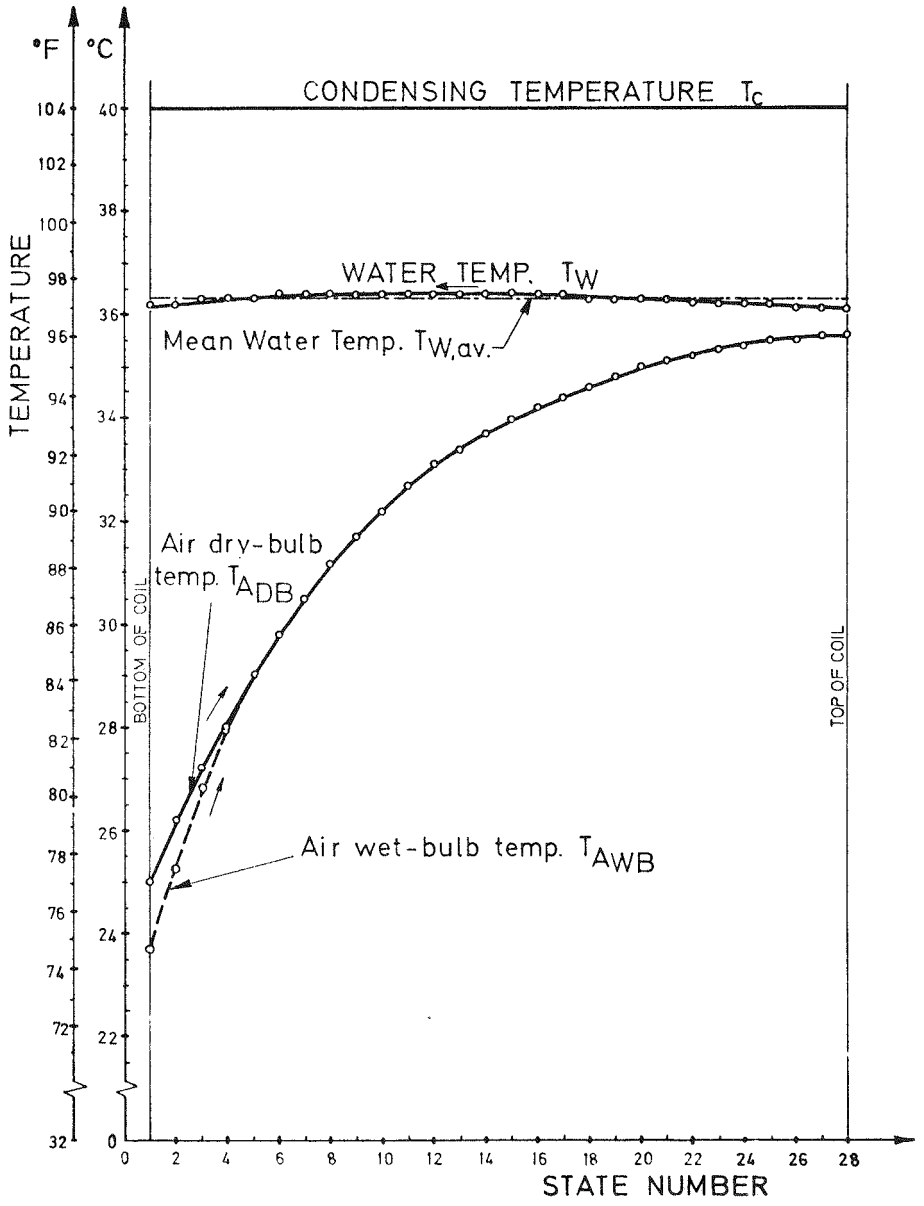

Figure 8. Temperature profiles of refrigerant, water and air, (computed for air velocity v_A = 2m/sec and relative humidity ϕA_{in} = 90%).

Table 1 is the result of the Analytical Study showing the substantially improved heat rejection of the wetted condenser over that of the dry condenser, expressed as the coefficient of enhancement Ke. We do not have here the direct comparison with a water cooled condenser. Some of the row headings may be of interest:

ΔNu_A = (dimensionless) increase in heat transfer

T_c^* = Temperature of Condensation

ε = Heat exchanger efficiency with dry condenser

Δ%COP = Increase in COP ranges from 30 to 65%.

Table 1 lists also the increase of the condenser COP due to changing $T_c \rightarrow T_c^*$; COP* given by eq. 2 can be evaluated from Q_e and AW_{act} data. These can be determined from T-S or p-i diagrams of the refrigerant and under the assumption that both the boiling temperature T_e and the overall compressor efficiency η_c are constant. For $T_e = 1.5^\circ$ C and $\eta_c = 0.8$, Q_e and W_{act} values and COP were determined for various T_c's and plotted in Figure 12. An iterative process was applied to determine the lowest possible temperature of the condensing refrigerant T_c^* which (within a specified limit of $\pm$ 10%) would provide the same heat rejection of the wetted condenser as that of the dry one. The T_c^* so obtained yield from Figure 12 the COP*. Percentage increase of coefficient of performance Δ%COP defined by Eq. 3 is listed in Table 1. Improved condenser performance has significant influence on the complete refrigeration system and is discussed in Section 5 of the paper.

Utilizing the computer facilities available in the Herrick Laboratories gave an opportunity to explore the improvement in the heat transfer by the continuously wet surface of an evaporative condenser. It has been determined that such substantial improvements are possible that a proposal is being developed that would specifically outline the possibility of a substantial improvement going from a dry coil to wetted coil surface with the accompanying energy conservation.

In many areas of the country, there are renewed and wider restrictions on the use of water for air conditioning or refrigeration purposes, and thus the use of water conserving condensers is becoming more of a requirement. The areas of restricted water usage would propose the use of a standard evaporative condenser such as is manufactured by Marley or Baltimore Air Coil sized with sufficient capacity that with outside dry bulb temperatures below 70°, auxiliary water cooling with the full evaporative condenser would not be brought into action. Thus, the multi-speed blower would be selected to handle the increased air requirements

Table 1

PERFORMANCE OF WETTED CONDENSER FOR CONSTANT INLET DRY-BULB TEMPERATURES OF AIR T_{Ain} = 25 C FOR VARIOUS RELATIVE HUMIDITIES AND DIFFERENT VELOCITIES

Air Velocity v_A [m/sec]	1		5		10	
Inlet Air Relative Humidity ϕA_{in} [%]	50	100	50	100	50	100
Air Reynolds Number Re_A [-]	165.5	165.5	827.5	827.5	1655.0	1655.0
Air Outlet Dry-Bulb Temp. $T_{A_{out}}$ [°C]	37.2	37.3	31.7	33.1	28.9	30.8
Outlet Air Relative Humidity ϕA_{out} [%]	99.9	100.0	96.6	100.0	91.8	100.0
Heat exchanged in setted channel $q_{cw}[\frac{kcal}{hr}]$	2.17	1.64	6.44	4.77	8.80	6.41
Latent heat transferred to air stream in channel $R_{\ell at}$ [%]	87.0	82.3	87.8	79.9	89.5	78.6
Average water temp. $T_{W,av}$ [°C]	37.3	37.7	32.7	34.2	30.0	32.4
Coefficient of Enhancement K_e [-]	5.58	4.22	4.24	3.14	3.53	2.57
Increase of Nusselt Number, ΔNu_A	5.649	3.425	7.044	3.108	7.552	2.576
Apparent Temperature of Condensation, T^*_c [°C]	24.2	30.2	24.8	31.0	25.6	32.0
Increase of COP, Δ%COP [%]	65.9	32.7	61.9	29.3	56.8	25.2
Air-cooled Heat Exchanger Effectiveness, ε [-]	0.94	0.94	0.74	0.74	0.60	0.60

caused by the higher ambients.

During the major portion of the year in those areas, little if any water would be required, and that in the northern half of the country water could be required during less than one third of the operating days.

The use of such a condensing system becomes attractive now that the cost of power is increasing and water is becoming more restricted. Substantially more sub-cooling than has ever been previously considered can be provided with some refrigerant tubes being submerged in the sump tank.

The optimum operating cycle could be developed to provide minimum power costs for the refrigerating equipment, yet providing the maximum savings in water where its use is restricted.

Figure 9 shows coefficients of enhancement K_e vs. Re_A and vs. V_A for different relative humidities of ambient air.

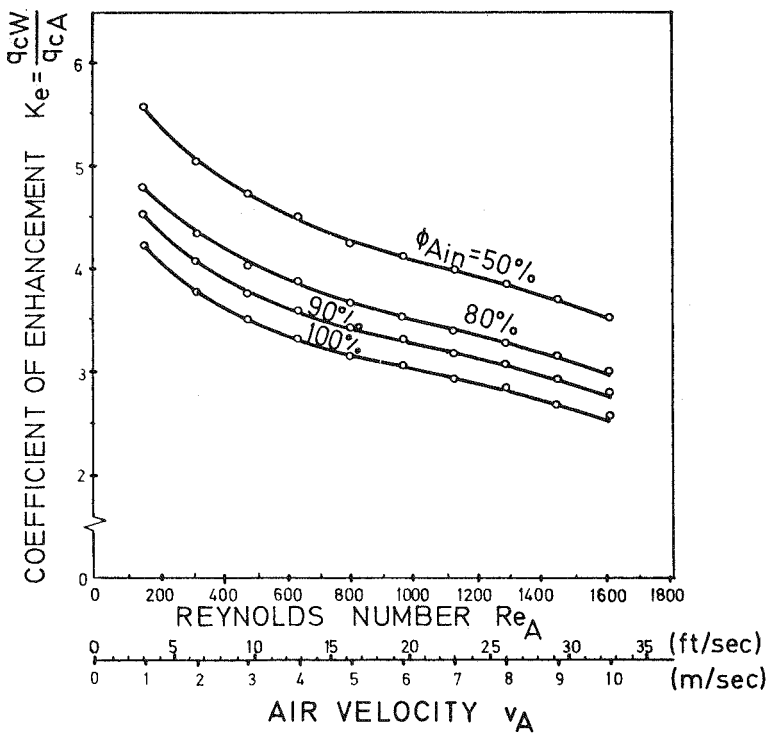

Figure 9. Coefficient K_e vs. Re_A for different relative humidities of ambient air (computed for air velocity v_A = 2m/sec and air dry-bulb temperature $T_{A_{in}}$ = 25°C).

Figure 10 shows ΔNu_A vs. Re_A and vs. V_A for different relative humidity of ambient air.

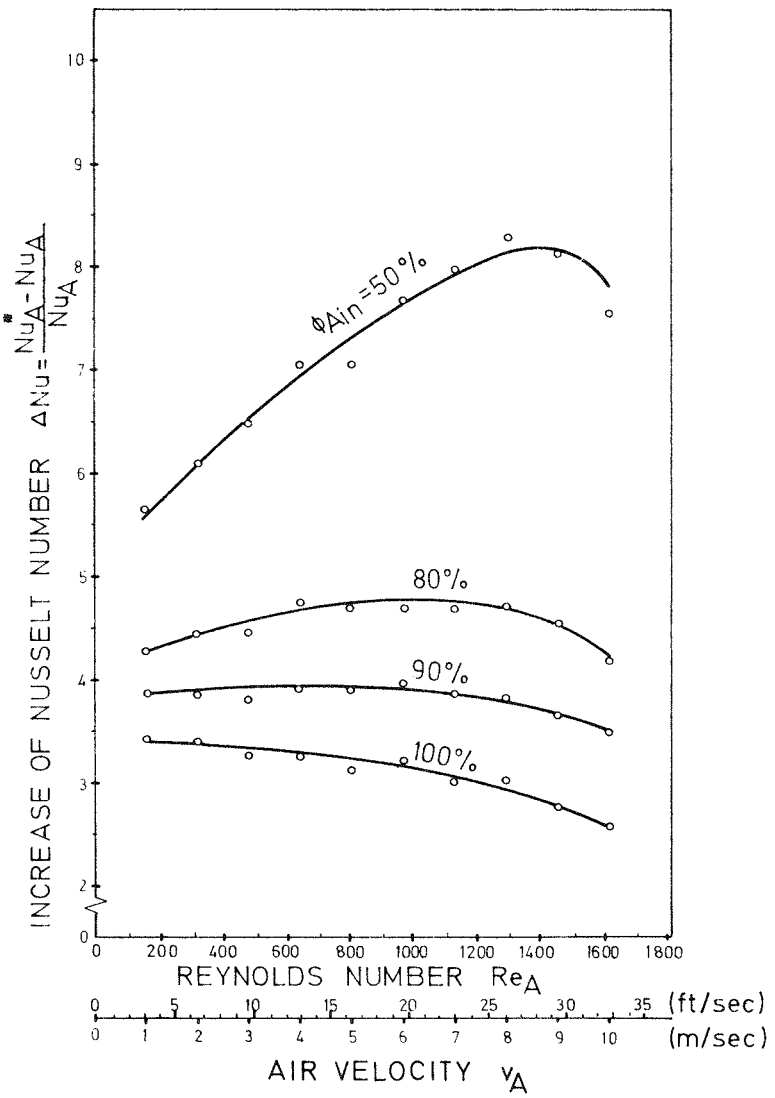

Figure 10. ΔNu_A vs. Re_A for different relative humidities of ambient air (computed for the same conditions as in Figure 9).

Figure 11 compares the actual heat exchanged in the dry and wetted heat exchanger as a function of air velocity and Reynolds number for different relative humidities. The enthalpy changes experienced by the air passing through the heat exchanger is indicated by the Δi_{cw} curve. It should be recognized that in some instances, Δi_{cw} reaches at some locations within the channel slightly larger values than between inlet and exit. This situation will occur when condensation is present (not shown in Table 1).

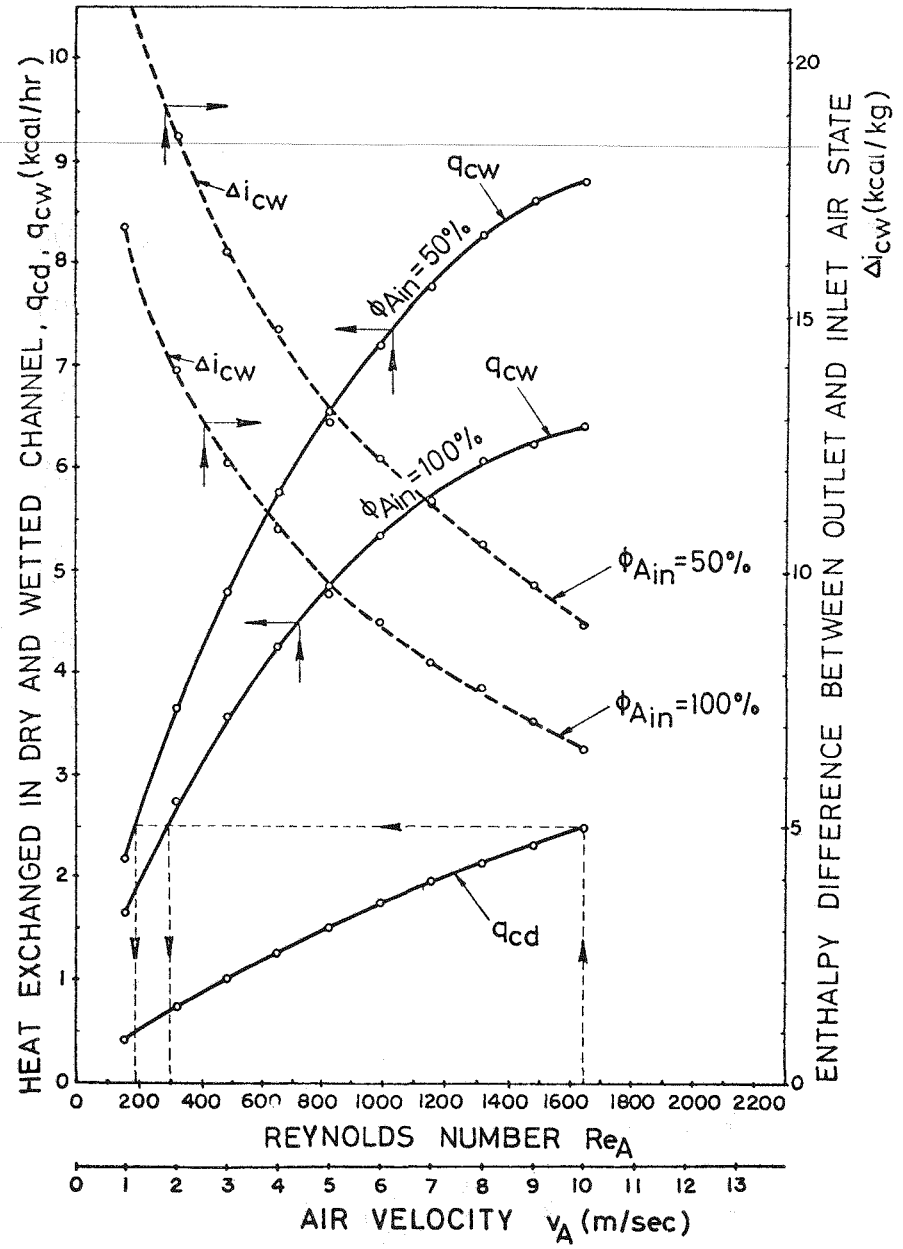

Figure 11. Comparison of heat exchange in dry and wetted channel--elemental extended surface (computed for the same conditions as in Figure 9).

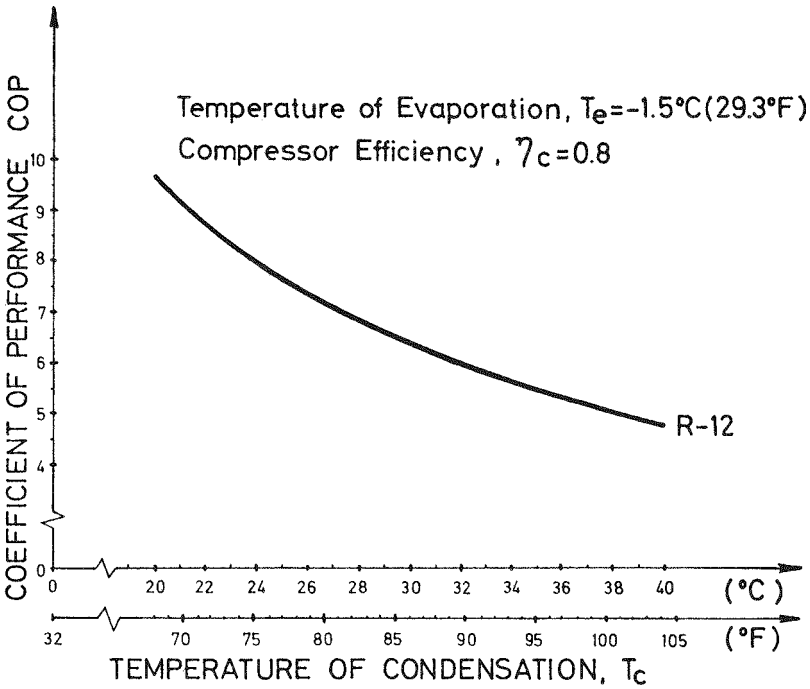

Figure 12. COP vs. T_C

Figure 13 shows that evaporative condenser might still operate successfully even at high temperatures where air-cooled condensers are inoperative. (Ambient temperature >> condensing temperature.) The changes of dry and wet bulb temperatures of the hot air and water temperature through the exchanger shown in the figure are valid for air velocity V_A - 2 m/s and $\phi_{A_{in}}$ = 20%.

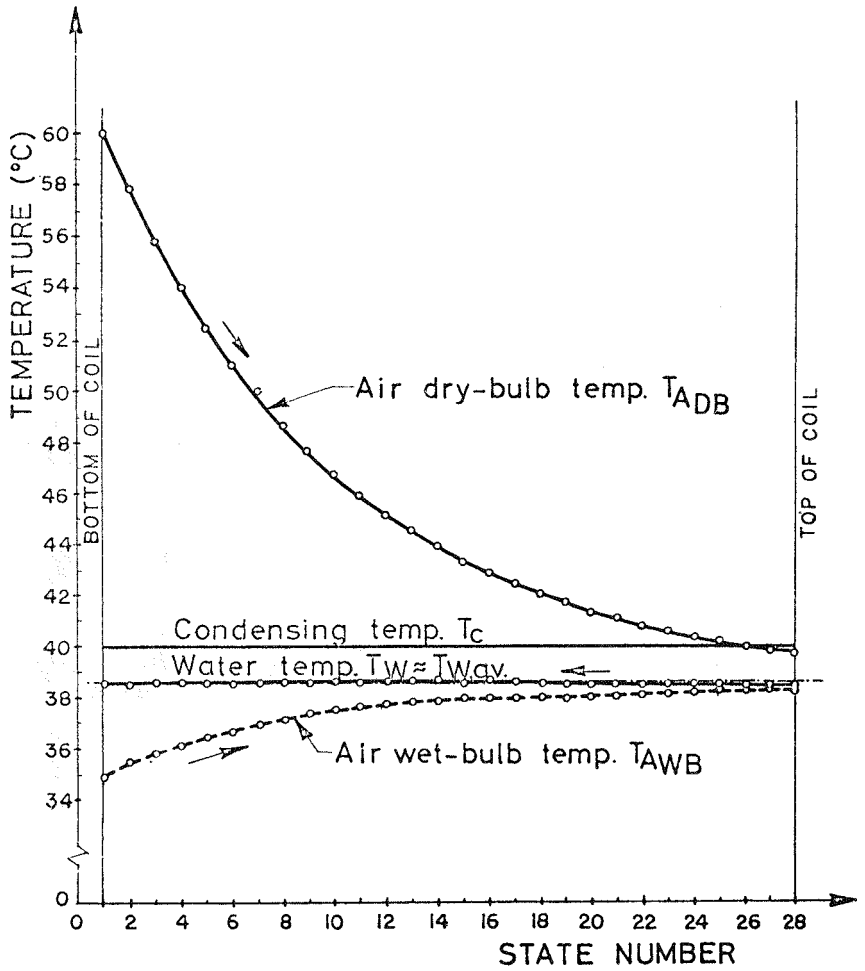

Figure 13. Temperature profiles of fluids in wetted condenser operating in ambient air of much higher temperature than the condensing fluid.

The temperature of the water T_W remains practically constant despite the fact that it receives heat from both air and condensing fluid. This implies that the heat received evaporates part of the water. The vapor generated is added to the air stream. T_{AWB} indicates the change of relative humidity experienced by the air.

5. PERFORMANCE OF REFRIGERATION SYSTEM

In order to evaluate what could the improved condenser performance do for the complete refrigeration system for chlorine storate, four different condenser arrangements were optimized [3]. The first system, shown in Figure 14, has shell-and-tube condenser and cooling tower. The second one, shown in Figure 15, has an air-cooled condenser. The third system, shown in Figure 16, works with Type 1 evaporative condenser and the last system (see Figure 17) operates with Type 2 evaporative condenser.

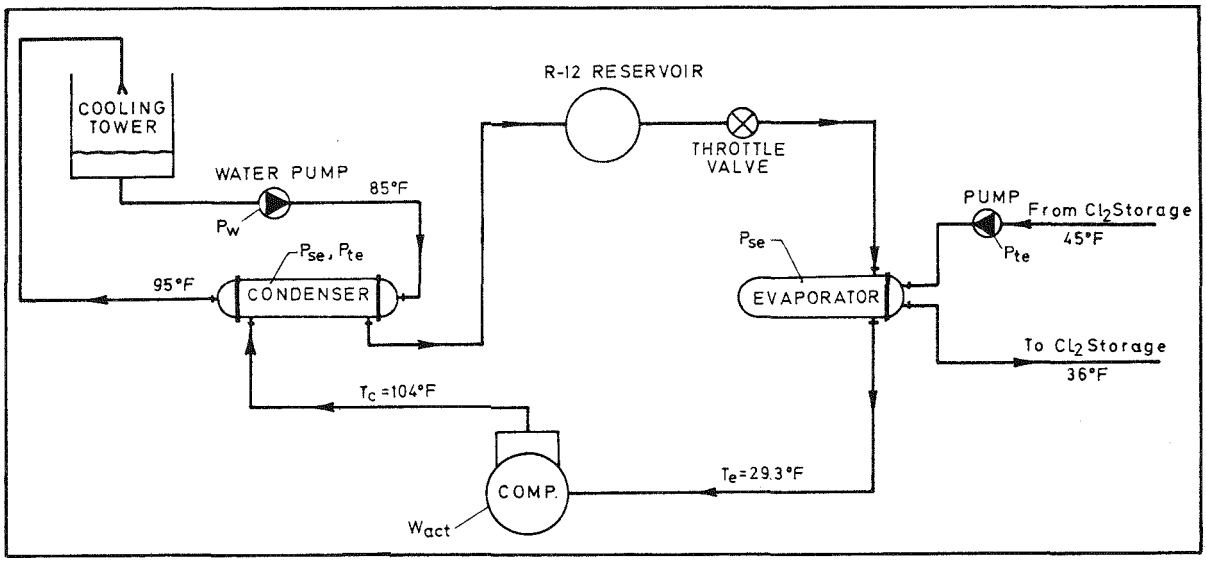

Figure 14. Refrigeration system for chlorine storage with air-cooled condenser.

Type 1 evaporative condenser operates at a lower condensing temperature T_c^*. Type 2 evaporative condenser uses much smaller heat transfer area ($A_c^* = A_c/K_e$) but operates with condensing temperature T_c.

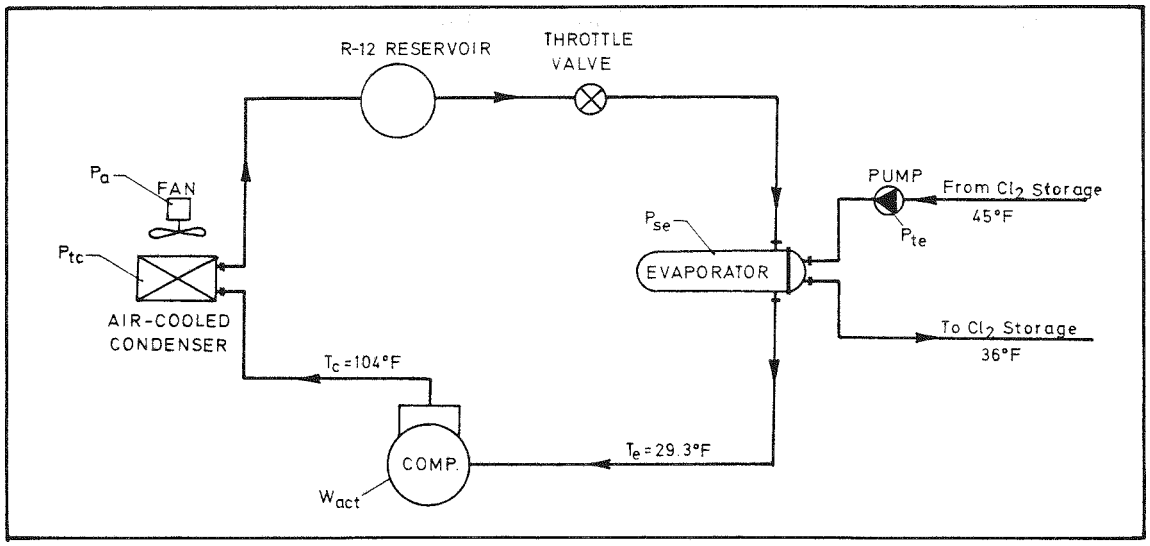

Figure 15. Refrigeration system for chlorine storage with air-cooled condenser.

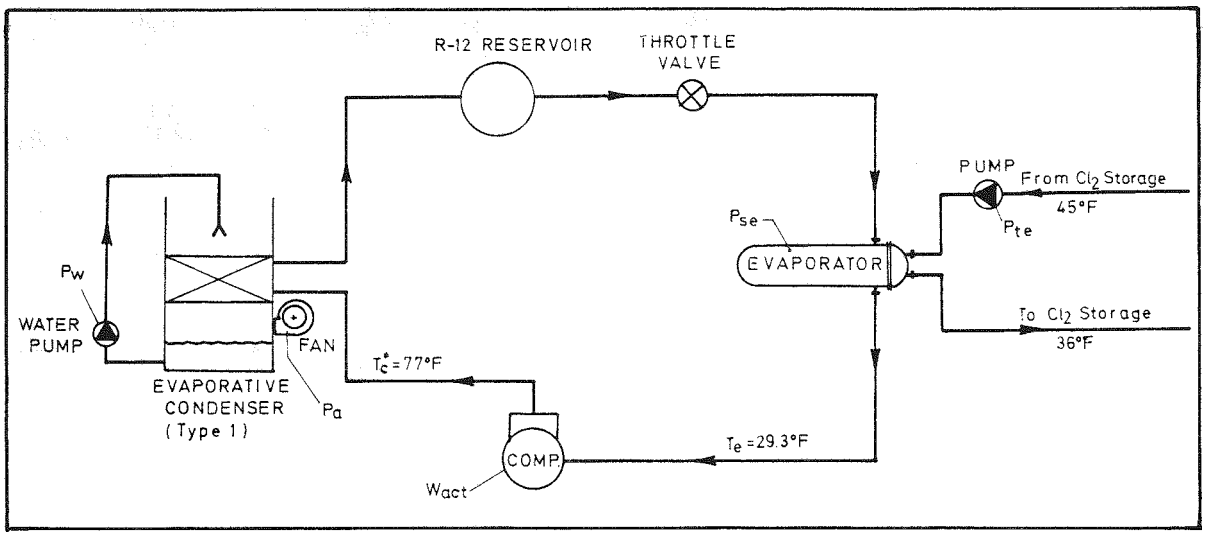

Figure 16. Refrigeration system for chlorine storage with Type 1 evaporative condenser (Design conditions: ambient air dry-bulb temperature $T_{A_{in}}$ = 25°C and relative humidity $\phi_{A_{in}}$ = 50%).

The lower condensing temperature T_c^* increases the capacity of the evaporator. Thus, refrigerant mass flow rate $\dot{m}_R$ can be reduced to maintain the same suction pressure and heating load. The lower discharge pressure at the compressor decreases the power requirement for the compressor. Thus, a substantial portion of the condenser performance is reflected in the improved $(COP)_s$ of the refrigeration system.

Comparative performance of the refrigeration system for chlorine storage with each of four condenser types is shown in Table 2. Power consumption of components is listed for each system. Coefficient of performance for each system is defined as:

$$(COP)_s = \frac{Q_e}{\Sigma P}$$

where

Q_e = heat of evaporation;

ΣP = Total power consumption for the system.*

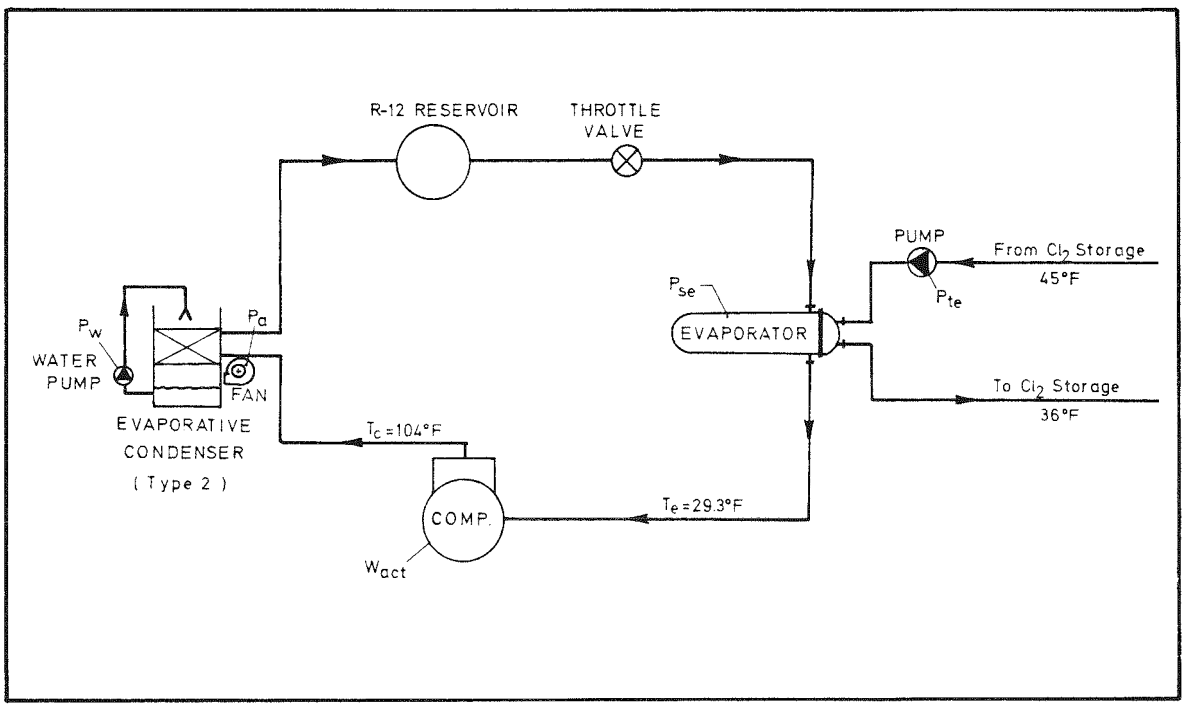

Figure 17. Refrigeration system for chlorine storage with Type 2 evaporative condenser (Design conditions remain the same as in Figure 16).

Table 2

PERFORMANCE OF REFRIGERATION SYSTEM FOR CHLORINE STORAGE WITH DIFFERENT CONDENSER ARRANGEMENTS (HEAT OF EVAPORATION Q_e = 2.57×10^3 kW).

Power Consumption of the components [kW]	1 With Shell-and-tube Condenser (R-12 shell fluid)	2 With Air-Cooled Condenser	3 With Type 1 Evaporative Condenser	4 With Type 2 Evaporative Condenser
Compressor power, W_{act}	530.00	530.00	332.00	530.00
Pumping Power on the tube side of Condenser P_{t_c}	0.80	99.90	67.70	21.70
Power due to shell side pressure drop in Condenser P_{sc}	15.00	-	-	-
Cooling Tower, P_w	29.80	-	-	-
Fan Power for Condenser P_a	-	13.80	25.50	6.64
Pumping Water in Evaporative Condenser, P_w	-	-	7.20	1.90
Pumping Water due to the pressure drop in evaporator, P_{te}	.81	.81	.81	.81
Power due to shell side pressure drop in Evaporator, P_{se}	33.23	33.23	33.23	33.23
Total Power Consumption ΣP	609.64	677.74	466.44	594.28
Coefficient of Performance for the system, $(COP)_s = Q_e/\Sigma P$	4.22	3.79	5.51	5.32

Table 2 clearly indicates that the system with air-cooled condenser has the lowest coefficient of performance: $(COP)_{S2} = 3.79$. Application of shell-and-tube condenser arrangement with cooling tower improves $(COP)_s$ by 11.4% Type 2 evaporative condenser improves it by 14%, while Type 1 evaporative condenser improves it by 45.5%. This is influenced by the relative humidity of ambient air. In Table 2, results are given for ambient dry bulb temperature $T_{A_{in}} = 25°C$ and relative humidity $\phi_{A_{in}} = 50\%$. Condensing temperature T_c^* was 25°C.

Therefore, we are quite convinced that the application of evaporative condenser operating with lower condensing temperature T_c^* is very attractive and reasonable.

6. SUMMARY

Thermodynamic processes requiring heat rejection into the surroundings which in most instances are river water, lakes, or ponds, cooling towers or by the air of our atmosphere. The lowest temperature of the process, however, is somewhat higher than that of the heat sink due to the temperature difference required for the transfer of the heat to be rejected. Increasing the heat transfer to make this necessary temperature difference smaller could improve the overall efficiency of a power plant by 1% for every degree the condensing temperature is lowered. Refrigeration processes operate between smaller temperature ranges than power plants and therefore lowering the condenser temperature yields an improvement of the efficiency or of the coefficient of performance. Refrigeration processes consume by far less energy than the power plants, but since these possible improvements are much higher, the overall reduction of consumption again could be very substantial.

Refrigeration systems commonly reject heat directly to the atmosphere. In this case, heat transfer can be increased by so-called evaporative cooling; i.e., by adding water to the air. This process has been dealt with in thermodynamic textbooks or in literature. However, the information given is still insufficient to permit independent calculation of evaporative cooling of condensers from physical data alone and without the need of performance data of a real unit.

---

*This does not include pumping power needed due to the losses in pipe network.

The Leidenfrost article develops design procedures for evaporative condensers by means of detailed analysis and computation of the state changes of the air passing through a wetted and partially wetted plate-fin-tube type condenser coil.

Our sponsor had requested an air-cooled condenser or a better condensing system than is ordinarily used.

The Herrick Laboratories has answered the challenge to use a more efficient condensing medium. There will still be air-cooled condensers for residential applications, and an evaporative condenser replacing a Utility Power Plant 450 ft high atmospheric cooling tower cannot be visualized. But in this energy conserving area we are moving into, the evaporative condenser will be considered for the first time in a new light.

This is almost completing the circle for me. Twenty-five years ago I was crisscrossing our country promoting air-cooled equipment for residential and commercial applications. There were advantages in lower maintenance over cooling towers but I did not foresee the closer fin spacing and no condenser cleaning whatever until the unit shuts off on high head pressure. So--to use a commercial phrase--"We found a better way."

Professor Leidenfrost has explored the basic principles to develop the several curves that are traced out from the calculations of evaporative cooling of condensers without the data being developed from tests. His presentation develops design procedures for evaporative condensers by means of detailed analysis and computer computations of the state changes of the air passing through a wetted and partially wetted plate-fin-tube condenser coil. The full explanation would require that Professor Leidenfrost do it himself, so if there are substantive questions I'll get answers from our two graduate students, Korenic and Lee.

Professor Leidenfrost's analysis challenges our interest because like most of energy conserving concepts it requires a larger capital investment to use an evaporative condenser than a traditional cooling tower with the shell and tube condenser.

REFERENCES

1. Leidenfrost, W. and B. Korenic, Analysis of Evaporative Cooling and Enhancement of Condenser Efficiency and of Coefficient of Performance, Wärme and Stoffübertragung, (to be published).

2. Korenic, B., Analysis of the Enhancement of Heat Transfer by Spraying Water on a Finned Condenser Coil, MS Thesis Purdue University, 1977 (results to be published, Reference 1).

3. Lee, K.H., Analysis and Design of a Refrigeration System of a 100 MWH Load Leveling $ZnCl_2$ Battery, MS Thesis, Purdue University, 1977 (to be published).

APPENDIX C

ANALYSIS OF EVAPORATIVE COOLING AND ENHANCEMENT OF CONDENSER EFFICIENCY AND OF COEFFICIENT OF PERFORMANCE*

W. Leidenfrost and B. Korenic
West Lafayette, Indiana U.S.A.

ABSTRACT.

The graphical method to determine with the aid of a Mollier i-x diagram (psychrometric chart) combined heat and mass transfer is simulated by a computer program. Heat rejection rates from a plate-fin tube type condenser are determined for various flow rates and inlet state conditions of air and for different degrees of wetting of the heat transfer surfaces. The presence of water and the cooling by latent heat makes it possible to exchange more heat than the unwetted exchanger would even for idealized conditions of infinite heat transfer coefficient of the air. The evaporative cooled condenser also can exchange heat with ambient air which has much higher temperature than the condensing fluid. Evaporative cooling increases heat transfer by a factor of more than three for saturated inlet air and greater than five for lower inlet humidities. Wetted heat exchangers require less extended surfaces and can operate effectively with bare tubes only. Wetting the condenser of a refrigeration or heat pump system makes it possible to exchange the condenser load at lower temperatures. This yields an increase of COP of the order of 30 to 60% and therefore a substantial decrease in compressor power and its energy consumption.

To be published in "Wärme-und Stoffübertragung",
Volume 11, Springer-Verlag, 1978.

---

*In honor of Prof. Dr. F. Bošnjaković to his 75th Birthday.
The article includes in part the M.S. Thesis of the second author.

NOMENCLATURE
of frequently used symbols

$A, A_1, A_2, \ldots$	Air states in the i-x diagram	-
A_c, A_c^*	Real and apparent heat transfer area of condenser other subscripts: b = interface area, d = dry surface, m = surface of a module, w = wetted surface	m^2
a_b	Unit evaporation surface	m^2
$B, B_1, B_2, \ldots$	Boundary state of air-water interface	-
b	Dimensionless multiplier in eq. 26	-
COP, COP*	Normal and improved Coefficient of Performance	-
c_{p_A}, c_{p_W}	Specific heat of air and water	$\frac{kcal}{kg°C}$
D_h	Hydraulic diameter subscripts: A = air channel, W = water film, R = refrigerant flow in tube, AW = wetted air channel	m
G	Mass flux subscripts: A = air flow through minimum cross-section area, AW = same but in wetted channel, R = refrigerant	$\frac{kg}{m^2 hr}$
g	Acceleration of gravity	$\frac{m}{sec^2}$
h	Heat transfer coefficient subscripts: A = air, AW = at air-water interface, R = refrigerant, W = water	$\frac{kcal}{m^2 hr°C}$
h_A, h_A^*	Real and augmented heat transfer coefficient at air side condenser surface	$\frac{kcal}{m^2 hr°C}$
$i, i_1, i_2, \ldots$	Enthalpy of air states	$\frac{kcal}{kg}$
i_b	Enthalpy of air-water interface	$\frac{kcal}{kg}$
i_W	Enthalpy of water	$\frac{kcal}{kg}$

i_{fg}	Latent heat of vaporization	$\frac{kcal}{kg}$
j_A	Colburn j factor for air	-
K_e	Coefficient of enhancement defined by eq. 3a	-
K_w	Coefficient of wetness	-
k	Thermal conductivity subscripts: F, R, T, W refer to fin, refrigerant, tube, and water	$\frac{kcal}{m\ hr^{\circ}C}$
Le	Lewis number	-
$\dot{m}_A, \dot{m}_W$	Total mass flow rates of air and water	$\frac{kg}{sec}$
$\dot{m}_{WC}$	Mass flow rate in a channel	$\frac{kg}{sec}$
$\dot{m}_{WVC}$	Volumetric mass flow rate of falling water film	$\frac{m^3}{sec}$
Nu_A, Nu_W, Nu_R	Nusselt numbers of air, water and refrigerant respectively	-
Nu_A^*	Apparent Nusselt number of air	-
n,n'	Number of unit surfaces (see eq. 22)	-
P	Total pressure of moist air	$\frac{kg}{m^2}$
p_{gb}	Partial pressure of water vapor at water-air interface	$\frac{kg}{m^2}$
Pr_A, Pr_W, Pr_R	Prandtl number of air, water and refrigerant	-
Q_{CD}, Q_{CW}	Heat loads of dry and wetted condensers	$\frac{kcal}{hr}$
Q_c, Q_e	Heat loads of condenser and evaporator	$\frac{kcal}{hr}$
q	Diagram values	$\frac{kcal}{kg}$
q'	Heat flux subscripts on q's: b = water-air interface, c = channel, d = dry surface, h = dry heat transfer, w = heating of water, σ = wet heat transfer	$\frac{kcal}{m^2 hr}$

q_{cd}, q_{cw}	Heat exchanged in dry and wetted channel	$\frac{kcal}{hr}$
R_A, R_F, R_T, R_R	Heat transfer resistances of air, fin, tube and refrigerant	$\frac{m^2 hr°C}{kcal}$
R_{lat}	Percentage of latent heat transfer to the air stream in a channel	%
R_{sen}	Same but for sensible heat	%
Re_A, Re_W, Re_R	Reynolds numbers of air, water, and refrigerant	-
T	Temperature subscripts: A = air, W = water, M = mixing temperature, A_{WB} = air wet bulb temperature, A_{DB} = air dry-bulb temperature, Amb = ambient air, b = air water interface, c,c* = normal and lower condensing temperature	°C
U,U*	Real and apparent overall heat transfer coefficients	$\frac{kcal}{m^2 hr°C}$
U_d	at dry wall	$\frac{kcal}{m^2 hr°C}$
U_W	at wetted wall	$\frac{kcal}{m^2 hr°C}$
U_{max}	Same for infinite heat transfer at air side	$\frac{kcal}{m^2 hr°C}$
v_A, v_R	Velocity of air and refrigerant	$\frac{m}{sec}$
W_{act}	Compressor work	$\frac{kcal}{kg}$
x	Humidity ratio subscripts: A = moist air, b = saturation at water state B	$\frac{kg}{kg}$
y	Interval fraction defined by eq. 19	-

Greek Symbols

Δ	Differences of parameters	
δ_W	Thickness of water film	m
ε	Heat exchanger effectiveness	-
η_o	Temperature effectiveness	-

μ_A, μ_R	Dynamic viscosities of air and refrigerant	$\frac{kg}{m \cdot sec}$
ν_W	Kinematic viscosity of water	$\frac{m^2}{sec}$
σ	Mass transfer coefficient	$\frac{kg}{m^2 hr}$
ρ_A	Density of air	$\frac{kg}{m^3}$
ρ_{R_f}, ρ_{R_g}	Densities of saturated refrigerant liquid and vapor at T_c	$\frac{kg}{m^3}$
$\phi_{A_{in}}, \phi_{A_{out}}$	Relative humidities of air at inlet and outlet conditions	%

1. Introduction

Thermodynamic cyclic processes of any kind require heat rejection into the surroundings which in most instances is represented by river water, lakes, or ponds of cooling towers or by the air of our atmosphere. The temperature of the surroundings represents the state of the heat sink. The lowest temperature of the cyclic process, however, is somewhat higher than that of the heat sink due to the temperature difference required for the transfer of the heat to be rejected. Augmenting heat transfer to make this necessary temperature difference smaller could increase the overall efficiency of a power plant by 1% for every degree the condensing temperature is lowered. This obviously would represent a tremendous saving of energy when considering the enormous consumption of power plants. Refrigeration processes operate between smaller temperature ranges than power plants and therefore lowering the condenser temperature yields an even more drastic improvement of the efficiency or of the coefficient of performance. These processes consume by far less energy than the power plants but since these possible improvements are much higher the overall reduction of consumption again could be very substantial.

Residential and small commercial refrigeration systems commonly reject heat directly to the atmosphere by means of air cooled condensers. Larger industrial equipment rejects heat indirectly by using cooling towers and water cooled condensers. These units require higher maintenance than the air cooled systems because of possible build-up of scale at the water-side of the condenser. The continual maintenance problem and dependent upon water conditions can be critical in many areas. Cooling towers in addition are expensive to build and costly to operate especially when the water use is restricted. It appears to be more beneficial to augment heat transfer at the air side of a condenser by so-called evaporative cooling, i.e. by adding water to the air. Substantial improvements can be achieved when the heat exchanger surfaces are continuously wetted by recirculated (possibly) untreated water of which only a small quantity which evaporates needs to be replenished. This process has been dealt with in thermodynamic textbooks or in literature

[1,10,11,12,13]. However, the information given is still insufficient to permit independent calculation of evaporative cooling of condensers from physical data alone and without the need of performance data of a real unit.

This article develops design procedures for evaporative condensers by means of detailed analysis and computation of the state changes of the air passing through a wetted and partially wetted plate-fin-tube type condenser coil.

2. Basic Principles of Evaporative Cooling

A refrigerant flowing through a heat exchanger condenses at T_c by means of heat transfer to air which enters the exchanger at T_{Amb}. The rate of heat transfer is given by

$$Q_{CD} = U \, \Delta T_m \, A_c \qquad (1)$$

where U is the overall heat transfer coefficient ΔT_m the logarithmic mean temperature difference LMTD and A_c the heat transfer area.

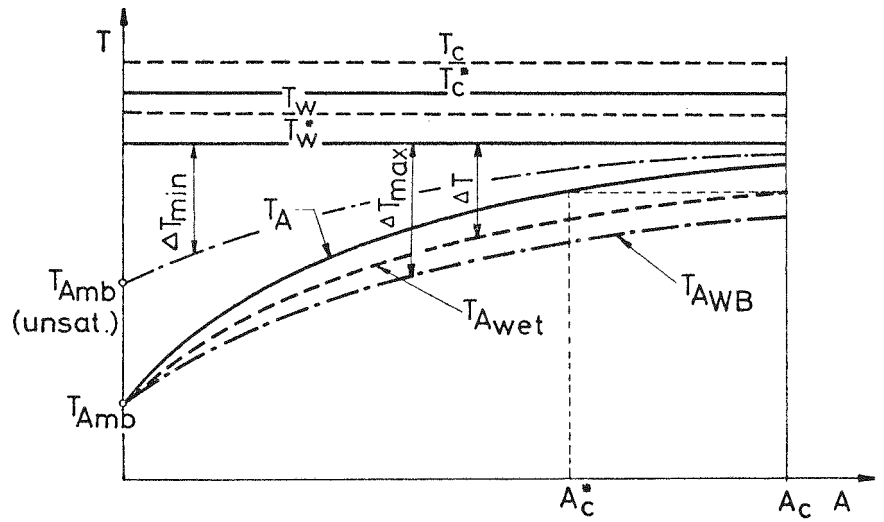

Figure 1. T vs. A_c Diagram, Wetting of Heat Exchanger Surfaces

Whenever the ambient air is not saturated, its temperature can be lowered by injecting water. The air enters then the heat exchanger at a temperature T_M. This mixing temperature will be lowest

when the cooling limit is reached, i.e., the entering air is saturated and at wet bulb temperature T_{AWB}. The precooled air will be heated within the exchanger its temperature difference to the wall of the condenser will be larger everywhere than in the first case and the LMTD will be larger.

$$Q_{CD1} = U_1 \Delta T_{ml} A_c \qquad (2)$$

Cooling the air before it enters the heat exchanger might not change the heat transfer properties or other heat transfer parameters within the exchanger and $U = U_1$. Equation (2) can therefore be written as

$$Q_{CD1} = U \Delta T_{ml} A_c$$

The LMTD $\Delta T_{ml} > \Delta T_m$ and $Q_{CD1} > Q_{CD}$. Since only Q_{CD} needs to be exchanged implies that A_c, the size of the condenser could be made smaller, or U could be decreased by lowering the velocity and pumping power of the air, or ΔT_{ml} could be made smaller by means of lowering the condensing temperature. The latter will be beneficial inasfar as the cooling capacity of the refrigeration system is increased and the compressor power decreased. Both will improve the coefficient of performance (see Fig. 2).

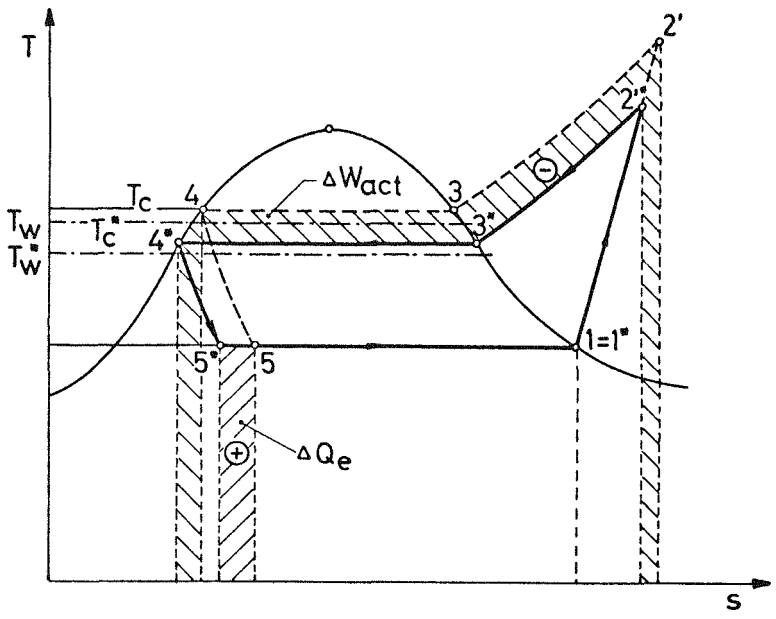

Figure 2. T-S diagram, possible decrease of temperature of condensing refrigerant due to evaporative cooling.

All these improvements resulted from cooling the air before it enters the condenser. The air moving through the heat exchanger is heated at constant moisture content and becomes unsaturated, therefore further improvement by adding more water is possible. Wetting the heat exchanger surface not only augments the heat transfer by mass transfer $U \rightarrow U_W$ but increases in addition the heat absorbing capacity of the air, i.e., its temperature change will be smaller and $\Delta T_m > \Delta T_{mw}$.

The rate of heat transfer in the wetted heat exchanger is

$$Q_{CW} = U_W \, \Delta T_{mw} \, A_c \tag{3}$$

$$U_W > U \text{ and } \Delta T_{mw} > \Delta T_m \text{ and } Q_{CW} >> Q_{CD}$$

Introducing the coefficient of enhancement K_e yields

$$Q_{CW} = K_e \, U \, \Delta T_m \, A_c \tag{3a}$$

where

$$K_e \equiv \frac{Q_{CW}}{Q_{CD}} = \frac{U_W \, \Delta T_{mw}}{U \, \Delta T_m}$$

or

$$Q_{CW} = U^* \, \Delta T_m \, A_c$$

where

$$U^* = U_W \, \Delta T_{mw} / \Delta T_m$$

The augmentation of heat transfer at the air side can be assumed to be of no influence to the convective heat transfer of the condensing refrigerant and to the conductive heat transfer through the wall. Therefore, the apparent air side convective heat transfer coefficient h_A^* can be determined from U^*. h_A^*, the hydraulic diameter D_h of the air passage, and the thermal conductivity of moist air k_A yield the Nusselt number Nu_A^* and the augmentation of heat transfer can be expressed as

$$\Delta Nu_A = \frac{Nu_A^* - Nu_A}{Nu_A} \tag{4}$$

Q_{CW} is larger than the required Q_c and in a similar way as discussed above the heat exchanger area either could be decreased to A_c^* or T_c could be lowered to T_c^* in order to lower LMTD. This is shown schematically in the T vs. A_c plot of Fig. 1. The uppermost curve represents

the temperature increase of air entering the dry channel at ambient unsaturated condition. The saturated air entering the heat exchanger will change in temperature along the curve T_A (unwetted) or along T_{Awet} (wetted) or along $T_{A_{WB}}$ if saturated at every location.

The T-S diagram of Fig. 2 demonstrates that lowering the condensing temperature to T_c^* lowers the compressor power by ΔW_{act} and increases the cooling capacity by ΔQ_e.

The coefficient of performance COP* can be expressed as

$$COP^* = \frac{Q_e + \Delta Q_e}{W_{act} - \Delta W_{act}} \tag{5}$$

and the enhancement of COP is given by

$$\Delta COP = \frac{COP^* - COP}{COP} \tag{6}$$

The above discussion can be extended to a special idealized case. It was demonstrated that $h_A \to h_A^*$. We assume that $h_A \to \infty$ resulting in $U \to U_{max}$. We assume furthermore that despite the infinite heat transfer the air is not of infinite specific heat but changes in temperature as in the unwetted channel, i.e., LMTD = ΔT_m. The heat exchanged in this idealized case is

$$Q_{CD_{max}} = U_{max}\ \Delta T_m\ A_c \tag{7}$$

In principle it is possible that

$$Q_{CW} > Q_{CD_{max}} \tag{8}$$

and the wetted condenser transfers more heat to air than the dry condenser of zero air side heat transfer resistance. At a first glance this is a surprising result but physically understandable because

$$U_W\ \Delta T_{mw} \gtrless U_{max}\ \Delta T_m \tag{9}$$

3. Modeling of a Plate-Fin Tube Type Condenser for Wetted, Partially Wetted and Unwetted Operation

A "Blow-Through" type condenser unit is shown in Fig. 3. The heat exchanger consists of horizontal tubes through which the refrigerant is channeled and vertical fins. Water is supplied by spray nozzles to the top of the heat exchanger and flows under the action of gravity downwards and is collected in a reservoir. Air

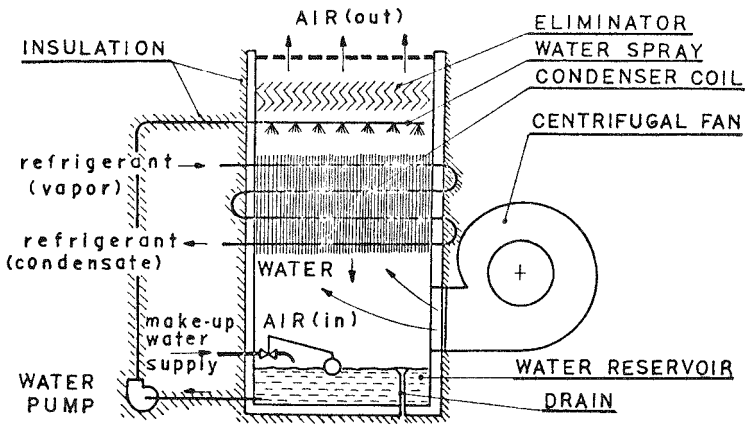

Figure 3. Evaporative Condenser Apparatus

enters the bottom of the exchanger, flows by forced convection upwards and leaves the top of the unit. The water is recirculated and arrangements are made to replenish the amount evaporating during the cooling process. Fig. 4 shows a close-up of the heat exchanger core being composed of identical elemental parallel channels each of which is subdivided vertically by modules of identical size and shape.

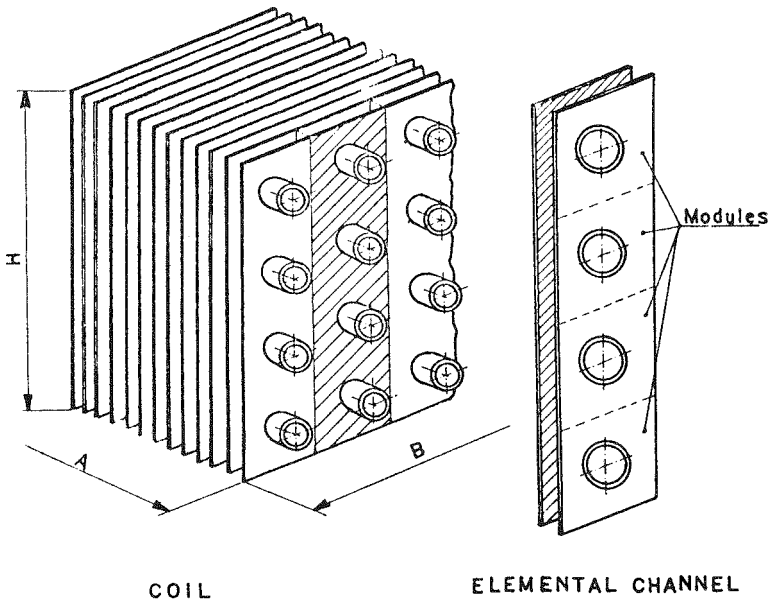

Figure 4. The elemental channel and its modules as a part of the condenser coil.

Pertinent information of the geometry of one module is given in Fig. 5.

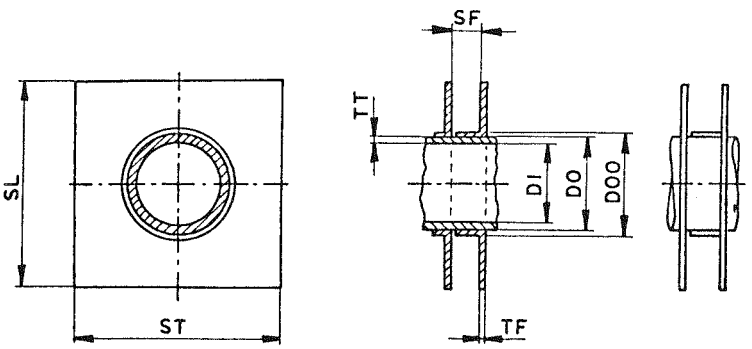

Figure 5. Module of the Plate Heat Exchanger Coil

The following basic assumptions were made for the analysis of heat, and mass transfer of the evaporative cooling of the condenser.

1. The water is recirculated for use.
2. The circulating paths are thermally insulated.
3. The temperature of the water at the top of the unit is equal to that at the bottom of the unit, i.e., temperature of the water entering the coil is equal to its temperature at the exit of the coil.
4. The refrigerant (R-12) is never heated in the course of its flow, due to the fact that the condensation process is required only.
5. The water flow $\dot{m}_W$ is many times the flow which should be sufficient for the complete evaporation, due to the requirement of its uniform and effective distribution between fins and the request that the concentration of impurities in water between the top and bottom of the coil should be negligible. Therefore, assumption to operate with an excess water quantity is a necessity. Otherwise fouling and dust collection could be so severe that the condenser becomes inoperative.
6. Both complete wetting of the fins and incomplete wetting are included in the analysis involving the coefficient of wetness K_w.
7. It is assumed that the wetting of the coil will be in the form of a water film flowing by gravity over the vertical fin.

8. The water film should flow laminarly in order to be thin, of smooth surface, and steady.

9. It is assumed that the interfacial area is equal to the wetted fin area.

10. Calculations are based on the constant temperature of the refrigerant T_c in the condensation process. The values of the thermodynamical properties of the refrigerant R-12 are specified for the temperature of condensation $T_c = 40°C$.

4. Method of Analysis of Combined Heat and Mass Transfer and Determination of Changes of State of Air and Water in the Wetted Heat Exchanger

The system for the analysis is shown in Fig. 6, representing a control volume in one of the passages (elemental channel) of the condenser coil. For reasons of generality the walls are assumed to be

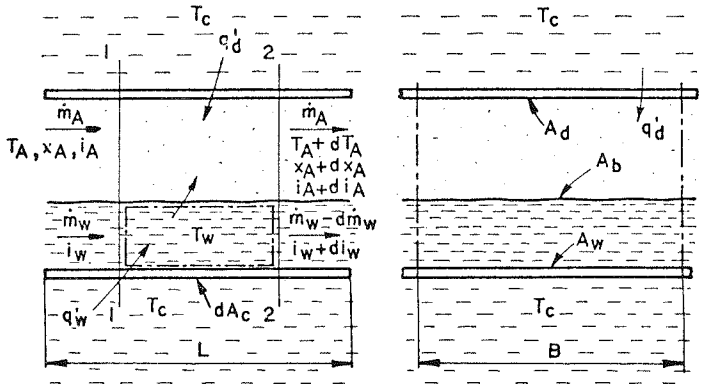

Figure 6. Evaporation in a channel heated both at wetted and unwetted walls.

only partially wetted. This flow arrangement would occur in a horizontal channel where only the lower part is filled with water, dry heat transfer occurs at the upper wall surface. The system in principle represents heat transfer from one fin having one dry and one wetted surface. It is assumed (only at present) that the fin efficiency is unity, i.e., the wall temperature is not influenced by conduction along the fins but governed by overall heat transfer from

the heat source (vapor condensing at T_c) to the air. Air enters the control volume at mass flow rate $\dot{m}_A$ and at state condition T_A, x_A, i_A. The water enters with mass flow rate $\dot{m}_W$ and enthalpy i_W. The water experiences heat and mass exchange with the air at the phase boundary surface A_b and heat exchange with the refrigerant at the wetted surface A_w. The air undergoes heat and mass transfer with the water at A_b and heat transfer at the dry surface A_d. Due to the transfer mechanism the state conditions of the air change by dT_A, dx_A and di_A ($\dot{m}_A$ = const.). The water state changes by di_W and its mass flow rate by $-d\dot{m}_W$. The processes within the control volume or for the condenser as a whole depend on nine parameters. Some are given, others can be specified and/or evaluated from conservation equations but three cannot be determined because additional equations are not available. However step-by-step procedure can be performed to determine heat transfer and changes of state of the air and the water. This has been done graphically in [1] with the aid of a Mollier i-x diagram (psychrometric chart). For the sake of easier reading a short outline is warranted here. It is assumed that the heat transfer from the refrigerant to air through the dry wall is governed by an overall coefficient U_d and to water (through A_w) by U_W. The overall heat transfer area is $A_c = A_d + A_w$. Between $\dot{m}_A$ and A_d and A_w a convective heat transfer coefficient h_A is employed. h_W is considered for the heat transfer of the water at the surface A_b and A_w, $h_W >> h_A$ and $T_W = T_b$.

The heat balance of the wetted part of the control volume surrounded by dashed lines is given as:

$$U_W \, dA_c \, (T_c - T_W) - i_{Wb} \, d\dot{m}_W = d \, (\dot{m}_W i_W) + q_b' \, dA_c \qquad (10)$$

where the second term on the left side represents the heat loss due to evaporation of $d\dot{m}_W$ having an enthalpy i_{Wb} at interface state conditions. The right side of eq. 10 is the heat added to the water and transferred to the air.

The heat flux q_b' is given by

$$q_b' = h_A \, (T_b - T_A) + \sigma \, (x_b - x_A) \, i_{fg} \qquad (11)$$

where i_{fg} is the latent heat of vaporization and σ a mass transfer coefficient. The x's are the moisture contents of the air (kg water/kg dry air) at water-air interface and free stream respectively. Introducing into eq. 10 $d(\dot{m}_W i_W) = m_W di_W + i_W(-d\dot{m}_W)$ and the mass balance $-d\dot{m}_W = \dot{m}_A dx_A$ yields

$$U_W(T_c - T_W)\, dA_c + i_{Wb}\dot{m}_A\, dx_A = \dot{m}_W\, di_W + i_W\dot{m}_A\, dx_A + h_A(T_b - T_A)\, dA_c + \sigma(x_b - x_A)\, i_{fg}\, dA_c \qquad (12)$$

The change of moisture content in the air is a result of mass transfer and can be expressed as

$$\dot{m}_A\, dx_A = \sigma dA_c\, (x_b - x_A)\ , \text{ or}$$

$$dA_c = \frac{\dot{m}_A\, dx_A}{\sigma(x_b - x_A)} \qquad (13)$$

Introducing eq. 13 into eq. 12 and rearranging yields

$$U_W\,(T_c - T_W) = \sigma(x_b - x_A)(i_W - i_{Wb}) + h_A(T_b - T_A) + \frac{\dot{m}_W\, di_W}{\dot{m}_A dx_A}\,\sigma(x_b - x_A) + \sigma(x_b - x_A)\, i_{fg} \qquad (14)$$

The ratio of the surface areas A_w/A_b will not change considerably along the channel and $dA_w/dA_b = A_w/A_b$ therefore $U_{Wb} \cdot A_b = U_W A_w$ or $U_{Wb} = (A_w/A_b)U_W$. Since $T_W \sim T_b$ and $i_W = i_b$, eq. 14 becomes

$$U_{Wb}(T_c - T_b) = h_A\,(T_b - T_A) + \sigma\,(x_b - x_A)(i_{fg} + \frac{\dot{m}_W\, di_W}{\dot{m}_A\, dx_A}) \qquad (15)$$

Each term in this equation represents a heat flux. Multiplying both sides of eq. 15 by c_p/h_A yields

$$c_p(T_c - T_b) = \frac{h_A}{h_A + U_{Wb}}\,[c_p\,(T_b - T_A) + \frac{\sigma c_p}{h_A}\,(x_b - x_A)(i_{fg} + \frac{\dot{m}_W}{\dot{m}_A}\frac{di_W}{dx_A})] \qquad (16)$$

In. eq. 16 the heat fluxes are given as enthalpies and can therefore be shown in the i-x diagram and are called the "diagram values" of the

fluxes. The factor $\sigma c_p/h_A$ is the so-called "Lewis factor" and is equal to unity for Le = 1. This is usually the case in technical problems involving moist air.

Equation 16 can be written as

$$q_{bw} = q_h + q_\sigma + q_w \tag{17}$$

indicating that the heat input to the control volume at the wet side heats the air by a dry and by a wet transport and heats the water.

The heat flux to the air through the unwetted surface A_d (and its diagram value) are given as

$$q'_d = U_d \, (T_c - T_A)$$

or

$$q_d = \frac{c_p}{h_A} U_d \, (T_c - T_A) \tag{18}$$

The diagram values of eqs. 17 and 18 are shown schematically in the i-x diagram of Fig. 7. The initial state of the air is A shown at the intersection of the vertical line through x_A with the isotherm T_A in the unsaturated region.

Due to heat and mass transfer the air of state A will change in enthalpy and moisture content. This is expressed by di/dx. As shown in Fig. 7 this change points towards B_h, the so-called "pulling point." (B_h represents an apparent state of air which is mixed with air of state A.) For $\sigma c_p/h_A = 1$, $B_h \equiv B$. The air in the control volume of Fig. 6 is also heated at the unwetted surface A_d therefore its enthalpy change is altered and will be $(di/dx)_R$ or towards the pulling point B_R. B_R is at the same moisture content x_h as B_h but at a higher enthalpy i_R. The higher enthalpy is represented by the diagram value of the heat flux $q'_d A_d/A_b$. This state change $(di/dx)_R$ obviously is not very desirable in respect of cooling the air as much as possible by the evaporative process. The diagram of Fig. 7 does not specify the final state the air will reach and does not indicate changes of state of the pulling point(s) which result from the state change of the air-water interface. These changes of A and B's can be determined stepwise and by geometrical means as shown in [1]. For reasons of brevity we shall demonstrate the approach only briefly

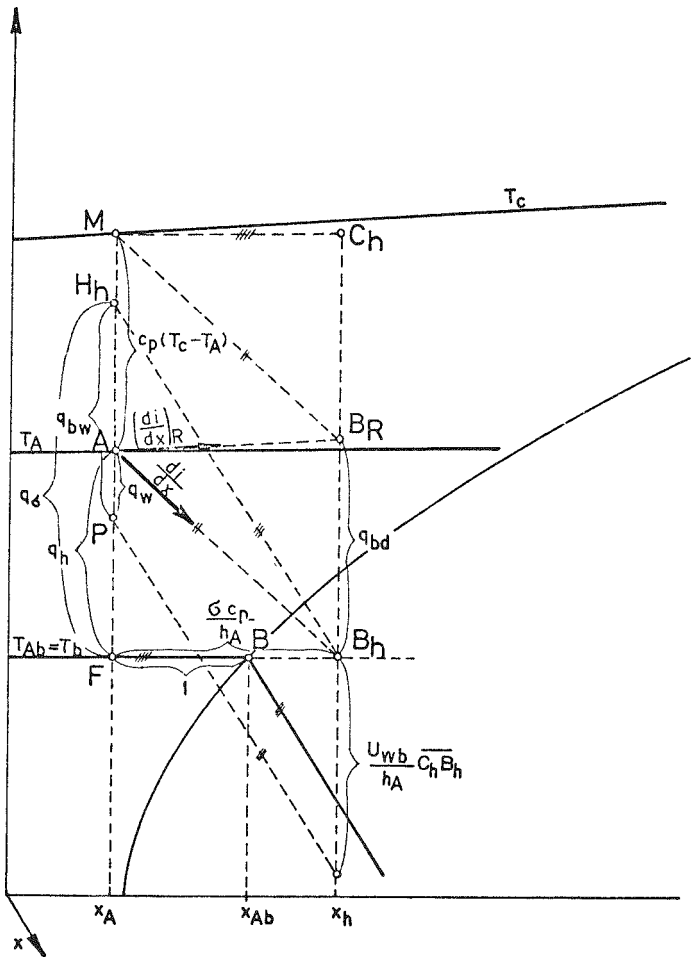

Figure 7. Distribution of diagram values in the i-x diagram cooling of wetted and dry walls.

and by assuming that all surfaces are wetted and the Lewis factor is unity. The latter means that the pulling points B_R and B_h coincide with the boundary point B and the change of air state is directed towards B. We assume that the air state A_1 of Fig. 8 has moved to A and the difference between the air and boundary states initially represented by a distance $\overline{A_1 B}$ of unity has diminished by a factor y. B has not changed. Under those conditions further changes of A, say to A', may be expressed by

$$\frac{dx_A}{x_b - x_A} = -\frac{dy}{y} \tag{19}$$

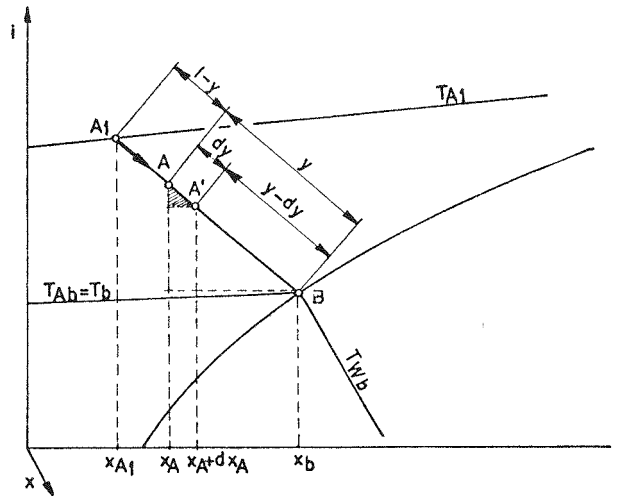

Figure 8. Determination of state changes by the partial value method.

where the negative sign accounts for the fact that an increase of x_A corresponds to a decrease of y. An energy balance yields a differential state change of the air

$$dA_b = \frac{\dot{m}_A \cdot c_p}{h_A} \frac{dx_A}{x_h - x_A} = \frac{\dot{m}_A c_p}{h_A} \cdot \frac{di}{i_R - i_A} \qquad (20)$$

$\frac{\dot{m}_A c_p}{h_a}$ in the above equation has the dimension of an evaporative surface area with respect to h_A and is called the unit surface a_b. With this equation (19) can be expressed as

$$-\frac{dy}{y} = \frac{dA_b}{a_b} \qquad (21)$$

Integrating of (21) by assuming x_b = const. yields

$$\ell n \frac{1}{y} = \frac{\Delta A_b}{a_b} = n' \qquad (22)$$

where ΔA_b is the evaporative surface required to change the air state A to A' along the mixing line. n' is the number of unit surfaces a_b contained in the partial surface ΔA_b.

For the stepwise integration of equation (19) (1-y) must be chosen small, otherwise, simultaneous displacement of B will occur and the assumption of x_b = const. is violated. Usually y can be selected to be 0.5 and n' = ℓn2 = 0.693. For the total surface A_b required $n\Delta A_b$ or $n(0.693\ a_b)$ must be provided. The increase of water enthalpy is given by

$$di_{Wb} = q_w \frac{\dot{m}_A}{\dot{m}_W} \frac{dx}{x_h - x_A} \tag{23}$$

and depends on the magnitude and sign of the diagram value q_w which can be determined for each pair of A and B in the i-x diagram (see Fig. 7). Integrating Eq. 23 for the finite step Δx along the finite exchange surface ΔA_b yields

$$\Delta i_{Wb} = c_{pW} \Delta T_b = q_w \frac{\dot{m}_A}{\dot{m}_W} \ln \frac{1}{y} \tag{24}$$

The integration procedure can be aided by involving the quantity Δi_F which is given as

$$\Delta i_F = c_{pA} \cdot \Delta T_b = \frac{c_{pA}}{c_{pW}} \Delta i_{Wb} \tag{25}$$

Eqs. 24 and 25 yield

$$\Delta i_F = q_w \left(\frac{\dot{m}_A c_{pA}}{\dot{m}_W c_{pW}} \ln \frac{1}{y} \right) \tag{26}$$

For fixed flow rates and selected y the product in the parentheses of eq. 26 is practically constant = b and $\Delta i_F = b q_w$.

The methods of determination of state changes of air and water due to heat and mass transfer processes discussed so far are summarized and demonstrated in Fig. 9.

For illustration of the state changes it is assumed in Fig. 9 that $\sigma c_p / h_A = 1$ and $A_d = 0$ (absence of dry surface). The water is supplied with the flow rate $\dot{m}_W$ and at temperature T_{W1}. The flow rate of air is $\dot{m}_A$ and its state conditions are specified by T_{A1}, x_{A1} and i_{A1}. The refrigerant condenses at T_c. Assuming that $T_{b1} = T_{W1}$ specifies the boundary state B (first pulling point). q_{w1} can be determined from the last term of eq. 10 which yields P_1 on the vertical line through x_{A1}, selecting y and applying eq. 19 yields x_{A2}

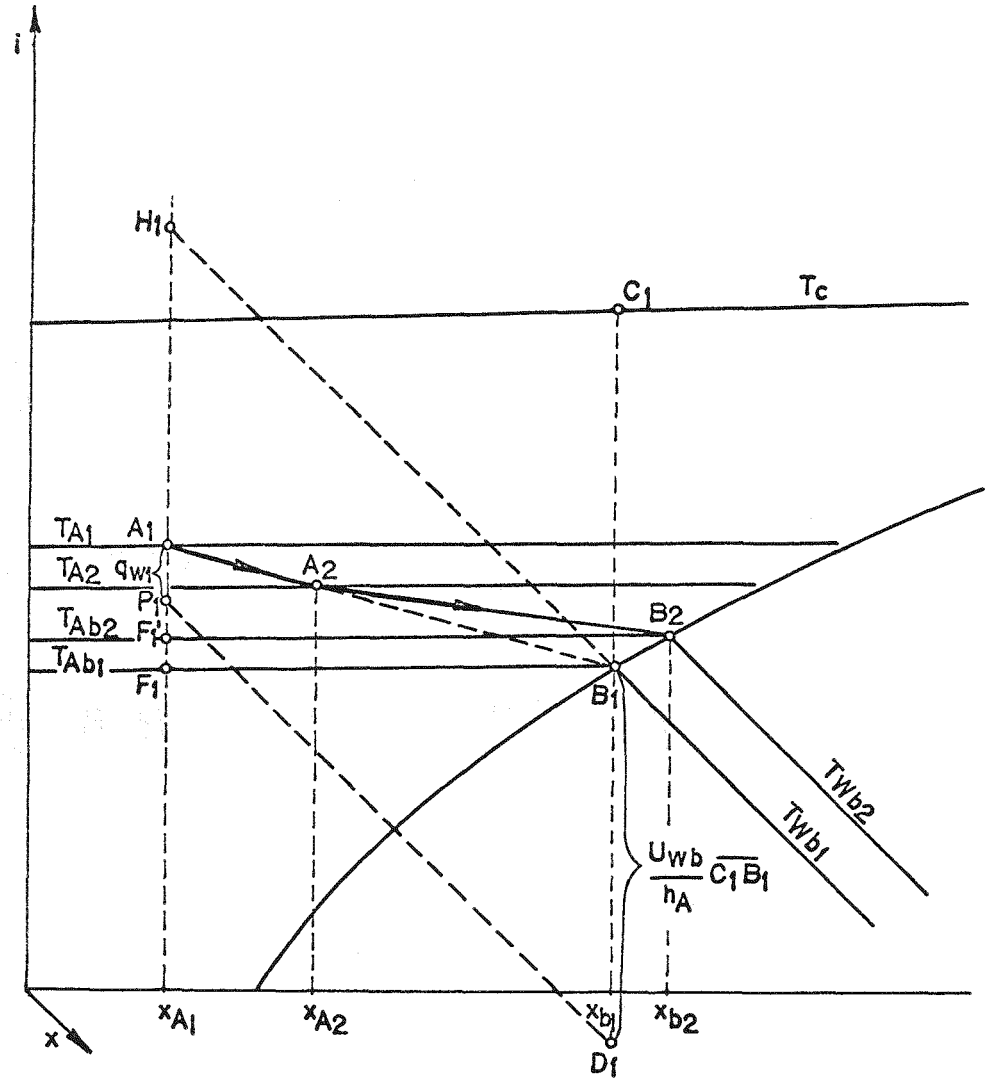

Figure 9. Successive Changes of Air and Water

and A_2 and the line $\overline{A_1 B_1}$. y introduced into eq. 26 yields Δi_{F1} and F_1' and T_{Ab_2} are determined as shown in Fig. 9. The saturated state of air at T_{Ab_2} represents the new pulling point B_2 and the respective moisture content x_{b2}. The above procedure is repeated for the required number of steps or until the required outlet state of the air is reached.

During the processes of evaporation the water flow rate changes and can be evaluated from

$$\Delta \dot{m}_W = \pm (1-y)\, \dot{m}_A\, (x_A - x_b) \qquad (27)$$

Positive sign (+) holds for parallel flow while negative sign (-) holds for counter flow. Δi's are above A_1 for positive and below A_1 for negative values. Generally,

$$\text{for parallel flow} \qquad \dot{m}_W > 0,\ b > 0$$

$$\text{for counter flow} \qquad \dot{m}_W < 0,\ b < 0 \tag{28}$$

The equations listed so far were used only to demonstrate the procedures to evaluate the state changes of the flow resulting from combined heat and mass transfer. For a specified heat load of a condenser and for specified flow rates and flow pattern within the channels transfer coefficients must be evaluated.

5. Basic Heat Transfer Equations

The hydraulic diameter of the elemental channel shown in Fig. 4 and of geometry given in Fig. 5, is

$$D_{h_A} = \frac{4 \cdot A_{AMo} \cdot SL}{A_m} \tag{29}$$

where A_{AMo} is the minimum cross-section area and A_m is the total surface area on the air-side of one module.

The Reynolds number of the air flow is defined as

$$Re_A = \frac{G_A \cdot D_{h_A}}{\mu_A \cdot 3600} \tag{30}$$

where G_A is the mass flux through the minimum cross-section area and μ_A is the dynamic viscosity of the moist air.

The heat transfer coefficient h_A is evaluated from experimental data given in heat transfer literature [2,3,4] in terms of Colburn j-factor. The experimental j-factor curve was replaced mathematically as

$$j_A = 0.17199\ Re_A^{-0.40307} \tag{31}$$

and

$$h_A = j_A \cdot G_A \cdot \frac{c_{p_A}}{Pr_A^{2/3}} \tag{32}$$

The heat transfer areas at the air-side of the heat exchanger are primary and extended areas and the temperature effectiveness η_o must be computed from the fin efficiency and from A_m and the total fin area A_F of a module.

The refrigerant flows inside tubes of hydraulic diameter D_{h_R} = DI and

$$Re_R = \frac{G_R \cdot D_{h_R}}{\mu_R \cdot 3600} \tag{33}$$

where G_R is the equivalent mass flux of the refrigerant defined as [3].

$$G_R = \frac{v_R \cdot \rho_{R_f}}{2} \left[1 + \left(\frac{\rho_{R_f}}{\rho_{R_g}}\right)^{0.5}\right] \tag{34}$$

where the ρ's are the densities of saturated liquid and vapor respectively at T_C and v_R is the velocity of the refrigerant.

The Nusselt number of fluids condensing inside tubes is given by [3]; for Re < 50,000

$$Nu_R = 5.03\, Re_R^{0.3}\, Pr_R^{1/3} \tag{35}$$

and for Re > 50,000

$$Nu_R = 0.0265\, Re_R^{0.8}\, Pr_R^{1/3}$$

The inside heat transfer coefficient h_R is

$$h_R = \frac{Nu_R\, k_R}{DI} \tag{36}$$

The overall heat transfer coefficient for the air-cooled module is obtained from

$$U \equiv \frac{1}{A_m(R_A + R_{FTR})} \tag{37}$$

where the convective and conductive resistances are given as

$R_A = 1/\eta_o h_A A_m$ (air-side convective resistance)

$R_F = TF/k_F A_{Fc}$ (fin resistance)

$$R_{FTR} = \Sigma \qquad R_T = \frac{TT/k_T A_{To}}{T\ To} \text{(tube resistance)}$$

$$R_R = 1/h_R A_{Ti} \quad \text{(refrigerant-side convective resistance)}$$

The above relationships are valid for heat transfer between air and dry surfaces of the heat exchanger. For the wetted surface and for the flow arrangements shown in Fig. 10 additional information is needed.

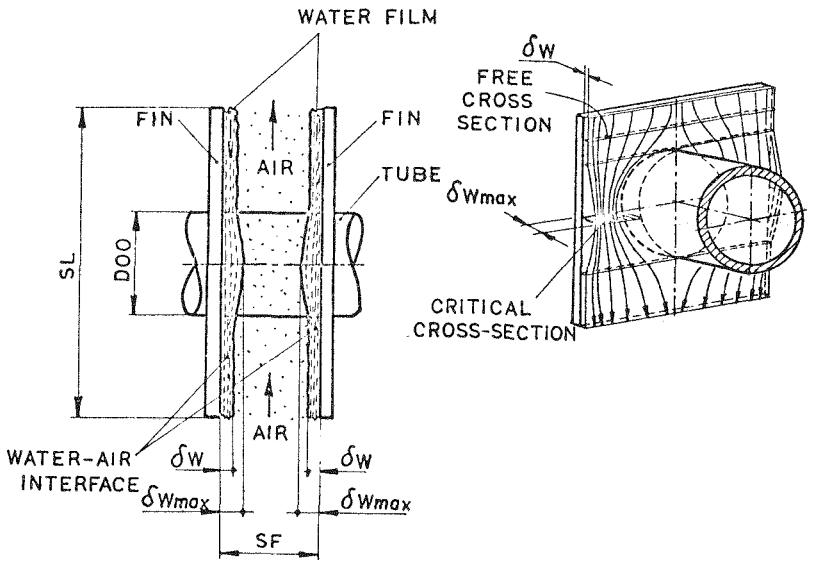

Figure 10. Flow Parameters of the Wetted Modules

The water film is assumed to flow laminarly downward under the influence of gravity. The air passage between the fin is smaller due to the presence of water on both channel walls. The passage is smallest where the water flows around the tube. Obviously the water flow must be selected such that the smallest cross-section is never blocked.

$$2\ \delta_{W_{max}} < SF \tag{38}$$

Water flow by gravity on inclined or vertical walls has been studied extensively [4,5,6,7]. It was shown that the flow is laminar for $Re_W \leq 250$. Under those conditions the water flow rate through the elemental channel of the module can be given as

$$\dot{m}_{W_c} = \frac{Re_W \cdot \mu_W}{2} \left[(ST - DOO) + SF\right] \tag{39}$$

The volumetric flow rate on one side is

$$\dot{m}_{WVC} = \frac{\dot{m}_{WC}}{2\rho_W} \tag{40}$$

and the thickness of the water film can be expressed by

$$\delta_W = \left[\frac{3 \cdot \nu_W \cdot \dot{m}_{WVC}}{ST \cdot g}\right]^{1/3} \tag{41}$$

or

$$\delta_{W_{max}} = \left[\frac{3 \cdot \nu_W \cdot \dot{m}_{WVC}}{(ST - DOO + SF)\, g}\right]^{1/3} \tag{42}$$

The mean velocities of the film are

$$v_{W,av} = \frac{g \cdot \delta_W^2}{3 \cdot \nu_W}$$

and (43)

$$v_{W_{av,cr}} = \frac{g \cdot \delta_{W_{max}}^2}{3 \cdot \nu_W}$$

The flow should remain laminar and therefore the Re number must be less or equal to 250 at the critical cross section

$$Re_{W_{in}} = Re_{W_{cr}} = \frac{4 \cdot v_{W_{av,cr}} \cdot \delta_{W_{max}}}{\nu_W} \tag{44}$$

and in areas above and below the tube Re should be not less than 10-30 [6] (otherwise the film will break up and dry spots occur).

$$Re_W = \frac{4 \cdot v_{W_{av}} \cdot \delta_W}{\nu_W} \tag{45}$$

ν_W in the above equation is the kinematic viscosity of the water at its respective temperature.

The film heat transfer coefficient h_W between water film and fin can be evaluated from [4]:

$$h_W = 0.01\left[\frac{k_W^3 \rho_W^2 g}{\mu_W^2}\right]^{1/3} Pr_W^{1/3} Re_{W_{cr}}^{1/3} \tag{46}$$

From h_W the convective resistance can be computed and the overall heat transfer coefficient U_W (refrigerant-water) can be evaluated.

The heat transfer from the water surface to the air can be treated in the same way as shown for the dry channel by correcting the hydraulic diameter to account for the smaller cross-section for the air flow.

The heat transfer coefficient h_A evaluated above will yield the mass transfer coefficient σ when the Lewis factor is specified. The state changes of the air and water flows can therefore be determined by stepwise integration graphically with the aid of the i-x diagram as was demonstrated above. The graphical approach can be simulated analytically when the thermodynamic parameteters of the moist air, such as the partial saturation pressure p_{gb} of water vapor, humidity ratio x_{gb} and i_{gb} can be given by mathematical relationships. For the computer simulation only $T = f(p_{gb})$ or $p_{gb} = f(T)$ needs to be established; all the others can then be determined from well-known equations.

For the temperature range of interest (10 to 42 C) a mathematical curve fit to tabulated data [9] yielded

$$T_A = -73.00 + 17.03 \ln p_{gb} \text{ , or}$$
$$P_{gb} = \exp (0.0587\, T_A + 4.2866) \qquad (47)$$

The coefficient of determination was $r^2 = 0.998768$ therefore the equations represent the data excellently.

Introducing eq. (47) into

$$x_A = 0.622 \frac{\phi_A \cdot p_{gb}}{100P - \phi_A \cdot p_{gb}}$$

or (48)

$$x_g = 0.622 \frac{p_{gb}}{P - p_{gb}}$$

yield humidity ratio x_A for unsaturated or x_g for saturated conditions. P is the total pressure of the moist air (= 760 mm Hg) and ϕ_A is the relative humidity of the air in percent.

The enthalpies of the air can be determined from x and T by

$$i_A = (0.46\ T + 597)\ x_A + 0.24\ T_A \qquad (49)$$

where the specific heat of the moist air is given by $c_{pA} = 0.24 + 0.46\ x_A$. The constant 597 is the latent heat of water at 760 mm Hg. The T's are in Celsius.

Computer simulation of the graphical method requires an additional procedure to determine the first water boundary state B_1 which should be below B_2. Otherwise the assumption of $T_{Wb1} < T_{Wb2}$ is not satisfied.

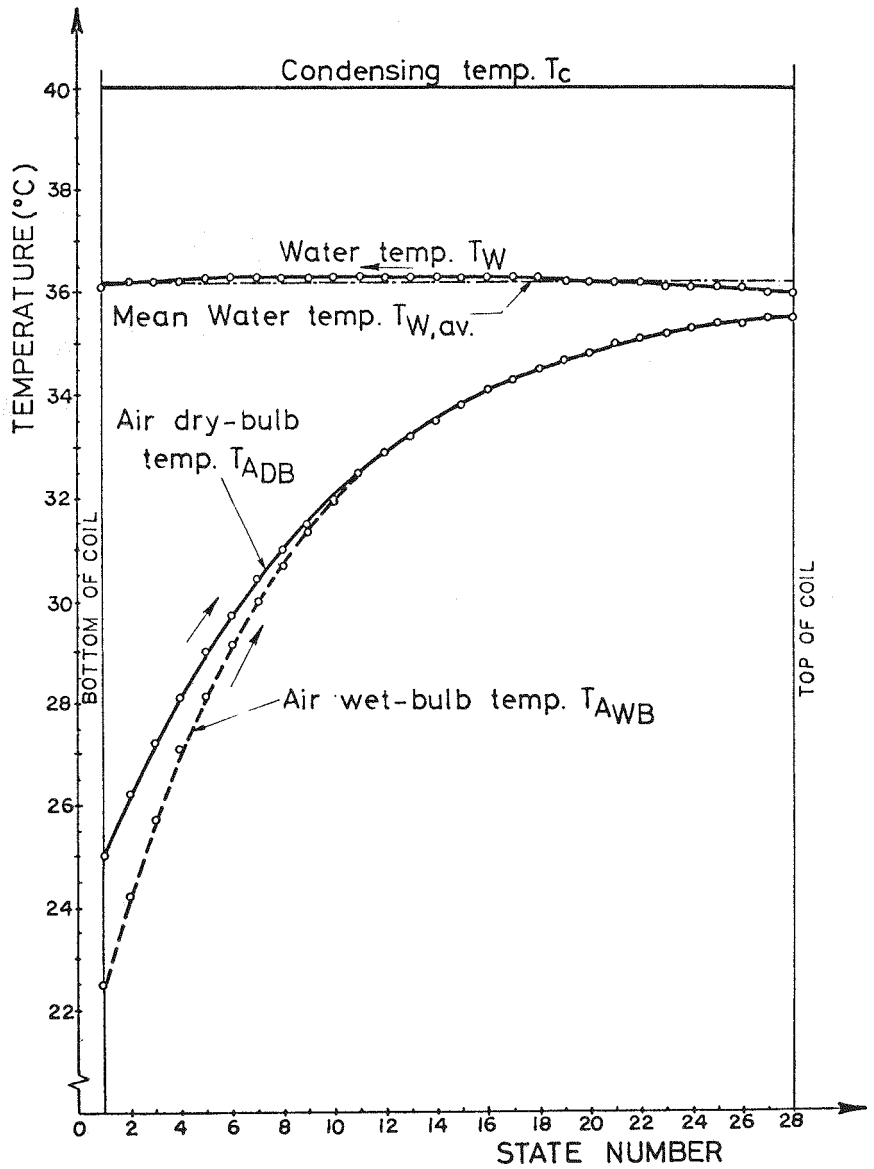

Figure 11. Temperature profiles of refrigerant, water and air.

Furthermore, it is desired that the water leaving the exchanger has the same temperature as the water entering. The last pulling point B_n must coincide with B_1. These requirements necessitate iterations which must be continued until B_1 and B_n are equal or differ only in temperature by a specified amount (selected to be ±0.15 C). That $B_n \rightarrow B_1$ can be explained by the fact that the state of air flowing through the wetted channel approaches gradually the saturation condition and the negative diagram value q_w approaches zero and becomes then increasingly positive and condensation might occur within the channel. The temperature of the water must for the same reason have a maximum somewhere along the channel [10,11]. This is shown in Fig. 11 (see case 6 of Table 1).

6. Results of Computations and Comparison of Performance of Dry and Wetted Condensers of Given Geometry

The plate-fin-tube heat exchanger shown in Fig. 3 and of design specified in Fig. 4 was selected for the performance analysis. The geometrical parameters of Fig. 4 were chosen to be of the following dimensions.

$$ST = SL = 2.54 \times 10^{-2} \text{ [m]}$$
$$TF = 1.78 \times 10^{-4} \text{ [m]}$$
$$TT = 8.89 \times 10^{-4} \text{ [m]}$$
$$DO = 1.58 \times 10^{-2} \text{ [m]}$$

(tube material: copper; fin material: aluminum)

Other parameters were selected to be:

Numbers of modules per elemental channel: $n_m = 3$

Number of fins per unit length of tube: $FPM = 315 \text{ [m}^{-1}\text{]}$

Velocity of the refrigerant R-12: $v_R = 1 \text{ [m/s]}$

Condensing temperature: $T_c = 40 \text{ [C]}$

Reynolds number of water film: $Re_W = 250$

Coefficient of wetness: $K_w = 1$

Ambient air temperature: $T_{A_{in}} = 25 \text{ [C]}$.

All other parameters were considered as variables:

Relative humidity: $\phi_{A_{in}} = 50, 80, 90, 100 \text{ [\%]}$

Velocity of air: $v_A = 1 - 10 \text{ [m/s]}$

Reynolds number of air: $Re_A = 160 - 1600$.

The results of the computations are presented in Table 1 for 40 different cases. For various inlet conditions the following parameters were computed: $T_{A_{out}}$, $\phi_{A_{out}}$, q_{cw}, $R_{\ell at}$ (percentage of heat load due to evaporation), $T_{W,av}$, K_e, T_c^*, ΔNu_A, ΔCOP and ε (heat exchanger effectiveness of unwetted exchanger). The augmentation of heat transfer expressed by K_e is high as shown in the table. This obviously influences the temperative effectiveness and efficiency of the fins which are difficult to evaluate due to their geometry and complex heat transfer distribution of the uneven water film. An average heat transfer coefficient on the water side was assumed such that the heat transfer from the condensing refrigerant to the water film equals the heat Δi_{cw} received by the air.

The effectiveness of the fins decreases on the average by 35% when compared with heat transfer to dry air. This decrease could be offset by using thicker fins but this was not considered because the decrease in effectiveness has only a very small influence on the overall performance of the wetted coil. This performance is mainly a function of surface of the coil and of uniform wetting conditions. This is in agreement with [12]. The state changes of the air and of the water interface of the case No. 6 of Table 1 are shown in the i-x diagram of Fig. 12. The data in this diagram demonstrates that 28

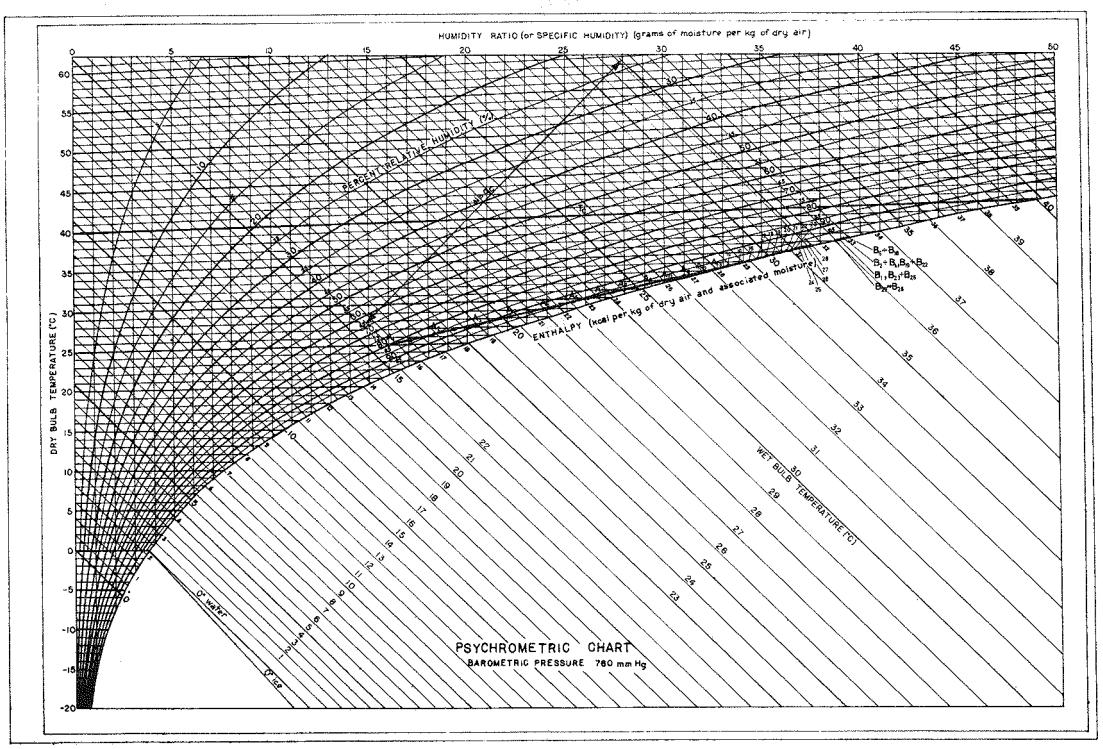

Figure 12. State changes of air and water interface.

changes of the air and the water states had to be computed.

Fig. 13 shows coefficients of enhancement K_e vs. Re_A and vs. v_A for different relative humidities of ambient air.

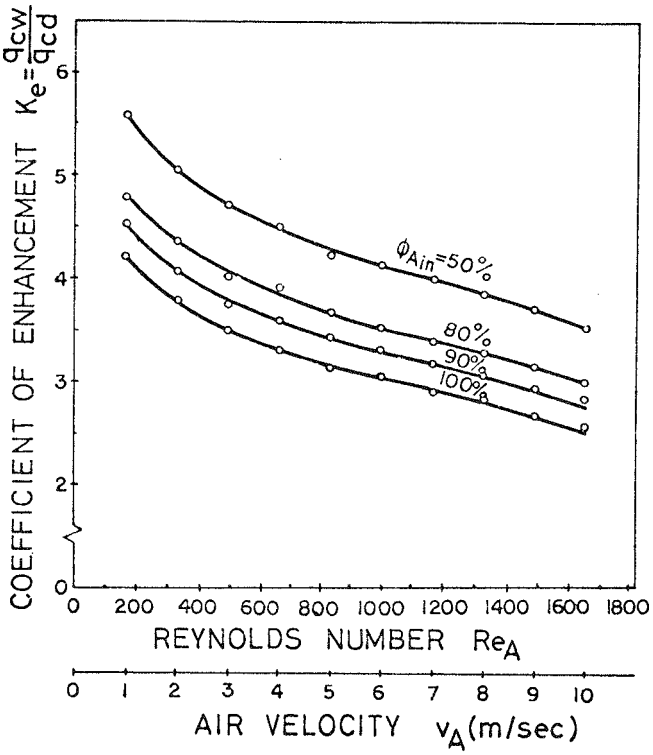

Figure 13. Coefficient K_e vs. Re_A for different relative humidities of ambient air.

Fig. 14 shows ΔNu_A vs. Re_A and vs. v_A for different relative humidity of ambient air.

Fig. 15 compares the actual heat exchanged in the dry and the wetted heat exchanger as a function of air velocity and Reynolds number for different relative humidities. The enthalpy changes experienced by the air passing through the heat exchanger is indicated by the Δi_{cw} curve. It should be recognized that in some instances Δi_{cw} reaches at some locations within the channel slightly larger values than between inlet and exit. This situation will occur when condensation is present (not shown in Fig. 12 or Table 1). The figure demonstrates clearly that a given heat load can be transferred to air flowing through the wetted condenser at a much lower velocity than through the dry one. This is beneficial in respect to

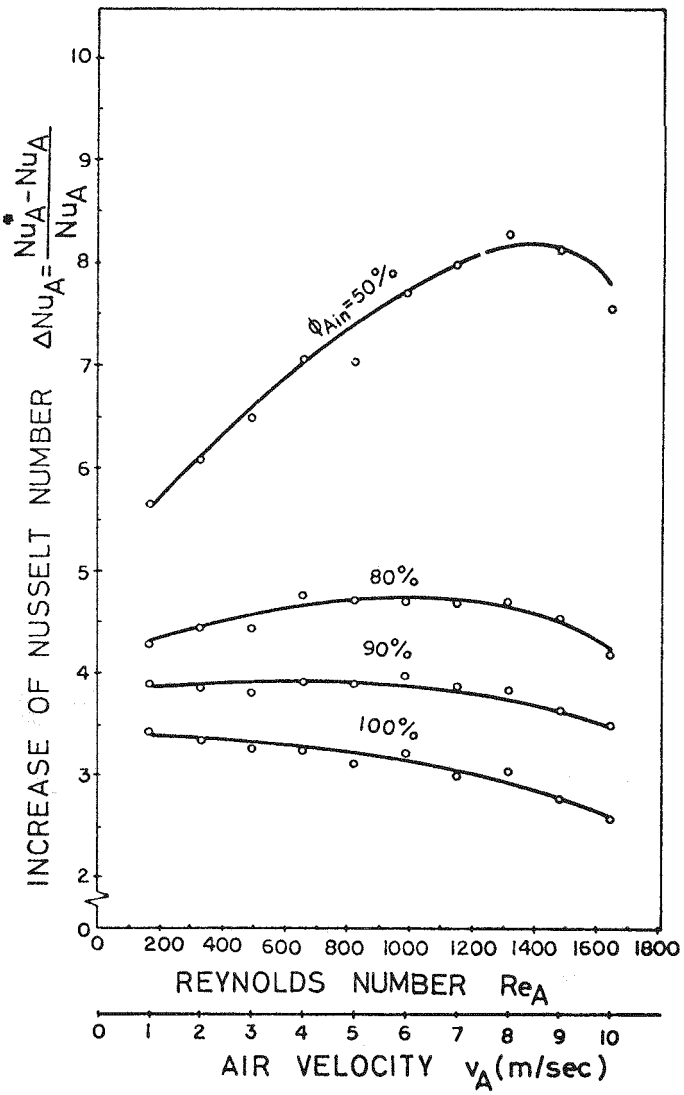

Figure 14. ΔNu_A vs. Re_A for different relative humidities of ambient air.

pressure drop in the air stream and pumping power, despite the fact that the friction coefficient itself increases. Calculation of pressure drops not included in the article assumed a doubling of friction coefficient due to wavy air-water interfaces.

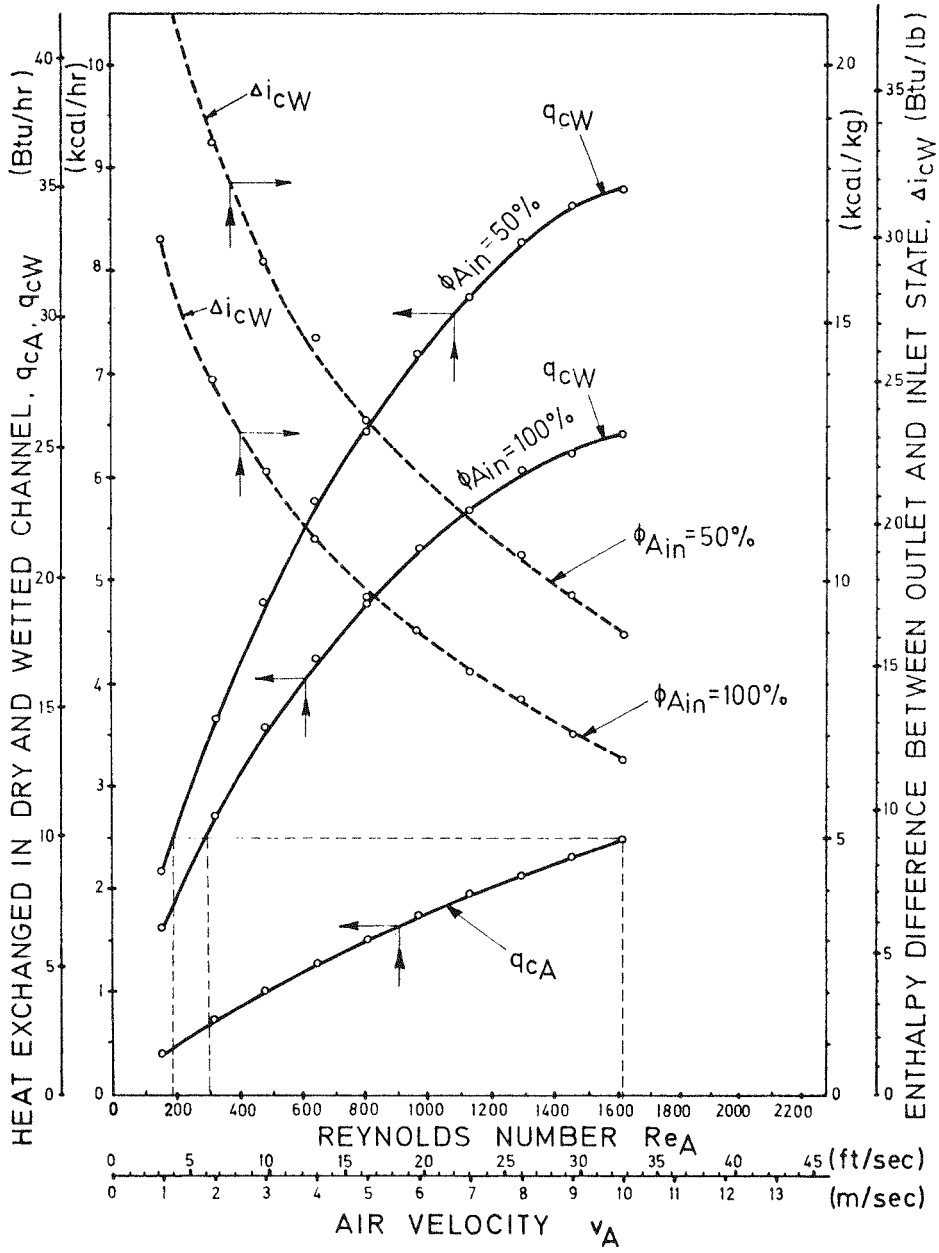

Figure 15. Comparison of Heat Exchange in Dry and Wetted Channel

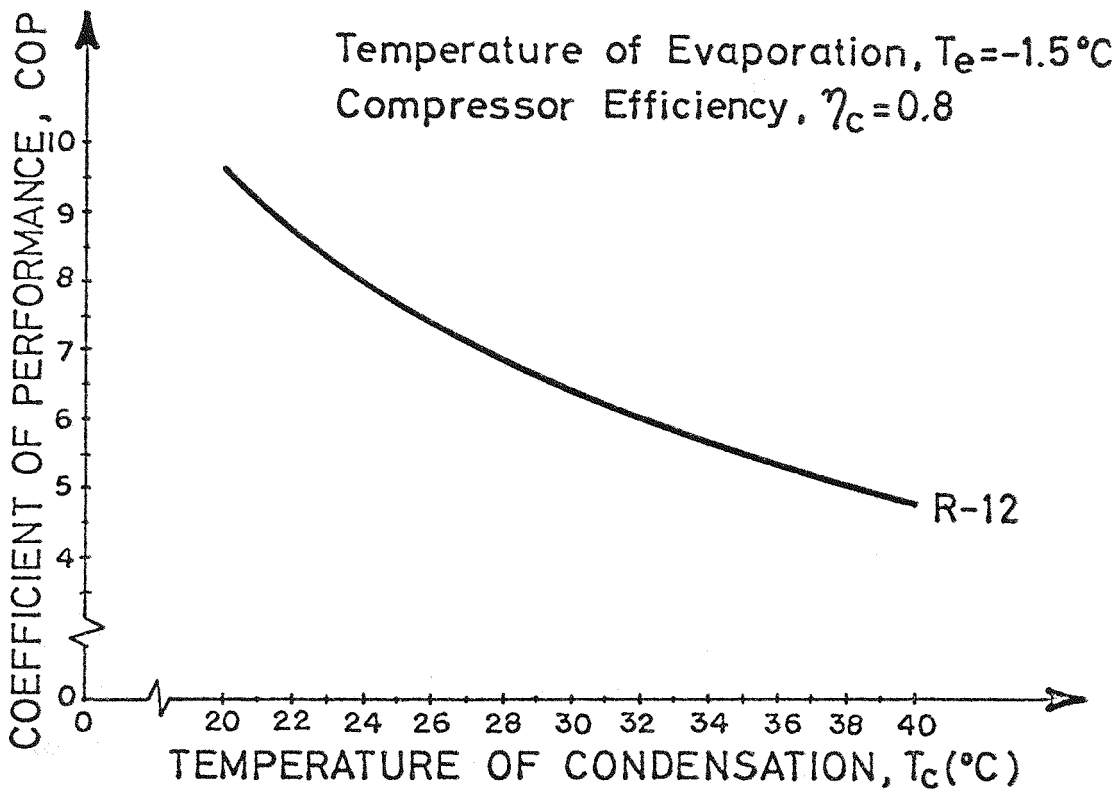

Figure 16. COP vs. T_c

Table 1 lists also the increase of COP due to changing $T_c \rightarrow T_c^*$, as was discussed in Section 2. COP* given by eq. 5 can be evaluated from ΔQ_e and ΔW_{act} data. These can be determined from T-S or p-i diagrams of the refrigerant and under the assumption that both the boiling temperature T_e and the overall compressor efficiency η_c are constant. For T_e = -1.5 C and η_c = 0.8 ΔQ_e and ΔW_{act} values and COP were determined for various T_c's and plotted in Fig. 16. An iterative process was applied to determined the lowest possible temperature of the condensing refrigerant T_c^* which (within a specified limit of ±10%) would provide the same heat rejection of the wetted condenser as that of the dry one. The T_c^* so obtained yield from Fig. 16 the COP* listed in Table 1.

TABLE 1. Performance of wetted condenser for constant inlet temperatures of air at various relative humidities and different velocities

case no.	v_A [$\frac{m}{sec}$]	$\phi_{A_{in}}$ [%]	Re_A -	$T_{A_{out}}$ [°C]	$\phi_{A_{out}}$ [%]	q_{cw} [$\frac{kcal}{hr}$]	$R_{\ell at}$ [%]	$T_{W,av}$ [°C]	K_e -	ΔNu_A -	T^*_c [°C]	ε -	ΔCOP %
1	1	50	165.5	37.2	99.9	2.17	87.0	37.3	5.58	5.649	24.2	0.94	65.9
2	1	80	165.5	37.2	100.0	1.86	84.5	37.6	4.79	4.292	28.0	0.94	43.2
3	1	90	165.5	37.3	100.0	1.76	83.5	37.7	4.53	3.893	29.0	0.94	38.3
4	1	100	165.5	37.3	100.0	1.64	82.3	37.7	4.22	3.425	30.2	0.94	32.7
5	2	50	331.0	35.0	99.3	3.65	87.0	35.6	5.05	6.075	24.4	0.87	64.5
6	2	80	331.0	35.5	100.0	3.14	84.2	36.2	4.35	4.439	28.2	0.87	42.2
7	2	90	331.0	35.6	100.0	2.94	82.9	36.3	4.07	3.862	29.2	0.87	37.3
8	2	100	331.0	35.7	100.0	2.73	81.4	36.4	3.78	3.339	30.4	0.87	31.8
9	3	50	496.5	33.6	98.4	4.79	87.2	34.5	4.72	6.480	24.6	0.82	63.2
10	3	80	496.5	34.2	100.0	4.08	84.0	35.1	4.02	4.431	28.4	0.82	41.2
11	3	90	496.5	34.4	100.0	3.82	82.5	35.3	3.76	3.808	29.4	0.82	36.4
12	3	100	496.5	34.6	100.0	3.57	80.8	35.5	3.51	3.273	30.6	0.82	31.0
13	4	50	662.0	32.7	97.7	5.77	87.4	33.6	4.51	7.056	24.8	0.77	61.9
14	4	80	662.0	33.5	100.0	4.98	84.0	34.5	3.90	4.757	28.4	0.77	41.2
15	4	90	662.0	33.6	100.0	4.60	82.3	34.6	3.60	3.908	29.6	0.77	35.4
16	4	100	662.0	33.8	100.0	4.25	80.4	34.8	3.32	3.241	30.8	0.77	30.1
17	5	50	827.5	31.7	96.6	6.44	87.8	32.7	4.24	7.044	24.8	0.74	61.9
18	5	80	827.5	32.6	99.6	5.60	83.9	33.8	3.68	4.698	28.6	0.74	40.2
19	5	90	827.5	32.9	100.0	5.21	82.2	34.1	3.43	3.894	29.8	0.74	34.5
20	5	100	827.5	33.1	100.0	4.77	79.9	34.2	3.14	3.108	31.0	0.74	29.3
21	6	50	993.0	31.1	95.8	7.20	88.0	32.1	4.13	7.693	25.0	0.70	60.6
22	6	80	993.0	32.0	99.3	6.14	83.9	33.2	3.53	4.696	28.8	0.70	39.2
23	6	90	993.0	32.3	100.0	5.78	82.1	33.6	3.32	3.967	30.0	0.70	33.6
24	6	100	993.0	32.6	100.0	5.34	79.7	33.9	3.07	3.206	31.2	0.70	28.4
25	7	50	1158.0	30.5	95.0	7.77	88.4	31.5	3.99	7.983	25.2	0.67	59.3
26	7	80	1158.0	31.4	99.0	6.61	83.9	32.7	3.39	4.680	28.8	0.67	39.2
27	7	90	1158.0	31.7	100.0	6.20	82.0	33.1	3.18	3.868	30.2	0.67	32.7
28	7	100	1158.0	32.1	100.0	5.66	79.4	33.3	2.90	3.004	31.2	0.67	28.4
29	8	50	1324.0	30.0	94.1	8.27	88.7	31.0	3.86	8.277	25.2	0.65	59.3
30	8	80	1324.0	31.0	98.7	7.05	84.0	32.3	3.29	4.707	29.2	0.65	37.3
31	8	90	1324.0	31.3	100.0	6.59	82.0	32.7	3.07	3.825	30.2	0.65	32.7
32	8	100	1324.0	31.7	100.0	6.07	79.2	33.1	2.84	3.026	31.6	0.65	26.8
33	9	50	1489.0	29.4	93.0	8.61	89.1	30.5	3.71	8.133	25.6	0.63	56.8
34	9	80	1489.0	30.5	98.3	7.34	84.0	31.9	3.16	4.539	29.2	0.63	37.3
35	9	90	1489.0	30.8	99.9	6.84	82.0	32.3	2.94	3.628	30.6	0.63	31.0
36	9	100	1489.0	31.2	100.0	6.23	78.9	32.7	2.68	2.757	31.6	0.63	26.8
37	10	50	1655.0	28.9	91.8	8.80	89.5	30.0	3.53	7.552	25.6	0.60	56.8
38	10	80	1655.0	30.0	97.8	7.50	84.1	31.5	3.01	4.190	29.6	0.60	35.4
39	10	90	1655.0	30.4	99.7	7.08	81.9	32.0	2.84	3.490	30.6	0.60	31.0
40	10	100	1655.0	30.8	100.0	6.41	78.6	32.4	2.57	2.576	32.0	0.60	25.2

TABLE 2

Evaporative Condenser Performance at Ambient Temperatures Higher Than Temperature of Condensation T_c = 40 C of Refrigerant R-12

case no.	$T_{A_{in}}$ [°C]	$\phi_{A_{in}}$ [%]	$T_{A_{out}}$ [°C]	$\phi_{A_{out}}$ [%]	q_{cw} [$\frac{kcal}{hr}$]	R_{lat} [%]	R_{sen} [%]	$T_{W,av}$ [°C]
1	40.1	10	36.0	93.9	3.60	105.3	-5.3	35.8
2	40.1	20	36.4	94.6	3.18	105.5	-5.5	36.2
3	40.1	60	38.0	97.5	1.53	106.4	-6.4	37.9
4	40.1	100		$T_{W,av} > T_c$				
5	50.0	10	37.2	91.5	3.02	120.0	-20.0	36.5
6	50.0	20	37.8	92.6	2.32	124.8	-24.8	37.2
7	50.0	60		$T_{W,av} > T_c$				
8	50.0	100		$T_{W,av} > T_c$				
9	55.0	10	37.9	90.4	2.66	130.5	-30.5	36.9
10	55.0	20	38.7	91.8	1.76	144.0	-44.0	37.7
11	55.0	60		$T_{W,av} > T_c$				
12	55.0	100		$T_{W,av} > T_c$				
13	60.0	10	38.5	89.3	2.25	145.1	-45.1	37.3
14*	60.0	20	39.6	91.0	1.14	184.8	-84.8	38.4
15	60.0	60		$T_{W,av} > T_c$				
16	60.0	100		$T_{W,av} > T_c$				

v_A = 2 m/s

*The changes of temperature and humidity of the hot air flowing through the exchanger are shown in Fig. 17.

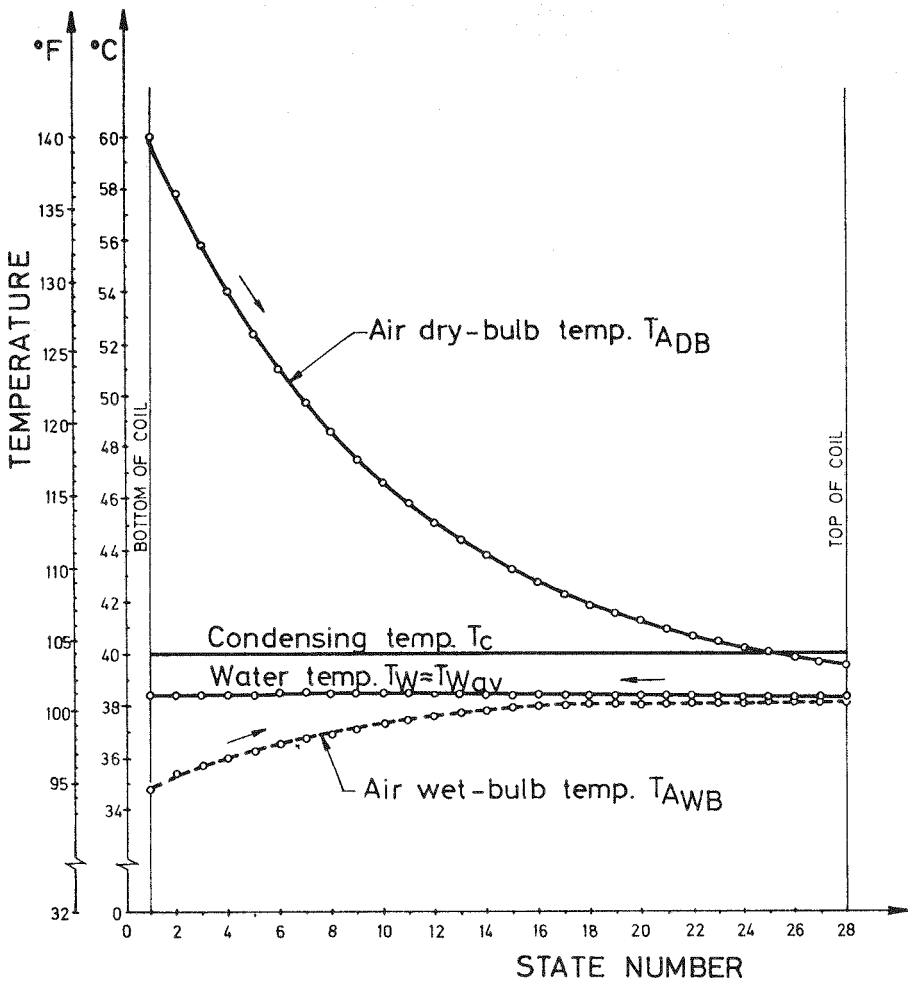

Figure 17. Temperature profiles of fluids in wetted condenser operating in ambient air of much higher temperature than the condensing fluid. The temperature of the water T_W remains practically constant despite the fact that it receives heat from both air and condensing fluid. The heat received evaporates part of the water. The vapor generated is added to the air stream. T_{AWB} indicates the change of relative humidity experienced by the air.

These data are not necessarily correct but possibly too low for the following reasons.

The heat load of the dry condenser is

$$Q_{CD} = Q_e + W_{act} \tag{50}$$

while the load of the wetted condenser is:

TABLE 3

Continuation of Table 2 Except
For v_A = 5 and 8 m/s

case no.	$T_{A_{in}}$ [°C]	$\phi_{A_{in}}$ [%]	$T_{A_{out}}$ [°C]	$\phi_{A_{out}}$ [%]	q_{cw} [$\frac{kcal}{hr}$]	$R_{\ell at}$ [%]	R_{sen} [%]	$T_{W,av}$ [°C]
				v_A = 5 m/s				
1	40.1	10	33.9	84.3	6.38	111.5	-11.5	33.0
2	40.1	20	34.6	86.4	5.63	111.6	-11.6	33.8
3	40.1	60	37.3	93.9	2.68	112.4	-12.4	36.9
4	40.1	100		$T_{W,av} > T_c$				
5	50.0	10	36.2	79.8	5.26	131.0	-31.0	34.1
6	50.0	20	37.4	82.9	4.11	136.2	-36.2	35.5
7	50.0	60		$T_{W,av} > T_c$				
8	50.0	100		$T_{W,av} > T_c$				
9	55.0	10	37.5	77.9	4.69	144.0	-44.0	34.9
10	55.0	20	39.0	81.4	3.15	160.1	-60.1	36.6
11	55.0	60		$T_{W,av} > T_c$				
12	55.0	100		$T_{W,av} > T_c$				
13	60.0	10	38.7	76.0	3.93	164.0	-64.0	35.6
14	60.0	20	40.5	79.9	1.97	216.7	-116.7	37.6
15	60.0	60		$T_{W,av} > T_c$				
16	60.0	100		$T_{W,av} > T_c$				
				v_A = 8 m/s				
17	40.1	10	32.9	77.6	8.12	116.8	-16.8	43.0
18	40.1	20	33.7	80.7	7.09	117.1	-17.1	37.5
19	40.1	60	37.0	91.6	3.38	117.5	-17.5	36.3
20	40.1	100		$T_{W,av} > T_c$				
21	50.0	10	35.9	72.4	6.72	139.6	-39.6	32.9
22	50.0	20	37.3	76.6	5.16	146.5	-46.5	34.5
23	50.0	60		$T_{W,av} > T_c$				
24	50.0	100		$T_{W,av} > T_c$				
25	55.0	10	37.5	70.1	5.86	156.3	-56.3	31.0
26	55.0	20	39.3	75.0	3.98	174.4	-74.4	35.9
27	55.0	60		$T_{W,av} > T_c$				
28	55.0	100		$T_{W,av} > T_c$				
29	60.0	10	39.2	67.9	5.00	178.5	-78.5	34.7
30	60.0	20	41.3	73.3	2.51	240.6	-140.6	37.2
31	60.0	60		$T_{W,av} > T_c$				
32	60.0	100		$T_{W,av} > T_c$				

$$Q_{CW} = Q_e + \Delta Q_e + W_{act} - \Delta W_{act} \qquad (51)$$

$Q_{CW} = Q_{CD}$ only for $\Delta Q_e = \Delta W_{act}$.

If these conditions exist or can be approached can be determined approximately from steam tables or diagrams or exactly by analyzing in addition the thermodynamic refrigeration cycle. This latter approach would require a rather extensive expansion of the already quite involved computer program and was not attempted at present also for reasons that the approximate analysis did indicate that $Q_{CW} \sim Q_{CD}$ (within 2-5%). Not to select the correct analysis is also due to the fact that COP* or ΔCOP are conservative values for the following reason.

A refrigeration system commonly specifies the cooling capacity Q_e and the evaporation temperature T_e. Lowering T_c to T_c^* increases this load by ΔQ_e. To maintain the specified load Q_e and T_e requires adjustments. These can be made either by decreasing the boiling heat transfer area or by lowering the mass flow rate. Whatever corrections are made will always result in a smaller condenser load. This implies that the condensing temperature could be decreased further to T_c^{**} yielding COP**, which is larger than COP*. The values of COP* or ΔCOP of Table 1 are therefore smaller than optimal possible.

7. Conclusions

The mathematical model developed in this article allows one to actually simulate the thermodynamic processes in the evaporative cooled condenser during steady state operations. The results obtained clearly demonstrate the considerable enhancement of heat transfer as indicated by ΔNu_A or by K_e in Table 1 or in Figs. 13, 14, and 15. In all cases $K_e > 3$ and in some instances $K_e > 5$.[1] These figures in addition show that K_e is largest for small velocities therefore the required air mass flow rate and the pumping power is many times less than for dry air-cooled unit of identical capacity.

---

[1] The experiments described in [13] did yield smaller values of $K_e \sim 1.4$ for practically identical ranges of Re_A than in this work. This is mainly due to the fact that the surfaces in [13] were not wetted uniformly because only water spray into the air stream through horizontal channels was investigated. Therefore cooling of air was the major influence and not wetting the heat transfer surfaces.

The results indicate also the advantage of adding more rows of tubes to the evaporative condenser under good wetting conditions. (This statement resulted from computations not included in Table 1 or the Figures.)

Evaporative condensers might still operate successfully even at high temperatures where air-cooled condensers are inoperative. (Ambient temperature >> condensing temperature.) Table 2 lists data for $T_{Amb} >> T_c$. Data for various ϕ_A's and different velocities are given in Table 3.

The evaporative condenser does not require close fin spacing (as was evaluated in other series of computations not included in Table 1) thus large extended outside surfaces are not needed. This is of importance because fouling or deposition of impurities of the water or the air can possibly be avoided with larger spacing between the fins.

Evaporative condenser performance decreases with increasing relative humidity of ambient air. This is due to the fact that less latent heat transfer can occur within the exchanger. The overall improvement however is still high even under conditions of saturated air entering the exchanger.

The increase of COP shown in Table I is very substantial for all cases shown. For conditions of $T_c^* = 25°C$ and fixed cooling load saving of compressor power of 37% can be achieved. Despite the increase of pressure drop of the air flow in the wetted condenser an even higher overall improvement of 45% results when the performance is defined as $(COP)_s = Q_e/\Sigma P$, where Q_e is the cooling load and ΣP is the total power consumption of the system. This dearly demonstrates that evaporative condensers will help to conserve energy.

The operating conditions of a wetted condenser assumed in this paper possibly cannot be realized in an actual device. In accordance also to [10,11,12] only a 10-12% lower performance may result.

In general it can be summarized that evaporative condensers can be used very beneficially whenever water supply is assured and whenever moisture content of exit air is of no concern or even desired. Continuously wetted heat transfer surfaces will minimize fouling and

treatment of the water might not be necessary. In addition only up to 1% of the water mass flow rate needs to be replenished. The evaporative condenser can be built from bare tubes and still smaller than an unwetted device.

Acknowledgments

The work described was part of a study to optimize a refrigeration system for a 100 MWH load leveling zinc-chloride battery. The chlorine gas evolving during charging of the battery must be stored in form of a hydrate for safety reasons. The hydrate formation is exothermal and heat must be removed by means of a heat pump. The work was supported by Energy Development Associates, Madison Heights, Michigan under a contract PRF 0050-57 with Purdue Research Foundation. The funds granted made possible the whole investigation and is gratefully acknowledged. The authors also owe gratitude to Mr. K. Lee, a graduate student who assisted to modify the computer programs for determination of enhancement of coefficient of performance.

References

1. F. Bošnjaković, Technical Thermodynamics, Holt, Rinehart and Winston, 1965.

2. William Kays and A.L. London, Compact Heat Exchangers, 2nd Edition, New York, McGraw-Hill, 1964.

3. J. Alan Chapman, Heat Transfer, MacMillan Publishing Co., Inc., 1974.

4. W.H. McAdams, Heat Transmission, McGraw-Hill, New York, 3rd Edition, 1954.

5. Thomas K. Sherwood, Robert L. Pigford, and Charles R. Wilke, Mass Transfer, McGraw-Hill Chemical Engineering Series, New York, 1975.

6. Levich G. Veniamin, Physicochemical Hydrodynamics, Prentice-Hall, Inc., Englewood Cliffs, NJ, 1962.

7. R.L. Cerro and S. Whitaker, "Entrance Region Flows with a Free Surface: The Falling Liquid Film," Chem. Eng. Sci., Vol. 26: 785 (1971).

8. F.C.K. Ho and R.L. Hummel, "Average Velocity Distributions Within Falling Liquid Films," Chem. Eng. Sci., Vol. 25:1225 (1970).

9. Recknagel and Spranger, Taschenbuch fur Heizung and Klima-Technik, 57, Ausgabe, Munchen, R. Oldenbourg, Verlag, 1972.

10. T. Mizushina, R. Ito and H. Miyashita, "Experimental Study of an Evaporative Cooler," Int. Chem. Engng., 7, 727 (1967), Translated from Kagaku-Kogaku, 31, 469 (1967).

11. T. Mizushina, R. Ito and H. Miyashita, "Characteristics and Methods of Thermal Design of Evaporative Coolers," Int. Chem. Engng., 8, 532 (1968), Translated from Kagaku-Kogaku, 32, 55 (1968).

12. T. Mizushina, "Design of Cooler Condensers and Evaporative Coolers," Heat Exchangers: Design and Theory Sourcebook, Chapter 16, McGraw-Hill, 1974.

13. Wen-Jei Yang and D.W. Clark," Spray Cooling of Air-Cooled Compact Heat Exchangers," Int. J. Heat Mass Transfer, Vol. 18, pp. 311-317, 1975.

Prof. Dr. Ing. W. Leidenfrost
School of Mechanical Engineering
Purdue University
West Lafayette, Indiana

Dipl. Ing. B. Korenic
Graduate Student at
School of Mechanical Engineering
Purdue University
West Lafayette, Indiana

Received:

APPENDIX D

100MWh ZINC-CHLORINE PEAK-SHAVING BATTERY PLANTS

100MWh ZINC-CHLORINE PEAK-SHAVING BATTERY PLANTS

Charles J. Warde, Philip C. Symons, Curtis C. Whittlesey, and Henry A. Catherino

Energy Development Associates
A Gulf + Western Company
Madison Heights, Michigan 48071

ABSTRACT

Energy storage in cost-effective high-efficiency battery plants would provide an attractive means for the electric-utility industry to conserve natural gas and oil. These plants sized in the 20-200MWh range would be located at substations in the utility subtransmission or distribution network. Energy Development Associates (EDA) has prepared three conceptual designs of a 100MWh zinc-chlorine battery plant for this application. The three designs, designated Marks 2, 3, and 4, were analyzed from the standpoints of cost, efficiency, land usage, safety, and environmental impact. All of the designs could meet the criteria for commercialization. Mark 4, based on the use of a 58kWh battery module, was found to be optimal in the areas of performance, safety, and manufacturability, while comparing favorably in cost and reliability to Marks 2 and 3. EDA has built and tested the prototype Mark 4 module, and will place a 4.8MWh battery system based on this design in the Battery Energy Storage Test (BEST) Facility during 1980.

IN ORDER TO SERVE THE NEEDS OF THE ELECTRIC-UTILITY INDUSTRY, zinc-chlorine peak-shaving battery plants will be located in the subtransmission or distribution network. The battery plants will be sized, generally in the 20-200MWh range, to meet the peaking needs of a specific industrial, commercial, or residential market. A 100MWh battery plant, which would serve the peaking requirements of a town of 60,000 people, is considered to be a typical size.

The zinc-chlorine battery system is based on the use of an aqueous zinc-chloride electrolyte in the temperature range 10-50°C.(1)* Chlorine, evolved during battery charging is stored as solid chlorine hydrate, external to the cell. Thus, it is possible to have a single chlorine-hydrate store for a 100MWh battery plant. During discharge of the battery, chlorine-saturated electrolyte must be delivered, by pumping, to every cell. A stack module - defined as an integral hydraulic unit with its own electrolyte pump - can be as small as a single cell. The more complex stack must be factory-assembled. Accordingly, the stack-module dimensions cannot exceed 40ft (length), by 8ft (width), by 10ft (height), i.e. the maximum size of package transportable by road without special permit.

In order for a 100MWh battery plant to be acceptable to the electric-utility industry, the following criteria must be met:(2)

- Installed Cost: $25/kWh + $75/kW (1977 $)
- Overall Plant Efficiency: 65%+
- Footprint: 8kWh/ft^2
- Maximum Height: 20ft
- Minimum Siting Restrictions

There is the usual trade-off between cost and efficiency. Efficiencies less than 65% may be acceptable provided the installed cost drops accordingly. This efficiency includes the penalties associated with rectification and inversion. The footprint criterion allows a 100MWh plant to be located on a half-acre site at a utility substation. The battery components of the plant would occupy approximately a quarter-acre. Observation of a maximum height criterion of twenty feet will minimize problems associated with siting of the plant. The environmental intrusion of the plant under normal and abnormal circumstances must be minimal to allow unrestricted siting. To minimize O & M costs, the plant must operate unattended. Thus, the stored energy would be dispatched from a central location. The 100MWh plant should be capable of being discharged for 5 hours at 20MW and charged over a period of 5 to 7 hours. Charging and discharging of the battery in shorter time periods should also be possible. The practicality of accomplishing this will be predetermined by the rating of the power-conditioning subsystem in the battery plant.

EDA has prepared three conceptual designs for 100MWh zinc-chlorine battery plants as part of the joint EPRI-EDA program to develop this battery for the peak-shaving application. The Mark 2 design was completed in early 1976. Exposure of this design to electric-utility, EPRI, and ERDA (DoE) representatives and to a detailed and critical review within EDA led to the evolution of the Mark 3 design in late 1976. A similar analysis of the Mark 3 design and a realization of its limitations led to conception of the Mark 4 design in March/April 1977.

These designs are described in the next three sections. The discussion section follows in which a comparison of the designs is presented, and the technical status of the joint EPRI-EDA program is briefly reviewed.

*Numbers in parentheses designate References at end of paper.

MARK 2 100MWh BATTERY DESIGN

An artist's rendition of the Mark 2 peak-shaving plant at a utility sub-station is shown in Figure 1. There are eleven 10MWh battery strings, each string consisting of ten 1MWh modules connected in series. Complete string discharge before recharge is desirable. Accordingly, the extra 10MWh string is provided to maintain rated capacity in every cycle. Figure 1 shows each string arranged in two layers to facilitate terminal-bus connection. A radiator for control of the electrolyte temperature in the battery module is located above the center of each string. In the left background, the power-conditioning equipment and the associated bus-work may be seen. The building in the right background contains refrigeration equipment, other auxiliaries, and control equipment. Adjacent to this building are the cooling towers for the refrigeration equipment.

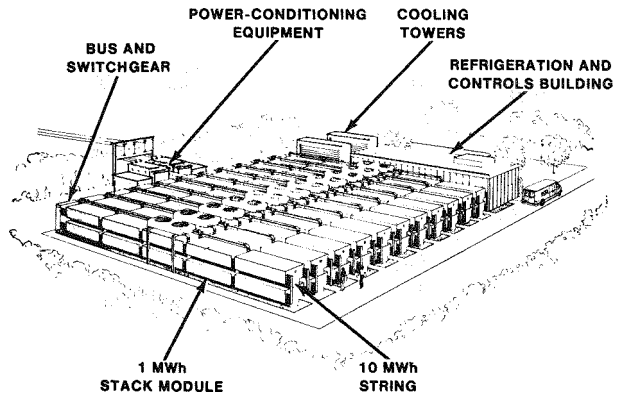

Fig. 1 - Mark 2 design of a 100MWh zinc-chlorine peak-shaving battery plant

Figure 2 shows plan and elevation views of this battery plant. There is a single chlorine-hydrate store consisting of a tank with equipment for hydrate formation and decomposition. This cylindrical tank is located below grade, with approximate height and diameter dimensions of 40ft and 35ft, respectively. Also located below grade are the electrolyte sumps and circulating pumps for each string. The pumps circulate electrolyte for module cooling and hydrate decomposition during discharge. Analysis of the dimensions of the plant reveals that the footprint is 9kWh/ft^2. The maximum height criterion of 20 feet is observed. The access aisles are 3 feet in width to allow servicing of the module-pump motors.

Figure 3 shows a 1MWh module, consisting of ten essentially independent 100kWh submodules, one of which is shown in total, running the length of the module. These submodules are arranged in two banks, each with five tiers. Each submodule has a power terminal at both ends and consists of fifty series-connected 2kWh cells, the design of which is based on the comb-type bipolar concept.(1) The cells are fed individually by a distribution-manifold system from a single pump located centrally within the 1MWh module. The return flow to the pump is by gravity flow from each cell over cascades into the sump.

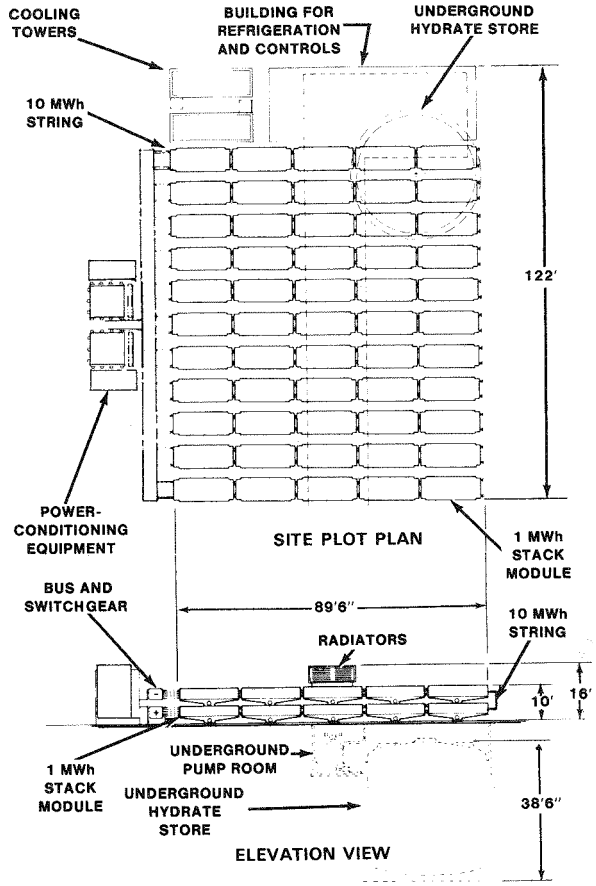

Fig. 2 - Plan and elevation views of a Mark 2 100MWh zinc-chlorine peak-shaving battery plant

The charge current density is 33mA/cm^2 at an average cell voltage of 2.25V. The discharge current density and voltage are 30mA/cm^2 and 2.00V, respectively. For the purposes of design, the

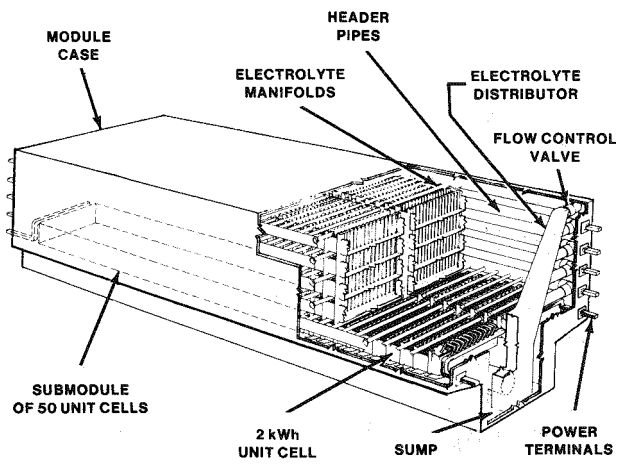

Fig. 3 - Interior view of Mark 2 1MWh module. Note five tiers of 100kWh submodules, two submodules per tier

electrochemical energy efficiency is assumed to be 80% in an ultimate Mark 2 peak-shaving plant. The voltaic efficiency--the ratio of the average voltages in discharge and charge, i.e. 2.00V/2.25V--is 88.9%. The usable coulombic efficiency is therefore 90%, i.e. the ratio of the electrochemical energy and voltaic efficiencies. The overall plant efficiency is in excess of 70%.

A simulated manufacturing plan was prepared in order to estimate the costs of the 1MWh battery modules. Costing information for graphite, plastics, pumps, motors, and other components was developed. The costing analysis study concluded that at a production rate of one-hundred 100MWh plants per year, the selling price in 1976 dollars would be $29/kWh. At a production rate of one 100MWh plant per year, this price would rise to $62/kWh. Bechtel were commissioned by the Electric Power Research Institute to estimate the cost for the chlorine-storage subsystem of a 220MWh zinc-chlorine battery plant. Their conservative estimating yielded a cost of $62/kWh for a one-of-a-kind system.(3) It can be shown that this cost is compatible with the costs for the chlorine-storage subsystems in the EDA costing efforts, quoted above.

Feedback from electric-utility, EPRI, and ERDA (DoE) representatives, Bechtel personnel, and internal EDA studies indicated that the Mark 2 design could be criticized on the following grounds:

Underground Store-As the store in this design is underground it is likely that the design will be limited to certain kinds of terrain.

Site Labor-Substantial on-site assembly work is required. The nature of this work requires skilled assembly and adherence to tight quality specifications. Site labor will therefore be a significant expense, particularly if utility labor is employed.

Piping Cost-In order to provide for decomposition of the chlorine hydrate during discharge, warm electrolyte must be circulated from each module to heat exchangers in the store. Substantial piping is required and, as a result, becomes a major cost for this design. In addition, the transport of chlorine gas to a single store during charge and back to every module during discharge will involve the use of large-diameter piping for which the valving technology is known to be expensive.

Electrolyte Distribution-Uniform distribution of electrolyte with a single pump to each and every chlorine-electrode pair in the five tiers of unit cells poses considerable problems from the standpoints of hydraulic-energy conservation and engineering.

MARK 3 100MWh BATTERY DESIGN

Minimization of site labor was the major goal of the Mark 3 design. Thus, all components of the battery plant were designed so that they could be transported without special permit to the substation. Each plant component, therefore, had to fit within a volume: 40ft by 8ft by 10ft.

An artist's rendition of the Mark 3 peak-shaving battery plant is shown in Figure 4. The plant consists of three superstrings, each delivering 36MWh. Each superstring is comprised of six 6MWh battery-stack modules, each of which is transported to the site separately. Associated with each superstring are eight cylindrical hydrate stores, each with hydrate-formation equipment. The eight stores are coupled, i.e. have a common gas space, with each other and with the six stack modules comprising the superstring. In the left background, the bus-work may be seen leading to the power-conditioning equipment. Also in the left background are three sets of refrigeration equipment on individual skids, each skid having been transported separately to the substation.

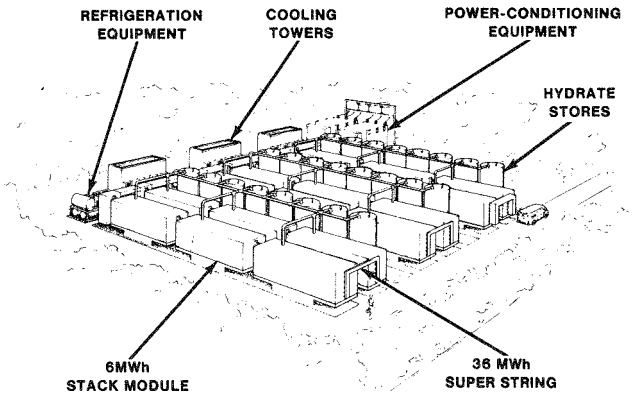

Fig. 4 - Mark 3 design of a 103MWh zinc-chlorine peak-shaving battery plant

Plan and elevation views of the battery plant are shown in Figure 5. The footprint of the battery

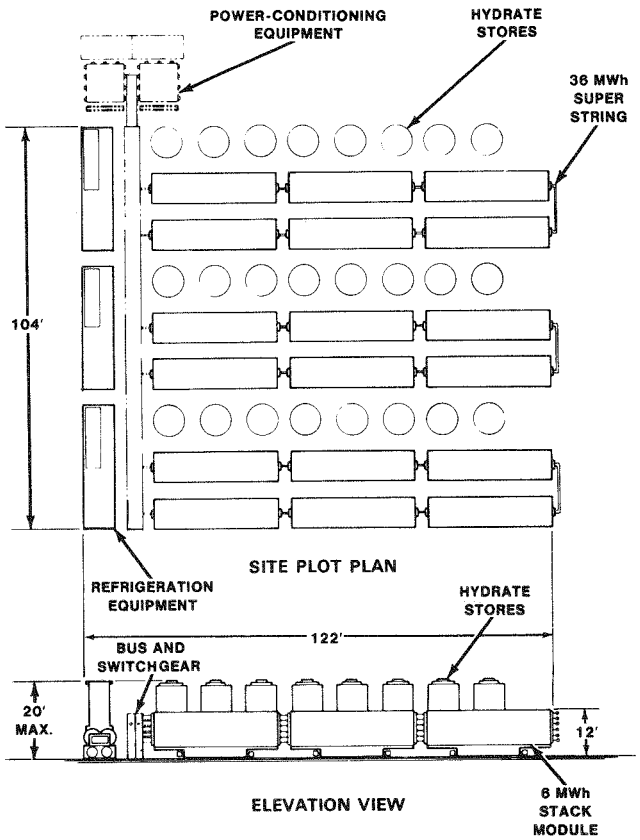

Fig. 5 - Plan and elevation views of a Mark 3 100MWh zinc-chlorine peak-shaving battery plant

plant is 8kWh/ft^2, and the height criterion of 20ft is observed. The access aisles are 4ft wide to allow for easy servicing of the motors of the six pumps in each module. In contrast to the Mark 2 design, the entire battery plant is located above grade. Thus, the cost of site preparation is significantly less. In addition, battery-plant assembly at the sub-station is simplified due to the extensive use of prefabricated components. The goal of a significant reduction in site-labor charges is thereby realized with the Mark 3 design.

The 6MWh battery-stack module is shown schematically in Figure 6. Although the module is a hydraulic unit with a single sump, there are six electrically-separable submodules. Each of the submodules is fed by its own pump located in the sump. These submodules consist of two levels, each with four parallel runs of seventy-two series-connected 1.76kWh cells. One consequence of the electrical isolation of the submodules within each module is that there can be six strings within a given superstring. This would be accomplished by busing together in series any given level of submodules in a superstring. In this way, it is possible to have six or less of these strings operating independently (but in the same charge or discharge mode) within the superstring at any time. This is useful for load-following. The rated capacity of the battery plant is 103MWh, i.e. seventeen 6MWh strings. One extra 6MWh string is provided because of the desirability of complete discharge of each string before recharge.

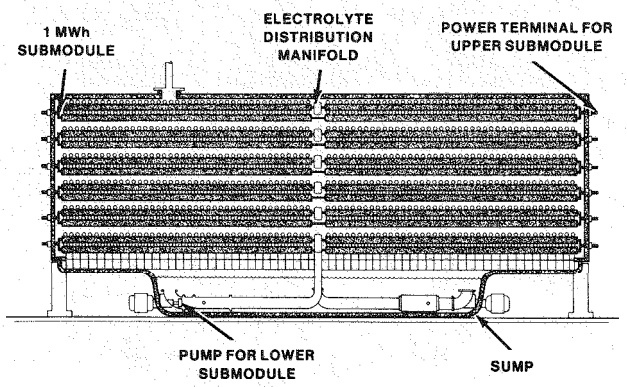

Fig. 6 - Cross-section of a Mark 3 6MWh module. Note six separate submodules, each fed by an electrolyte pump mounted in the sump

In the stack module, the charge current density was assumed to be 45mA/cm^2 at an average voltage of 2.25V. The discharge current density and voltage were assumed to be 40mA/cm^2 and 2V, respectively. This reflects improvements in cell technology during 1976. The electrochemical energy efficiency was assumed, for the purpose of design, to be 80% with a voltaic efficiency of 89.9% and a usable coulombic efficiency of 90%. The overall plant efficiency was in excess of 70%.

Preliminary cost estimates indicated that relative to the Mark 2 design the increased costs due to the replacement of the single underground store by twenty-four above-grade stores are approximately offset by savings in site-preparation, piping, valving, and installation. A further savings results from the increased discharge current density (40mA/cm^2 in Mark 3 vs. 30mA/cm^2 for Mark 2) which significantly reduced graphite-electrode costs. This was however substantially offset by increases in the price of graphite during 1976. Nevertheless, a selling price of approximately $21/kWh (1976 $) was generated for a production rate of one-hundred 100MWh battery plants per year. (4)

Criticism of the Mark 3 design by electric-utility representatives centered mainly on the safety and environmental aspects of these plants. Rupture of a single hydrate store could spill up to 3 tons of chlorine hydrate and, because of the design, open the other seven stores of the superstring to the ambient. Despite the safety of chlorine hydrate, which decomposes very slowly to release gaseous chlorine and water above 9.6°C, representatives of Southeast-U.S. utilities indicated that obtaining siting permits for residential areas might be difficult. Representatives of one major Midwest utility, which has experience with chlorine both at its generating plants and on its railroad lines, were less concerned. A more serious criticism was leveled at the Mark 3 design as a result of analysis performed at EDA. It was concluded that the stack module would be very difficult to manufacture efficiently and cheaply because of its size and the high packing density of cells.

MARK 4 100MWh BATTERY DESIGN

Realization of overall plant efficiencies of 65% or greater is dependent on the achievement of electrochemical energy efficiencies in excess of 75%. The major contributor to electrochemical inefficiencies is the coulombic inefficiency during charging of the battery. It may be shown that coulombic efficiencies on charge must lie in excess of 90% if a 75%+ electrochemical energy efficiency is to be achieved. This takes into account the expected imbalances between cells within a module and between modules in a string. The only technique known to EDA at this time that allows achievement of these coulombic efficiencies, involves desorption of chlorine from the electrolyte by generation of a partial vacuum over the stack during charge. This reduces the chlorine concentration in the electrolyte and thus the chemical corrosion of electrodeposited zinc. It should be noted that the only reported electrochemical energy efficiency in excess of 70% for a zinc-chlorine system was reported for a 1kWh cell in which the stack was operated under a partial vacuum during charge.(5)

Application of this concept to the battery stack in the Mark 2 and Mark 3 designs was considered to be impractical because of the additional structural requirements necessary to place the stacks under a -5psig vacuum. In order to use this desorption technique for improving the electrochemical energy efficiency, drastic reduction of the battery-stack size relative to the Mark 2 and 3 designs was deemed necessary. Simultaneously, a substantial reduction in the size of the hydrate stores was considered appropriate in order to improve the desirability of 100MWh battery plants for siting at substations in residential areas. Greater dispersal of chlorine hydrate in multiple stores would greatly reduce the probability of accidentally releasing a significant quantity of chlorine.

In view of the need for a diminished size of stack and store, an integrated battery module concept--battery stack, store, heat exchangers, pumps, and hydrate formation equipment in a single package--became desirable. The size of these modules was fixed in the 50-60kWh range, in order to take advantage of existing EDA technology for electric-vehicle batteries.

An artist's rendition of a 100MWh battery plant based on this concept is shown in Figure 7. The battery portion of the plant consists of forty racks--each rack containing forty-four 58kWh modules. The refrigeration equipment--compressors, condensors, glycol pumps, and cooling towers, all mounted on skids--is located in the background, as is the power-conditioning equipment. The bus-work and glycol piping are shown running centrally through the plant. Glycol is supplied to each module by means of a distribution system built into the rack structure supporting the individual modules. This glycol provides for cooling of the battery during discharge, and, more importantly, for chilling of the store during charge. To simplify busing, a pair of racks are connected to form two electrical strings. Thus, there are forty 2.5MWh dc strings in the battery plant, each with its individual disconnect.

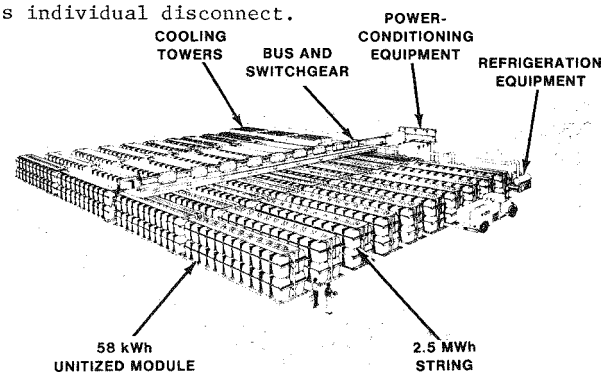

Fig. 7 - Mark 4 design of a 100MWh zinc-chlorine peak-shaving battery plant

The 100MWh plant is shown in plan and elevation in Figure 8. The footprint of the battery component of the 100MWh plant is 8kWh/ft^2. The highest point--the switchgear enclosures on the bus-work--lies 17.5ft above grade, well below the maximum height criteria of 20ft. The access aisles are 4ft wide permitting easy substitution for a faulty module.

An exploded view of the 58kWh module is shown in Figure 9. The six submodules--three tiers of two per level--are shown at the top of the module in the stack compartment. The store, hydrate former, and electrolyte sump are seen in the lower section. Magnetically-coupled electrolyte and gas pumps are located at the bottom of the module. Their motors are bolted to the case. Operation of the gas pump during charge results in hydrate formation and allows the maintenance of a partial vacuum over the submodules. The operation of the module is discussed elsewhere.(6)

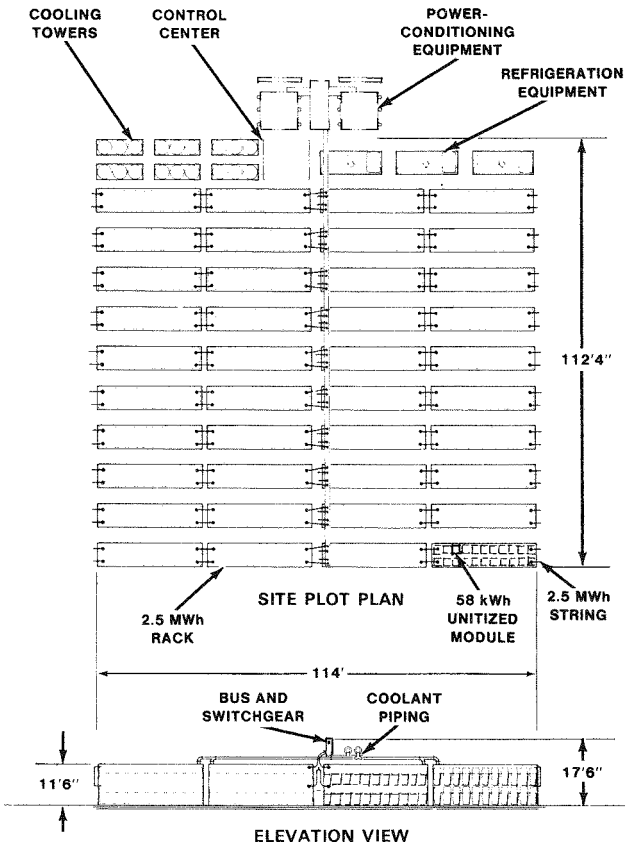

Fig. 8 - Plan and elevation views of a Mark 4 100MWh zinc-chlorine peak-shaving battery plant

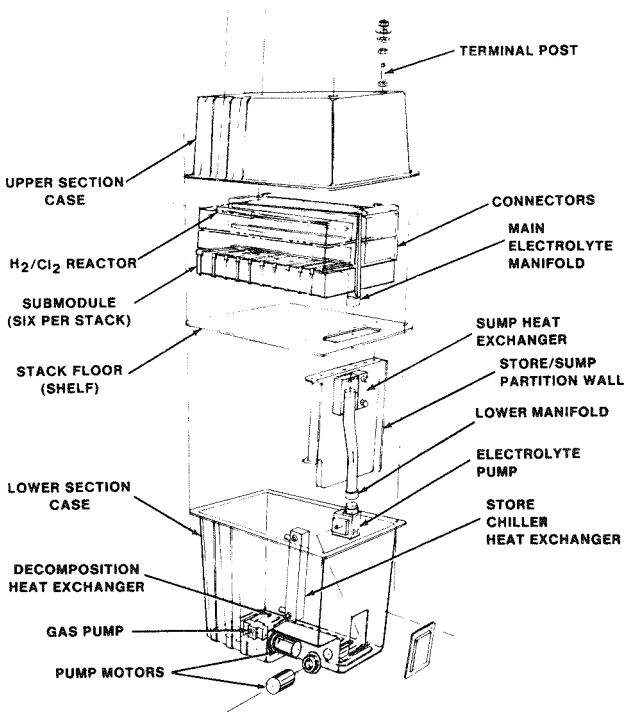

Fig. 9 - Exploded view of Mark 4 battery module

The stack portion of the battery consists of six 9.7kWh ten-cell submodules bused in parallel. The charge current density is 30mA/cm^2 at an average cell voltage of 2.18V. The discharge current density and average cell voltage are 36mA/cm^2 and 1.96V, respectively. A charge time of seven hours is employed, significantly greater than the five-hour charge times for the Mark 2 and Mark 3 designs. However, the discharge time remains at five hours. A list of the sizes and voltages of all electrochemical units contained in the Mark 4 design is provided in Table 1.

Table 1 - Mark 4 Battery-Design Definitions

Component	Delivered Energy	Average Voltage Charge	Discharge
String	2.5MWh	959V	862V
Rack	2.5MWh	--	--
Module	58kWh	21.8V	19.6V
Submodule	9.7kwh	21.8V	19.6V
Unit Cell	0.97kWh	2.18V	1.96V

The charge and discharge coulombic efficiencies are assumed for the purposes of design to be 91% and 96%, respectively, for a round-trip efficiency of 87.4%. Because of anticipated cell imbalance within the module and between modules in a string, a further 2% coulombic inefficiency is assumed. Thus, the usable coulombic efficiency is 85.4%. The electrochemical efficiency is therefore the product of (85.4%) and (1.96V/2.18V), or 76.7%. An energy flow diagram shown in Figure 10, illustrates that the overall energy efficiency

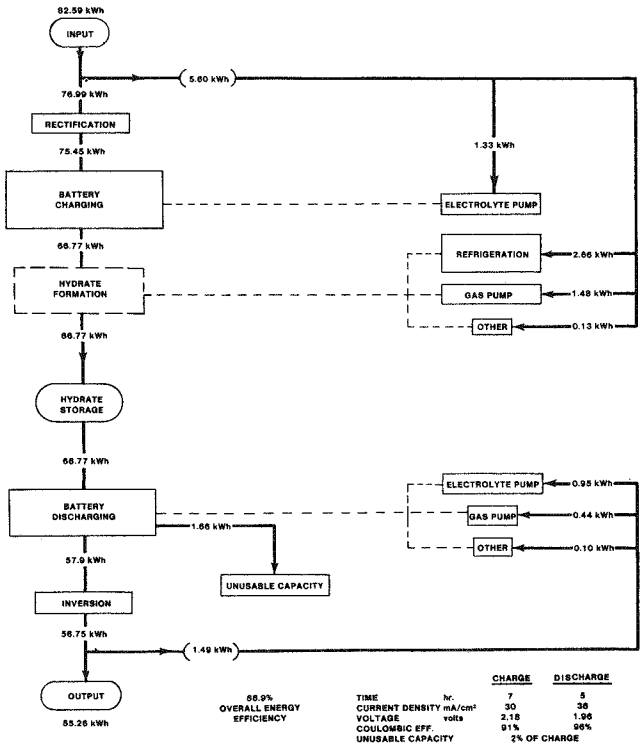

Fig. 10 - Energy flow diagram for a battery module in the Mark 4 100MWh peak-shaving plant

after rectification, inversion, and all parasitic losses--pumps, refrigerator, and the ultra-violet light source for hydrogen recombination with chlorine--is 67%. The refrigeration system is expected to operate at a coefficient of performance of 5.5. The assumed efficiencies of the electrolyte and gas pumps are 60% and 25%, respectively.

Five years after initial commercialization of the battery system, EDA has projected that the battery module will deliver 66kWh at electrochemical energy efficiency of 79%. These capacity and efficiency improvements will be made by slight increases in charge and discharge current densities and by better control of battery-stack manufacture. A manufacturing plan was devised and a facility layout was prepared (6) for the production of one-hundred modules per day, corresponding to the sale of over fifteen 100MWh battery plants per year. The materials and labor costs for module production are shown in Table 2. Direct quotes and engineering estimates were used for purchased materials and components. In all cases the estimated losses associated with manufacturing have been included.

Table 2 - Mark 4 Module Materials and Labor Costs (1977 $)

Category	Direct Materials	Direct Labor
Zinc electrodes	$ 63.00	$ 5.40
Chlorine electrodes	271.20	5.40
Electrode masking	9.62	.00
Bus bars	58.21	7.50
Comb assembly	.00	7.20
Submodule trays	10.61	.00
Submodule assembly	.00	5.40
Chassis structure	37.31	2.40
Hydrogen reactor	9.60	.00
Store coil and filter	10.56	.00
Case components	117.22	.00
Pumps	199.40	.00
Heat exchangers	156.62	.00
Electrical connectors	35.95	.00
Miscellaneous	18.00	.00
Module assembly	.00	14.40
Electrolyte	71.52	.00
TOTALS	$1068.82	$47.40

It is clear from Table 2 that the important components from a cost standpoint are: porous graphite for chlorine electrodes, electrolyte and gas pumps, heat exchangers, and the case components. This costing exercise is useful mainly in that it serves to set targets for the development programs. The yearly battery sales projections for a production rate of one hundred modules per day are computed as shown in Table 3. Sales of $41 million

Table 3 - Battery Sales (1977 $) for Yearly Production of 25,000 Modules

Category	Cost ($000)
Direct Materials	26,721
Direct Labor & Fringes	1,551
Overhead	4,130
FACTORY COST	$32,402
G.S.&A. (9%)	2,916
Return on Investment	5,687
PROJECTED BATTERY SALES	$41,005

correspond to a selling price of approximately $25/kWh. Balance of plant, e.g. refrigerator, power-conditioning, and installation costs may be shown to lie at approximately $90/kW.(6)

DISCUSSION

Each of the three battery designs represent extremes in design philosophy--Mark 2 with its single underground store and large 1MWh stack modules, Mark 3 with its larger 6MWh stack modules and multiple stores above ground, and Mark 4 with its integrated and much smaller 58kWh modules. EDA has judged the Mark 4 design to be optimal from the standpoints of efficiency, safety, acceptability, for siting in residential areas, and manufacturability, while comparing favorably in cost and reliability to the other designs. The reasons for and the consequences of this selection are summarized below:

ELECTROCHEMICAL PERFORMANCE-The plant efficiency is a strong function of the electrochemical energy efficiency. A comparison of the electrochemical design points for the three designs is provided in Table 4. In single-cell work, the current-voltage performances called for in all of the designs have been exceeded. EDA recognizes, however, the challenge in reproducibly extending this performance to batteries. In a 1kWh battery with ruthenia-catalyzed porous-titanium chlorine electrodes, usable coulombic efficiencies ranging from 80% to 86% have been demonstrated (5) when the battery stack was operated under vacuum during charge, thus dechlorinating the electrolyte. The Mark 2 and Mark 3 target of 90% may be overly-optimistic for three reasons: cell imbalance within the submodules; module imbalance within the string; and the inability of these designs to achieve the desired reduction of chlorine concentration in the electrolyte during charge. There remains the possibility that acceptable coulombic efficiencies may be attainable in separator-less zinc-chlorine cells without reduction of the chlorine partial pressure. However, there is no question that desorption techniques will improve electrochemical efficiencies and most likely lead to greater fuel conservation by electric utilities. Mark 4--by virtue of its module size permitting chlorine desorption on charge--has a strong edge in potential performance over the Mark 2 and Mark 3 designs. Further, as the maximum voltages applied to the Marks 2, 3, and 4 modules are 113V, 162V, and 21.8V, respectively, it is anticipated that effects associated with parasitic currents and uniformity of electrolyte delivery to individual cells, potentially strong contributors to cell imbalance within the submodule, will cause least problems in the Mark 4 design.

Table 4 - Comparison of Electrochemical Design Points

PARAMETERS	MODE	DESIGN MARK 2	DESIGN MARK 3	DESIGN MARK 4
Current Density (mA/cm^2)	Charge	33	45	30
	Discharge	30	40	36
Cell Voltage (V)	Charge	2.25	2.25	2.18
	Discharge	2.00	2.00	1.96
Time (h)	Charge	5	5	7
	Discharge	5	5	5
Usable Coulombic Eff.		90%	90%	85%
Electrochem. Energy Eff.		80%	80%	77%

RELIABILITY-The unit quantities of major components in the three battery-plant designs are listed in Table 5. It should be noted that the hydrate stores are integrated in the Mark 4 modules. The striking difference between the Mark 4 and the other two designs lies in the number of electrolyte and gas pumps employed. In general, the major source of problems with plant reliability is expected to involve these pumps and their motors. For the Mark 4 design, magnetic coupling of the pump and motor is possible with conventional technology. These seal-less pumps are known to be more reliable and to require less maintenance than the pump technology involving stuffing-boxes required in the Mark 2 and Mark 3 designs. From an overall power plant reliability and availability standpoint, if a pump fails in a Mark 4 module, the 2.5MWh string can be shut down, dropping only 2.5% of the plant capacity. Further, servicing of the module will take place in general after module removal, easily accomplished in this design. Thus, despite the multiplicity of pumps called for in the Mark 4 design, the availability of the battery plant is likely to be greater than for plants based on the Mark 2 and Mark 3 designs.

Table 5 - Unit Quantities of Major Components

COMPONENT	DESIGN MARK 2	DESIGN MARK 3	DESIGN MARK 4
Modules	110	18	} 1760
Stores	1	24	
Pumps	125	132	3520

COST-Each of the costing efforts for the Mark 2, 3, and 4 conceptual designs was forced to meet the required cost targets. Within each design, this exercise is useful as it establishes cost targets for the components and provides guidance for the development programs. However, the significance of comparisons between these costing efforts for the three designs is unclear because of the different probability of meeting the cost target for each design. Nevertheless, some of these cost aspects are compared below:

Battery Stack-In general, there are few if any economies of scale in electrochemical systems. Once the electrode size and current density are fixed, as they have been to a first approximation for the present comb-type bipolar concept based on theoretical and experimental current-distribution studies (7), the electrode cost per square foot for a 100MWh plant will be independent of the module size. As chlorine desorption from the electrolyte can be better accomplished in smaller modules, there is a cost penalty associated with battery-stack scale-up because of the inverse relationship of cost and coulombic efficiency.

Pumps-Economies of scale for the large pumps in the Mark 2 and 3 designs are offset by the economies of production for the greater number of small magnetically-coupled pumps in the Mark 4 design. These smaller pumps do not require the stuffing boxes and

associated water-purification equipment necessary for much larger pumps.

Module Packaging-The cost of packaging of modules is a small fraction of total battery cost because of the use of low-cost plastics in the low-temperature aqueous system. The greater surface area of module case in the Mark 4 design is counterbalanced by the reduced material thickness.

Manufacturability-The battery module is the major cost component in all designs. Because of its size, the Mark 4 module will be more easily manufactured--a hidden factor in most cost analyses for conceptual designs--which will lead ultimately to significant cost advantages relative to the Mark 2 and 3 designs.

SAFETY AND ENVIRONMENTAL ASPECTS-Public acceptance of peak-shaving battery plants will hinge ultimately on meeting stringent safety and environmental-impact criteria. For the zinc-chlorine system, these criteria revolve mainly around the question of accidental release and dispersion of toxic amounts of chlorine, the only potential hazard. The total amounts of chlorine which might be released per single line rupture are 75 tons, 25 tons, and 0.05 tons for the Mark 2, Mark 3, and Mark 4 designs, respectively. Mark 4 is by far the most acceptable because of its use of a large number of non-interconnected hydrate stores. It should be noted that chlorine storage in all designs is based on the use of solid chlorine hydrate, which decomposes only slowly above 9.6°C. The use of liquid chlorine, which decomposes above -34°C at ambient pressure, as the chlorine storage medium significantly reduces the potential health and environmental hazards in the immediate vicinity of an accidental spill. The solid hydrate would not spread along the ground like liquid chlorine and thus would expose much less surface area to ambient heat-transfer sources. Hydrate also has a latent heat for chlorine-gas release 3.8 times that for liquid chlorine. This difference, as well as the higher temperature, substantially reduces the release rates for gaseous chlorine under all ambient conditions. A simple first-approximation analysis suggests a reduction of two orders of magnitude or greater when hydrate is employed. Credible accident scenarios have been developed and analyzed at EDA in terms of causes, human hazard, atmospheric dispersion, and possible clean-up operations.(6) Figure 11 shows plan and elevation views of the effects of a hydrate spill at a 100MWh Mark 4 battery plant, located on a one-acre utility-substation site. Even after a worst-case accident and under worst-case meteorological conditions, hazardous levels of chlorine, 50ppm or greater, are not found outside the substation perimeter. For zoning purposes, it is likely that the battery portion of the plant will be enclosed in a building. This will result in the total containment of accidentally-released gaseous chlorine. From these and similar studies, EDA has concluded that with proper design the zinc-chlorine peak-shaving battery plant will pose negligible health or environmental hazards at a substation location in a residential area.

SCALE-UP-For the Mark 2 design, final scale-up would not occur until construction of a 100MWh demonstration plant because of its single hydrate store. Final scale-up for the Mark 2 1MWh battery-stack module would occur much earlier. A BEST-Facility battery based on this concept would deliver 10MWh dc. It would consist of ten series-connected 1MWh modules coupled to a single chlorine-hydrate store, specially designed and built for this facility. Final scale-up for the Mark 3 plant would occur earlier because of its use of multiple stores. The 6MWh module prototype, however would be built for the BEST Facility, and tested there. This is true also for the hydrate

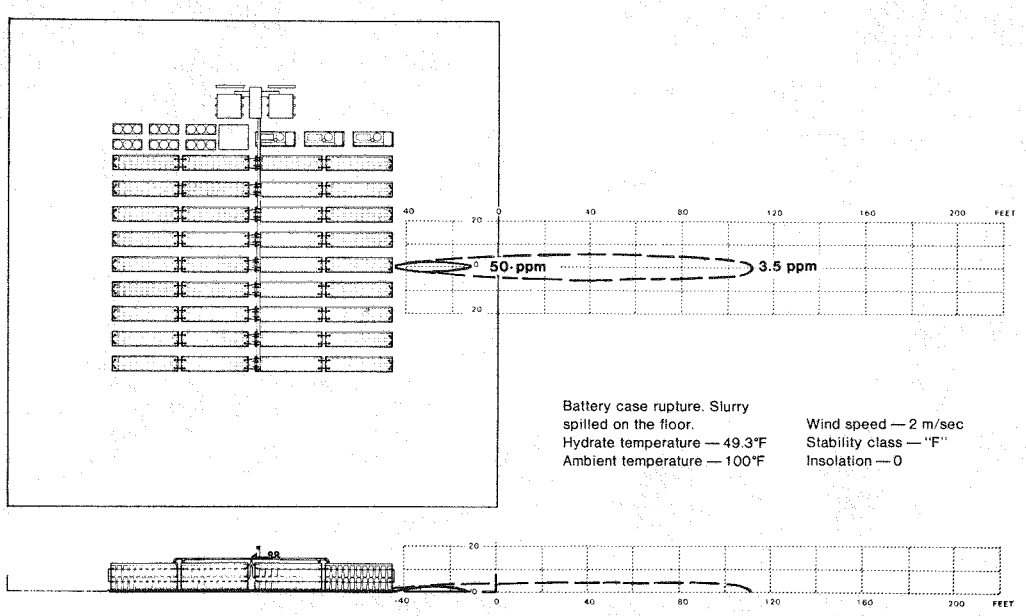

Fig. 11 - Maximum chlorine dispersion after accidental spillage of chlorine hydrate from a battery module under worst-case meteorological conditions. Isopleths of 50ppm and 3.5ppm indicate hazardous and odor-threshold levels, respectively

stores in this conceptual design. Two stores (see Figure 4) would be required in order to form the 6MWh battery system to be tested at the BEST Facility. The Mark 4 prototype module has already been built and tested as part of the joint EPRI-EDA program. The 45kWh module, assembled and tested in late 1977, is shown in Figure 12. To date, the battery has delivered in excess of the design capacity but at a reduced efficiency.(6) Refurbishing of the module is presently underway to raise the delivered energy to 50kWh at an electrochemical energy efficiency of 70%.

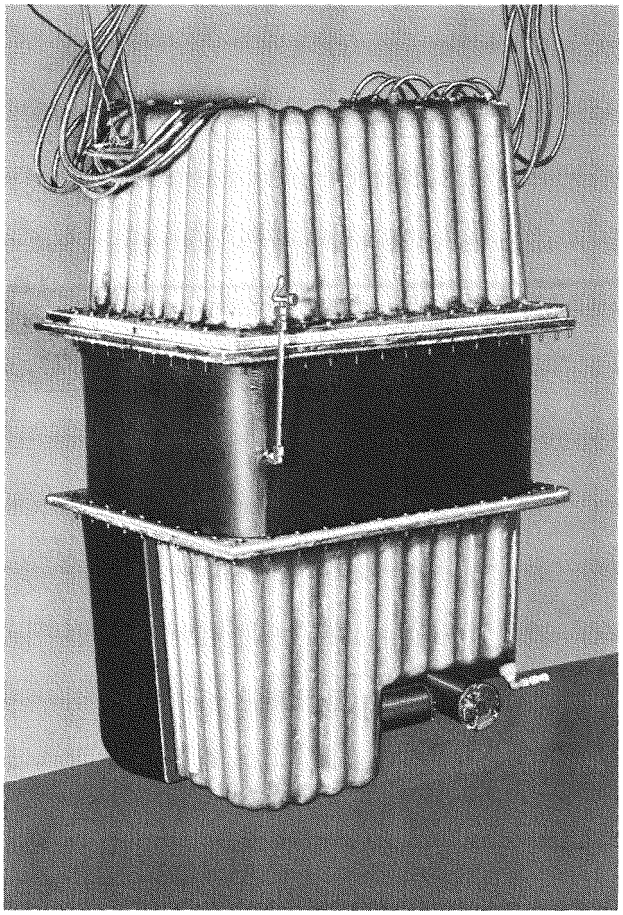

Fig. 12 - 45kWh zinc-chlorine battery module

The zinc-chlorine battery system to be tested at the BEST Facility in late 1980 will deliver 4.8MWh dc. The system will consist of two racks, each comprised of forty-four modules as in the Mark 4 100MWh battery plant design. Each module will deliver 55kWh, approximately 3kWh less than the anticipated energy delivered by a module in the first commercial zinc-chlorine battery plant.

ACKNOWLEDGEMENTS

The authors wish to thank Mr. P. Carr, Dr. Chen Chi, Mr. G. Henriksen, and Dr. S. Kodali, of EDA, Dr. J. Birk and Mr. W. Spindler of the Electric Power Research Institute, Mr. J. C. Smith and Mr. Kurt Klunder of the U.S. Department of Energy, and members of the EPRI utility panel for many useful discussions. The financial support provided for this work by Gulf + Western Industries and EPRI is also gratefully acknowledged.

REFERENCES

1. P. C. Symons and C. J. Warde, "Zinc-Chlorine Batteries for Load-Leveling". Proceedings of the Symposium on Load-Leveling, N. P. Yao and J. R. Selman, Editors, Volume 77-4, The Electrochemical Society, Princeton, N.J., 1977; pp. 334-352.

2. J. R. Birk and N. P. Yao, "Batteries for Utility Applications: Progress and Problems". Proceedings of the Symposium on Load-Leveling, Reference 1, pp. 229-238.

3. R. F. Battey, "Engineering Design and Cost Analysis of Chlorine Storage Concepts for a Zinc-Chlorine Load-Leveling Battery". Prepared by Bechtel Corporation, San Francisco, Ca. EPRI EM-259, Final Report, 1976.

4. P. C. Symons, "Development of High-Efficiency Cost-Effective Zinc-Chlorine Batteries for Utility Peak-Shaving, 1976". Prepared by Energy Development Associates, Madison Heights, Michigan. EPRI EM-711, Interim Report, 1978: p. 5-2 of Part IV.

5. P. C. Symons and M. J. Hammond, "Evaluation of a 1kWh Zinc-Chloride Battery System". Prepared by Energy Development Associates, Madison Heights, Michigan. EPRI EM-249, Interim Report, 1976.

6. Interim Report on EPRI RP226-3 for 1977. In preparation.

7. W. J. Coughlin III and C. J. Warde, "Current Distribution in Zinc-Chlorine Batteries". To be presented at the Fall Meeting of the Electrochemical Society, Pittsburgh, Pa., October, 1978.